

University of Nottingham
UK | CHINA | MALAYSIA

# Developing Porous Microspheres for Water Treatment Applications

**By**

**Sabrin Abdus Samad**

Thesis submitted to the University of Nottingham for the degree of Doctor of Philosophy

**July 2021**

# Abstract

Water pollution produced by micropollutants has increased in recent decades posing a significant threat to environment and human development. This has fuelled the need for cost effective and sustainable water treatment options to meet demand. Existing porous materials used for wastewater treatment are manufactured based on synthetic approaches which requires use of expensive and or toxic chemicals, long processing time and expensive manufacturing approach. Hence, developing adsorbents using simple, rapid synthesis pathways and with a reduced environmental footprint are still challenging. The principal focus in this thesis was to develop systematic and robust manufacturing of porous materials using flame spheroidisation process which excludes the use of these expensive and toxic chemicals during manufacturing. To date, no research has demonstrated the use of flame-spheroidised porous microspheres for wastewater treatment. As a proof of concept, porous phosphate-based glass (PBG) microspheres developed using flame spheroidisation process were explored for dye removal from water. The porosity levels of PBG microspheres were optimised by exploring the manufacturing process parameters for enabling enhanced and successful separation of micropollutants from water. Organic dye was used as a target contaminant for exploring the separation capability of the porous structure manufactured. The second part of this work involved transferring this proof-of-concept processing method to manufacture porous microspheres, particularly environmentally friendly, low-cost materials such as waste recycled glass and naturally occurring magnetite with suitable micropollutant removal capacities.

In the preliminary studies, 45-63 µm porogen were used to fabricate porous microspheres from phosphate-based glass (PBG) via flame spheroidisation technique. The influence of starting phosphate glass particle size and varied porogen ratios were investigated for optimising the surface area and porosity profile of phosphate-based glass (PBG) microspheres suitable for removing Acid Red 88 (AR88) dye from water. 16 different batches of microspheres were prepared that fall under size range of 125-355 µm. The surface and cross-sectional morphological properties of the microspheres were investigated by scanning electron microscopy (SEM) and mercury intrusion analysis, which revealed the surface pores to be 5-45 µm with interconnected porosity of the microspheres manufactured. This study has also shown that use of higher porogen ratios provided with more interconnected porosity. The greatest surface area (0.54$m^2$ /g) was achieved for 125-150 µm (size S) microspheres in the BET surface area analysis (using Kr gas). The porous microspheres with greater surface area gave better batch adsorption profile compared to microspheres with less surface area. To further improve the adsorption property of porous PBG microspheres, the influence of smaller size porogen (≤5 µm) followed by heat-treatment was investigated. Use of smaller porogen followed by heat-treatment

caused further pore narrowing with the pore size distribution analysis revealing a shift from macropore to mesopores (2-50 nm), giving a surface area recorded 1.33 $m^2/g$ (using $N_2$ gas) for microsphere heat treated at 520°C. The effect of heat-treatment (125 mg/g) demonstrated significant differences in the adsorption studies compared to non-heat-treated microspheres (83 mg/g). This improved adsorption capacity was ascribed to several factors such as increased surface area, open and interconnected porosities, surface charge, presence of porogen and presence of crystalline phases. Furthermore, enhanced column adsorption capacity was observed for heat-treated microspheres which was attributed to the unique geometry and microstructure that provided sufficient residence time for the dye molecules to diffuse into the porous structure. The dye interaction with surface of the microspheres were observed via electrostatic interaction, hydrogen bonding and Lewis acid-base interaction without any internal or external functionalisation of the microspheres.

This study also showed successful manufacture of porous recycled glass microspheres (PRGMs) using a revised methodology considering higher viscosity profiles and melt temperatures of recycled glasses (RG) compared to PBG. In this method, porogen/RG glass mixtures were ground at different time and speed (300 and 500 rpm, for 1 to 15 min.) and mixed with 2% poly vinyl alcohol (PVA) and made into 3D globules (RG-Granular) for spheroidisation. The surface area, porosity and pore size distribution were influenced by the grinding time, grinding speed and porogen to glass particle ratio. Increasing grinding time and porogen ratio revealed an increased specific surface area (from 0.03 to 7.6 $m^2$ /g) of PRGMs retaining 63-65 % porosity. The large and smaller pore diameter of the microspheres ranged from 5.00-0.45 µm and 0.45-0.02 µm, respectively. Results have shown that removal of AR88 and methylene blue (MB) by PRGMs is influenced by pH of dye solution, porogen ratio during PRGMs manufacturing, PRGMs dose, and dye concentrations. In batch process, adsorption and coagulation process was observed for AR88 dye removal whilst MB dye removal capacity was attributed to only adsorption process. The maximum monolayer adsorption capacity ($q_e$) recorded for AR88, and MB were 78 mg/g and 20 mg/g, respectively. XPS and FTIR studies further confirmed that the adsorption process was due to electrostatic interaction and hydrogen bond formation.

Column adsorption data for PRGMs were fit best with the Yoon-Nelson and Thomas models. Based on the Thomas model, the calculated adsorption capacities at flow rate 2.2 ml/min and 0.5 ml/min were 250 mg/g and 231 mg/g, respectively which were much higher than batch scale Langmuir $q_e$ values. It was suggested that a synergistic effect of adsorption/coagulation followed by filtration process was responsible for showing higher adsorption capacities. Furthermore, PRGMs possess high recyclability, and can be directly applied to the next cyclic experiment with nearly similar dye removal efficacy.

This study also demonstrated successful manufacture of porous magnetitic microspheres (PMMs) with the potential for wastewater treatment applications. In addition, XRD and MLA investigations revealed the existence of $Ca_2Fe_2O_5$ brownmillerite mineral in PMMs, confirming a noble single route synthesis utilising the flame-spheroidisation method. Grinding time and the porogen to magnetite particle ratio had an impact on total porosity and pore size distribution. The number of pores and surface area increased when the grinding time and porogen ratio were increased. The surface area of PMMs increased from 0.02 ± 0.01 $m^2/g$ for magnetite particles to 4.70 $m^2/g$ ± 0.01 for PMMs ground for 15 minutes with a 1:3 porogen ratio. The adsorption kinetics of AR88 and MB using unwashed and washed PMMs revealed complete adsorption within 360 mins for all dye concentrations. The maximum monolayer adsorption capacity calculated for UW-PMMs and W-PMMs were 80 mg/g and 50 mg/g respectively for AR88 and 14.5 mg/g and 6 mg/g respectively for MB. The interaction of MB dye with PMMs was primarily caused by a combination of variables including surface area, phase structure, surface hydroxyl density, surface charge, and possible photoactivity. However, more work required to investigate the possible photocatalytic activity of the $Ca_2Fe_2O_5$ which would be a potential area of research for future work.

# Table of Contents

**Abstract** ..... i

**Acknowledgements** ..... ix

**List of publications** ..... xi

**List of Abbreviations** ..... xii

**List of Figures** ..... xiv

**List of Tables** ..... xx

**Chapter 1: Introduction and review of literature** ..... 1

1.1 Primary research motivation ..... 1

1.2 Type of impurities ..... 2

1.2.1 Suspended matter ..... 3

1.2.2 Colloids ..... 3

1.2.3 Dissolved Solids ..... 3

1.3 Wastewater treatment technologies ..... 5

1.3.1 Primary water treatment technologies ..... 6

1.3.2 Secondary water treatment technologies ..... 9

1.3.3 Tertiary treatment technology ..... 10

1.4 Glasses and glass ceramic materials in water treatment ..... 24

1.4.1 Silicate Based Glasses ..... 24

1.4.2 Phosphate based Glass (PBG) ..... 24

1.4.3 Application of glasses and glass ceramic materials for water treatment ..... 25

1.4.4 Common approaches for fabricating porous glass structures. ..... 29

1.4.5 Glass Microspheres ..... 30

1.5 Magnetic materials for water treatment ..... 34

1.6 Challenges in water treatment and novelty of the research ..... 36

1.7 Aims and objectives. ..... 39

1.8 Thesis outline ..... 40

**Chapter 2: Materials and methodology** ..... 41

2.1 Raw materials and Chemicals ..... 41

2.2 Preparation of microspheres ..... 42

2.2.1 Solid microspheres ..... 42

2.2.2 Porous microspheres ..... 43

2.3 Microsphere characterisation methods ..... 45

2.3.1 Scanning electron microscopy (SEM) and Energy dispersive X-ray spectroscopy (EDX)/Elemental mapping ..... 45

2.3.2 X-ray diffraction analysis (XRD) ..... 46
2.3.3 Coulter Laser Diffraction analysis ..... 46
2.3.4 Density measurement ..... 46
2.3.5 Specific Surface area, pore size and pore volume analysis ..... 47
2.3.6 Porosity measurement via mercury porosimetry analysis ..... 47
2.3.7 Mineral Liberation Analysis (MLA) ..... 48
2.4 Viscosity and melt behaviour study of starting glass particles ..... 48
2.4.1 Thermal analysis ..... 48
2.4.2 Ash fusion Test (AFT) ..... 48
2.4.3 Viscosity Analysis ..... 49
2.5 Dye Adsorption studies ..... 49
2.5.1 Adsorbate Dyes ..... 49
2.5.2 Batch adsorption experiment ..... 50
2.5.3 Ultraviolet-Visible Light Spectroscopy ..... 50
2.5.4 Batch adsorption isotherm models ..... 51
2.5.5 Batch kinetic models ..... 52
2.5.6 Fixed bed adsorption experiment ..... 52
2.5.7 Analysis of column data ..... 53
2.5.8 Adsorbent Recyclability ..... 53
2.5.9 Coagulation study ..... 54
2.5.10 Statistical analysis ..... 54
2.6 Microsphere-dye interaction study ..... 54
2.6.1 Optical Microscopy analysis ..... 54
2.6.2 FTIR analysis ..... 54
2.6.3 X-ray Photoelectron Spectroscopy (XPS) analysis ..... 55
**Chapter 3: Optimisation of surface area and porosity and preliminary dye removal studies of PBG microspheres ..... 56**
3.1 Introduction ..... 56
3.2 Results ..... 56
3.2.1 X-Ray Diffraction analysis ..... 56
3.2 2 Energy Dispersive X-Ray analysis ..... 57
3.2.3 Coulter Laser Diffraction analysis ..... 58
3.2.4 Scanning Electron Microscopy (SEM) analysis ..... 60
3.2.5 Density Analysis ..... 61
3.2.6 Surface area and porosity analysis ..... 63

3.2.7 Dye adsorption for batch studies ..... 67
3.2.8 Dye adsorption for column studies ..... 68
3.3 Discussion ..... 69
3.4 Summary ..... 73
**Chapter 4: Effect of Heat-Treatment on Porous Glass Microspheres and Subsequent Dye Removal studies. ..... 74**
4.1 Introduction ..... 74
4.2 Results ..... 74
4.2.1 Scanning Electron Microscopy (SEM) analysis ..... 74
4.2.2 Surface area, pore size and pore volume analysis ..... 78
4.2.3 X-Ray Diffraction analysis ..... 79
4.2.4 Energy Dispersive X-Ray analysis ..... 80
4.2.5 Batch dye adsorption studies ..... 81
4.2.6 Fixed bed adsorption studies ..... 86
4.2.7 FTIR and SEM analysis of microspheres after adsorption ..... 89
4.3 Discussion ..... 90
4.3.1 Influence of smaller size porogen (≤5 μm) and heat-treatment ..... 90
4.3.2 Dye removal study of heat-treated microspheres in batch process ..... 92
4.3.3 Dye removal study of heat-treated microspheres in column setup ..... 93
4.3.4 Factors influencing dye interaction and high adsorption efficacy of heat-treated microspheres ..... 96
4.4. Summary ..... 97
**Chapter 5: Developing porous microspheres from recycled glass. ..... 98**
5.1 Introduction ..... 98
5.2 Structural and compositional analysis of starting recycled glass particles. ..... 98
5.3 Processing of RG materials into Solid microspheres ..... 99
5.4 Porous recycled glass microsphere manufacture using a 'conventional process'. ..... 99
5.5 Structural characterisation of RG particles ..... 100
5.5.1 Thermal analysis of RG ..... 100
5.5.2 Compositional analysis of RG ..... 102
5.5.3 Ash fusion test (AFT) ..... 102
5.5.4 Viscosity analysis ..... 105
5.6 Optimising PRGMs manufacture ..... 107
5.6.1 Effect of grinding time and grinding speed ..... 107
5.6.2 Effect of porogen ..... 109

5.7 Surface area, porosity, and structural analysis of PRGMs ..... 112
5.7.1 Surface area and pore volume analysis PRGMs ..... 112
5.7.2 X-ray diffraction analysis ..... 114
5.8 Adsorption studies ..... 115
5.8.1 Effect of Initial pH ..... 115
5.8.2 Effect of Adsorbent Dose ..... 116
5.8.3 Effect of concentration on Reaction Kinetics ..... 117
5.8.4 Adsorption Isotherms ..... 120
5.9 Coagulation study ..... 122
5.10 Fixed bed adsorption studies ..... 123
5.11 Interaction of Dye with PRGMs ..... 126
5.12 Reusability of PRGMs ..... 133
5.13 Discussion ..... 136
5.13.1 Initial processing trails of RG particles into microspheres using conventional process ... 136
5.13.2 Processing of RG into PRGMs via alternate granular method ..... 138
5.13.3 Factors influencing dye removal by PRGMs ..... 140
5.13.4 Dye removal mechanism and desorption study ..... 145
5.14 Summary ..... 148
**Chapter 6: Developing porous microspheres from natural magnetite. ..... 150**
6.1 Introduction ..... 150
6.2 Results ..... 150
6.2.1 Structural and Compositional analysis of initial (as received) magnetite particles. ..... 150
6.2.2 Solid magnetite microsphere manufacture ..... 151
6.2.3 Developing porous magnetite microspheres. ..... 151
6.2.4 PMMs characterisation ..... 161
6.2.5 Adsorption studies ..... 166
6.3 Discussion ..... 184
6.3.1 Processing of magnetite particles into microspheres via flame-spheroidisation ..... 185
6.3.2 Structural analysis of PMMs: ..... 186
6.3.3 Surface area and porosity profile of PMMs ..... 189
6.3.4 Factors influencing dye adsorption on UW-PMMs and W-PMMs ..... 189
6.3.5 Adsorption mechanism and possible photocatalytic activity ..... 192
6.4 Summary ..... 193
**Chapter 7: Conclusions and future work ..... 195**
7.1 Conclusions ..... 195

7.2 Suggestions for future work ..... 198
**References ..... 201**

# Acknowledgements

''Proclaim! (Or read!) in the name of thy Lord and Cherisher, Who created – Created man, out of a (mere) clot of congealed blood: Proclaim! And thy Lord is Most Bountiful, He Who taught (the use of) the pen, Taught man that which he knew not" [Quran, 96:1-5]'' Indeed, this dissertation and my journey towards a PhD would not have been possible without the grace and the blessings of Allah,

I deeply grateful to Dr. Ifty Ahmed for his unwavering academic support and advice, as well as commitment for keeping me on track and the patience he offered during the difficult period of my PhD. I'd also want to express my gratitude to my other supervisor, Professor Edward Lester, for his unwavering support and advice, and unending encouragement.

I am grateful to my Advanced Materials Research Group friends and colleagues for their the constant support and endless discussions; Arafat, Dr Zakir, Dr Reda, Dr Towhid, Dr Sumaya, Dr Uresha, Dr Matthew, Caitriona, Ellena, Farah, Dr Gabriel, Dr Laura, Jesus, Benjamin, Lauren, Henry and Saira are only to name a few. Some special thanks go to Dr Ian Clark, Tasan, Scott Priest, Cameron Jackson, Patrick Daley, and Jacob Smith. Especially Ian and Jacob helped me with a lot of information and training in the early stages related with dye adsorption experiment.

I'd also want to thank the ITRC, Wolfson Building, and nmRC technical team for their advice and technical help during my PhD. I would especially like to name, Dr Nigel Neate, Dr Hannah Constantin, Jason Greaves, John Kirk, Max Mason, Kieran Orange, Richard Homer, Rory Screaton, Martin Roe and Dr Elisabeth Steer.

I would also like to acknowledge the Department of Chemical and Environmental Engineering and Department of Material, Mechanical and Manufacturing Engineering for offering me part-time teaching activity at University of Nottingham, especially Dr Katy McKenzie and Dr Setia Hermawati. Thanks both for your kind support and help all the time.

I am also grateful to the Faculty of Engineering Research Excellence PhD Scholarship, University of Nottingham for funding my studentship.

I am thankful to have met and worked with a nice bunch of people in Jubilee Campus. Dr. Mohamed Elmaghrbi, Dr. Kamal alskaf, Dr Subhasish, Dr. Rony, Dr. Marina, Ishrar, Tanvir, Wafaa, Ahmed, Xuelei, Joe, Amy, Jiarui, Mina, Lei, Kristina, Yvonne, Sally and Jenny. We have had a lot of fun and had some intriguing conversations about life. The time I spent with you will be remembered fondly for the rest of my life.

Huge thanks also go to Mesbah vaia, Tumpa apu, Shaquie vaia, Mahabub, Purba apu, Shadab vai, Kashfia, Qur Vai, Shahadat Vai, Kaafi vaia, Rimon Vai, Sanchita apu, Adil vai, Sumaya apu, Touseef vai, Meem apu, Tamal, Sakib vaia, Faisal vaia, Mofakkar vaia and Runa apu for their unconditional friendship, time, and support during my PhD.

A very special thanks to my husband Arafat, my best friend, my greatest support, my biggest comfort, my strongest motivator and for his unconditional love, patience, and support. I am highly grateful for his positivity and simplicity.

Finally, I would like to express my deepest gratitude to my family especially my father and my late mother for always believing in me and being my foundation and strength in life. A very special thanks to my younger brother Salhin for his lame jokes and limitless smiles that kept me going. I thank them from the bottom of my heart. I love you all so so much!! I also would like to express my gratitude to my in-laws for their care, love, and support for me and always encouraging me for my works.

# List of publications

## Journal articles

1. **Samad, S. A**., Arafat, A., Ferrari, R., Gomes, R. L., Lester, E., & Ahmed, I. Adsorption Studies and Effect of Heat-Treatment on Porous Glass Microspheres. *International Journal of Applied Glass Science 2021*. (In press).
2. Díaz, J. M., **Samad, S. A**., Steer, E., Neate, N., Constantin, H., Islam, M. T., ... & Ahmed, I. (2020). Flame spheroidisation of dense and porous $Ca_2Fe_2O_5$ microspheres. *Materials Advances, 1(9), 3539-3544*.
3. Arafat, A., **Samad, S. A**., Titman, J. J., Lewis, A. L., Barney, E. R., & Ahmed, I. (2020). Yttrium doped phosphate-based glasses: structural and degradation analyses. *Biomedical Glasses*, *6*(1), 34-49.
4. Arafat, A., **Samad, S. A**., Wadge, M. D., Islam, M. T., Lewis, A. L., Barney, E. R., & Ahmed, I. (2020). Thermal and crystallization kinetics of yttrium-doped phosphate-based glasses. *International Journal of Applied Glass Science*, *11*(1), 120-133.

# List of Abbreviations

| | |
|---|---|
| Acid red 88 | AR88 |
| Advanced oxidation processes | AOP |
| Backscattered electron | BSE |
| Biological oxygen demand | BOD |
| Bridging oxygen | BO |
| Brunauer-emmett-teller | BET |
| Carbon nanotubes | CNT |
| Chemical oxygen demand | COD |
| Circular economy | CE |
| Criticality ratio | CR |
| Dissolve organic matter | DOM |
| Dissolved ozone flotation | DOF |
| Emerging contaminants | ECs |
| Empty bed residence time | EBCT |
| Endocrine disruptor's | ECDs |
| Energy dispersive X-ray spectroscopy | EDX |
| Environmental quality standards | EQS |
| Flame-spheroidisation | FS |
| Granular activated carbon | GAC |
| Graphene oxide | GO |
| Layered double hydroxides | LDH |
| Low fouling composite | LFC |
| Lowest unoccupied molecular orbital | LUMO |
| Magnetic resonance imaging | MRI |
| Magnetite solid microspheres | MSM |
| Mercury intrusion porosimetry | MIP |
| Metal-organic frameworks | MOFs |
| Methylene blue | MB |
| Microfiltration | MF |
| Mineral liberation analysis | MLA |
| Multi effect distillation | MED |
| Multistage flash distillation | MSF |

| | |
|---|---|
| Nanofiltration | NF |
| Natural organic matter | NOM |
| Nephelometric turbidity units | NTU |
| Network forming oxide | NFO |
| Non-bridging oxygen | NBO |
| Osmotic membrane bioreactor | OMBR |
| Phosphate-based glass | PBG |
| Poly vinyl alcohol | PVA |
| Porous magnetite microspheres | PMMs |
| Porous recycled glass microspheres | PRGMs |
| Porous wall hollow glass microsphere | PWHGM |
| Powdered activated carbon | PAC |
| Recycled glass | RG |
| Reverse osmosis | RO |
| Salicylic acid | SA |
| Savannah river national laboratory | SRNL |
| Scanning electron microscopy | SEM |
| Secondary building units | SBUs |
| Slow sand filters | SSF |
| Solid recycled glass microspheres | SRGMs |
| Sulfosalicylic acid | SSA |
| Sustainable development goals | SDGs |
| Total dissolved solid | TDS |
| Trihalomethyanes | THMs |
| Ultrafiltration | UF |
| United nations world water development report | WWDR |
| Urban wastewater treatment directive | UWWTD |
| Vapour compression distillation | VCD |
| Water framework directive | WFD |
| X-ray diffraction analysis | XRD |

# List of Figures

Figure 1.1: States of impurities in water [23]. ..... 3
Figure 1.2: Illustration of the classification of water purification technologies. ..... 6
Figure 1.3: Illustration of the coagulation and flocculation process in water treatment [89]. ..... 9
Figure 1.4: Schematic image of a trickling filter [96] ..... 10
Figure 1.5: Size range of particles of concern and pore size of filter medium in water treatment in µm range [109]. ..... 12
Figure 1.6: Different membrane filters with contaminants removing abilities [119]. ..... 13
Figure 1.7: SEM images of a) porous hydroxyapatite microspheres [1], b) $TiO_2$ microspheres [2] and TEM image of c) $Fe_3O_4$/Fe with a ZnO core nanospheres [3], d) $Fe_3O_4$/polypyrrole (PPy) microspheres [4]. ..... 20
Figure 1.8: 2D filtered XMT images (565 $mm^2$) taken from axial planes of PA80G glass ceramic foam with 2 wt-% SiC, sintered at a) 975°C, b) 1000°C, c) 1050°C, d) 1100°C [272]. ..... 28
Figure 1.9: SEM image of SCHOTT CoralPor ® a porous silica glass produced from borosilicate glass by phase separation [276]. ..... 29
Figure 1.10: SEM image of SRNL microsphere showing surface porosity [283] ..... 31
Figure 1.11: SEM image of microsphere produced by flame spheroidisation a) Phosphate glass-based microspheres (Sene et al. [292]) b) dysprosium phosphate glass ceramic microsphere that had been heat-treated at 1400°C for 15 min (Conzone et al., 2009 [293]). ..... 31
Figure 2.1: Photograph of starting particles of a) magnetite < 45µm and b) recycled glass (45-63µm). ..... 41
Figure 2.2: a) Photograph showing the apparatus set up of the oxy-acetylene spray gun and b) schematic diagram of oxy-acetylene flame spheroidisation apparatus. ..... 43
Figure 2.3: (a) Photograph of adsorption column, pump and wastewater source, (b) Inset of the column fittings. ..... 53
Figure 3.1: X-ray diffraction pattern for a) glass particles, b) glass microspheres of size 25-150 µm, c) 150-200 µm d) 200-355 µm and e) 200-355 µm with different porogen ratios. ..... 57
Figure 3.2: Comparison of composition of glass particles with microspheres of a) S, b) M, c) L and d) XL sized porous glass microspheres manufactured vis varying the porogen ratio using EDX analysis. ..... 58
Figure 3.3: Histogram for a) glass particles and b) flame spheroidised microspheres manufactured from different starting particle size ranges (Coulter Counter). ..... 59
Figure 3.4 : SEM images of 125-150 µm porous microspheres (S) with cross-sections of a) 0.5, b) 1, c) 2 and d) 3 porogen ratios, generated via resin embedding. ..... 60
Figure 3.5: SEM image of 150-200µm porous microspheres (M) with cross-sections of a) 0.5, b) 1, c) 2 and d) 3, porogen ratios, generated via resin embedding. ..... 60
Figure 3.6: SEM image of 200-355 µm porous microspheres (L) with cross-sections of a) 0.5, b) 1, c) 2 and d) 3, porogen ratios, generated via resin embedding. ..... 61
Figure 3.7: SEM image of 200-355 µm porous microspheres (XL) with cross-sections of a) 0.5, b) 1, c) 2 and d) 3, porogen ratios, generated via resin embedding. ..... 61
Figure 3.8: Apparent density of glass chunk, particles and microspheres. ..... 62
Figure 3.9: Figure showing tapped density and respective % theoretical porosity of glass microspheres produced. ..... 62
Figure 3.10: Surface area measurement from BET analysis for the different size porous microspheres investigated. ..... 63
Figure 3.11: BET isotherm for adsorption into a) S, b) M, c) L and d) XL sized porous glass microspheres. ..... 64

Figure 3.12: Figure showing cumulative intrusion of mercury into different size microspheres. Zone A, B and C represents the interparticle space among microspheres, low pressure intrusion and high-pressure intrusion within the pores of microspheres, respectively. ..... 65
Figure 3.13: Figure showing log differential intrusion and cumulative intrusion for different pore diameter for a) 3S microsphere with 70 % porosity b) 3M microsphere with 66 % porosity and c) 3L microsphere with 68 % porosity. ..... 66
Figure 3.14: Adsorption of dye by different size glass particles at different contact time in terms of a) amount of dye adsorbed per g of adsorbent and b) % dye removal..... 68
Figure 3.15: Column adsorption using acid red88 on phosphate-based glass microsphere where image showing a) colourless solution coming out the tip of the column after getting adsorbed within the glass microsphere bed and b) instrument assembly..... 69
Figure 3.16: Breakthrough curves for adsorption of acid red 88 onto porous phosphate glass microspheres..... 69
Figure 4.1. Representative SEM images of heat-treated and untreated porous P40 microspheres: a) and b) shows the distribution and yield of unwashed and acid washed P40 microspheres respectively , c) cross-section of resin embedded washed porous P40 microspheres, d), g) and e), h) showing distribution and yield of heat-treated unwashed and acid washed 510-P40 microspheres at low ang high magnification respectively, j), m) and k), n) shows distribution of heat-treated unwashed and washed 520-P40 microspheres at low ang high magnification respectively, f), i) and l), o) shows cross-section of porous washed 510-P40 and 520-P40 microspheres at low ang high magnification respectively. ..... 77
Figure 4.2: (a and b) SEM images of P40 microspheres heat-treated at 530℃ and (c and d) SEM images of P40 microspheres heat-treated at 540℃. ..... 77
Figure 4.3: Nitrogen adsorption-desorption Isotherm of a) P40, 510-P40, and 520-P40 microspheres and b) a comparison of pore size and pore volume analysis for P40 and heat-treated 510-P40 and 520-P40 porous microspheres. ..... 78
Figure 4.4. XRD diffraction pattern for heat treated (before and after acid wash) and untreated P40 phosphate-based glass microspheres. ..... 80
Figure 4.5: Elemental compositional analysis of the porous microspheres produced as measured by EDX. ..... 81
Figure 4.6: Isotherm plots for adsorption of AR88 dye on P40 and heat-treated porous microspheres (the conditions of the isotherm adsorption experiment are as follows: microsphere dose 1 g/L, pH 7, temperature 22 ± 2 °C and stirring time 24 h. ..... 82
Figure 4.7: Effect of dye concentration on adsorption in a) P40, b)UW-P40, c) 510-P40, and d) 520-P40 microspheres at the microsphere dose of 1g/L, pH 7 and temperature of 22 ± 2℃. ..... 84
Figure 4.8: Breakthrough curve of AR88 dye adsorption for P40, 510-P40 and 520-P40 microspheres at 2.2 ml/min and 0.5 ml/min flow rates with starting dye concentration of 300 mg/L, pH 7 and temperature at 22 ± 2 ℃..... 86
Figure 4.9: Figure showing a) SEM images after dye adsorption and b) FTIR spectra (before and after dye adsorption). ..... 89
Figure 4.10: Schematic representation of the proposed mechanism for changing the textural property of the heat-treated glass porous microspheres during the heat-treatment process..... 91
Figure 4.11: Schematic diagram showing a) packing of the microsphere, b) dye diffusion inside multichannel created by interconnected porosity in column adsorption and c) Possible interactions of AR88 dye with different sites on the surface of microspheres. The arrows show flow direction. .. 95
Figure 5.1: (a) SEM image with inset showing XRD pattern & (b) EDX spectrum of recycled glass (RG) as received (particle size ≤63 um). ..... 98

Figure 5.2: a) Representative SEM image and b) X-ray diffraction of solid recycled glass microspheres (SRGM) obtained via flame spheroidisation. ..... 99
Figure 5.3: Initial attempts to prepare PRGMs using conventional process a) 2:1, b) 1:1 and c) 1:3 porogen ratio using below 5µm porogen and d) 1:0.5, e) 1:1 and f) 1:3 porogen ratio using below 63µm porogen. ..... 100
Figure 5.4: DSC analysis of a) colour sorted RG and b) bulk RG and P40. ..... 101
Figure 5.5: EDX analysis of white, brown, and green glasses investigated for $Al_2O_3$, $SiO_2$ and FeO content. ..... 102
Figure 5.6: Plots demonstrating the change in area with temperature based AFT instrument for a) RG with and without porogen and RG made into granules and b) P40 glass with and without porogen. ..... 103
Figure 5.7: Temperature difference among flow, hemisphere, and sphere point for RG and P40 based samples explored by ash fusion test (AFT). ..... 103
Figure 5.8: Images of hemisphere for a) RG without porogen , b), c) and d) RG granules, e) and f) P40 with and without porogen at temperature 770°C and 850°C, respectively obtained by HD camera inside AFT furnace. ..... 104
Figure 5.9: Rate of viscosity change at softening temperature, hemisphere temperature and flow temperature for P40 and RG. ..... 105
Figure 5.10: Viscosity curve for P40 and RG glass particles from a) high temperature viscometer and b) Avramov–Milchev (AM) model. ..... 106
Figure 5.11: SEM images from (a-c) displaying the effect of grinding time in a ball-mill on manufacturing PRGMs for various time points a) 1 min, b) 5 min and c) 15 min grinding time at 300 rpm. ..... 107
Figure 5.12: SEM images from a-c displaying the effect of grinding time in a ball-mill on manufacturing PRGMs for various time point a) 1 min grinding, b) 5 min grinding and c) 15 min grinding at 500 rpm. ..... 108
Figure 5.13: SEM images showing elemental mapping of unwashed, and acid washed PRGMs a) 2:1, b) 1:1 and c) 1:3 glass to porogen ratios. ..... 110
Figure 5.14: Cross-sectional SEM images showing unwashed PRGMs with a) 2:1, b) 1:1 and c) 1:3 glass to porogen ratios. ..... 111
Figure 5.15: a) surface area analysis using BET method with inset showing nitrogen sorption isotherms of microsphere samples and b) macropore volume and porosity analysis using mercury porosimetry analysis of PRGMs. ..... 112
Figure 5.16: XRD of UW-PRGMs with porogen ratio 2:1, 1:1 and 1:3. ..... 114
Figure 5.17: Impact of the initial pH of solution on the adsorption of a) AR88 and b)MB by PRGMs with varying porogen ratios after equilibrium ($C_0$=200mg/L for AR88 and 25mg/L for MB; dye volume=10mL; adsorbent loading=10 g/L; T=22 ± 2 ℃). ..... 115
Figure 5.18: Influence of the PRGMs loading on the adsorption of a) AR88 and b) MB after equilibrium ($C_0$=200mg/L for AR88 and 25 mg/L for MB, pH= 2.5 for AR88 and 20mg/L, pH=7 for MB; dye volume= 10mL; T= 22 ± 2 ℃) ..... 116
Figure 5.19: Effect of dye concentration on adsorption into UW-PRGMs for a) AR88 and, b) MB. (PRGMs dose= 10 g/L and 6 g/L with pH 2.5 and pH 7 for AR88 and MB respectively and temperature of 22 ± 2 ℃). ..... 117
Figure 5.20: Effect of dye concentration on adsorption into UW-PRGMs for AR88 (PRGMs dose= 10 g/L with pH 2.5 and temperature of 22 ± 2 ℃). ..... 117
Figure 5.21: a) Linear pseudo 1st order kinetic model and b) Linear pseudo 2nd order for the adsorption of AR88. (Volume of dye= 10mL; adsorbent loading= 10 g/L, pH= 2.5 for AR88) ..... 118

Figure 5.22: Isotherm data fitted with Langmuir and Freundlich models for a) AR88 and b) MB dye. (PRGMs dose= 5 g/L, pH 2.5 and pH 7 for AR88 and MB respectively and temperature of 22 ± 2 ℃ equilibrium time 24 hrs). ..... 120
Figure 5.23: Effect of UW-PRGMs and W-PRGMs dose on removing AR88 dye by coagulation. ($C_0$= 200mg/L, pH= 2.5, dye volume=10mL; T= 22 ± 2 ℃)..... 122
Figure 5.24: Breakthrough curve of AR88 dye adsorption for RG, UW-PRGMs and W-PRGMs microspheres at a) 2.2 ml/min and b) 0.5 ml/min flow rates with starting dye concentration of 100 mg/L at 22 ± 2 ℃..... 123
Figure 5.25: a) Adams-Bohart model, b) Thomas model, and c) Yoon-Nelson model at different flowrates ($C_0$= 100mg/L) ..... 124
Figure 5.26: FTIR spectra for PRGMs before and after a) AR88 and b) MB dye adsorption..... 126
Figure 5.27: XPS survey scan and optical microscope images for PRGMs before and after a) AR88 and b) MB dye adsorption. ..... 127
Figure 5.28: High resolution XPS spectra of C 1s for PRGMs before and after AR88 and MB adsorption ..... 128
Figure 5.29 :High resolution XPS spectra of O 1s for PRGMs before and after AR88 and MB adsorption ..... 129
Figure 5.30: High resolution XPS spectra of Ca2p for PRGMs before and after AR88 and MB adsorption ..... 131
Figure 5.31: High resolution XPS spectra of Si 2p for PRGMs before and after AR88 and MB adsorption ..... 132
Figure 5.32: Recycling of the PRGMs for the removal of AR88 upto 6$^{th}$ cycle and MB upto 1$^{st}$ cycle : (For AR88 $C_0$ = 180 mg/L, Adsorbent dose = 5g/L and pH = 2.5; MB, $C_0$= 25 mg/L, Adsorbent dose = 5g/L and pH =7) with photograph showing microspheres after regeneration..... 133
Figure 5.33: DTG graph of PRGMs with a) AR88 dye and b) MB dye before and after dye adsorption and desorption..... 134
Figure 5.34: a) XRD patterns and b) SEM images of PRGMs before dye adsorption, after dye adsorption and desorption..... 135
Figure 5.35: Schematic representation of PRGMs formation via FS …. ..... 139
Figure 5.36: Structure of AR88 [469, 470] and MB [470]. ..... 143
Figure 6.1 : (a) EDX spectrum & (b) XRD analysis of irregular shaped as received magnetite ($Fe_3O_4$) particles (size <45um). ..... 150
Figure 6.2: SEM images, XRD profile and particle size distribution histogram for MSM..... 151
Figure 6.3: Initial attempts to prepare PMMs using conventional process a), b) and c) unwashed magnetite and d) and e) magnetite samples after acid wash and f) cross section of acid washed magnetite sample ..... 152
Figure 6.4: Initial trial to prepare PMMS using granular method (5 min ball milled at 500 rpm) via flame spheroidisation process. a) SEM images of washed samples and b) elemental mapping showing distribution of Fe, O and Ca in pink, blue and green colour within the cross-sectioned samples. .... 153
Figure 6.5: SEM images from a-c displaying the effect of grinding time in a ring-mill on manufacturing PMMs for various time point a) 1 min grinding, b) 5 min grinding and c) 15 min grinding. ..... 154
Figure 6.6: a) X-Ray diffractograms for PMMs produced at 1min, 5 min and 15 min grinding time, B) semi-quantitative analysis of minerals for grinded powders before spheroidisation and c) PMMs after spheroidisation. ..... 156
Figure 6.7: SEM images of PMMs (manufactured with 1:0.5 porogen ratio and 15 min grinding time)after a) 1$^{st}$ spray, b)2$^{nd}$ spray, c) 3$^{rd}$ spray and d) 4$^{th}$ spray. ..... 157

Figure 6.8: a) TGA analysis of grinded and re-spheroidised PMMS after 1st , 2nd and 4th spray. b) Graph showing weight % of $CaCO_3$ with inset showing the derivative weight of PMMS after 1st, 2nd and 4th spray and c) semi-quantitative analysis by XRD after 1st, 2nd, and 4th spray (acid washed). ..... 158
Figure 6.9: SEM images of PMMs(unwashed) a) 1:0.5, b)1:1 and c)1:3 magnetite to porogen ratios. ..... 159
Figure 6.10: SEM images of W-PMMs a)1: 0.5, b)1 1 and c)1 3 magnetite to porogen ratios. ..... 160
Figure 6.11 : SEM images with cross-section of magnetite microspheres prepared using granular method without any porogen. ..... 160
Figure 6.12: a) X-Ray diffractograms for unwashed (UW) and acid washed(W) PMMs produced with varying porogen ratios, b) semi-quantitative analysis of minerals for PMMs with varying porogen ratios. ..... 161
Figure 6.13: SEM image and mineral distribution map of UW-PMMs with a) 1:0.5 porogen ratio, b) 1:1 porogen ratio and c) 1:3 porogen ratio ..... 162
Figure 6.14: SEM image and mineral distribution map of W-PMMs with a) 1:0.5 porogen ratio, b) 1:1 porogen ratio and c) 1:3 porogen ratio ..... 163
Figure 6.15: Graph showing a) mineral proportions in unwashed and acid washed PMMs with varying porogen ratio and b) size distribution of PMMs with varying porogen ratio. ..... 164
Figure 6.16: a) Nitrogen adsorption isotherms and b) surface area of PMMs with varying grinding time and porogen ratios. ..... 165
Figure 6.17: a) Displaying the cumulative intrusion and their possible corresponding intrusion points and b) Pore diameter against Log differential pore volume of PMMs with1:1 and 1:3 porogen ratio as obtained from mercury porosimetry ..... 166
Figure 6.18: Adsorption using acid red88 on a) unwashed PMMs prepared using different flowrates, grinding time and porogen ratio and b) washed PMMs prepared using different porogen ratio using oxidising flame. Each vial contained 50 mg/L AR88 and 5 g/L of PMMs at pH 7 and temperature 22 ± 2 °C ..... 167
Figure 6.19: Impact of the initial pH of solution on the adsorption of a) AR88 and b) MB after equilibrium ($C_0$ = 300mg/L for AR88 and 50mg/L for MB; dye volume= 10mL; adsorbent loading = 5 g/L; T= 22 ± 2 °C) ..... 168
Figure 6.20 : Influence of the PMMs loading on the adsorption of a) AR88 and b) MB after equilibrium ($C_0$ = 300mg/L for AR88 and 50 mg/L for MB, pH= 2 for AR88 and 20 mg/L, pH = 10 for MB; dye volume = 10mL; T = 22 ± 2 °C) ..... 169
Figure 6.21: Effect of dye concentration on adsorption into UW-PMMs and W-PMMs for a) AR88 and, b) MB. (PMMs dose= 6 g/L, pH 2 and pH 10 for AR88 and MB respectively and temperature of 22 ± 2 °C) ..... 170
Figure 6.22: Linear pseudo 1st order kinetic model for the adsorption of a) AR88 and b) MB. (V of dye=10mL; adsorbent loading=6 g/L, pH= 2 for AR88 and pH=10 for MB) ..... 171
Figure 6.23: Linear pseudo 2nd order kinetic model for the adsorption of a) AR88 and b) MB. (V dye=10mL; adsorbent loading=6 g/L, pH= 2 for AR88 and pH=10 for MB) ..... 171
Figure 6.24: AR88 and MB dye isotherm data fitted with Langmuir and Freundlich models (PMMs dose = 6 g/L, pH 2 and pH 10 for AR88 and MB respectively and temperature of 22±2 °C) ..... 173
Figure 6.25: XPS survey scan for Magnetite, UW-PMMs and W-PMMS before and after dye adsorption. ..... 176
Figure 6.26: High resolution XPS spectra of C 1s in a) W-PMMs before and after MB adsorption b) MB dye ..... 177
Figure 6.27: High resolution XPS spectra of C 1s for UW-PMMs before and after MB adsorption ..... 178
Figure 6.28: O1s spectra for a) W-PMMs and b) UW-PMMs before and after dye adsorption. ..... 179

Figure 6.29: Ca 2p spectra for a) W-PMMs and b) UW-PMMs before and after dye adsorption. ..... 181
Figure 6.30: Ca 2p spectra for a) W-PMMs and b) UW-PMMs before and after dye adsorption. ..... 182
Figure 6.31: FTIR spectra for MB, UW-PMMs and W-PMMs before and after dye adsorption. ..... 183
Figure 6.32: Absorbance spectrum of a) UW-PMMs and b) W-PMMs microspheres before and after MB dye adsorption from 480-600 $cm^{-1}$. Solid and broken lines are before and after adsorption with arrow showing band shift. ..... 184
Figure 6.33: : XRD patterns for a) UW-PMMs and b) W-PMMs before and after adsorption with semi-quantitative analysis. ..... 184
Figure 6.34 Phase diagram of the Ca–Fe–O system at 1173 K calculated using MTDATA studied by Ismail et *al.* [522]. Where C = CaO, F = $Fe_2O_3$, W = FeO, CF = $CaFe_2O_4$ ($CaO.Fe_2O_3$) and $C_2F$ = $Ca_2Fe_2O_5$ ($2CaO.Fe_2O_3$). The green arrow indicating the molar ratio investigated. ..... 187
Figure 6.35: Effect of granule size and porogen on the final morphology of microspheres. Position 1, 2 and 3 directing the exit point of microspheres. ..... 188
Figure 7.1: A schematic of target specific porous glass microspheres packed in a column for purification of water contaminated by mixtures of (i) bacteria, (ii) organic pollutants and (iii) metal ions. ..... 200

# List of Tables

Table 1.1: List of chemicals for coagulation and flocculation.... 8
Table 1.2: Adsorption of hazardous organics from water over various MOFs and dominant mechanisms reported by Hasan et *al.* [206] 18
Table 1.3: Table showing microspheres in water treatment applications. 22
Table 1.4: A table showing comparison among common commercial glasses. 27
Table 1.5: List of glass and glass ceramic microspheres prepared by different methods. 32
Table 1.6: List of magnetic materials used in various wastewater treatment applications. 35
Table 1.7: Applicability, challenges, quality problem addressed and costs of wastewater treatment technologies [23, 76] 38
Table 2.1: Porous glass Microspheres prepared with different porogen ratios. 44
Table 2.2: Code used for different microspheres. 44
Table 3.1: Size distribution for glass particles and flame spheroidised microspheres of different sizes on different cumulative volume % 59
Table 4.1: Specific surface area and pore volume of the porous microspheres prepared. 78
Table 4.2: Parameters of fitting the adsorption isotherm data using Langmuir, Freundlich, Temkin equations for P40, UW-P40, 510-P40 and 520-P40 (The conditions of the isotherm adsorption experiment are as follows: microsphere dose 1 g/L, pH 7, temperature 22 ± 2 ℃ and stirring time 24 hr). 83
Table 4.3: Comparison of the pseudo-first-order, pseudo-second-order adsorption rate constants and calculated and experimental $q_e$ values obtained at different initial AR88 concentrations at the microsphere dose of 1g/L, pH 7 and temperature of 22 ± 2 ℃. 85
Table 4.4: Total adsorption and equilibrium adsorption capacity of AR88 at different flow rates for P40 and heat-treated microspheres (Starting dye concentration of 300 mg/L, pH 7 and temperature at 22 ± 2 °C). 87
Table 4.5: Breakthrough curve models with their parameters (At 2.2 ml/min and 0.5 ml/min flow rates with starting dye concentration of 300 mg/L at 22 ± 2 °C). 88
Table 5.1: Summary of DSC analyses (±SD) conducted on colour coded glasses, bulk RG and P40 having particle size ≤ 63 µm. 101
Table 5.2: EDX analyses (±SD) conducted on colour coded glasses 102
Table 5.3: Pore size and pore volume analysis using t-plot and BJH method by nitrogen adsorption desorption analysis. 113
Table 5.4: Summery of % crystalline phase in UW-PRGMs 114
Table 5.5: Kinetic rates for the adsorption of AR88 and MB on UW-PRGMs 119
Table 5.6: Isotherm constants for adsorption of AR88 121
Table 5.7: Isotherm constants for adsorption of MB 121
Table 5.8: Total adsorption and equilibrium adsorption capacity of AR88 at different flow rates for RG, UW-PRGMs and W-PRGMs. 124
Table 5.9: Breakthrough curve models with their parameters. 125
Table 6.1: Yield (%) and Dye removal (%) of unwashed PMMs prepared using varying flowrates, grinding time and porogen ratios. 166
Table 6.2: Dye removal (%) of SMS, magnetite particles and washed PMMs prepared using varying porogen ratios 167
Table 6.3: Kinetic rates for the adsorption of AR88 and MB on UW-PMMs and W-PMMS 172
Table 6.4: Isotherm constants for adsorption of AR88 174
Table 6.5: Isotherm constants for adsorption of MB 174

# Chapter 1: Introduction and review of literature

## 1.1 Primary research motivation

Water is a finite resource, fundamental to human health and only renewable if well managed. Efficient water management plays a vital role in strengthening social, economic and environmental systems in the face of rapid and unpredictable changes [1, 5]. By 2050 the global population are expected between 9.4 to 10.2 billion people, an increment of 22% to 32% [6]. It is estimated that around 4 billion people worldwide experience to have no or little access to clean and sanitised water supply, and millions of people die of severe waterborne diseases annually [7, 8]. This figure will grow increasingly due to overwhelming discharge of pollutant in waterbody [8-11]. According to the United Nations World Water Development Report (WWDR) 2018, approximately 6 billion people will face clean water scarcity by 2050 [12].

While water demand is rising, water availability is decreasing due to limited supplies. Approximately 97% of earth's water is in the ocean which has 35,000 mg/L of salt content which is unusable without proper treatment [13]. 2% of earth's water is in glaciers, 1% in rivers and lakes and the rest of it is as groundwater aquifers of which half of it occurs at depth greater than 800 m [13] . The storage of rainwater and increasing catchment capacity will contribute only in minor levels to resolve the issue due to non-uniform distribution of rain fall and long drought challenges depending on geography.

The term "criticality ratio" (CR) is commonly used to identify the demand for water on a certain area, which is the ratio of average annual water withdrawals to water availability [14]. The higher the ratio the more the stress placed on that area. Ratio's between 0.4 and 0.8 means '' very high water stress'', below 0.4 is mild water stress and greater than 0.8 means "severe water stress'' which includes desert area (Middle East 88%) and Central Africa (5%) [15]. Approximately 2.1 billion people living near river areas are already on severe water stress, and 50% of them are from Southern Asia and China. Much of Central Asia, coastal areas in Latin America, parts of Europe, and much of the Western United States are also in the high or very high stress categories [16]. By 2050 nearly two-thirds (4.8 to 5.7 billion) of all nations will experience water stress [17, 18].

Population growth, economic development and changing water consumption patterns all contribute to increased water scarcity. Similarly, pollution of water is also correlated with population density and economic growth. Every year, 730 million tonnes of sewage and other effluents are dumped into the lake and industries releases 300 to 400 megatons of garbage into the sea [19]. In order to minimise pollution, developed nations have established a number of legislative processes and practises that must be followed for industrial and municipal wastewater. These legislative documents fall under a

number of directives with the most prominent including Water Framework Directive-2000/60/EC (WFD) [20], the Urban Wastewater Treatment Directive-91/271/EEC (UWWTD) [21] and Environmental Quality Standards in the field of water policy- 2013/39/EU (EQS) [22]. Regulatory pressure and water scarcity plays important role towards water security to reduce the discharge of contaminants especially hazardous and toxic micro-pollutants into water bodies.

Scarcity of water is not the only issue, concerns are also more related to the average per capita cost of pure water production, with the desired quantity and quality. The demand for water treatment equipment's is growing day by day. It was estimated that the equipment cost for proper water treatment is expected to grow 6.9 percent per year to $53.4 billion in 2017. To ensure properly treated drinking water and sanitation facilities, filtration and membrane systems are highly used in Developing parts of the world -- the Asia/Pacific and Africa/Mideast regions, Eastern Europe, and Central and South America. The issue is complicated since not only the treatment cost resulting in increased water cost, but also the rising cost of raw materials, changes in material production methods, and discharge standards all impact the ultimate wastewater management decision. Especially after Covid 19 pandemic, millions of people have been dragged into poverty, and a handful of nations will experience the worst economic crisis of our lifetime. Therefore, ensuring good quality water availability at lower cost, reducing the impact on the environment by minimizing the use of chemicals and sustainable management of water for all by the year 2030 is one of the top priorities of the United Nations Sustainable Development Goals (SDGs) [17].

## 1.2 Type of impurities

The origin of pollutant in wastewater depends on the source of water, impact by geology, humans such as use of chemicals, industrialization, and increase in population etc. [15]. One of the ways to classify impurities that are found in water can be explained in terms of their states within water, such as, suspended, colloidal and dissolved materials (see Figure 1.1).

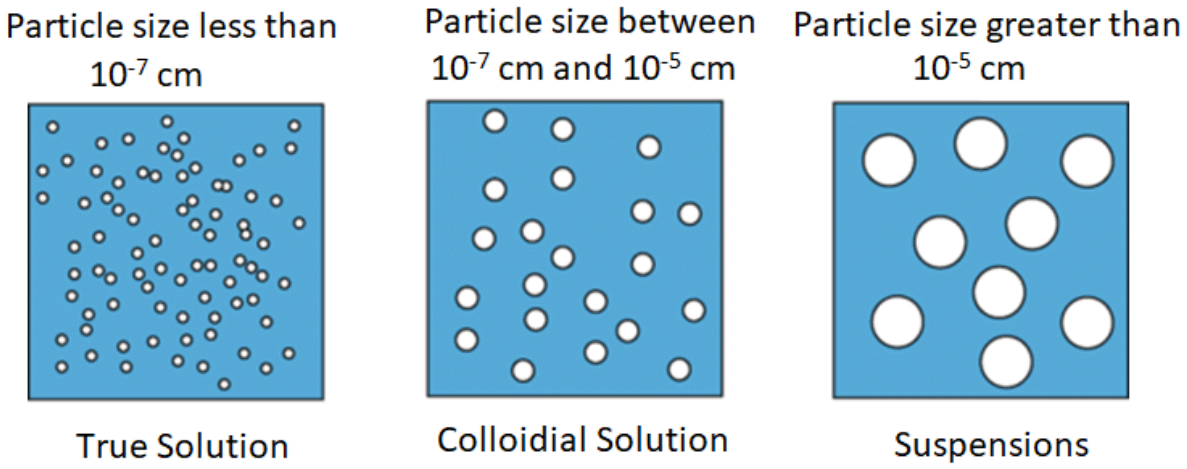



*Figure 1.1: States of impurities in water [23].*

### 1.2.1 Suspended matter

Due to flow ability of water, it can pick-up and transport particles of greater density than water, this capacity increases with increasing velocity of water. This produces turbid water, which sometimes hinders the effect of photosynthesis of aquatic plant [23]. Some suspended materials include functional groups that can combine with metals to produce complex compounds, rendering them poisonous [24]. Such debris encourages the growth of germs and fouling in the water, resulting in an unpleasant taste and odour, and hence must be removed [24].

### 1.2.2 Colloids

Colloids are macromolecules or aggregates with sizes ranging from 1 nanometre to 1 millimetre [25]. At this small size, gravity forces are small compared to other forces, so particles can remain in suspension for very long times. These are the fine particles that do not settle and at the same time are electrically charged. These particles impart colour and turbidity into water [23]. The processes of coagulation and filtration involve removing substances of a colloidal nature from wastewater.

### 1.2.3 Dissolved Solids

All ions and complex chemicals that are not visible in naked eyes are mainly known as dissolved pollutants. These are solids derived from man-made chemicals such as pesticides or herbicides or dyes etc. These are very expensive and quite challenging to remove [23].

#### *1.2.3.1 Organic Pollutants*

Industries such as textile, leather, coal, printing, iron-steel, petroleum, pesticide, paint, paper, herbicides, solvent, pharmaceutics, wood preserving chemicals, consume large volumes of water, and discharge organic based chemicals into water. These have difference in chemical compositional complexity, molecular weight, toxicity etc. Dyes, herbicides and pesticides affect photosynthesis and may also be toxic to some aquatic life due to the presence of aromatics, metals, chlorides [26-29]. Faecal pollutants on the other hand are associated with ammonia, nitrates and nitrites. Cleaning and washing processes also lead to discharge of water containing high levels of Trihalomethyanes (THMs) [30]. Excessive use of rocket fuel, missiles, flares and fireworks, herbicides, in industries in wet digestion, chemical synthesis and electro polishing leads to formation of stable perchlorates [31-34]. This can lead to perchlorate-induced iodine deficiency, and thereby thyroid hormone level alterations which results in infertility, and neurodevelopmental issues [35-37]. Domestic and industrial use results in discharge of medicines, plastics, personal care products, and material additives which results in pollutants named as endocrine disruptors. These Endocrine disruptor's (ECDs) results in chronic toxicity, pathogen resistance and serious health issues [38-43]. There are more than 100 chemicals identified as endocrine disruptors [44, 45] and these chemicals are considered as emerging contaminants (ECs) [44, 46] .

#### *1.2.3.2 Inorganic Pollutants*

Soluble ions such as calcium and magnesium results in hardness of water. This parameter is a crucial factor in industrial aspects due to scale formation, heat losses and head losses etc. Heavy metals such as Cd, As, Cr, Fe, Mn, Hg, Ni, Pb, and Cu have been reported by several authors to be non-biodegradable and above the marked threshold level are toxic and tend to accumulate in living organisms. These can act progressively over a long period of time through food chains [47]. In plants these can cause decrease in seed germination and lipid content by cadmium [48, 49], decreased enzyme activity and plant growth by chromium [50, 51], the inhibition of photosynthesis by copper and reproductive dysfunction, neurological impacts, due to mercury [52-54], the reduction of seed germination by nickel [55] including the reduction of chlorophyll production and plant growth, genetic mutation and immune-toxicity in human [56]. Other serious impacts can include cancer, organ damage, nervous system damage and in extreme cases, deaths [57-59]. Metals such as iron and manganese are responsible for imparting colour in water and can also lead to staining. Presence of iron is responsible for corrosion in pipelines, including typical events such as pipe bursts, changes in

flow pattern etc. Arsenic can cause arsenicosis which is associated with the risk of non-fatal outcomes and deaths mostly in the South East of Asia [60]. Anions such as chlorides above 600 mg/l leads to salty taste, fluorides above 1.5 mg/l affects bones and teeth, bromide containing water may cause formation of bromates after ozonation, and sulphates of magnesium and sodium causes laxatives [23]. Ions like phosphate and nitrate often are responsible for causing eutrophication [61].

#### *1.2.3.3 Microbial pollutants*

Mainly four bacteriological parameters are used to assess the quality of drinking water. Parameters such as coliform bacteria count, faecal coliforms count, colony/plate counts, and faecal streptococcus counts are normally analysed to regulate the potential presence of organisms pathogenic to humans. Although it is not practicable for virus detection. It appears that viruses are inactivated by disinfection process. Some algae toxin (cyanotoxines) produced by blue-green algae [62] are responsible for producing toxic species such as –hepatotoxins [63], neurotoxins [64], lipopolysaccharides [65], dermatotoxins [66]. These are also responsible for producing the objectionable odours and sometimes taste.

#### *1.2.3.4 Radioactive pollutants*

Radionuclides are also increasing in consideration day by day due to massive human activities such as power generation, diagnosis, and treatment process [67]. Exposure to relatively high levels of radionuclides in drinking water for long periods may arise serious health problems, such as cancer, cataracts, osteoporosis, anaemia, bone growths, kidney disease, liver disease and impaired immune systems [68]. Radionuclides uranium ($^{238}$U, $^{235}$U), radium ($^{228}$Ra, $^{226}$Ra, $^{223}$Ra), lead ($^{210}$Pb), thorium ($^{228}$Th, $^{229}$Th), strontium ($^{90}$Sr), cesium ($^{137}$Cs) etc. are of major concern [69-71].

## 1.3 Wastewater treatment technologies

Wastewater treatment processes are classified as primary, secondary, and tertiary and comprise mainly of unit operations and processes [72]. Primary treatments comprise of physical and chemical process whilst secondary treatments are based on biological treatment processes. After the primary and secondary treatment processes, a tertiary process for the water is utilised which converts it into good quality water that can be used for different purposes, i.e. drinking, industrial, water and for medicinal use. In order to achieve different levels of contaminant removal, individual waste-water treatment procedures are combined with more rigorous processes (see Figure 1.2). The sludge resulting from treatment operations is further treated by various methods in order to reduce its organic and toxic content and makes it more suitable for final disposal in landfill and reused in

agriculture and industries [73]. The whole treatment process depends on the nature of wastewater, the space available, climate, living standards, a considerable operation cost, capital costs and degree of industrialisation [23, 74].

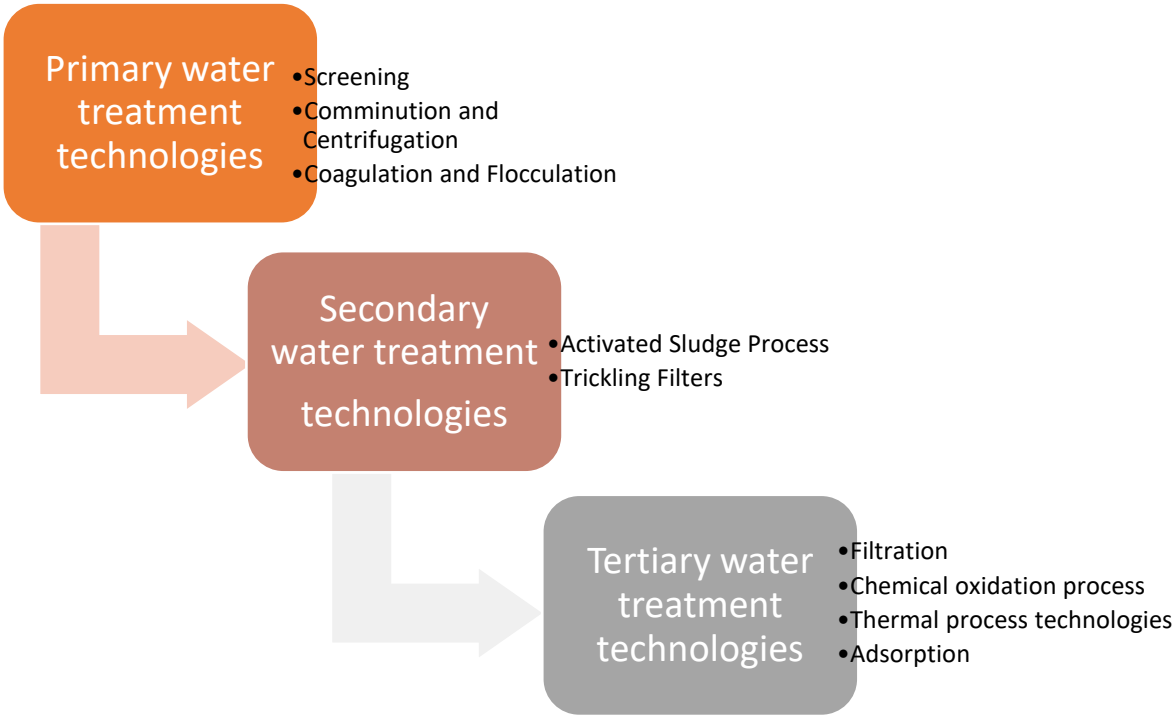



***Figure 1.2: Illustration of the classification of water purification technologies.***

### 1.3.1 Primary water treatment technologies

At the primary level methods such as screening, filtration, centrifugation, sedimentation, coagulation, gravity and floatation processes are used. These process aims to remove mainly course and suspended particles, colour, turbidity of the water.

#### *1.3.1.1 Screening*

Screening processes remove gross pollutants and any large, suspended matters utilising parallel bars, rods or wires, grating, wire mesh, or perforated plates. The materials retained from the screens are either disposed of by landfilling or incineration [75]. To remove suspended solids, the fine screens used are between 1.5 to 6 mm are used to remove greases, oils, bacteria etc. Suspended solids to 100 mg/L and for oil 25mg/L which can be reduced by up to 99% can be achieved by placing very fine screens with openings of 0.2 to 1.5 mm (0.01 to 0.06 in) after coarse screens [76].

#### *1.3.1.2 Comminution and Centrifugation*

Comminutors are used to cut down large floating material in the waste flow. They are installed between the grit chamber and the primary settling tanks. Their use reduces odours, flies and unsightliness. Comminutors and grinders can create problems for downstream processes, such as increasing plastics build up in digestion tanks or rag accumulation on air diffusers [77]. Separation using centrifugation process is based on the density difference of different non-colloidal suspended particles of size below 1 µm [23]. Wastewater is allowed to pass through centrifugal devices which is rotated at different speeds and the solids (sludge) are separated and discharged. This process is useful to reduce sludge load, removing suspended, floating, and greasy materials. The main disadvantage of such a process is that it increases the overall water treatment cost.

#### *1.3.1.3 Sedimentation and gravity separation*

Sedimentation, a fundamental and widely used unit operation in waste-water treatment, involves the gravitational settling of heavy particles suspended in a mixture for different time intervals. This process is used for the removal of grit, particulate matters in the primary settling basin, biological floc in the activated sludge settling basin, and chemical flow when the chemical coagulation process is used [78, 79]. The suspended solids settle under the influence of gravity which depends on the size and density of the contaminants. Sedimentation takes place in a settling tank, also known as a clarifier. This process can reduce suspended solid content below 1000 mg/L [23]. Water treated in this process is used for industrial water supply, ion exchange and membrane processes [80].

#### *1.3.1.4 Coagulation and Flocculation*

Both of these processes are used to remove suspended colloidal particles by forming large aggregates. The aggregates are then removed by physical treatment such as settling, floatation or filtration (see Figure 1.3). Colloids are very small particles with size ranged from 10 nm to 10 µm [23]. There are two types of colloids, hydrophilic and hydrophobic. The hydrophobic ones are made into large aggregates by destabilisation using one of the four processes listed below [23]:

a) Double Layer compression- compounds that can form trivalent cations are used, such as aluminium and ferric salts.
b) Charge neutralisation-compound that can form cations are mainly used, such as ferric and aluminium salts.
c) Particle bridging – both anionic and cationic polymers are used to destabilise negatively charged colloids. Long cationic molecules are mostly giving the effective results. Synthetic

cationic, anionic and non-ionic polymers are effective but are usually more costly than natural coagulants.

d) Trapping in a precipitate- compound that form hydroxide floc, or a carbonate precipitate are mainly used. Again, alum and ferric but other metal salts such as calcium and magnesium carbonate, activated silica are also used.

In these processes high energy mixing has to be ensured for proper distribution of coagulants pH, temperature and contact time which are most important controlling factors in the coagulation process [81]. Small particles that are formed during coagulation are subsequently processed using the flocculation technique. Flocculation occurs by Brownian motion, stirring, differential settling processes. List of chemicals used in coagulation and flocculation processes are tabulated in Table 1.1.

***Table 1.1: List of chemicals for coagulation and flocculation process.***

| Type | Chemical | Advantage | Disadvantage | Reference |
|---|---|---|---|---|
| Inorganic Alum | Alum, filter alum | Effective for pH in the range of 5-7, a coagulant aid is generally not required | Forms acidic solution in water, large doses require. Forms turbidity at high doses | [82, 83] |
| Inorganic ferric salts | Chloride of iron | Same as Alum | The liquid form of ferric chloride is difficult to handle. Required more dosing than alum. Increases corrosive tendency of the water and treatment costs | [23, 84] |
| Polymerised aluminium and iron salts. | Poly aluminium chloride and polyaluminium silicate sulfate. | Effective in low temperature, faster floc formation, saves pH adjustment chemicals, more effective with algae. | Not so effective as organic polymeric coagulants | [85, 86] |
| Organic polyelectrolyte | Polyacrile amide, Poly (diallyldimethyl ammonium chloride) | Effective in water containing manganese and iron | Normally used as coagulant aid. Less frequently used as a main coagulant, does not give effectiveness in low turbidity | [23, 87] |
| Electrocoagulation | Electricity | saves pH adjustment chemicals, less time required for the process, Reduce sludge content | Not very cost effective | [88] |

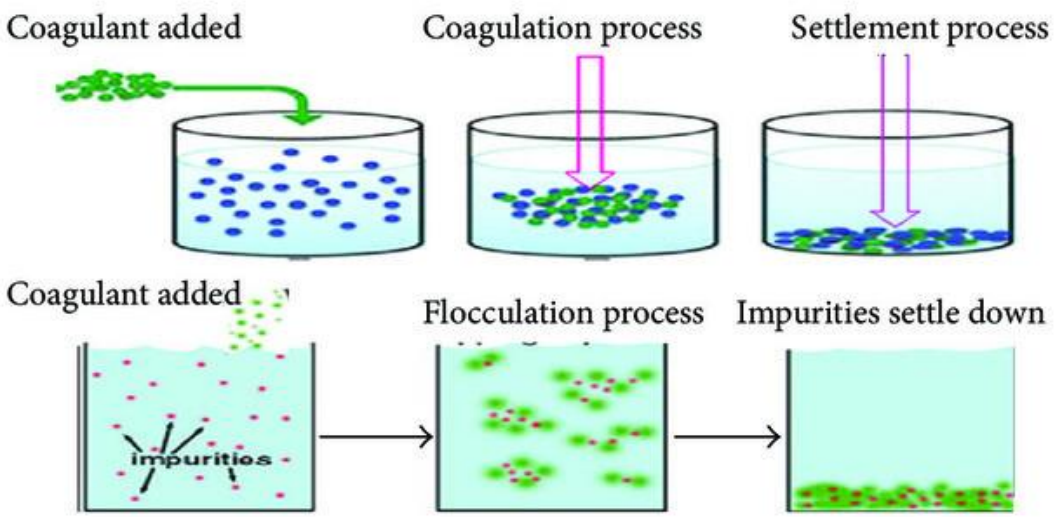



***Figure 1.3: Illustration of the coagulation and flocculation process in water treatment [89].***

#### *1.3.1.5 Flotation process*

Flotation process is based on buoyancy effect of adhered particulate matters such as, suspended solids, oils, greases, and biological solids with either air or gas from a liquid phase under pressure [90]. These particulate matters adhere to gas or air and form agglomerates and float on the water surface which can then be skimmed off easily. Compressed air and sometimes chemicals such as alum and activated silica are used for this process [74]. There are several flotation methods used in industries for municipal wastewater treatment such as air floatation, vacuum flotation, electro flotation and chemical flotation. Electro-flotation (electro-flocculation) has been the most effective to remove up to 75% of suspended solids and up to 99% of oil and grease from wastewater [91].

### 1.3.2 Secondary water treatment technologies

Secondary treatment processes include microbes to remove organic and inorganic soluble and insoluble materials through biological route. Microbes such as, bacterial and fungal stains are used to convert organic matter into small molecules such as water, carbon dioxide, ammonia, alcohols and glucose nitrates [92-94]. As a consequence, the level of Biological Oxygen Demand (BOD) drops significantly through the process. There are two systems that follow this biological route named as anaerobic and aerobic treatment. In the aerobic process the organic matter undergoes degradation caused by aerobic and facultative bacteria with the aid of dissolved or free air in waste. Anaerobic processes don't have dissolved or free air in water [95]. Secondary treatments may require a separation process to remove the micro-organisms from the treated water prior to discharge or tertiary treatment. Some of the major processes of secondary or biological treatment are as follows:

(i) Activated Sludge Process: The organic matter is brought into intimate contact with the sludge. This sludge is heavily laden with micro-organisms which are in an active state of growth. Air is introduced into the tank either in the form of bubbles through diffusers or by surface aerators. The effluent from the aeration tank containing the flocculent microbial mass, known as sludge, is separated in a settling tank. A portion of separated sludge is activated and reused and rest of it is disposed off.

(ii) Trickling Filters Process: The influent is sprinkled over the packed bed made of rock, lava, coke, gravel, slag, peat mass, ceramic and polyurethane foam, which is coated with a biological film or slime layer (approximately 0.1 to 0.2 mm thick). As the liquid trickles over the packed bed, oxygen and the dissolved organic matter diffuse into the film to be metabolized by the micro-organisms on a slime layer. As the biofilm layer thickens, it eventually sloughs off into the liquid flow and subsequently forms part of the secondary sludge.

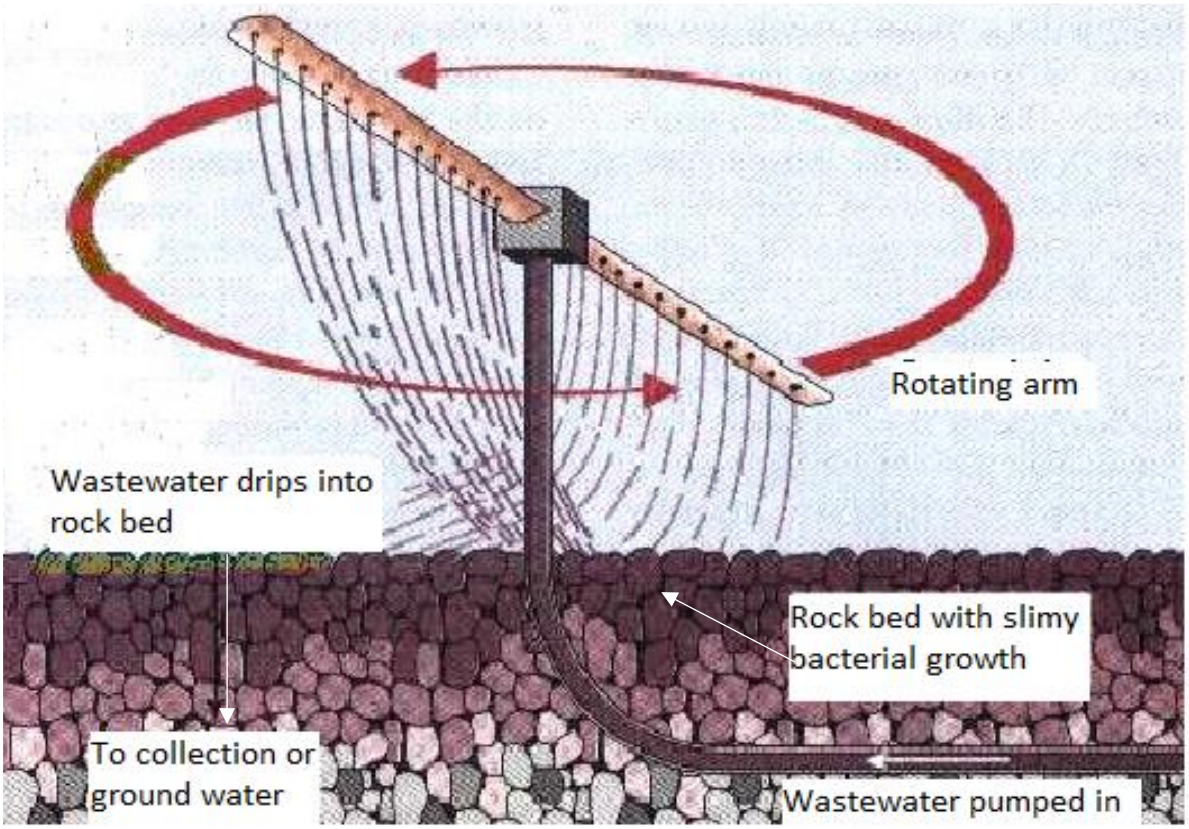



*Figure 1.4: Schematic image of a trickling filter [96].*

### 1.3.3 Tertiary treatment technology

This includes an advanced level of treatment in order to obtain safe water for consumption by humans. These processes remove significant amounts of nitrogen, phosphorus, heavy metals, biodegradable organics, bacteria and viruses. These technologies include filtration, adsorption, chemical oxidation process, thermal treatment and electrical treatment.

#### *1.3.3.1 Filtration*

Filtration is the core stage of water treatment, which basically consists of passing water through a bed of sand or other suitable medium at low speed. The filtrate should ideally be crystal clear and have a turbidity of around 0.1 nephelometric turbidity units (NTU) [23]. Figure 1.5 shows the most commonly used filtration processes available in water treatment, the pore size of the filter media and the sizes of different particles. These size spectra are useful for understanding removal mechanisms and efficiencies, and for developing strategies to remove microbes by different filtration processes.

##### 1.3.3.1.1 Granular filters

There are three types of granular filters: a) slow sand filter, b) rapid gravity filter, and c) pressure filter.

a) Slow Sand Filters (SSF): This is the oldest of the technologies and capable of achieving high standard of water without use of additional chemicals. The bed is made of sand grains of size 0.15mm to 0.35mm size with a uniformity co-efficient of 1.5-3 (preferably less than 2) [97].The treatment process is based on two mechanisms: i) Physical straining and ii) biological action. Micro-organisms such as bacteria, viruses and parasites are allowed to travel through the sand, they collide with and adsorb onto sand particles. The organisms and particles collect in the greatest density in the top layers of 1-3 cm above the sand, gradually forming a biological zone sometimes referred to as ‘schmutzdecke‘ or ‘filter cake’. In several studies, it was reported that SSF is effective for removal of 99% of bacteria, suspended solids and waterborne pathogens [98-102]. Although the disadvantages associated with this filtration technique include reduced efficacy at low temperature, high turbidity, ineffective removal of coloured materials, treating stable fine colloidal suspensions and imbalance in biological equilibrium due to frequent scraping [99, 103-105].
b) Rapid gravity filters: This type of filter works at high loading rates. The bed is made of coarse media (0.3-0.45 mm size) with certain level of porosity that allow high permeability. Coagulation is a pre- requirement. In some cases, granular activated carbon (GAC) is also used which adsorbs chemicals. The beds can be composed of use single medium (such as, sand) or

mixed of two or more mediums such as, sand with GAC. Disadvantages of rapid sand filtration include high capital and operating costs and extensive operator training [106-108].

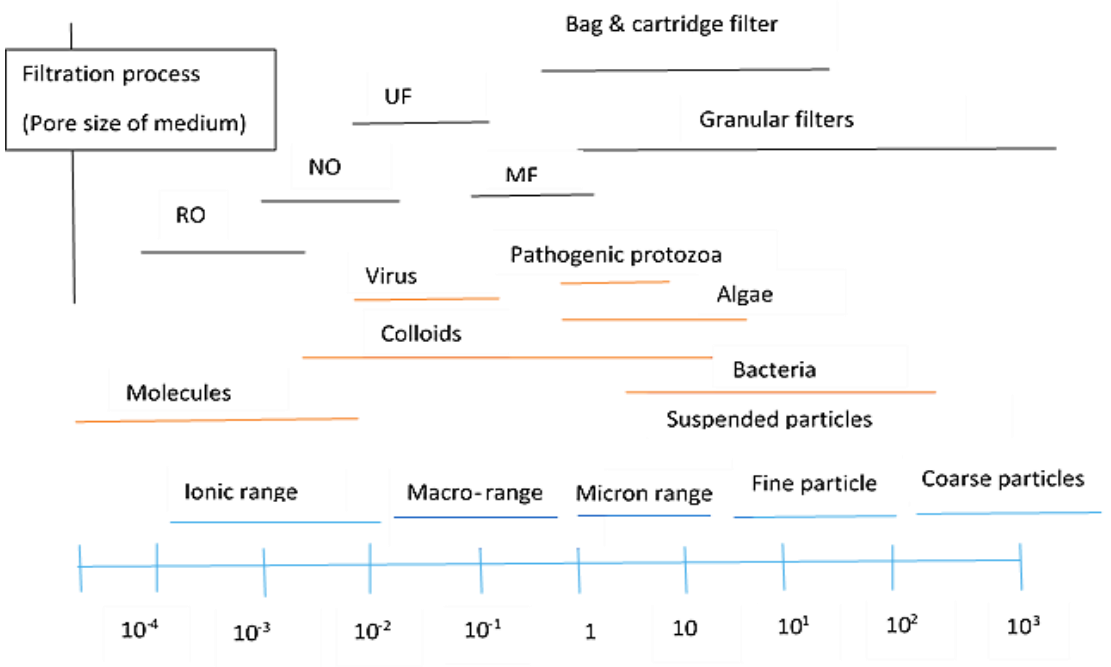



***Figure 1.5: Size range of particles of concern and pore size of filter medium in water treatment in µm range [109].***

c) Pressure filters: Pressure filters are the same as rapid gravity filters, with the only difference being that the pressure is applied in a large, closed vessel. These are mainly used for treating ground water with less turbidity as well as iron and manganese as impurities. This process can be employed for the removal of iron from ground water up to 10 mg/l [110, 111].

#### 1.3.3.1.2 Membrane filtration:

Membranes are films with specific pore or permeability ratings, which selectively separate a fluid from its solid or liquid particulate, molecular and even ionic components. Microfiltration (MF), Ultrafiltration (UF), Reverse Osmosis (RO) and Nanofiltration (NF) are the four established membrane separation processes used in water purification [112]. The filtration spectrum (as presented in Figure 1.5) shows the size range of particles and the type of filtration used for each range.

a) Microfiltration (MF): Microfiltration widely uses membranes which have a microporous barrier having pores of 1-10 µm which can remove small particles. MF is typically used for turbidity reduction and removal of suspended solids specially bacteria, algae, protozoa, such as Giardia and cryptosporidium [113]. The operational pressure of MF process is about 1–3 bar [114]. The filters used in this process are usually made of cotton, wool, rayon, cellulose,

fiberglass, polypropylene, acrylics, nylon, asbestos and fluorated hydrocarbon polymers [115, 116].

b) Ultrafiltration (UF): The aperture of ultra-filtration membranes is much smaller than MF membranes (pore diameter ranges from 0.001 – 0.1 µm). UF is the most effective method for de-oiling water produced compared to traditional separation methods [44]. UF is also much more efficient than MF. In desalination operation UF is used as a pre-treatment method [117, 118].

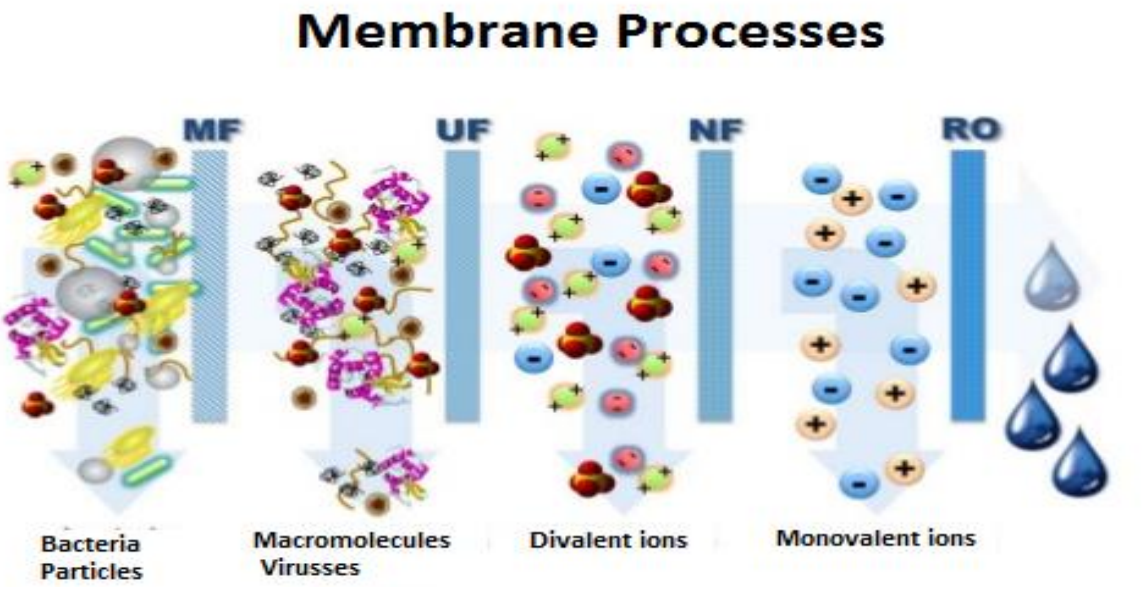



*Figure 1.6: Different membrane filters with contaminants removing abilities [119].*

c) Nanofiltration (NF): Nanofiltration membranes are designed to remove contaminants as small as 0.001 µm for water softening and metals removal. The nano filtration strategies accomplish a sharp diminishment in chemical oxygen demand (COD) alongside the expulsion of colours, applicable for water containing total dissolved solid (TDS) in the range of 500 to 25,000 mg/L [120, 121]. Nanofiltration can be used to treat groundwater where the levels of natural organic matter (NOM) are very low, or as an end treatment when water has been pre-treated to reduce the NOM levels [122, 123].

d) Reverse osmosis (RO): In reverse osmosis, pressure greater than osmotic pressure is applied through permeable membranes, separating contaminants from water. It virtually removes all organic compounds and 90 to 99% of all ions with 99.9% rejection of viruses and bacteria [109, 124]. It is one of the most efficient methods for water desalination as well as production of ultra-pure water for use in pharmacy, medicines and electronics. Operating costs depend on energy price and the level of total dissolved solids (TDS) in the feed water [125]. However,

RO processes have disadvantages such as membrane fouling and scaling. To significantly reduce fouling tendency, low fouling composite (LFC) membranes were also developed. The LFCs are composed of hydrophilic membranes with low surface charge [126, 127]. Recent advancement in reverse osmosis process is osmotic membrane bioreactor (OMBR) process which utilises natural osmosis pressure with minimal fouling tendency [128-131].

#### *1.3.3.2 Chemical oxidation process*

This process reduces biological oxygen demand (BOD), chemical oxygen demand (COD), dissolve organic matter (DOM), natural organic matter (NOM) into minimal considerable amounts due to degradation of organic molecules such as alcohols, aldehydes, ketones and carboxylic acids [132]. This process uses ozone [133], combined ozone and peroxide [133], ultraviolet (UV) enhanced oxidation such as UV/Fenton [133], UV/hydrogen peroxide [134], UV/ozone [135], UV/air), wet air oxidation and catalytic wet air oxidation (where air is used as the oxidant) [134], photocatalysis [136, 137] and supercritical water [138, 139]. These processes involve production of highly reactive hydroxyl free radicals through a series of chemical reactions. The hydroxyl radicals have high oxidising potential and therefore can attack most organic pollutants due to oxidation [11, 140]. However, it cannot be used as a single process for water purification due to highly expensive process and sometimes an incomplete degradation of organic pollutants leads to formation of undesirable free radicals and by-products that can leach back into the environment [141-144].

#### *1.3.3.3 Thermal process technologies*

Thermal processes involve various types of distillation processes such as multistage flash distillation (MSF), vapour compression distillation (VCD), multi effect distillation (MED), hybrid thermal desalination plants (such as MED – VCD) and have been used to achieve higher efficiency. This process is applicable in the regions where the cost of energy is relatively cheap. This process is also mainly utilised to supply water in laboratories and medicinal preparations [145]. Although membrane technologies are typically preferred, recent innovations in engineering make thermal processes more attractive and competitive in demand of highly pure water [146]. Other heat treatment operation involves evaporation processes and crystallisation which are used to make concentrated effluent volume and used alongside other water treatment processes. Evaporation is effective for the removal of inorganic and organic (except volatile organic) contaminants, and it works even at very high concentrations (about 10%) of pollutants. However, these processes are very costly and associated with foaming, scaling and fouling problems.

### *1.3.3.4 Adsorption*

The adsorption process is one the simplest techniques based on surface phenomena of the adsorbent [147-149]. Activated carbon from various sources such as coconut coir, jute stick, rice husk, fly ash, metal oxides, zeolites, moss, biomass, molecular sieve, silica gel, alumina and geothites, nanomaterials (such as carbon nanotubes) are the most popular of the adsorbents [150-155]. The treatment sometimes includes combination of adsorption with catalytic treatment methods, redox processes and magnetic processes [11, 156-159]. Adsorption efficiency can depend on several factors such as temperature, the presence of other pollutants, the nature of the adsorbent, adsorbate, and experimental conditions (pH, concentration of contaminants, contact time and particle size of the adsorbent). Presence of oils and greases and suspended particles reduces the efficiency of the process and, therefore, pre-filtration is sometimes required [160, 161]. Adsorption experiments are first carried out in a batch process and conditions are then optimised. The developed and optimised conditions (from the batch process) are then transferred to the column (fixed bed) process. Batch process give a brief knowledge about equilibrium isotherm that gives an idea about the concentration of pollutant adsorbed on a particular adsorbent. Well-known models of Langmuir, Freundlich, Hutchins, Redlich-Peterson, Brunauer-Emmett-Teller (BET) and McKay, are used to verify the feasibility of the batch adsorption process [162]. Adsorption process not only depends on the bulk concentration but also on the process in which the technique is carried out. A Fixed bed adsorption is a dynamic process representative of industrial and point-of-use applications [163].

**Activated carbon**

Granular activated Carbone (GAC) and powdered activated carbon (PAC) are heavily used in water treatment processes as adsorbents. Activated carbon has high surface area with heterogeneous multifunctional groups (mainly hydroxyl, carboxyl, phenol, lactone, lactol, and quinone), and inorganic ash [164]. These anchoring groups also contribute towards specific activity and with definite sorption selectivity. The porosity is optimised by selecting the activation parameters such as, physical, chemical, and electrochemical treatments [165-168], choice of activating agent [169-171], impregnation ratio [172], activation sequence [173] and pyrolysis or activation temperature [174]. Several batch and column adsorption studies have been reported for adsorption of dyes, phenols, heavy materials, carbon dioxide. Activated carbon is practically the best adsorbent, however, high operating cost associated with separating fine activated carbon from wastewater [175]. The surface of Activated carbon is a strong reducing agent, therefore it reacts with chlorine and other disinfectants which create a problem controlling biological growth [23]. Some authors have reported poor adsorption of toxic metals such as arsenic, in presence of other competing ions (e.g. $Ca^{2+}$, $Mg^{2+}$, and

$Na^+$) [176] and endocrine disrupting chemicals EDCs (ibuprofen, sulfamethoxazole, meprobamate) [177]. Another major drawback of activated carbon is its low adsorption affinity for low molecular weight polar organic compounds [178]. Several authors report the synthesis of activated carbon from low-cost raw materials such as bagasses [179], sugarcane [180], rice husk [181], molasses [182], coconut shell [183] and agricultural waste [184, 185] as these raw materials are renewable and potentially less expensive to manufacture. To ease in separation, magnetic activated carbon was synthesised. Different surface modifications such as selective adsorption of antibiotics with magnetic activated carbon, heavy metals such as Cu (II) and Pb (II) by iron loaded activated carbon [186], lead by gelatine-activated carbon composite [187], pesticides by Ag/AgCl- activated carbon composites [187], dyes by zeolite-activated carbon composite [188, 189] or Cu $(OH)_2$-nanoparticle loaded activated carbon [190] were explored. However, very few of these studies highlighted column adsorption process using activated carbon prepared using low-cost resources and surface modifications.

**Oxidic adsorbents**

Aluminium oxide, activated aluminium oxide and iron oxide have been reported to selectively adsorb phosphorous [191, 192], zinc [193], cobalt, copper, manganese [194], fluoride [195].

**Zeolites**

Zeolites occur in nature in high diversity. Zeolites have high cationic exchange capacity. However, their adsorption performance in multi component system shows selective adsorption [148]. In addition, adsorption of anionic ions and organics is possible only by further surface modification using cationic surfactant that can change the surface charge of natural zeolite, making them applicable for adsorption of anions and organics [148]. Some promising experimental results for several organic adsorbates were published in the past, zeolites have not found broad application as adsorbents in water treatment until now [196].

**Polymers**

Polymeric materials such as starch, cellulose, polystyrene, chitosan, polydopamine, synthetic resin and chitin, are gaining much more interest, since they are nontoxic, environment-friendly, low-cost, and highly efficient [197-200]. The adsorption capability of reactive dyes using chitosan was reported at 1000–1100 g $kg^{-1}$ [201], which is several times larger than activated carbon. This high adsorption capacity of chitosan is due to the high contents of amino and hydroxyl functional groups on its surface, forming high binding ability between chitosan and contaminants. However, their application is still limited due to impractical regeneration process [202], poor mechanical property, biodegradability and selective absorbability.

**Metal-organic frameworks (MOFs)**

Metal-organic frameworks (MOFs) are organic-inorganic hybrid functional materials with high porosity and large surface area which typically range from 1000 to 10,000 $m^2/g$ and unique morphology [203]. Their functional property is based on the metal ion and organic bridging ligand. [204]. Metal-containing units [secondary building units (SBUs)] are joined with organic linkers (ligands), using strong bonds to create open crystalline frameworks with permanent porosity. The architecture of the frame structure containing metal SBUs and organic linkers can be varied leading to thousands of compounds. Since 1999 more than 20,000 different MOFs have been reported and studied [203]. The first study of the adsorptive removal of dye using MOFs was reported by Haque et al. using two highly porous Cr-based MOFs, namely MIL-101-Cr and MIL-53-Cr (MIL: Material of Institute Lavoisier) for the adsorptive removal of methyl orange. He concluded that the adsorption was based on porosity and pore size of MOFs and later he prepared more efficient adsorbent using same material by surface functionalisation [205]. Hasan et al. reported removal of hazardous organics from water using metal-organic frameworks (MOFs) highlighting plausible mechanisms for selective adsorptions [206]. They explained the mechanisms of interactions such as electrostatic interaction, acid–base interaction, hydrogen bonding, π–π stacking/interaction, and hydrophobic interaction organics over MOFs. In their review adsorption of several dyes such as methylene blue, uranine, naproxen, clofibric acid, phthalic acid, nitrobenzene and many other organic pollutants were demonstrated using different types of MOF (see Table 1.2).

*Table 1.2: Adsorption of hazardous organics from water over various MOFs and dominant mechanisms reported by Hasan et al. [206].*

| MOFs | Adsorbates | Amount adsorbed (mg/g) | Dominant mechanisms |
|---|---|---|---|
| MIL-101-Cr | MO | 114 | Electrostatic interaction |
| ED-MIL-101-Cr | MO | 160 | Electrostatic interaction |
| PED-MIL-101-Cr | MO | 194 | Electrostatic interaction |
| MOF-235 | MO | 477 | Electrostatic interaction |
| MOF-235 | MB | 187 | Electrostatic interaction |
| MIL-100-Fe | MO | 1045 | Electrostatic interaction, metal effect |
| MIL-100-Fe | MB | 645 | Electrostatic interaction |
| MIL-100-Cr | MO | 211 | Electrostatic interaction, metal effect |
| MIL-100-Cr | MB | 736 | Electrostatic interaction |
| $NH_2$-MIL-101-Al | MB | 762 | Electrostatic interaction |
| $NH_2$-MIL-101-Al | MO | 188 | Electrostatic interaction |
| MIL-101-Cr | Uranine | 126 | Electrostatic interaction |
| ZIF-8 | Uranine | 10 | Electrostatic interaction |
| MIL-101-Cr | Naproxen | 119 | Electrostatic interaction |
| MIL-100-Fe | Naproxen | 104 | Electrostatic interaction |
| MIL-101-Cr | Clofibric acid | 315 | Electrostatic interaction |
| AMSA-MIL-101 | Clofibric acid | 105 | Acid–base interaction |
| ED-MIL-101-Cr | Clofibric acid | 347 | Acid–base interaction |
| ZIF-8 | Phthalic acid | 654 | Electrostatic interaction, acid–base interaction |
| UiO-66 | Phthalic acid | 187 | Electrostatic interaction, acid -base interaction |
| NH2-UiO-66 | Phthalic acid | 224 | Electrostatic interaction, acid -base interaction |
| MIL-101-Cr | Bisphenol A | 156 | π–π interaction and hydrogen bonding |
| MIL-100-Fe | Bisphenol A | 26 | π–π interaction and hydrogen bonding |
| NH-MIL-101-Al | p-Nitrophenol | 192 | Hydrogen bonding |
| CAU-1 | Nitrobenzene | 970 | Hydrogen bonding |
| MIL-68-Al | Nitrobenzene | 1130 | Hydrogen bonding |

**Nanomaterials**

The ongoing opportunities of nanomaterials has introduced numerous aspects for its application including in water treatment. Nano materials such as layered double hydroxides (LDH), carbon nanotubes (CNT) including single and multiwall, and graphene oxide (GO) nano sheets have been used in nanofiltration and adsorption processes, where these nanomaterials act as a catalyst for breaking down of contaminants [207]. Nanomaterials have larger surface area compared to their bulk materials. Surface of nanomaterials have also been functionalised to increase their affinity towards target compounds. For example, Luo *et al.* reported that carbon nanotubes were functionalised by ozone to increase their catalytic activity [208]. Zhang *et al.* stated that thiol functionalised CNTs were investigated for heavy metals such as $Hg^{2+}$ and $Pb^{2+}$ removal [209].

Layered double hydroxide (LDHs) nanoparticles possess brucite type structure with positively charged layers of mixed metal hydroxides [210]. This charge is compensated by exchangeable anions located within interlayers. Numerous studies have been reported for adsorption of heavy metal, dyes, antibiotics and toxic materials using LDH [211]. LDH containing CNT, graphene oxide (GO), other metal oxide hybrids were suggested to be more efficient in adsorption process reported by Zubair *et al.* [212]. The maximum adsorption capacities of various toxic heavy metals and dyes on different LDH hybrids were reported at 483 mg/g for $Pb^{2+}$, 95 mg/g for $Cd^{2+}$, 181 mg/g for $Cu^{2+}$,649 mg/g for $Cr^{6+}$, 180 mg/g $As^{5+}$, 813 mg/g for $Hg^{2+}$, 450 for $Ag^{+}$, 277 mg/g for $U^{6+}$, 1062 mg/g for methyl orange, 185 mg/g for methylene blue, and 1250 mg/g for Congo red, which was comparatively higher than other commercial adsorbents.

**Spheres**

Various spherical structures have been fabricated via emulsion, sol-gel, and flame spheroidisation methods with features such as tailorable surface area, reactivity, and tuneable pore volume, electrostatic, hydrophilic and hydrophobic interactions which are useful in adsorption, catalysis, sensor and optoelectronics applications. Several reports have demonstrated application of micro and nanospheres in water treatment applications. For example, Qi *et al.* reported that hierarchical porous hydroxyapatite microspheres had high adsorptive capacity approximately 213 and 59 mg/g for heavy metals $Pb^{2+}$ and $Cu^{2+}$ [1]. Li XZ *et al.* also reported that $TiO_2$ microspheres were investigated for photodegradations of salicylic acid (SA) and sulfosalicylic acid (SSA) [2]. Ruqaiya *et al.* synthesised acrylate polymer microspheres embedded with $TiO_2$ for photocatalytic water treatment using

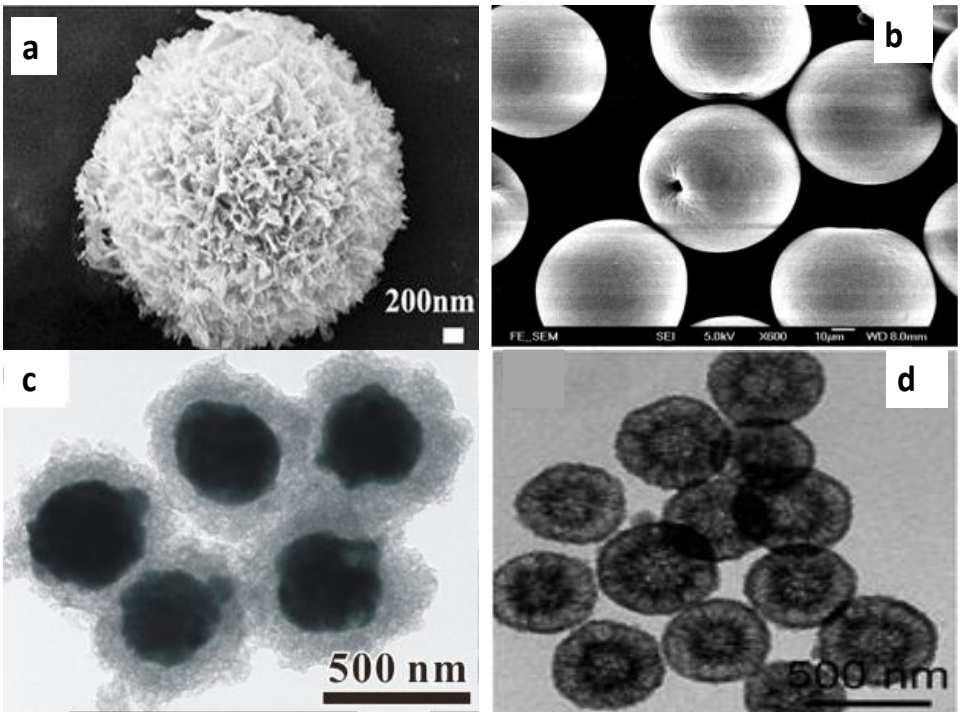



***Figure 1.7: SEM images of a) porous hydroxyapatite microspheres [1], b) $TiO_2$ microspheres [2] and TEM image of c) $Fe_3O_4$/Fe with a ZnO core nanospheres [3], d) $Fe_3O_4$/polypyrrole (PPy) microspheres [4].***

microfluidic processes [213]. The shell and core type $Fe_3O_4$/Fe with a ZnO core heterostructure nanospheres with ferromagnetic properties were suggested for removal of Pb(II) and methylene blue dye [3]. Additionally, Ag core–$TiO_2$ shell nanospheres were studied for anthraquinone dye removal [214] and core bioceramic and LDH shell microspheres were investigated for phosphate removal [215]. Composite microspheres were also suggested for variuous types of dyes and heavy metal removal. For example, porous chitosan/$TiO_2$/$Fe_3O_4$ microspheres were investigated for acid dye removal [216], $Fe_3O_4$/polypyrrole (PPy) microspheres for adsorption of Cr(VI) ion [4], composites of

polyaniline,starch, polypyrrole, chitosan aniline and chitosan pyrrole for dye adsorption [217]. Photosphere® a hollow glass coated with $TiO_2$, Materium- a porous hollow silica sphere and hollow spheres from Nalco are the commercially available microspheres that are currently used for water treatment. A list of spherical shaped particles (spheres/microspheres/nanospheres) investigated for water treatment applications is presented in Table 1.3.

*Table 1.3: Table showing microspheres in water treatment applications.*

| Microsphere | Preparation method | Surface area and porosity | Purpose | Reference |
|---|---|---|---|---|
| Porous Magnetic polydivinylbenzene (PDVB) microsphere | Chemical template | 239 $m^2/g$ pores are bigger than 30 nm size-(350–450 µm) | Removal of cationic dye with the aid magnetic property of microsphere | [218] |
| $Fe_3O_4$@$SiO_2$ core and perpendicularly aligned meso-porous $SiO_2$ shell | surfactant-templating sol–gel | 365 $m^2/g$, pore volume (0.29 $cm^3/g$), and uniform mesopore (2.3 nm). Size (~500 nm) | As an absorbent to remove microcystins from eutrophic water | [219] |
| $TiO_2$ microspheres | Reversed suspension polymerization and sol–gel | 87 $m^2/g$; 200–500 µm | As photo catalyst in water treatment | [220] |
| $TiO_2$ microsphere | A sol spraying calcination | 112 $m^2$ /g; 30-160 µm | Effective photo-oxidation with ease of recovery | [2] |
| flower-like $Fe_3O_4$ microspheres | Hydrothermal | 70 $m^2$ /g | Removal of dye material (Congo red) | [221] |
| $CeO_2$ nanocrystal spheres | Sol–gel | 50-100 nm in diameter, surface areas 65 $m^2/g$ and total pore volume of 0.037 $cm^3/g$ | Removals of Cr (VI) and rhodamine B organic dye (RhB) in batch process | [222] |
| Mesoporous $TiO_2$ with fluorinated surface | Hydrothermal | 0.1-0.6 µm diameter range, 21 $m^2/g$ surface area | Photocatalytic activity aid in filtration with the commercially available Degussa P25 $TiO_2$ particles | [223] |
| Ce-doped $TiO_2$ nanoparticles supported on porous soda lime glass | Subcritical water treatment followed by solution dispersion | 95–105 µm, Surface area 101 $m^2/g$, Pore diameter 5.9 nm | Effective in adsorbing rhodamine blue and methylene orange | [224] |
| Hollow $MnO_2$ microspheres | Self-assembly with an intermediate crystal-templating | 6 µm in size | Used as adsorbents or catalysts to remove organic (Congo red) waste from water | [225] |

| | | | | |
|---|---|---|---|---|
| Alpha-$Fe_2O_3$ Hollow Microsphere | Hydrothermal process followed by sequential calcinations | 13 $m^2/g$, | Removal capacities over Cd(II), Pb(II), and phenol | [226] |
| Aluminium oxyhydroxide microsphere | Hydrothermal | 3 µm diameter, 91-269 $m^2/g$ and a pore volume of 0.35-0.47 $cm^3/g$ | Adsorption of organic (Congo red, phenol) pollutants in water | [227] |
| $Fe_2O_3$ sphere | Thermal decomposition followed by calcination | 100 nm in size, 40 $m^2/g$ | Excellent ability to remove heavy metal ions As (V), Cr (VI) and Orange II dye | [228] |
| BiOBr nanospheres | Ionothermal | 14 $m^2/g$ with narrow pore size distribution 4nm to 25 nm | Suitable for removing heavy metals and treatment of organic dyes. Effective in killing Micrococcus lylae, a Gram-positive bacterium, in water under fluorescent light irradiation | [229] |
| NiO network-like hierarchical nano spheres | Hydrothermal | 215-242 $m^2/g$ | Effective removal of congo red dye | [230] |
| Magnesium silicate nano spheres | Chemical template | 521 $m^2$ /g<br>Size 500 nm | To remove organic pollutant (methylene blue) and toxic metal ions (lead) | [231] |
| Calcium phosphate hollow microsphere | Gas diffusion | 130$cm^3/g$, the pore volume of 0.36 $cm^3/g$, and the pore size of 4.7nm. | Selective adsorption of $Pb^{2+}$and $Cu^{2+}$ | [1] |
| Nano hollow $SnO_2$ spheres | Self-assembly via solvent route | 5.3 nm in size<br>Surface area e 88.6 $m^2$ /g | Cleaning wastewater by adsorbing basic fuchsine from aqueous solution | [232] |
| Surface functionalized silica sand microsphere | Hydrothermal process followed by chemical functionalization | 4 µm | Adsorption of $Cr^{6+}$ | [233] |
| Aluminosilicate-alginate hybrid spheres | One-pot synthesis | 2-4 mm | Effective in adsorption of Cu (II) ion from water | [234] |

## 1.4 Glasses and glass ceramic materials in water treatment

Glass is amorphous material, exhibit different physical, chemical, and optical properties due to their compositional differences. On the other hand glass ceramics are glasses which have undergone heat treatment that results in one or more crystalline phases within it [235]. Complying with the demand of application, glasses and glass ceramics have specific composition and manufacturing processes.

### 1.4.1 Silicate Based Glasses

Silicate based glasses are composed of a three-dimensional network of $SiO_4$ tetrahedral units. This $SiO_4$ tetrahedral unit is connected with four other units via bridging oxygen bonds to form a continuous, 3-dimensional network giving the stoichiometry of $SiO_{4/2}$ or $SiO_2$. Silicate glasses are primarily made of the glass network former $SiO_2$; however, multivalent (e. g., $Fe^{2+/3+}$) and rare-earth oxides, and volatile elements (H, C, S, Cl, F, I) are used to vary the qualities of the finished product [236]. Addition of these oxides (known as modifier oxides) disrupt the Si-O-Si bond and generate Si-O- terminals causing depolymerisation of the silicate structure. Bridging oxygen (BO) is known as the oxygen in the Si-O-Si connection, whereas non-bridging oxygen (NBO) is oxygen in the Si-O- linkage (NBO) [237]. The common form of silicate glasses are soda-lime silicate, aluminosilicate, borosilicate etc manufactured as window glasses for buildings and automobiles and display glasses for TV panels and mobile phones [238]. Silicate glasses have been used where high service temperature, very high thermal shock resistance, high chemical durability, very low electrical conductivity, and good ultraviolet transparency are desired.

### 1.4.2 Phosphate based Glass (PBG)

Phosphate based glass (PBG) are glasses whose backbone is made of $P_2O_5$. In vitreous $P_2O_5$, P-O-P bonds are formed when a phosphorous atom is covalently bonded to three bridging oxygens (BO) by a single bond. The fourth terminal oxygen atom (TO) is joined to the others by producing the P=O bond [239, 240]. The oxygen to phosphorus ratio (O/P) determines the number of tetrahedral links between neighbouring $PO_4^{3-}$ tetrahedral glasses via bridging oxygens (BO), can be used to classify phosphate glass networks. $PO_4$ tetrahedra with three BO and one non-bridging oxygen (NBO) (the percentage of O/P = 2.5) are represented by ultra-phosphate glasses ($Q^3$), whereas metaphosphate glasses ($Q^2$) are characterized by tetrahedra with two BOs and two terminal oxygens (O/P = 3) [241]. Furthermore, pyrophosphate ($Q^1$) species (O/P = 3.5) are phosphate tetrahedra with one bridging oxygen (BO) and three non-bridging oxygens (NBO), whereas orthophosphate glasses ($Q^0$) represent four non-bridging oxygens (NBO) (the fraction of O/P = 4) [242, 243]. The addition of alkali (MeO) and alkaline earth

($Me_2O$) oxides causes depolymerisation and the creation of NBO in this three-dimensional network. The number of NBOs grows as the number of MeO and $Me_2O$ modifiers increases, and hence the number of $Q^n$ species decreases from $Q^3 \rightarrow Q^2 \rightarrow Q^1 \rightarrow Q^0$. Depending on the number of modifier oxides added the PBGs can be further divided into binary, ternary, quaternary and quaternary phosphate glasses.

PBG can be easily fabricated into glass and have a lower glass transition temperature. For example alkali aluminophosphate compositions have glass transition temperatures under 400°C and thermal expansion coefficients greater than $150 \times 10^{-7}$/ °C which is much lower compared to alkali alumina silicate glasses [240]. PBG can be tailored from fully resorbable to non-degradable glass formulations by simply altering their compositions [244-246]. Phosphate glasses have been investigated for their use in various fields ranging from biomaterial [247], semiconductor [248] and sensor design [249] to nuclear waste encapsulation [250]. Considerable interest of PBG for a variety of clinical applications has developed including dental, maxillofacial and orthopaedic implants and as scaffolds for bone tissue engineering [247, 251-254] because of its intrinsic features, such as their near chemistry to natural bone [255, 256], completely resorbable qualities, controlled degradation rates, and biocompatible nature [257-259]. Patel *et al.* performed in vitro cellular testing on phosphate glass disc made of $40P_2O_5$-(16-x)CaO·$20Na_2O$·24MgO·xSrO (x = 0, 4, 8, 12, and 16 mol%) for bone regeneration application and they reported that the near invert glass system are cytocompatible and promoted adhesion and growth of human MG63 and hMSCs, respectively, up to 14 days which suggested that these materials are appropriate for the culture, expansion, and cellular activity of human cells constituting as excellent candidates for bone regeneration [260]. Islam *et al.* conducted the research on structural and crystallisation behaviour of titanium phosphate based glass formulation in the glass system of $40P_2O_5$–(24 − x)MgO–(16+x)CaO–(20−y)$Na_2O$–y$TiO_2$ (where $0 \leq x \leq 22$ and y = 0 or 1) and they reported that substitution of MgO with CaO in the glasses lead to a decrease in glass transition, onset crystallisation, crystallisation, melting temperature, density and activation energy of crystallisation due to the replacement of higher field strength $Mg^{2+}$ by lower field strength $Ca^{2+}$ [261]. Due to their highly controlled solution degradation characteristics, these glasses may be doped with antibacterial ions such as silver and copper at a consistent pace [247, 262].

### 1.4.3 Application of glasses and glass ceramic materials for water treatment

Table 1.4 highlights the most commonly used glass and glass ceramic compositions, their properties, and typical applications. In comparison to the studies above, relatively little research been done with glass and glass ceramics for water treatment applications. Glass has mainly been used as silica glass

frit as slow sand filters and rapid sand filters in replace of sand. Elif *et al.* reported that filter containing crushed glass reduced effluent turbidity and particle counts similar to those obtained with the sand filter. They showed that crushed glass had significant promise as an alternative to silica sand in rapid filtration [263]. Another recent development was photocatalytic water treatment by using glass as substrate for immobilizing the photocatalyst such as $TiO_2$ [264]. It has also been reported that soda-lime glass, borosilicate, and fused quartz substrates retained a constant photocatalytic activity of titania without deactivation during the reaction either by inhibition, loosening or poisoning of the catalyst and could be re-utilized in subsequent runs [264]. More recently, Singh et *al.* reported methylene blue dye degradation using transparent silicate glass–ceramics containing $LiNbO_3$ piezoelectric crystals. They demonstrated 90% degradation of methylene blue dye within 150 min of ultrasonication due to polarization field that forces free holes (h+)/electrons (e−) to participate in catalytic redox reactions [265]. Nishida *et al.* reported fabrication of porous glass ceramic sintering waste soda lime silicate and charcoal for water purification [266].

*Table 1.4: A table showing comparison among common commercial glasses.*

| Name | Type | Principal components | Linear thermal expansion ($10^{-7}$/K) | Thermal shock resistance | Chemical resistance | Application |
|---|---|---|---|---|---|---|
| **Borosilicate** | Glass | $SiO_2$, $B_2O_3$ | -30-60 | High | High | -Industrial equipment<br>-Laboratory and kitchen glassware<br>-nuclear waste management [276] |
| **LAS system** | Glass ceramic | $Li_2O$, $Al_2O_3$, $SiO_2$ system | n/r | Very high | Very high | Cookware, bakeware,<br>Thermal insulation,<br>Refractory material [263] |
| **96 % - silica glass** | Porous glass | 96% $SiO_2$ | n/r | High thermal shock resistance | Very high | Dental implant, chromatographic application, composite preparation, Hyper filtration and ultrafiltration process [263] |
| **Silica glass** | Glass | $SiO_2$ | 55 | High thermal shock resistance | Very high | Water treatment as glass frits, semiconductors, optical lenses [238] |
| **MAS system** | Glass ceramic | MgO, $Al_2O_3$, $SiO_2$ | 70-120 | High | High chemical stability | Refractory application, Dental material [277] |
| **Lead Phosphate** | Glass | PbO, $P_2O_5$ | | | | Nuclear waste immobilization [250] |
| **ZAS system** | Glass ceramic | ZnO, $Al_2O_3$, $SiO_2$ | Low coefficient of thermal expansion | n/r | High chemical stability | Optical fibre application [249] |
| **Soda-lime silicate** | | $SiO_2$, $Na_2O$, CaO | -80-100 | Low | Average | -Food and beverage<br>-window etc. [238] |
| **Phosphate glasses** | | $P_2O_5$ | -90-110 | Low | Low, except high resistance to hydrofluoric acid | -Bone scaffold<br>-Optics fiber [267]<br>-Heat absorber [268]<br>-Nuclear waste management [269] |

Their results demonstrated that the porous glass ceramic produced was also useful for removing water turbidity and the pores were able to maintain suitable environment for microbial proliferation. Similar porous glass ceramics using waste recycled soda lime glass via sintering process using volcanic ash [270], fly ash [271], coal ash [272] were also reported. These types of glass ceramic have shown potential in drinking water purification and fish preserving water under aerated conditions. All the reports concluded that the purification tendency of these glasses was attributed to 3D-channels (pores) with diameters of several nm to several µm, which caused an increase in surface area (i.e., 0.05–7.5 $m^2 g^{-1}$ as reported by Nishida *et al.*) compared to solid (non-porous) glass ceramics [273]. Similarly, Sheng et *al.* reported presence of mesopores/micropores for adsorption of methylene blue by silica using a fixed bed system [274].

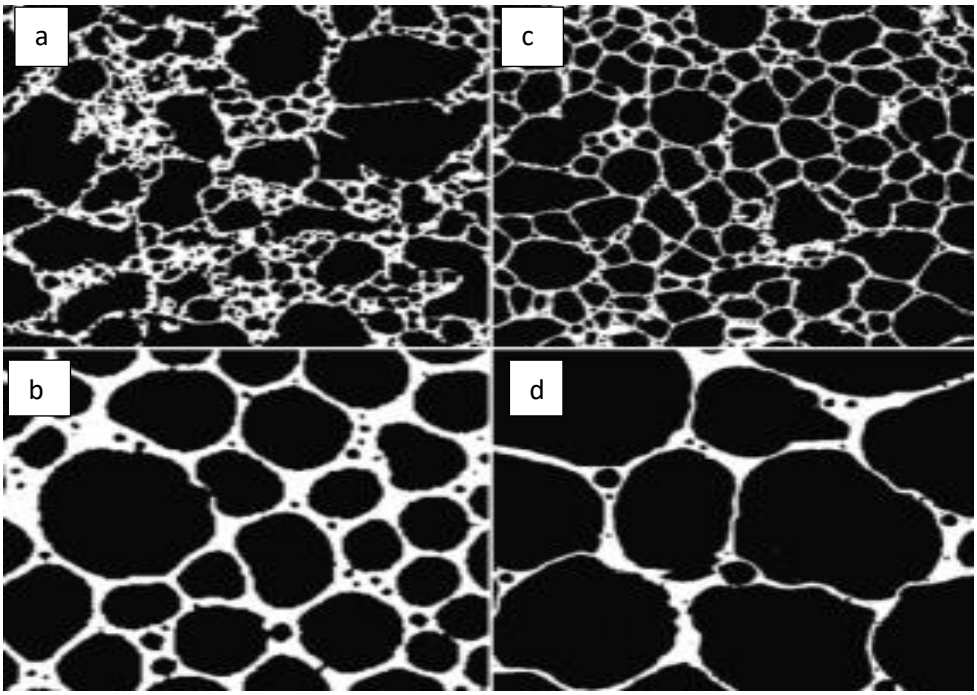



***Figure 1.8: 2D filtered XMT images (565 $mm^2$) taken from axial planes of PA80G glass ceramic foam with 2 wt-% SiC, sintered at a) 975 ℃, b) 1000 ℃, c) 1050 ℃ and d) 1100 ℃ [272].***

Comparing the porosity types, the column packed with the microporous silica showed longer breakthrough and exhaustion times than with the mesoporous ones [274]. Various companies (e.g. Dryden Aqua, Duran Group GmbH, SCHOTT) have also produced porous glass frits and filters in the pore size range between 1 and 300 µm, which are used for direct replacement for sand, as a filtering media. Below some of the common methods used for making porous glass are illustrated.

### 1.4.4 Common approaches for fabricating porous glass structures.

**Dry pressing/sintering**

In this process heat treatment is applied to adhere particles into a solid or porous mass without liquefaction. The sintering temperature is kept below the melting temperature. Commercially available sintered glass is borosilicate filter which is widely used in filtering corrosive effluents.

**Phase separation**

This process involves heat treatment followed by an leaching leaching operation [275]. A well-known commercial porous glass is VYCOR glass that contains 96% $SiO_2$. SCHOTT CoralPor ® a commercial porous glass with 4 – 300 nm pore diameter is one of the products that is used for filtration, moisture absorption or molecular separations (see Figure 1.9).

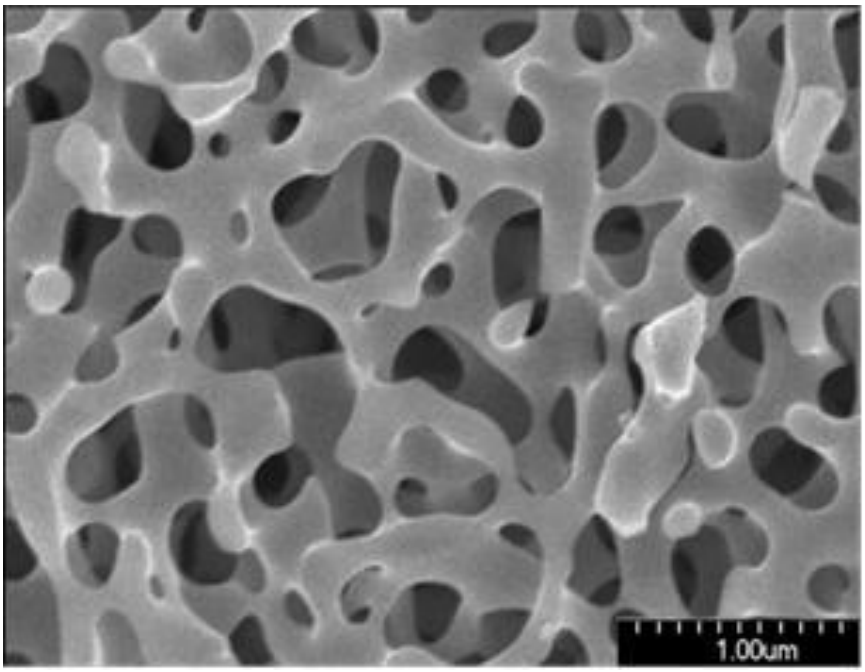



*Figure 1.9: SEM image of SCHOTT CoralPor ® a porous silica glass produced from borosilicate glass by phase separation [276].*

**Sol-Gel Process**

Uses chemical route to synthesize glassy or glass ceramic materials at relatively low temperatures, which involves the preparation of a sol, gelation of the sol and the removal of the liquid to establish fine interconnected channels within the gel. Zheng *et al*. reviewed silicate-based bioactive glass nano particles as regenerative bone implant materials prepared by this method [277]. Typical pore sizes were below 1 µm.

**Foaming process**

A surfactant is used along with glass precursors to produce foam under vigorous stirring. This causes rapid increase in viscosity with gelation. The gel can be cast into moulds which can be further sintered or freeze dried [278].

**Add/remove pore former**

The process also requires sintering of glass powder with sacrificial additional fillers (e.g. salts, organic materials) to add as pore forming agents. Pore sizes between 20 and 200 µm are possible [278].

**Polymer sponge replication**

Templates made of natural or synthetic organic polymers are mixed with a suspension of glass particles. After drying of the infiltrated templates all organic components are burned off by sintering to achieve pore sizes >10 µm [278].

### 1.4.5 Glass Microspheres

Glass microspheres were first introduced in 1960s in the form of hollow spheres for buoyancy applications [279]. These microspheres have been used as strong, light weight fillers for a variety of products ranging from foams to coatings [280-282]. Around 2005, a new type of alkali borosilicate glass microspheres was developed at the Savannah River National Laboratory (SRNL) named as Porous Wall Hollow Glass Microsphere (PWHGM) [283] (see Figure 1.10). The wall porosity achieved is on a scale of approximately 100 to 1,000 Angstroms, via phase separation including thermal treatments and subsequent leaching operations. They reported that these microspheres could contribute towards numerous applications by filling the hollow cavity of the microsphere with different valuable materials suggesting applications in storage and encapsulation processes [284-286]. Jianping Ge *et al.* reported nano catalyst encapsulated porous silica microspheres which suggested to be efficient in catalytic application [287]. Recent emphasis has thus been given on porous glass microspheres of degradable nature in biomedical applications, such as bone implants [288], drug carrier [289], MRI contrast agent [285], radiotherapy application [290].

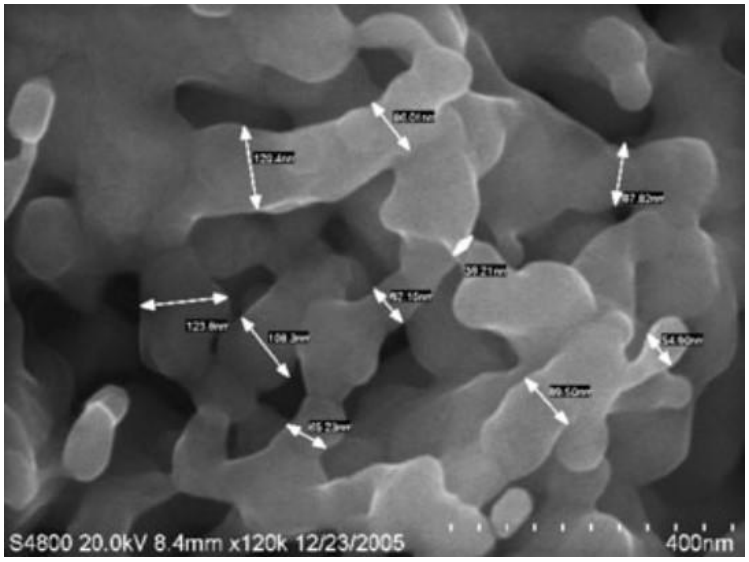



*Figure 1.10: SEM image of SRNL microsphere showing surface porosity [283].*

Various methods including vertical tube furnace, pouring molten glass onto stainless steel plates to create droplets, sol–gel method and the flame spheroidisation process have been reported by Hossain *et al.* [290] for the manufacture of glass microspheres and/or beads. Glass and ceramic microspheres investigated so far for various applications have been tabulated in Table 1.5. In the sol-gel technique, sols of varying glass compositions were usually produced by chemical precipitation method and then the microspheres were formed either by spray drying of the sols or via a solvent evaporation process [291].

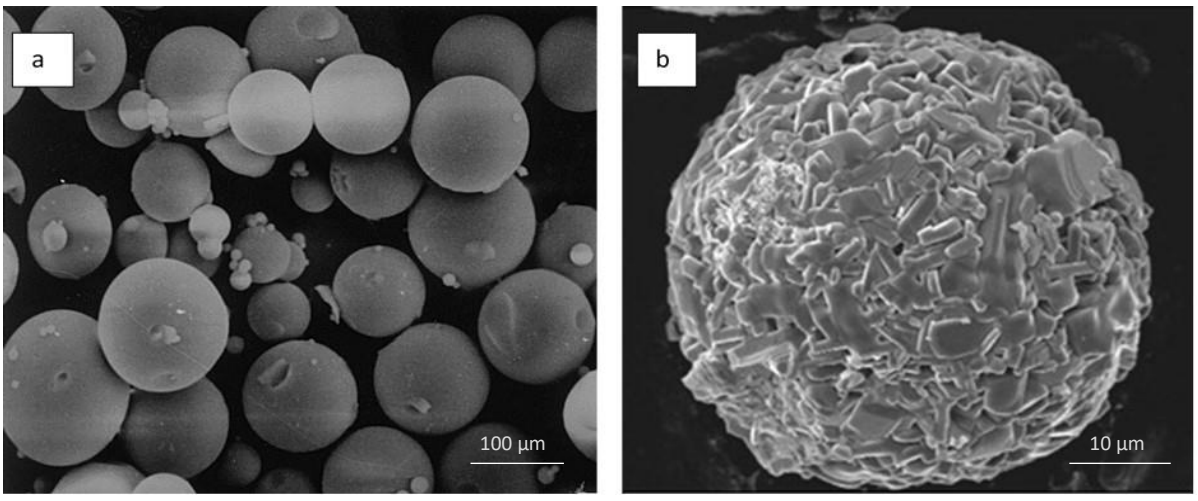



***Figure 1.11: SEM image of microsphere produced by flame spheroidisation a) Phosphate glass microspheres (Sene et al. [292]) b) dysprosium phosphate glass ceramic microsphere that had been heat-treated at 1400°C for 15 min (Conzone et al., 2009 [293]).***

*Table 1.5: List of glass and glass ceramic microspheres prepared by different methods.*

| Name | Type | Method | Porosity level | Reference |
|---|---|---|---|---|
| Hydroxyapatite (HA) microspheres | Hollow | Vertical tube furnace method | Mesoporous wall | [294] |
| Titanium phosphate glass microsphere | Solid | Flame spheroidisation | - | [295] |
| Aluminosilicate microspheres | Solid | Sol-gel process | - | [291] |
| Borate glasses Microsphere | Solid | Vertical tube furnace method | - | [296] |
| Aluminium borosilicate | Porous | Flame spheroidisation followed by leaching | Nano porous wall hollow glass | [283] |
| Silver doped silica microsphere | Solid | Sol-gel method | - | [297] |
| Silica Microsphere | Porous | Sol-gel method | Macroporous | [298] |
| $Er^{3+}$-doped modified-silica and phosphate glasses | Solid | Plasma torch | - | [299] |
| Lithium aluminoborate glasses | Hollow and Solid | Flame spheroidisation | - | [300] |
| Alkali Aluminosilicate microspheres | Solid | Flame spheroidisation | - | [301] |
| Dysprosium lithium borate | Solid | Flame spheroidisation | - | [293] |
| Dysprosium lithium-borate glass microspheres | Porous | Flame spheroidisation followed by solution reaction. | Macroporous | [302] |
| Phosphate glass microspheres | Solid | Flame spheroidisation | - | [292] |
| Soda-lime glass | Porous | Flame spheroidisation followed by hydrothermal processing | Nanoporous | [303] |

Spheroidisation is literally 'moulding' of glass microparticles into spherical form via surface tension forces whilst in the molten state. Gerhardt and Day first used this process in year 1987 for $Y_2O_3$–$Al_2O_3$–$SiO_2$ glasses for radiotherapeutics studies [304]. Generally, the process steps involve (1) melting glass particles, (2) forcing the molten particles to travel along the flame flow axis with high velocity, where the surface tension and shear forces induce the molten irregular shape particles into spherical shape, and (3) cooling the spherical shape particles [305]. It has been also reported that fuel flow rate, temperature of the fuel and feed particle size, feeding rate were the major influencing factors of flame spheroidisation process [306-308]. In order to prepare porous microspheres, these solid microspheres

underwent several post processing steps such as, heating for phase separation and then subsequent leaching process [302], hydrothermal process [303], chemical etching process, chemical reaction [223]. In our research group, Hossain *et al.* successfully prepared highly porous and fully interconnected calcium phosphate-based glass ($40P_2O_5 \cdot 16CaO \cdot 24MgO \cdot 20Na_2O$ in mol%) microspheres through the flame spheroidisation technique without post-processing [295]. According to Hossain *et al.,* manufacture of porous microspheres relies on various factors [309]. These included chemical and physical interaction of the porogen with the glass formulations, glass viscosity, along with both components (porogen and glass particles) being delivered within a suitable thermal processing window and a sufficient residence time within the flame [309, 310].

**Starting particle size**

According to Hossain et *al.* the starting size of the particles, play an important role because larger particle sizes are likely to have a greater mass, and thus may fall directly into the flame or be unlikely to reach melt temperature while in the flame's trajectory.

**Effect of porogen**

For manufacturing porous microspheres, the choice of the pore-forming agent also the size of the porogen and in some cases how they were applied to affect the pore sizes and levels produced. Addition of porogen during the spheroidisation process introduces porosity. Furthermore, Hossain et *al.* also suggested that varying the initial particle size and porogen quantities, could enable control over the size of the surface and interconnected pores.

**Glass Viscosity**

Viscosity is the most essential feature in glassmaking, and it is determined by the chemical composition of the glass as well as the temperature. The viscosity affects the temperatures during the glass cooling process. The material viscosity profile has a significant impact on the porous glass microsphere [340]. Viscosity is influenced by the chemical composition of the glass and, as a result, the melting conditions of the glass.

**Flame length and gas flowrate**

The degree of spheroidisation is determined by the length of the microparticles inside the flame's trajectory; the longer the microparticles remain within the flame's trajectory, the more likely they are to be spheroidised. Changes in gas flow ratio influences flame length and hence particle residence time in the flame as well as cooling rate of microspheres [311].

## 1.5 Magnetic materials for water treatment

The use of magnetic materials for the development of novel materials for advanced technical applications, such as biomedicine [312-314], robotics [315, 316], catalysis [317, 318], magnetic resonance imaging (MRI) [319, 320], data storage [321-323], and engineering [324, 325], have been made in recent decades including environmental remediation processes. Various magnet-responsive materials such as magnetite ($Fe_3O_4$), maghemite ($\gamma$-$Fe_2O_3$), and hematite ($\alpha$-$Fe_2O_3$), ferrihydrite, goethite, hematite was used in conventional wastewater treatment methods including coagulation, dissolved air flotation (DAF), or electro-coagulation, adsorption, and membrane filtration [326-328]. Furthermore, using magnetic materials for alternative treatment methods including photocatalysis, dissolved ozone flotation (DOF), and advanced oxidation processes (AOP), such as Fenton, zero-valent Fenton, photo-Fenton was found very promising route [326-329]. After wastewater treatment magnetic materials are easily removed and recycled by applying external magnetic field which attractive material [326-328]. Magnetic materials investigated so far for various wastewater treatment applications have been tabulated in Table 1.6. In the coagulation/flocculation method, different magnetic particles with or without functionalisation have been used. Mateus *et al.* investigated magnetic nanoparticles functionalised with proteins from Moringa oleifera seeds to treat surface water with high turbidity [330]. This showed a removal efficiency of 96.8% for turbidity, 97.1% for the apparent colour removed after 10 mins of magnetic sedimentation. Ferrites and ferrite-containing composites were used as adsorbing materials for the removal of pollutants [331-334]. Ferrites were recently explored as adsorbing substrates for the removal of heavy metal ions from polluted waters, namely Pb(II), Cd(II), As(III), As(V), Cr(VI), and Hg(II) [334]. For instance, Badruddoza *et al.* investigated cyclodextrin/magnetite nano composite for removing $Pb^{2+}$, $Cd^{2+}$ and $Ni^{2+}$ ions from contaminated water [335]. Jia *et al.* reported Cr (VI) removal by extremely porous Zn-ferrite nanorods with a sorption capacity of 34.2 mg /g just after 10 minutes of contact time [336]. These studies demonstrated the adsorption capability using magnetic materials. However, it is still an important challenge to develop a facile, cost effective and environmentally friendly method for synthesising ferrite and ferrite-containing composites [336]. Besides, there has not been a significant amount of research conducted with naturally occurring magnetic material, as such much attention was given in terms of synthetic magnetic materials.

*Table 1.6: List of magnetic materials used in various wastewater treatment applications.*

| Magnetic material | Material synthesis process | Water treatment types | Material removed from wastewater |
|---|---|---|---|
| Natural plant protein coagulant functionalised- $Fe_3O_4$ nanoparticles | Co-precipitation | Coagulation/flocculation | Removal of apparent colour, turbidity of raw water [330] |
| Moringa oleifera Lam functionalized magnetic iron oxide nanoparticles | Sol-gel | Coagulation/flocculation | Removal of turbidity of raw water [337] |
| Ferric chloride (FC) and polyaluminum chloride (PAC) hybrid | Mixing | Coagulation | Removal of turbidity, Chemical oxygen demand (COD), iron, aluminium from high-phosphorus hematite flotation wastewater [338] |
| Magnetite and Hematite | N/A | Advanced Oxidation | Removal of turbidity, total organic carbon (TOD) and 23 organic chemicals from cosmetic wastewater [339] |
| $Fe_3O_4$-coated pre-treated biochar | Impregnation and calcination of Fe (III)-ethanol solution | Photo-Fenton | Removal of Metronidazole [340] |
| $Fe_3O_4$ | N/A | Heterogeneous-Fenton | textile azo-dye, Orange G (OG) [331] |
| Magnetite Nanoparticles Functionalized with a Poly (ionic liquid) | Co-precipitation | Fenton Oxidation | Methylene blue [341] |
| Magnetic activated carbon | Co-precipitation | Adsorption | Ceftriaxone [342] |
| Iron oxide nanoparticles immobilized-sand material | Coating on waste silica-gel | Adsorption | Lead removal [343] |
| Cyclodextrin/magnetite nano particles | Chemical synthesis | Adsorption | Lead, cadmium and nickel [335] |
| $Ca_2Fe_2O_5$ brownmillerite nano powders | Sol-gel auto-combustion | Photocatalysis | Methylene blue [332] |
| $Mg_{0.5}Zn_{0.5}FeMnO_4$ nanoparticles | Sol-gel | Photocatalysis | Reactive blue 21 [333] |
| Zeolite imidazolate frameworks-67 (ZIF-67) loaded on magnetic nanoparticles named MZIF-67 composites | Chemical synthesis | Adsorption | Direct blue 86 (DB-86) and Methyl orange (MO) [344] |

## 1.6 Challenges in water treatment and novelty of the research

New technologies to remove micropollutants from water are being investigated all around the world. However, economic, effective and rapid water treatment at a commercial level is still a challenging problem [345]. A comparison of currently used tertiary treatment technologies for wastewater treatment in terms of addressing the quality problem, challenges to overcome, life span and cost associated with these technologies are tabulated in Table 1.7. On the basis of the literature review (discussed above), the overall beneficial processes for tertiary water treatment are filtration and adsorption processes.

Considering adsorption efficiency, activated carbon is the best material due to its high surface area. Although, high regeneration cost (which results in material with 5-10% reduced separation efficiency [346]), problem in separation of fine activated carbon from bulk water and surface activation limits its applicability [175, 178]. Furthermore, activated carbon is prepared from a variety of carbonaceous precursors, including coal, peat and coconut shells which are carbonised and then "activated" either by oxidisation with steam, or by treatment with acids, bases or other chemicals. The consumption of activated carbon grew 1.2 percent per year to almost 1.3 billion pounds in 2017, with market value reaching almost $1.8 billion [347]. The consumption of activated carbons for industrial use has now become an indicator for development of sustainable advanced materials, which can be utilised within a circular economy (CE) approach and with efficient environmental management.

Nanomaterials (such as MOFs, LDHs, ferrites) are also associated with high surface area with high adsorption capacity. However, according to literature, their selective adsorption/degradation ability, environmental fate and issues such as the separation cost associated to remove these nanoparticles from bulk water phase limits their practical application [348]. The toxic effects of nanoparticles on the environment and health are not clear. The integration of nanomaterials into existing water purification systems is also a key challenge. Although a number of existing nano material (such as CNT), composite filtration membranes (UF, NF, MF) are available, however they require high maintenance cost and waste generated by backwashing needs further treatment to remove pollutants [349]. Furthermore, the methods highlighted in the literature to prepare materials for wastewater treatment are based on synthetic approaches such as sol-gel route, or single /double emulsion, solvent evaporation, polymerisation, spray drying or acid-based phase separation techniques [350-352]. These synthetic approaches consist of a number of processing steps, requiring special reaction conditions (such as the use of capping agents), expensive or toxic solvents and often the time involved for preparing the materials can require days or weeks [353-356].

Taking into consideration the above highlighted issues, the main challenge is to develop cost effective and environmentally acceptable separation and reactive media, which could potentially be manufactured via within a circular economy (CE) approach. CE concept has evolved as a means of achieving long-term manufacturing sustainability. The conservation of energy and natural resources is a fundamental objective of sustainable production. To deal with rising global population, growing environmental stress, a quick and drastic shift to a CE will be necessary to ensure minimal environmental effect. As such, development of alternate approaches with easier preparation processes, reducing / eliminating the use of toxic solvents while manufacturing could deliver a step-change in materials processing, whilst also targeting reduction, reusability, and recyclability of waste materials thus waste valorisation.

Besides, on reviewing the available literature, it was apparent that much attention is required for developing low cost, environmentally friendly materials that will effectively utilise, reusing and recycling waste materials. Recently developed a unique method for preparing highly porous inorganic microspheres (from phosphate glasses) via a single stage flame-spheroidisation (FS) process excludes use of hazardous chemicals in the manufacturing process. These microspheres usually possess external pores (55 ± 8 μm) with highly interconnected porosities [309]. Furthermore, the process developed enables production of materials at kilograms per hour scale [309]. Microspheres manufactured via FS could be considered more environmentally friendly as their production does not require the use of toxic chemicals [29, 30]. Hence, FS method offers a simple and rapid processing route that could deliver a step-change in porous inorganic materials manufacturing. Till date, no research has demonstrated the use of flame-spheroidised porous microspheres for wastewater treatment. The novelty in the research lies in developing the porous material via FS which would significantly reduce the chemical footprint during manufacturing, thus addressing the grand challenge of sustainable and cleaner manufacturing.

*Table 1.7: Applicability, challenges, quality problem addressed and costs of wastewater treatment technologies [23, 76].*

| Processes | Membrane filtration | Chemical oxidation process | Activated carbon Adsorption | Oxidic adsorbents | Polymeric adsorbent | Nano adsorbents Such as MOFs, LDH, CNT, GO |
|---|---|---|---|---|---|---|
| Key challenges | Associated with membrane fouling, waste generated by back washing requires further treatment, high pressure cost. | highly expensive process, formation of undesirable free radicals that may be hazardous | low adsorption affinity for low molecular weight polar organic compounds, high operating cost associated separation and regeneration | Selective adsorption, costly | pH dependent, low sensitivity, poor mechanical property | High cost associated with separation after use. High regeneration cost. |
| Organic chemical removal | | | √ | | | √ |
| Dye removal | √ | √ | √ | √ | √ | √ |
| Heavy metal removal | √ | √ | √ | √ | √ | √ |
| Bacteria removal | √ | | | | | |
| Radio nuclide removal | | | | | | √ |
| Lifetime | 3-7 years | 10 years | It depends on media type | 7-10 years. | Not available | Not available |
| Costs (US$ per one million liters of treated water) | 15–450 | 100–2000 | 50–150 | Not available | Not available | Not available |

## 1.7 Aims and objectives

This thesis aimed to develop new porous materials, particularly environmentally friendly, low-cost materials that would completely eliminate the use of toxic and hazardous chemicals during manufacturing. To date none have shown the incorporation of flame-spheroidised porous microspheres for wastewater treatment. Thus, for initial studies highly porous phosphate glass microspheres developed within the research group would be explored for dye removal as a proof-of-concept. Since porosity is one of the main parameters describing the properties of porous materials. The ultimate goal would be then to transfer the manufacturing knowledge developed to alternate low-cost glass types, and preferably to use waste recycled glass and other naturally available materials such as magnetite. The major advantage of using glass is that once it reaches its end of service life, it can be re-melted (as glass does not degrade during re-melting) and remanufactured into porous microspheres, for re-use as water treatment materials. Besides, recycling and or upcycling of waste glass would provide an added economic value. Magnetite on the other hand is a member of the cubic ferrites, also called ferrospinels, a naturally available, low cost, ecologically friendly and non-flammable material [357]. Thereby, potentially providing a CE approach for manufacturing material for wastewater treatment.

In order to achieve the above aims, the following objectives will be considered:

1. The exterior pores of porous PBG were 55 µm in diameter, which is ideal for cell adhesion and proliferation in bone implants. Considering most micro-pollutants are within the size range of 10 µm-0.001 µm thus, a porous structure with a decrease in pore size is required for wastewater treatment. Hence, as a proof-of-concept, the manufacturing process parameters of porous PBG microspheres were explored to identify conditions that would influence the pore dimeters with better dye removal efficacy. PBG was considered as a starting material as the group already had vast experience on manufacturing them into porous microspheres via FS.
2. To develop porous recycled glass microspheres (PRGMs) from recycled glass (RG) particles and then optimising the manufacturing process to fabricate PRGMs with maximum dye removing capabilities.
3. Investigating parameters such as dye removal kinetics, equilibrium and capacity of the porous materials manufactured in batch process and the dynamic behaviour representing industrial and point-of-use applications in column setting.

4. Developing porous magnetite microspheres (PMMs) from naturally occurring magnetite particles as they are considered ideal candidates for separation studies as they can be easily separated via application of a magnetic field. To optimise and characterise the microspheres in terms of improved adsorption capacity.

## 1.8 Thesis outline

The thesis has been organised into several chapters as outlined below:

**Chapter 2**: Describes details of materials used and the experimental and analytical methods. This includes information about the experimental and analytical conditions as well as the theory behind the analytical techniques.

**Chapter 3**: Details the effect of starting glass particles size and porogen ratio (particle size 45-63 µm) on optimising the surface area and porosity of porous phosphate-based glass (PBG) microspheres. The relationship of surface area and porosity with adsorption capacity of the PBG microspheres was also demonstrated.

**Chapter 4**: Expands on chapter 3, by discussing the effect of using smaller size porogen (≤5 µm) and subsequent heat-treatment on the porous structure. The adsorption property of heat-treated and non-heat-treated microspheres were then explored in batch and column adsorption process for removing anionic dye (acid red 88) with the modelling of breakthrough curves.

**Chapter 5**: The experimental challenges of processing RG using conventional flame-spheroidisation process and details on alternate manufacturing process to manufacture porous recycled glass microspheres (PRGMs) are described in chapter 5. This chapter also discusses the applicability of PRGMs for removing anionic dye (acid red 88) and cationic dye (methylene blue) in both batch and column adsorption studies with the modelling of breakthrough curves.

**Chapter 6**: Explores the potential for manufacturing porous magnetite microspheres (PMMs) from naturally occurring magnetite and demonstrates the transformation of magnetite porogen mixture into dense and highly porous $Ca_2Fe_2O_5$ brownmillerite via a single stage thermochemical reaction using flame-spheroidisation. Also, the adsorption capabilities of PMMs were explored and experimental details were provided to explain the dye removal mechanism.

**Chapter 7:** Summarises the findings of all the work in this thesis and puts forward areas of future work.

# Chapter 2: Materials and methodology

This chapter describes experimental methods used in this thesis as well as the analytical techniques utilised to characterise and investigate the microspheres developed using flame spheroidisation method. Organic dye was used as a target contaminant for exploring the separation capability of the porous structure manufactured. This chapter will also address the theory underlying the analytical approaches and the operational settings, as well as the experimental procedures used in the research for removing dyes from water.

## 2.1 Raw materials and Chemicals

All chemicals for precursor were reagent grade and were used as received. Chemicals such as sodium dihydrogen phosphate ($NaH_2PO_4$, Sigma Aldrich, UK, ≥ 99%), calcium hydrogen phosphate ($CaHPO_4$, Sigma Aldrich, UK, 98–105 %), magnesium hydrogen phosphate ($MgHPO_4$, Sigma Aldrich, UK, ≥ 99%) were used as starting materials for manufacturing phosphate glass. Porous microspheres were prepared by adding calcium carbonate porogen ($CaCO_3$, Fisher Scientific UK Ltd, ≥ 98 %, 45-63 µm and ≤5 µm). Adsorption of dye onto porous microspheres utilised two different dyes: Acid red 88 (AR88) from ACROS organics (USA) and Methylene blue (MB) obtained from Sigma Aldrich (Dorset, United Kingdom). Recycled glasses (45-63µm) are recovered from municipal solid waste (MSW) recycling facilities and were collected from Dryden aqua. Natural magnetite was purchased from Sigma-Aldrich, UK ($Fe_3O_4$, >96.8%; < 45µm).

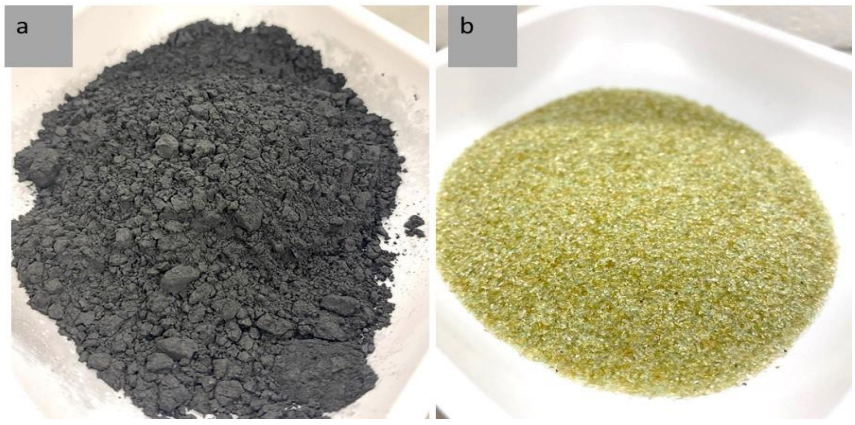



*Figure 2.1: Photograph of starting particles of a) magnetite < 45µm and b) recycled glass (45-63µm).*

## 2.2 Preparation of microspheres

### 2.2.1 Solid microspheres

Calcium phosphate glass with formulation $40P_2O_5{\cdot}16CaO{\cdot}24MgO{\cdot}20Na_2O$ (mol% denoted as P40) was prepared using melt quenching technique. Chemicals such as $NaH_2PO_4$, $CaHPO_4$, $MgHPO_4$ and $P_2O_5$ (Sigma-Aldrich, UK) were used as starting materials. The required amounts of precursors were weighed, mixed and transferred to a 100 ml volume Pt/Rh crucible (Birmingham Metal Company, U.K.) which was then placed into a furnace. The furnace followed a controlled program using 10 °C /min ramp for melting (at 350 °C for 0.5 hours to remove $H_2O$ and at 1150 °C for 1.5 hours for melting) The resulting molten glass was poured onto a steel plate and left to cool to room temperature. The phosphate glasses produced from the melt quenching process were then ground using a ball mill (Retsch PM 100) and the particle size range of 63-45 µm, 63-125 µm, 125-150 µm, 125-200 µm and 200-355 µm were achieved using sieves. The particles were then processed utilising a flame spheroidisation process to prepare solid microspheres. The flame spheroidisation equipment consisted of the following components: (1) thermal flame spray gun, (2) hopper feeder and (3) collection trays (see Figure 2.2). The thermal flame spray gun used was a MK74, developed by Metallisation Ltd (UK) which was connected to oxygen and acetylene gas cylinders using gas flowmeters (Platon, Roxspur, UK), a vibratory funnel feeder. To enable particle separation, the vibratory funnel feeder was fitted with a mesh size of 200 µm at its opening and placed directly over the hottest area of the flame. A 3V DC motor was also used to feed the powder at a rate of 1.5 g/min. Powder flow behaviour is complex and depends on a variety of factors, which was outside the scope of this research. The glass particles were passed through the hopper feed placed 380 mm above the base and 130 mm away from the oxygen-acetylene connection point on the gun, top of the flame (see Figure 2.2). The collection trays consisted of three rectangular glass trays placed at varying distances in from of the gun. The first tray was placed directly below the flame so as to collect particles that did not pass through the flame. The glass particles that underwent spheroidization due to surface tension forces as the particles passed through the flame, were collected from the second and third glass trays.

**Preparation of Solid P40 glass microspheres**

The solid microspheres from each collection tray were initially visualized using light microscopy. The materials in the 1st collection tray were spheroidised again as it usually contained a mixture of glass microspheres along with a significant proportion of non-spherical particles.

**Preparation of solid recycled glass microspheres**

Solid recycled glass (RG) microspheres were produced by introducing as received particles into the flame of the thermal spray gun (using oxy-acetylene ratio of 3:3). The microspheres were collected after 2 munities from cooling trays.

**Preparation of magnetic solid microspheres**

The starting magnetite (<45µm) particles were flame-spray processed using a thermal spray gun coupled with oxy-acetylene ($O_2/C_2H_2$; 3:3 gas flow ratio). The microsphere products exiting the flame were collected after 2 munities from cooling trays.

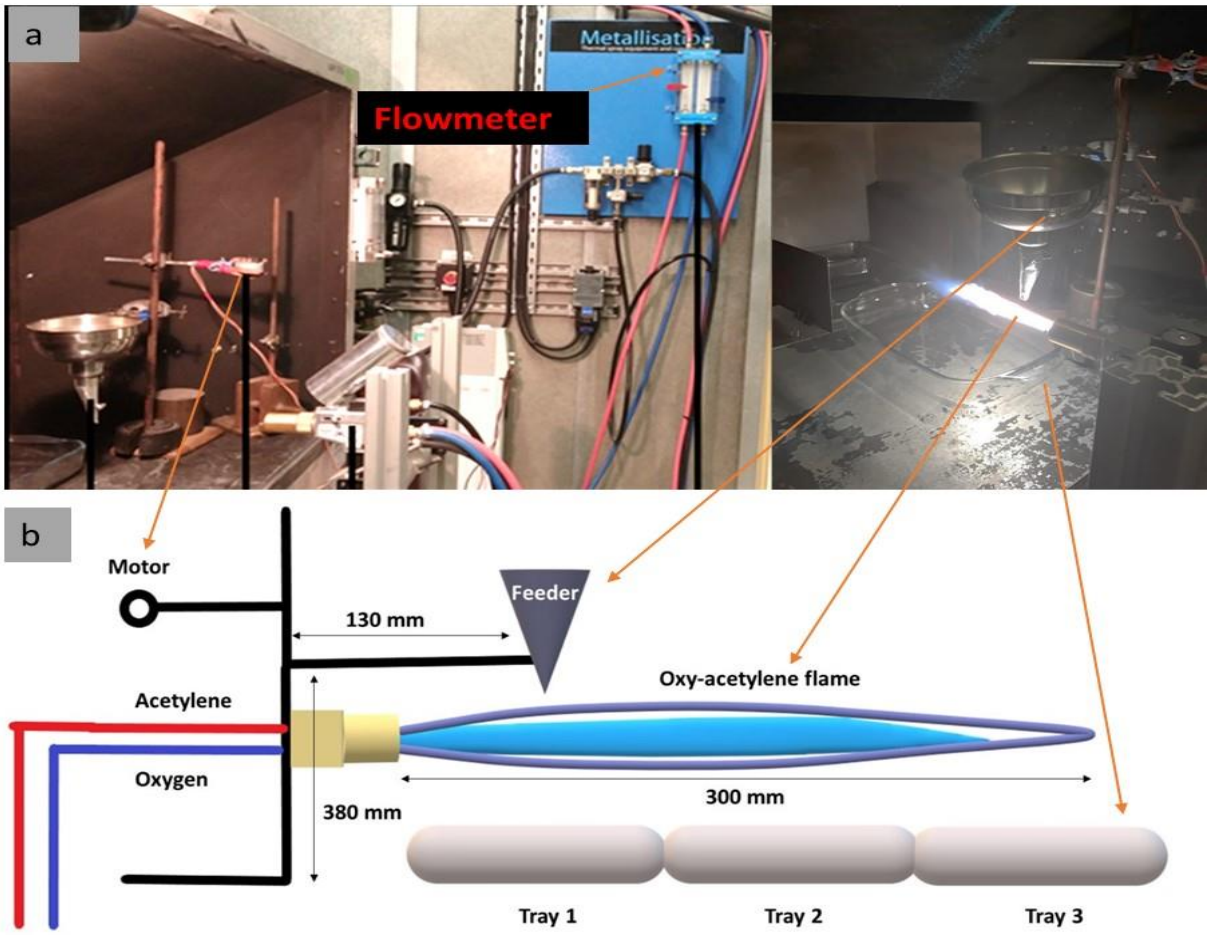



*Figure 2.2: a) Photograph showing the apparatus set up of the oxy-acetylene spray gun and b) schematic diagram of oxy-acetylene flame spheroidisation apparatus.*

## 2.2.2 Porous microspheres

Porous P40 microspheres were prepared by adding porogen (carbonate porogen) to the phosphate glass particles and then processed via a flame spheroidisation process. Crushed glass powders of

different size ranges with different porogen ratios were fed to the flame. The spheroidised porous microspheres were then collected using a collector plate. Spheroidised microspheres were then sieved into different size ranges for evaluation. Table 2.1 outlines the experiments conducted using varying porogen to glass particle ratios along with their respective sample codes. Where S, M, Land XL stand for microsphere size 125-150 µm, 150-200 µm, 200-355 µm (starting particle size 125-200 µm), 200-355 µm (starting particle size 200-355 µm) and 0.5, 1, 2 and 3 refers to porogen ratios.

***Table 2.1: Porous glass Microspheres prepared with different porogen ratios.***

| **Starting P40 glass particle size range (µm)** | | | |
|---|---|---|---|
| **63-125 µm** | **125-200 µm** | | **200-355 µm** |
| **Sieved microsphere** | **Sieved microsphere** | | **Sieved microsphere** |
| **125-150 µm (Glass Code)** | **150-200 µm (Glass Code)** | **200-355 µm (Glass Code)** | **200-355 µm (Glass Code)** |
| 0.5S | 0.5M | 0.5L | 0.5XL |
| 1S | 1M | 1L | 1XL |
| 2S | 2M | 2L | 2XL |
| 3S | 3M | 3L | 3XL |

To prepare heat-treated P40 microspheres, the glass particles of phosphate with the size range of 63-125 µm were mixed with carbonate porogen (at ratios of 1:1 size; particle size ≤5 µm) and processed via flame spheroidisation as described earlier (using oxy-acetylene ratio of 3:3) to prepare solid microspheres. The microspheres produced (125-150 µm) were collected from the collection tray after being allowed to cool down for a period of 2 minutes. The microspheres were then subjected to heat treatment in a furnace at 510 °C to 540 °C with ramp 10°C/minute for 3 hr (see Table 2.2) for sample codes used in this study). Post-heat treatment, the microspheres were acid washed in acetic acid (5 M) for 2 min followed by washing using deionised water (for 5 min) and then dried in an oven at 50 °C for 24 h.

***Table 2.2: Code used for different microspheres.***

| **Sample Code** | **Microsphere type** |
|---|---|
| **P40** | Porous Calcium phosphate |
| **UW- P40** | Unwashed Porous Calcium phosphate |
| **UW-510-P40** | Unwashed Porous Calcium phosphate heat-treat at 510$^{O}$C |
| **UW-520-P40** | Unwashed Porous Calcium phosphate heat-treat at 520$^{O}$C |
| **510-P40** | Washed Porous Calcium phosphate heat-treat at 510$^{O}$C |
| **520-P40** | Washed Porous Calcium phosphate heat-treat at 520$^{O}$C |

On the other hand, porous recycled glass microspheres (PRGMs) were prepared using a modification to the existing (Conventional) method named 'Granular method'. In granular method, RG particles of below 45 µm size were mixed thoroughly with porogen (size ≤5 µm) with 2:1, 1:1 and 1:3 by weight glass particles to porogen ratio and ground using a ball mill (Retsch PM 100, 20 small balls) for 1 min, 5 mins and 15 mins at 300 rpm and 500 rpm. The grinded particle blend was mixed with 2% PVA at ratio 2:1 w/v to form granules. The granules of size ≤200 µm were collected by sieving and were then flame-spheroidised using the same parameters for the solid recycled glass microspheres. Later PRGMs were acid washed in acetic acid (5 M) for 2 min followed by washing using deionised water (for 5 min) and then dried in an oven at 50 °C for 24 h and denoted as W-PRGMs.

Similarly, porous magnetite microspheres (PMMs) were prepared by grinding various ratios (at ratios of 2:1, 1:1 and 1:3 by weight) of magnetite particles (size ≤45 µm) and calcium-based carbonate porogen (size ≤5 µm) blend for 1min, 5 mins and 15 mins in a ring mill.

## 2.3 Microsphere characterisation methods

### 2.3.1 Scanning electron microscopy (SEM) and Energy dispersive X-ray spectroscopy (EDX)/Elemental mapping

SEM micrographs were captured on two different microscopes, one was a Philips XL30 and the second was a FEI Quanta 600 using the SE/BSE detector. Acceleration voltage was 15 kV for both microscope and spot size was fixed at 5, in order to examine morphologies of the microparticles, solid microspheres and porous microspheres manufactured. Prior to analysis samples were adhered to a carbon tab and a coating was applied to make the surface more conductive. Platinum coating was applied using a sputter coater (Agar Sputter Coater) with ~15nm thickness only to glass samples.

Compositional analysis was carried out on samples which were carbon coated with a thickness of ~15 nm. Energy dispersive X-ray analysis (EDX, Oxford Instruments INCA, UK) was conducted with accelerating voltage of 15 kV and a working distance of 10 mm was used to examine the elemental composition of the microspheres. EDX analysis was performed on 5 separate spots on each sample and an average value was taken.

For elemental mapping, resin embedded polished cross-sectioned samples were carbon coated using the same technique highlighted earlier. The samples were then mount in FEI Quanta 600 microscope that combines EDS software (BRUKER) to identify elemental distribution. The microscope is operated at 15 kV, spot size 5 with a working distance 13 mm.

### 2.3.2 X-ray diffraction analysis (XRD)

Structural characterisation of microparticles, solid microspheres and porous microspheres was performed using a Bruker D8 Advanced diffractometer (BRUKER AXS, Germany) and Bruker D8 Advance Da Vinci (BRUKER AXS, Germany). Bruker D8 Advanced diffractometer was operated at room temperature and ambient atmosphere with Ni-filtered CuKα radiation (λ=0.15418 nm), generated at 40 kV and 35 mA. Data were collected from 10° to 70° with a step size 0.05° and scan step time of 5s for phosphate glass samples with and without heat treatment.

XRD analysis for RG and magnetic samples were explored using Bruker D8 Advance with Da Vinci using a LYNXEYE XE-T detector in 1D mode; Cu Kα radiation (λ = 0.15406 nm); 40 kV and 40 mA. Step size 0.02°; step time 0.3 s; total time/step were used for RG samples. Step size 0.02°; step time 0.2 s; total time/step were used for magnetic samples. Phases were identified using the EVA software (DIFFRACplus suite, Bruker-AXS) and the International Centre for Diffraction Data (ICDD) database (2005).

### 2.3.3 Coulter Laser Diffraction analysis

The size distribution of different size ranged particles was determined by laser diffraction. A sample of approximately 50 mg was dispersed in 13 ml of deionised $H_2O$. The suspension was then added to the chamber of a Coulter LS230 particle size analyser (Beckman, UK) under moderate stirring to the 8-10 % concentration as recommended. The sample size distribution was then determined as a function of the particle diffraction using the Coulter software (version 2.11a) and plotted as a function of volume percentage.

### 2.3.4 Density measurement

The theoretical porosity of the microspheres produced were calculated from density measurements using the following Equation 2.1 [358]:

$$\text{Porosity of the microspheres, } \varepsilon = \left(1 - \frac{\rho_{tap}}{\rho_{apparent}}\right) x100 \qquad \textit{Equation 2.1}$$

Where $\rho_{tap}$ is tapped density and $\rho_{apparent}$ is apparent density.

The apparent density values for the microspheres produced were analysed using a Micromeritics AccuPyc 1330 gas pycnometer. A stainless-steel ball (3.18551 $cm^3$) was used as a calibration standard, with 10 readings for calibration. For each samples an average mass of 2 g was used and the tests were done in triplicate.

Tapped density of the samples were carefully measured using a 10 ml graduated cylinder. The microspheres were placed into the cylinder and then tapped 15 times at 2-sec intervals. The tapped density of each sample was then obtained by dividing the weight of sample in grams by the final tapped volume in $cm^3$ of the sample contained in the cylinder. For each sample, the process was repeated 10 times and an average tapped density was calculated using the Equation given below (see Equation 2.2):

$$\rho_{tap} = \frac{M}{V_p} \qquad \textit{Equation 2.2}$$

Where *M* is weight of samples in grams and *Vp* is final tapped volumes of granules in $cm^3$.

### 2.3.5 Specific Surface area, pore size and pore volume analysis

BET analysis was used for microparticles and microspheres to investigate specific surface area by Nitrogen or Krypton adsorption-desorption measured as a function of relative pressure. The process was also used to determine external area and pore area to evaluate the total specific surface area in $cm^2/g$. This analysis was carried out on a Micromeritics ASAP 2420 instrument at -196 °C. Prior to analysis, approximately 2.0 g of sample was weighed into a clean sample tube with filler rod. The samples were degassed under high vacuum at 350 °C for 15 hours prior to analysis. Isotherms were acquired from 0.001 - 0.990 relative pressure (P/Po). BET specific surface area was acquired from a relative pressure range of 0.05 – 0.20. T-plot model (Harkins Jura correction) was used to calculate micropore volume and area, and BJH model (Harkins Jura correction) was used to determine meso and macropore volume [359]. Total pore volume was calculated by adding both t-plot and BJH volumes together.

### 2.3.6 Porosity measurement via mercury porosimetry analysis

Mercury intrusion porosimetry (MIP) was carried out using a Micromeritics Autopore IV 9500, operating between 0 to 345 kPa at low pressure and up to 228 MPa at high pressure, enabling characterisation of pore diameters ranging from ~360 µm to ~0.0055 µm. Prior to any experiment, the samples were dried under vacuum at 50°C overnight to remove any physiosorbed water on the sample. A micrometrics 5 cc powder penetrometer with 1 cc intrusion volume was used for all samples. An empty penetrometer was run before sample runs in order to calibrate the equipment. The experimental procedure consisted of increasing the external pressure to force the non-wetting mercury penetrate gradually the smaller pores in the microspheres. At each pressure step (once equilibrium has been reached) the apparent volume of mercury entering the sample was measured. The material was first placed in a low-pressure port where the intruded volume was recorded as a function of pressure. This was followed by placing the sample in the high-pressure port. The pressure

was increased incrementally up to a maximum given ultimate pressure of 228 MPa. The process was then reversed by decreasing the pressure stepwise, which allowed the mercury to extrude from the solid material, thus generating an extrusion curve.

### 2.3.7 Mineral Liberation Analysis (MLA)

The Quanta 600 by FEI scanning electron microscope incorporates with EDX software (Bruker, Berlin, Germany) and Mineral Liberation Analysis (MLA) software (JKTech/FEI) and backscattered electron (BSE) and SE detectors for Mineral Liberation Analysis. MLA is used for exploring elemental distribution, mineral distribution, mineral quantification, and particle size distribution. Cross-sectioned samples were obtained by embedding the microspheres in cold epoxy resin, followed by sequential mechanical grinding and polishing using silicon carbide discs and diamond cloths, respectively. Polished samples were cleaned and dried before being carbon coated prior MLA analysis. The analysis associates with a survey of a sample using BSE image, at 20 kV acceleration voltage. The instrument-specific working distance was at 13 mm. Mineral grains with high average atomic numbers and molecular masses appear in light grey in the BSE image. The calibration of the BSE greyscale with contrast and brightness was performed with a reference block. After automated image analysis, grid of EDX spectra is gained with distinct BSE grey values. The classification of the measured EDX spectra from the sample is performed by a comparison to a list of labelled reference EDX spectra.

## 2.4 Viscosity and melt behaviour study of starting glass particles

### 2.4.1 Thermal analysis

The thermal properties of the samples, specifically the glass transition ($T_g$) (measured at the midpoint), onset of crystallisation ($T_x$), crystallisation peak ($T_c$) and melting peak ($T_m$) temperatures were characterised using a simultaneous thermal analysis instrument (SDT, TA Instruments SDT Q600, USA). Approximately 30 mg of sample powder or microspheres was placed into a platinum (for phosphate) or alumina (for RG and magnetite) pan and then heated from room temperature to up to 1300 °C at heating rates 10 °C $min^{-1}$ under 100 mL/min of nitrogen gas flow. An empty pan was also analysed in order to determine the baseline which was then subtracted from the thermal traces using TA Universal Analysis 2000 software. Triplicate were used for these measurements.

### 2.4.2 Ash fusion Test (AFT)

RG and P40 glass particles were carefully loaded into a 5 mm pelleting die and compressed by Instron 3369 tensometer system to produce cylindrical pellets. Same compression profile was followed for every sample (10 s holding time under 5000 psi pressure).

An SDAF2000d Ash Fusion Analyser was used for this test operating in an air atmosphere. For each experiment, two different cylindrical ash pellets were simultaneously loaded and tested in the system. The furnace (loaded with samples) was heated up to 1520 °C at a rate of 10 °C/min, while the high-resolution camera (closed circuit digital camera VC-523D) captured images of the samples at a rate of 1 frame/°C increment.

### 2.4.3 Viscosity Analysis

Viscosity of the recycled glass was measured at high temperatures (≥700°C) using rotational viscometer (Brookfield DV-III UTRA, USA). The viscosity was measured by measuring the force required to rotate a spindle in a fluid. The viscosity was determined by measuring the shear stress and the shear rate exerted by the viscous fluid on a rotating cylindrical platinum spindle according to Equation 2.3 below:

$$\eta = \tau\gamma \qquad \textit{Equation 2.3}$$

where, η is the viscosity in poise, τ is the shear stress in dynes/cm$^2$ and γ is the rate of shear in sec$^{-1}$.

In order to derive a viscosity curve for glasses, the fixed viscosity at glass transition temperature and the viscosity data obtained via rotational method were used and fitted to the Avramov–Milchev (AM) model [360]. As high temperature viscosity measurements provide values in the < 2 Log Pa·s region [361]. Equilibrium viscosity measurements cannot be carried out at temperatures much below the glass transition owing to the long structural relaxation time. The data is then applied to the well-known and generally accepted Avramov–Milchev equation in order to predict a complete viscosity profile. The Equation is:

$$f(\eta) = A + (B/T_o) \qquad \textit{Equation 2.4}$$

where, T is the temperature in °C, η is the viscosity in Pa s and A, B and $T_o$ are constants.

## 2.5 Dye Adsorption studies

### 2.5.1 Adsorbate Dyes

Adsorption of dye onto porous microspheres utilised 2 different dyes: Acid red 88 (AR88) from ACROS organics (USA) and Methylene Blue (MB) obtained from Sigma Aldrich (Dorset, United Kingdom). Dye solutions were made fresh before each experiment in deionised water. AR88 was selected as an adsorbate as it is widely used in dyeing textile fabrics, silk, nylon, wool, and leather, and its degradation

by-products have carcinogenic effects [362]. MB is a dark, blue-coloured dye, which is highly soluble in water and toxic for aquatics [363]. Due to high intense colour even at low concentration MB is used in paper, cottons, and wool industries [363]. Therefore, the hazardous and intensely coloured dyes should be removed from wastewater before releasing it into the environment. Furthermore, AR88 is an anionic dye while MB is a cationic dye. The impact of charge differences in dye molecules is important to understand the adoption property for porous microspheres for synthetic dyes.

### 2.5.2 Batch adsorption experiment

The batch experiments were carried out using 250 ml erlenmeyer flasks with 1 g/L microspheres dosing and 50 ml dye volume based on scoping studies. The solution was stirred at room temperature (22 ± 2 ℃) on a shaker (Orbital shaker, Thermo Scientific,UK) at 180 rpm with various concentrations of dye solution (20- 450 mg/L) until equilibrium was reached for isothermal studies. After the adsorption, adsorbents were separated using 10 µm mesh sieve as a filter. The concentration of the dye in solution was determined using a UV–VIS spectrophotometer (Varian Cary 50 UV-Visible spectrophotometer Agilent, Santa Clara, CA, USA) at 505 nm ($\lambda_{max}$). The adsorption capacity was measured using the following Equation (see Equation 2.5):

$$q_e = \frac{(c_0 - c_e)}{M} * V \qquad \textit{Equation 2.5}$$

Where $C_o$ is the initial concentration of acid red 88 (mg/L), $C_e$ is the equilibrium concentration which represents the remaining dye in the flask (mg/L); $V$ is the volume of the solution used (L) and $W$ is the weight of the adsorbents (g).

For the kinetics studies, the concentration of dye solution was measured after each time interval keeping all the adsorption conditions the same as in isothermal adsorption studies.

### 2.5.3 Ultraviolet-Visible Light Spectroscopy

The operating principle of UV-Visible spectroscopy is the absorption of UV-Visible region (λ=200-800 nm) of electromagnetic radiation to molecules. When an incident beam impacts a molecule, which contain π electrons or non-bonding electrons, known as chromophores, the beam experiences various phenomena, absorption, reflectance, transmittance and scattering. When a sample is exposed to light that has an energy that matches the energy gap between, the highest occupied molecular orbital (HOMO) and lowest unoccupied molecular orbital (LUMO) some of the energy will be absorbed and the electron will be transported to an excited state. The absorption spectrometer records the amount

of absorption of radiation as well as the characteristic wavelength of the electromagnetic radiation absorbed.

According to the Beer-Lambert law (see Equation 2.6), the absorbance of the sample will be proportional to the concentration of the sample, and this is used to quantify the amount of analyte in the sample.

$$\textit{Absorbance, } A = \varepsilon C l \qquad \textit{Equation 2.6}$$

Where, *A* is the absorbance, *C* (mol/L) is the concentration of the analyte, *l* (cm) is the path length of the sample (which is normally around 1 cm) and *ξ* (L/mol/cm) is the molar absorptivity of the analyte.

The UV-Vis spectrophotometer was calibrated with dye in experiment. A calibration curve with regression value $R^2 \geq 0.99$ was considered for the analysis. In a fume hood, desired amount of a standard stock solution was prepared, which is then diluted to prepare solutions for calibration curve. Deionised water was set as a baseline absorbance for UV-Vis instrument.

### 2.5.4 Batch adsorption isotherm models

The effectiveness of the microspheres can be determined from their capacities to adsorb. This capacity is related to fitting experimental data with given adsorption isotherms. Adsorption isotherms such as the Langmuir and Freundlich Isotherm are the most commonly found isotherms [309, 364]. Three types of adsorption isotherm models were used for modelling the experimental data. These isotherm Equations are the following:

$$\textit{Langmuir model: } q_e = \frac{q_m K_1 C_e}{1 + K_1 C_e} \qquad \textit{Equation 2.7}$$

$$\textit{Freundlich model: } q_e = K_f C_e^{\frac{1}{n}} \qquad \textit{Equation 2.8}$$

$$\textit{Temkin model: } q_e = \frac{RT}{b_T} ln A_T + \frac{RT}{b_T} ln C_e \qquad \textit{Equation 2.9}$$

Where $q_e$ (mg /g) is the equilibrium adsorption, $q_m$ is the maximum dye capacity (mg/g), $C_e$ (mg /L) is the equilibrium dye concentration, $K_1$ the Langmuir equilibrium constant (L/mg), $K_f$ the Freundlich constant (L/g), *n* the heterogeneity factor, $b_T$ is the Temkin constant related to the heat of adsorption (J/mol), $A_T$ is the Temkin isotherm equilibrium binding constant (L/g), *R* is the gas constant (8.3145 J /mol/K) and *T* is the absolute temperature at 303 K. All the model parameters were evaluated by linear regression [365].

### 2.5.5 Batch kinetic models

Pseudo-first and pseudo-second order models were used to analyse the kinetic data [366]. The linearized form of pseudo-first and pseudo-second order model are shown below as Equation 2.10 and 2.11, respectively:

$$log(q_e - q_t) = log(q_e) - \frac{K_1 t}{2.303} \quad \textit{Equation 2.10}$$

$$\frac{t}{q_t} = \frac{1}{k_2 q_e^2} + \frac{t}{q_e} \quad \textit{Equation 2.11}$$

where $q_e$ is the amount of dye adsorbed at equilibrium (mg/g), $q_t$ the amount of dye adsorbed at time t (mg/g), $k_1$ the first-order rate constant (1/min), and $k_2$ is the second-order rate constant (g/mg min).

### 2.5.6 Fixed bed adsorption experiment.

Continuous adsorption tests were also conducted using a fixed bed column (Swagelok ¼" inch) of 3.86 mm internal diameter by 200 mm height to determine the columns operational functionality and adsorption capacity using the porous glass microspheres produced (see Figure 2.3). A known quantity of microspheres were packed in the column to set the desired bed height. Dye solution of concentration 300 mg/L was gravity fed using a pump (Gilson 305 UK) into the column. Operational flow rate for the experiment was based on the empty bed residence time (EBCT) that is the total time needed to occupy the empty column, a parameter that influences adsorption capacity and breakthrough in the adsorption column [367]. The dye solution exiting at the other end of the column was collected at regular intervals and analysed using a UV–VIS spectrophotometer to determine the output dye concentrations ($C_t$). The breakthrough time is the time when concentration of the solution reaches 1-5% of initial concentration. This was determined using the breakthrough graph by plotting $C_t/C_0$ Vs time t [368]. Total adsorption was calculated by integrating the $C_0$-$C_t$ vs t curve according to Equation 2.12:

$$q_{total} = \frac{Q}{1000} \int_0^t C_{ad}\, dt \quad \textit{Equation 2.12}$$

Where $q_{total}$ (mg) is the total adsorption, $Q$ (mL/min) is the flow rate, $C_{ad}$ (mg/L) is the adsorbed concentration ($C_0$-$C_t$), $t$ (min) is the adsorption time. Equilibrium uptake ($q_{eq}$ / mg/g) in the column was calculated using $q_{tot}$ from Equation 2.12 and Equation 2.13 [368].

$$q_{eq} = \frac{q_{total}}{m} \quad \textit{Equation 2.13}$$

Where $m$ (g) is the amount of microspheres used.

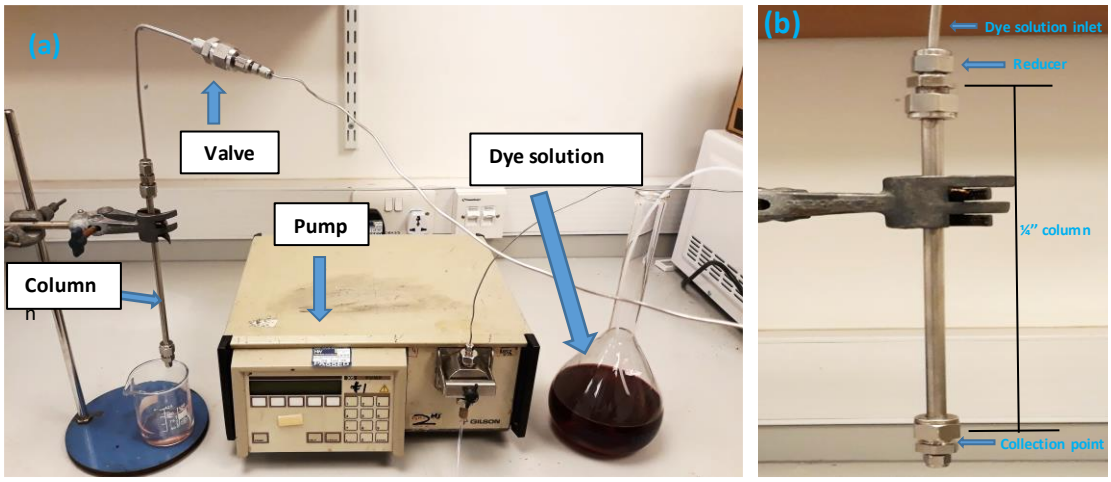



***Figure 2.3: a) Photograph of adsorption column, pump and wastewater source, b) Inset of the column fittings.***

### 2.5.7 Analysis of column data

Three commonly utilised models in the literature named Thomas, Adams-Bohart and Yoon Nelson models were explored for the kinetic studies [162]. The linearized form of the models are shown below as Equation 2.14, 2.15 and 2.16, respectively.

$$\textit{Thomas model: } ln\left(\frac{C_o}{C_e}-1\right)=\frac{k_{Th}q_{Th}m}{Q}-k_{Th}C_o t \qquad \textit{Equation 2.14}$$

$$\textit{Adams-Bohart model: } ln\left(\frac{C_t}{C_o}\right)=k_{AB}C_o t-k_{AB}N_o\frac{z}{U_o} \qquad \textit{Equation 2.15}$$

$$\textit{Yoon-Nelson model: } ln\left(\frac{C_t}{C_o-C_t}\right)=k_{YN}t-\tau\, k_{YN} \qquad \textit{Equation 2.16}$$

Where $C_t$ (mg/L) is the dye concentration at time, t (min), $C_0$ (mg/L) is the initial concentration, $q_{Th}$ (mg/g) is the adsorption at capacity at exhaustion, m (g) is the mass of the adsorbent, Q (L/min) is the volumetric flow rate through the column, and $k_{Th}$ (mL/min/mg) is the Thomas rate constant. $k_{AB}$ (L/mg/min) is the Adams-Bohart constant, $N_0$ (mg/L) is the adsorbate concentration at exhaustion, $z$ (cm) is the column height and $U_0$ (cm/min) is the flow velocity through the column, obtained by dividing the volumetric flow rate by the cross-section area. $k_{YN}$ ($min^{-1}$) is the Yoon-Nelson rate constant and τ (min) is the time taken for 50% exhaustion to occur.

### 2.5.8 Adsorbent Recyclability

Regeneration and recyclability of dye adsorbed porous microspheres is a key characteristic that enhances sustainability of the adsorption process. Adsorbent regeneration was investigated only for AR88 dye as the dye was not the focus of the experiment, rather than the regeneration method and the subsequent performance of the porous microspheres.

A solution of AR88 (180 mg/L) was stirred at 293K with 5g/L of porous microspheres until equilibrium was reached. A 1mL aliquot was taken for analysis and the adsorption capacity was calculated. In the first study, the dye adsorbed microspheres were heated in a furnace at 400°C for 1hrs to burn off the dyes from the microspheres. TGA and XRD analysis were performed after heating in furnace to confirm the dye was completely removed. These desorbed microspheres were reused in the next adsorption cycle. The process was followed for 5$^{th}$ cycle.

### 2.5.9 Coagulation study

In the second set of experiment, coagulation effect of PRGMs were investigated via Jar coagulation test. The optimum dose was chosen 1g/L at pH 2-4 with dye concentration 200 mg/L for AR88 and 50 mg/l for MB dye. These parameters were chosen based on scoping studies. Experiments were conducted with 1L glass jar using a magnetic stirrer (IKA, C-MAG HS 7, UK). The experimental procedure consisted of two subsequent stages: a rapid mixing stage at 200 rpm for 1 min followed by slow mixing at 40 rpm for 20 min. The stirring was then stopped, and the mixture was allowed to settle for 6 hrs. Finally, the supernatant was removed from the beaker for UV analysis.

### 2.5.10 Statistical analysis

$R^2$ and chi-square tests were performed to find out the suitability of various kinetic and isotherm models in the present study [369]. The Equation is as follows:

$$X^2 = \sum_i^N \frac{(q_{exp} - q_{cal})^2}{q_{cal}} \qquad \textit{Equation 2.17}$$

Where, $q_{e,exp}$ and $q_{e,cal}$ (mg/g) are experimental and calculated dye concentration at equilibrium, respectively and $q_{e,cal}$ (mg/g) is average value of $q_{e,cal}$.

## 2.6 Microsphere-dye interaction study

### 2.6.1 Optical Microscopy analysis

The optical observations were made in transmitted light with a Leica microscope DM 3000 for post dye adsorbed microspheres. The images were recorded with Leica DFC420 camera. The sample was placed on slide so as to have minimum possible destruction. The observations for microspheres were made at different magnifications viz., 20x and 40x.

### 2.6.2 FTIR analysis

Infrared spectroscopy of the microparticles and microspheres were performed using a Brüker Tensor 27 spectrometer (Brüker Optics, Germany) which was operated in absorbance mode. Spectra were measured in the region of 480 to 4000 $cm^{-1}$ utilising a Standard Pike ATR cell (Pike Technologies, Inc., UK). OPUS software version 5.5 was used for the analysis.

### 2.6.3 X-ray Photoelectron Spectroscopy (XPS) analysis

XPS was performed using a VG Scientific ESCA Lab Mk2 electron spectrometer with a monochromatic Al KaX-ray source (1,486.6 eV) operated at 15 mA and 10 kV anode potential. For the XPS measurement, samples were adhered to a carbon tab attached to an aluminium stub. The shift of the binding energy due to surface charging effect was calibrated by referencing the measured binding energy of C 1s to 284.8 eV. For high-resolution spectra, 20 scans were taken using pass energy of 20 eV. CASA-XPS software was used for data processing and curve fitting of XPS spectra. These spectra were deconvoluted by using a best fit programme with Gaussian distributions.

# Chapter 3: Optimisation of surface area and porosity and preliminary dye removal studies of PBG microspheres

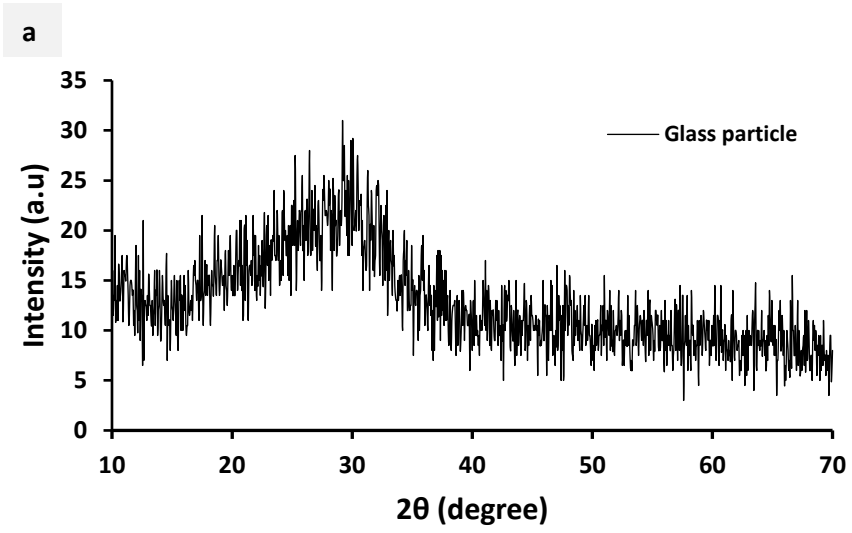
## 3.1 Introduction

To manufacture porous microspheres, several factors must be considered, including the chemical and physical interaction of the porogen with the glass particles, and the delivery of both porogen and glass particles within an adequate thermal processing window and within a sufficient residence time [309]. However, further studies were required to manufacture controlled pore size porous microspheres suitable for wastewater treatment. The present investigation was to understand the effects of manufacturing process parameters such as use of specific starting glass particle size and porogen ratios in flame spheroidisation process and to identify conditions that worked best to maximise surface area and porosity levels of the microspheres produced. In the current chapter phosphate-based glass (PBG) were considered as the group has vast experience with this glass system for bone repair applications. The effect of varied surface area and porosity of porous PBG microspheres upon adsorbing dye (acid red 88) on batch and fixed bed adsorption studies were also investigated.

## 3.2 Results

### 3.2.1 X-Ray Diffraction analysis

The glassy nature of the phosphate glass particles and microspheres prepared were examined using X-ray diffraction analysis. A high sigal to noise ratio was observed for Figure 3.1. However, upon re examining the microspheres using Bruker D8 Advance with Da Vinci revealed no sharp peaks for both the glass particles and microspheres prepared, with only a broad peak seen between 20-40$^{o}$ diffraction angle, which confirmed the amorphous naure of the materials prepared (see Figure 3.1).



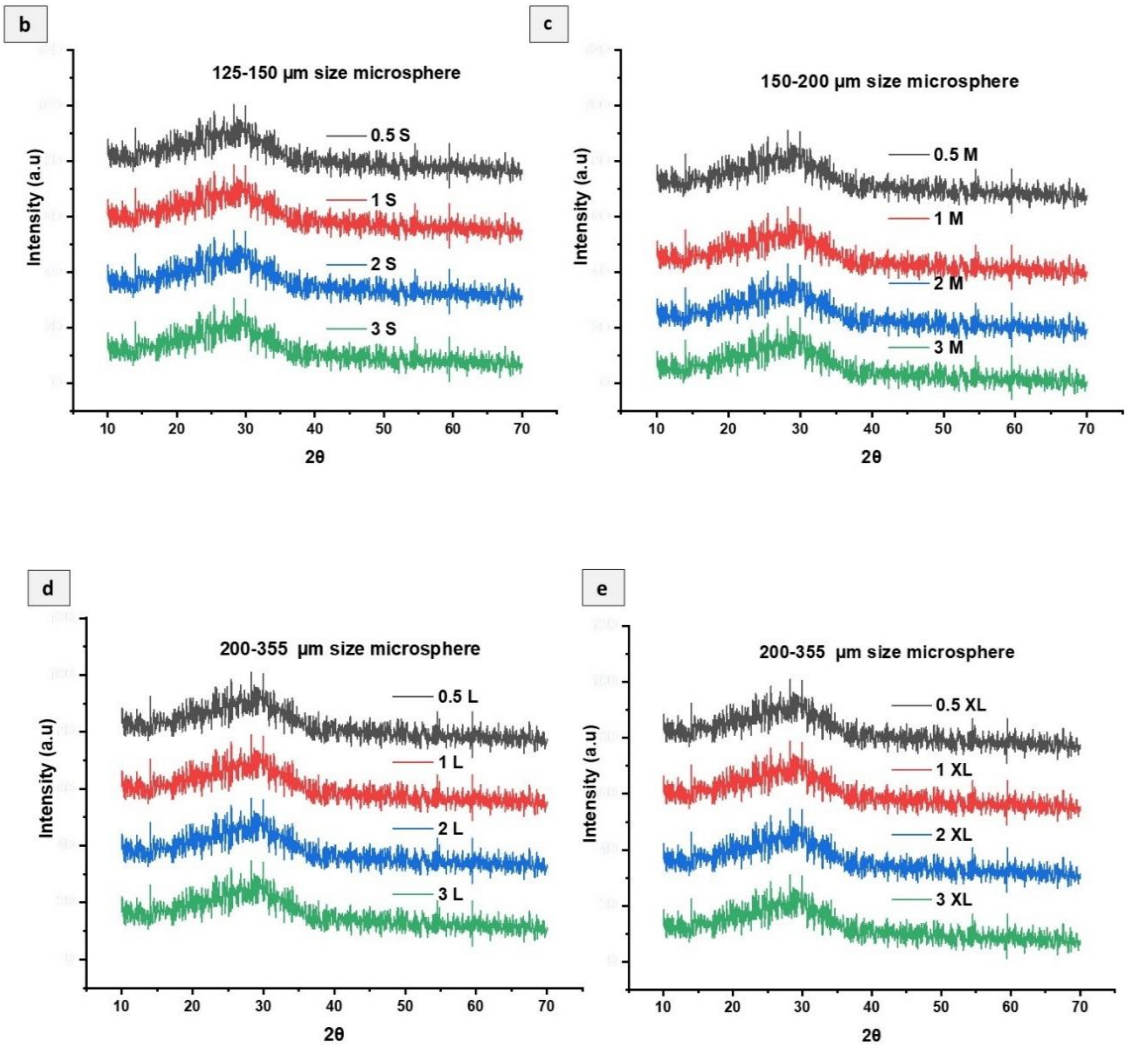



***Figure 3.1: X-ray diffraction pattern for a) glass particles, b) glass microspheres of size 25-150 µm, c) 150-200 µm d) 200-355 µm and e) 200-355 µm with different porogen ratios.***

## 3.2 2 Energy Dispersive X-Ray analysis

The composition of phosphate glass and microspheres prepared with different porogen ratios after flame spheroidisation are shown in Figure 3.2. The glass particles showed small variation (±0.6 mole %) from the actual theoretical compositions required. On the other hand, the flame spheroidised microspheres showed a small change in composition which was seen mainly with the increase in CaO mole % (0.8-3 mole %) from the actual theoretical value required and with increasing particle to porogen ratios.

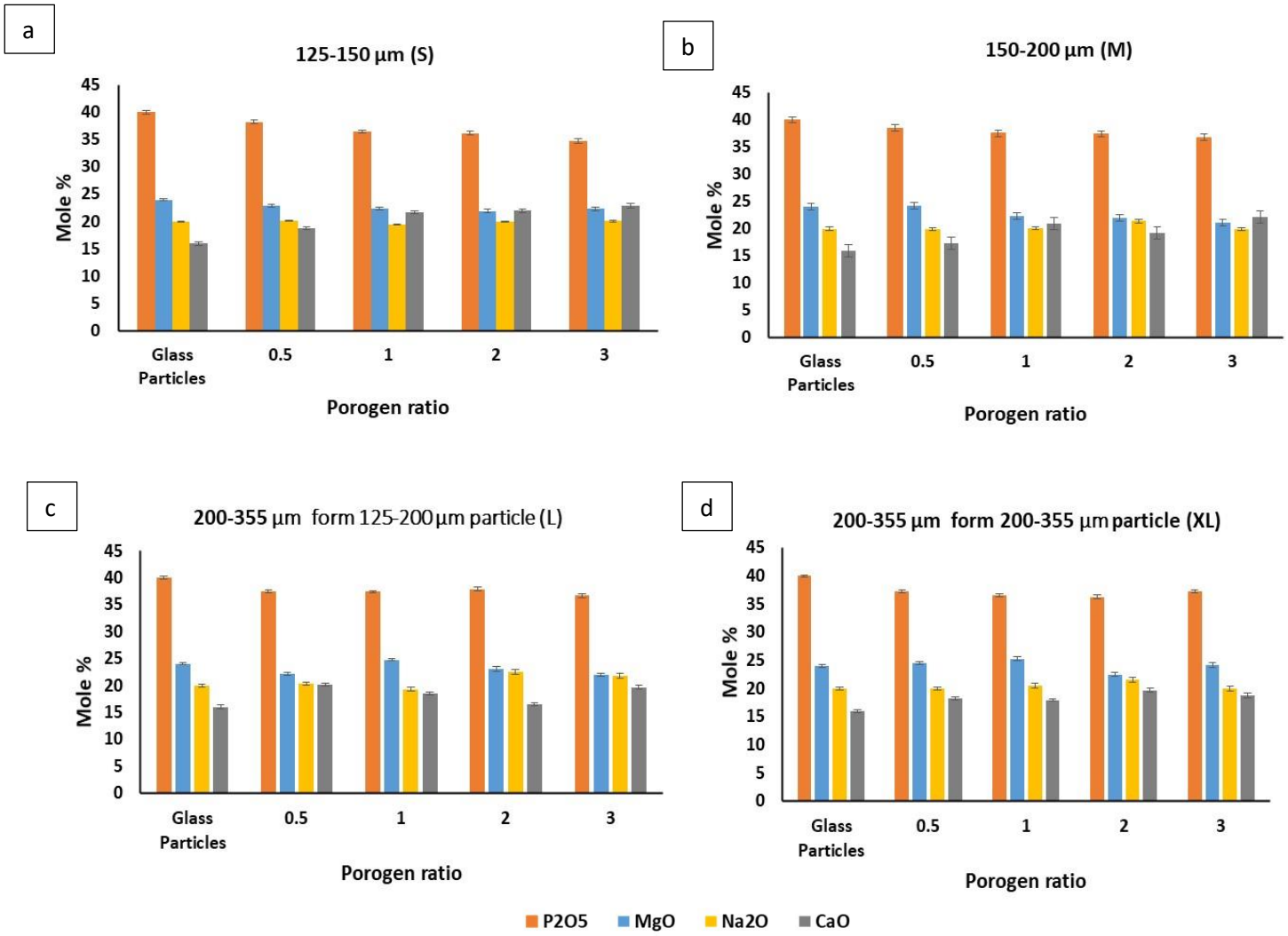



***Figure 3.2: Comparison of composition of glass particles with microspheres of a) S, b) M, c) L and d) XL sized porous glass microspheres manufactured vis varying the porogen ratio using EDX analysis.***

### 3.2.3 Coulter Laser Diffraction analysis

The particle size distribution of the initial glass particles of size range 63-125 µm, 125-200 µm and 200-355 µm is presented in Table 3.1. For the 63-125 µm particles the size distribution was quite broad (as seen in Figure 3.3) with particle diameters from 50 to 150 µm. Particle size distributions for the 125-200 µm and 200-355 µm particles revealed that 50% volume of the particles had sizes below 172 µm and 255 µm, respectively. The microspheres on the other hand showed diameters lower than expected, with the exception of 200-355 µm size range microspheres (labelled as XL), which were

spheroidised using starting particle size ranges between 200-355 µm. For each histogram broad peaks were observed indicating a random distribution of particle sizes (See Figure 3.3).

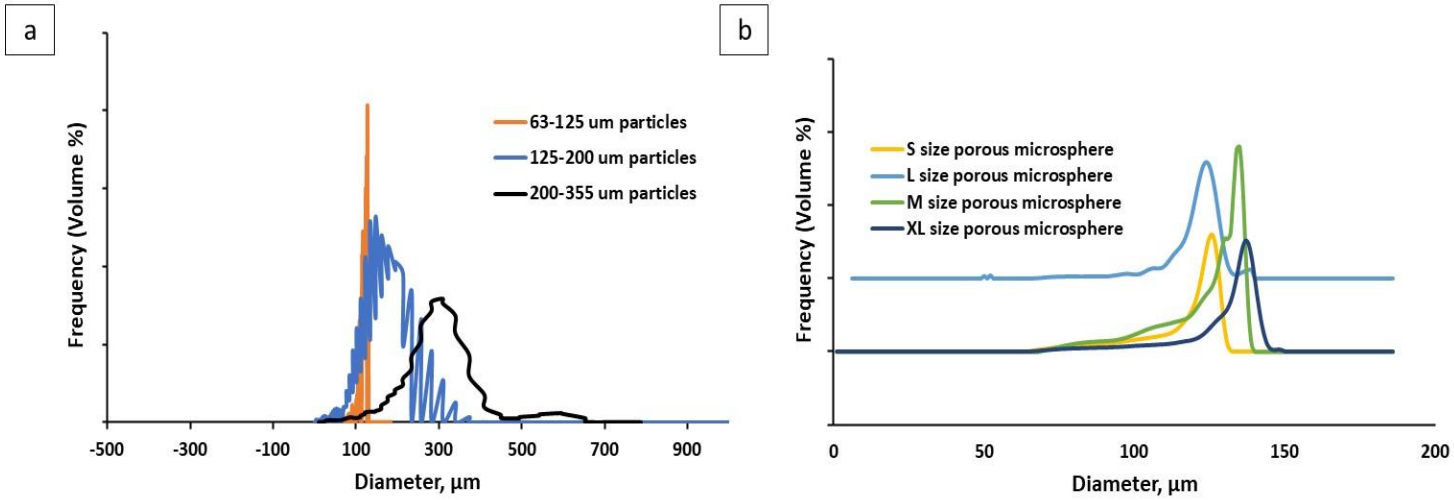



*Figure 3.3: Histogram for a) glass particles and b) flame spheroidised microspheres manufactured from different starting particle size ranges (Coulter Counter).*

*Table 3.1: Size distribution for glass particles and flame spheroidised microspheres of different sizes on different cumulative volume %.*

| | Size distribution in µm range | | | | | | |
|---|---|---|---|---|---|---|---|
| **Volume %** | **A** | **B** | **C** | **S** | **M** | **L** | **XL** |
| **$D_{10}$ (%)** | 50 | 85 | 76 | 7 | 6 | 5 | 18 |
| **$D_{50}$ (%)** | 104 | 172 | 255 | 85 | 90 | 66 | 226 |
| **$D_{90}$ (%)** | 134 | 257 | 343 | 136 | 155 | 170 | 355 |

*A= Particles of 63-125 µm, B= Particles of 125-200 µm, C= Particles of 200-355 µm, S= Microspheres of 125-150 µm, M= Microspheres of 150-200 µm, L= Microspheres of 200-355 µm and XL= Microspheres of 200-355 µm size ranges.

### 3.2.4 Scanning Electron Microscopy (SEM) analysis

The morphologies of the microspheres evaluated using SEM analysis revealed that glass microspheres with surface pores and interconnected porosity were generated from the varying ratios of glass particles to porogen used during the fabrication process, as shown in Figure 3.4, Figure 3.5 and Figure 3.6. The cross-sectional images for the 125-150 µm microspheres (S), 150-200 µm (M) and 200-355 µm microspheres (L) revealed that the microspheres produced had interconnected porosity which increased with increasing glass particles to porogen ratios (see Figure 3.4, Figure 3.5 and Figure 3.6).

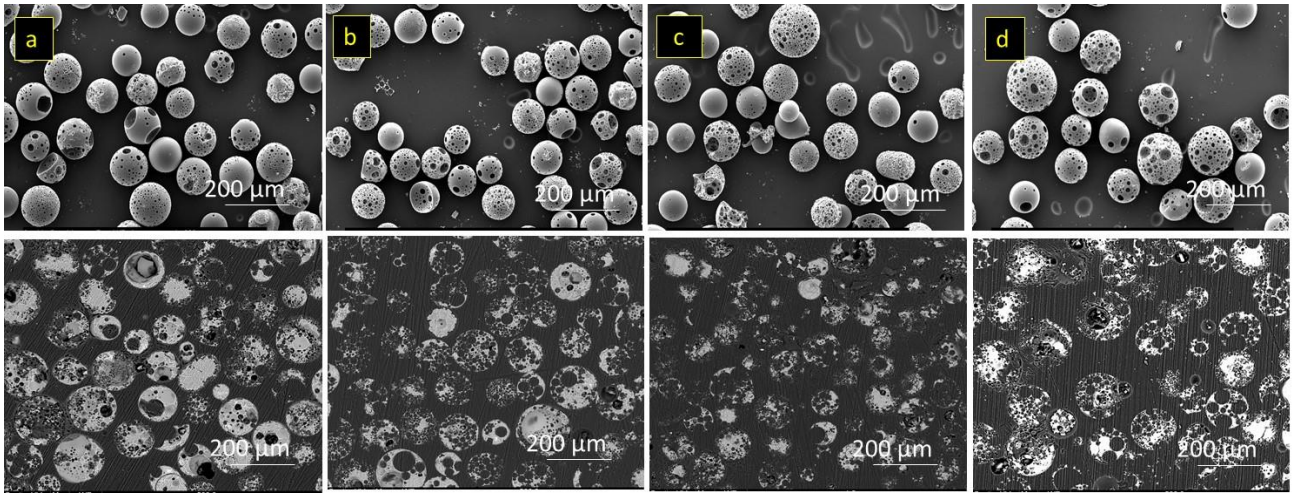



*Figure 3.4: SEM images of 125-150 µm porous microspheres (S) with cross-sections of a) 0.5, b) 1, c) 2 and d) 3 porogen ratios, generated via resin embedding.*

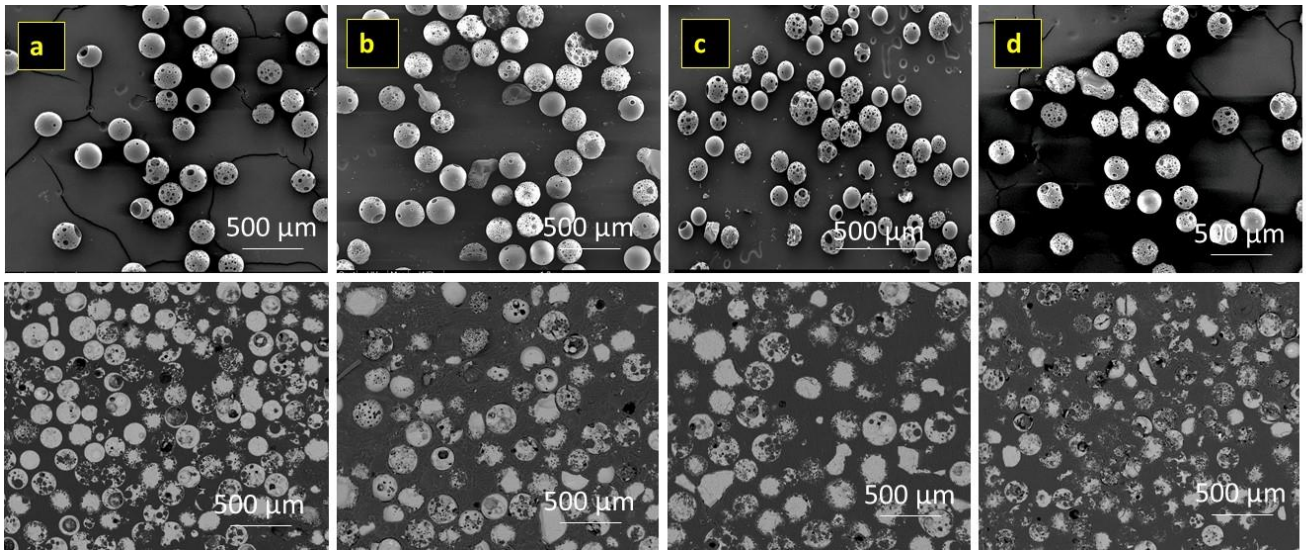



*Figure 3.5: SEM image of 150-200 µm porous microspheres (M) with cross-sections of a) 0.5, b) 1, c) 2 and d) 3, porogen ratios, generated via resin embedding.*

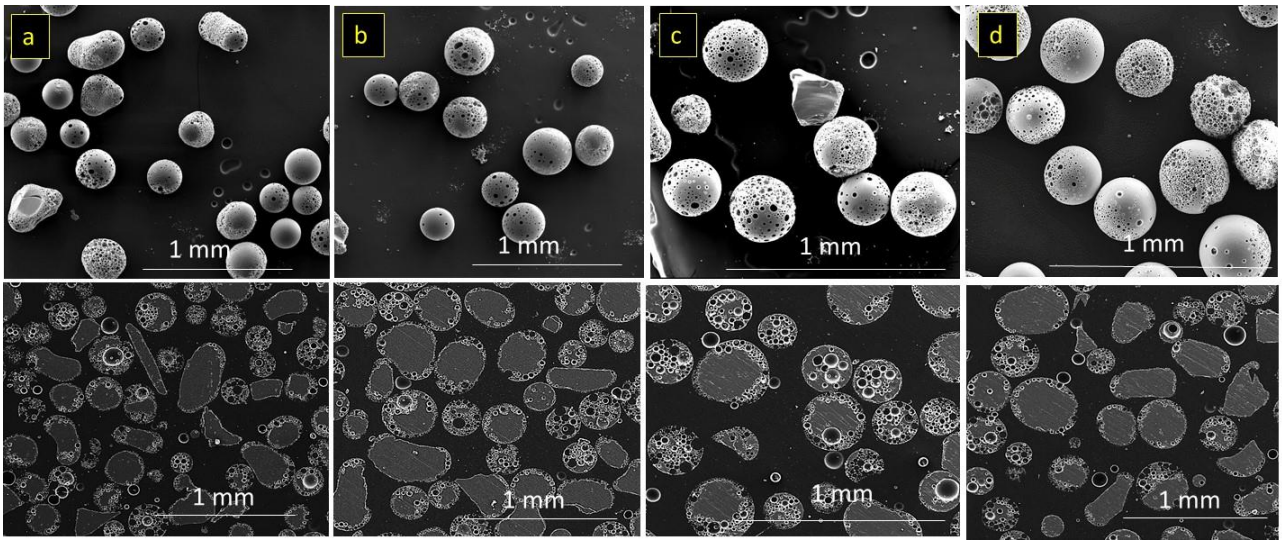



*Figure 3.6: SEM image of 200-355 µm porous microspheres (L) with cross-sections of a) 0.5, b) 1, c) 2 and d) 3, porogen ratios, generated via resin embedding.*

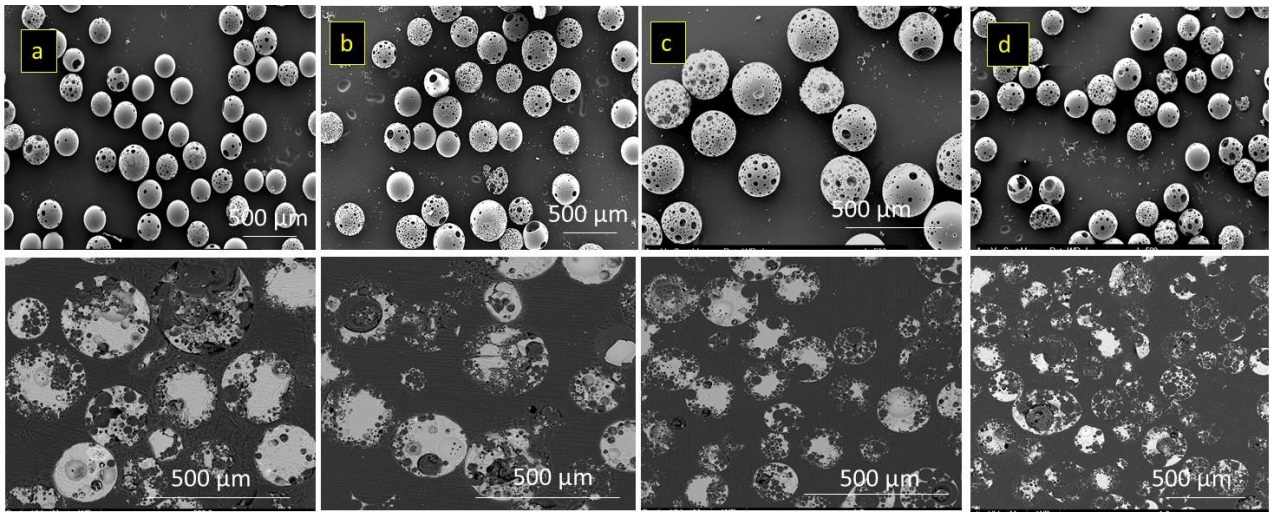



*Figure 3.7: SEM image of 200-355 µm porous microspheres (XL) with cross-sections of a) 0.5, b) 1, c) 2 and d) 3, porogen ratios, generated via resin embedding.*

However, the 200-355 µm size (XL) microspheres revealed a dense solid core with a porous surface shell and absence of interconnected porosity. Some of the microspheres also had a distorted shape rather than purely spherical compared to the other batches.

### 3.2.5 Density Analysis

The apparent density of the microspheres is shown in Figure 3.8. Spheroidisation of porous microspheres revealed a decrease in apparent density of glass from 2.64 (±0.005) g/cm$^3$ to 2.48 (±0.101) g/cm$^3$. The different size microspheres prepared from different porogen ratios showed similar apparent density. The tapped density was also measured as shown in Figure 3.9. The

microspheres of size S and L showed a decrease in tapped density with increasing particle to porogen ratio. On the other hand, the other size ranges showed a higher tapped density. The theoretical porosity of the microspheres was also calculated from density measurement using Equation 2.1, detailed in Chapter 2. The tapped density and apparent density, as shown in Figure 3.9.

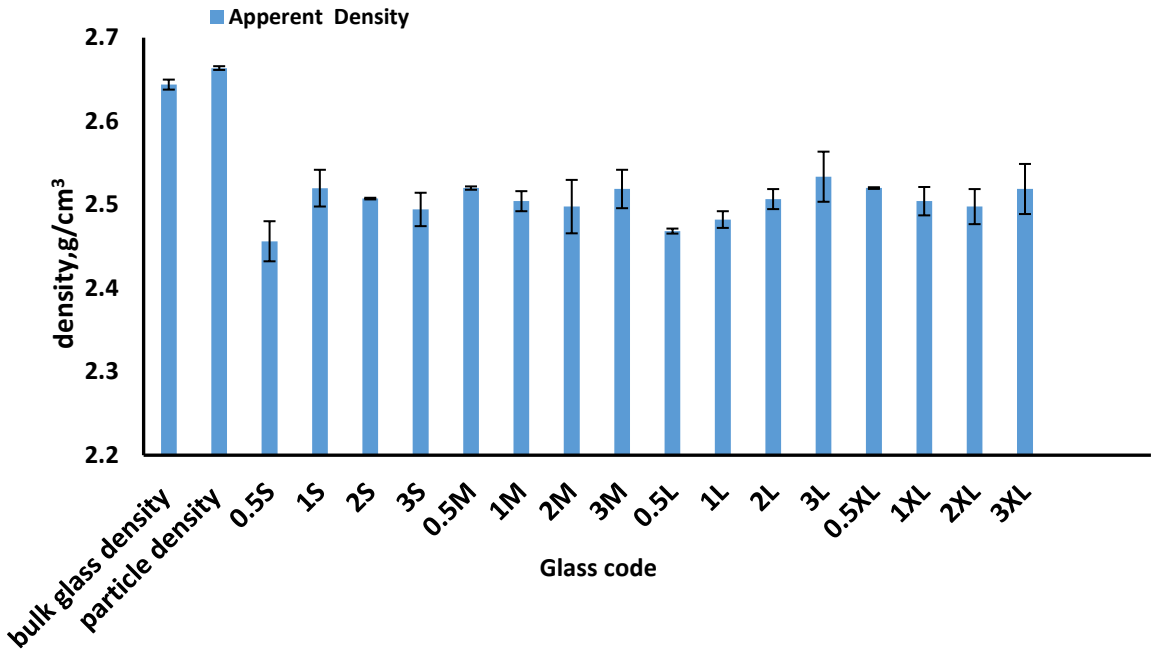



*Figure 3.8: Apparent density of glass chunk, particles and microspheres.*

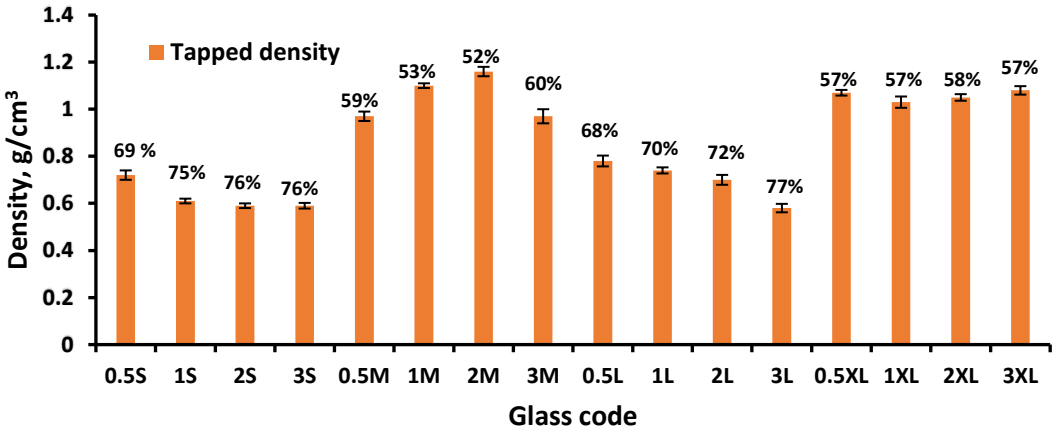



*Figure 3.9: Figure showing tapped density and respective % theoretical porosity of glass microspheres produced.*

Based on the theoretical analysis, the porosities of the microspheres produced were 57-75%. The highest porosity was calculated for the small size microspheres (size S) and the lowest porosity was seen for the XL size microspheres.

### 3.2.6 Surface area and porosity analysis

The krypton adsorption isotherm related to surface area from BET analysis is shown for the different microspheres prepared using varying glass particle to porogen ratios. From this Figure 3.10, it can be observed that the smaller sized glass microspheres showed greater surface area compared to the others. The surface area of glass microsphere prepared increased with increasing glass particle to porogen ratio during spheroidisation. For the other glass microsphere size ranges the same trend was observed with the exception of the last four types of XL size microspheres. The corresponding isotherms from each size of the porous glass microspheres are shown in Figure 3.11 (a, b, c and d).

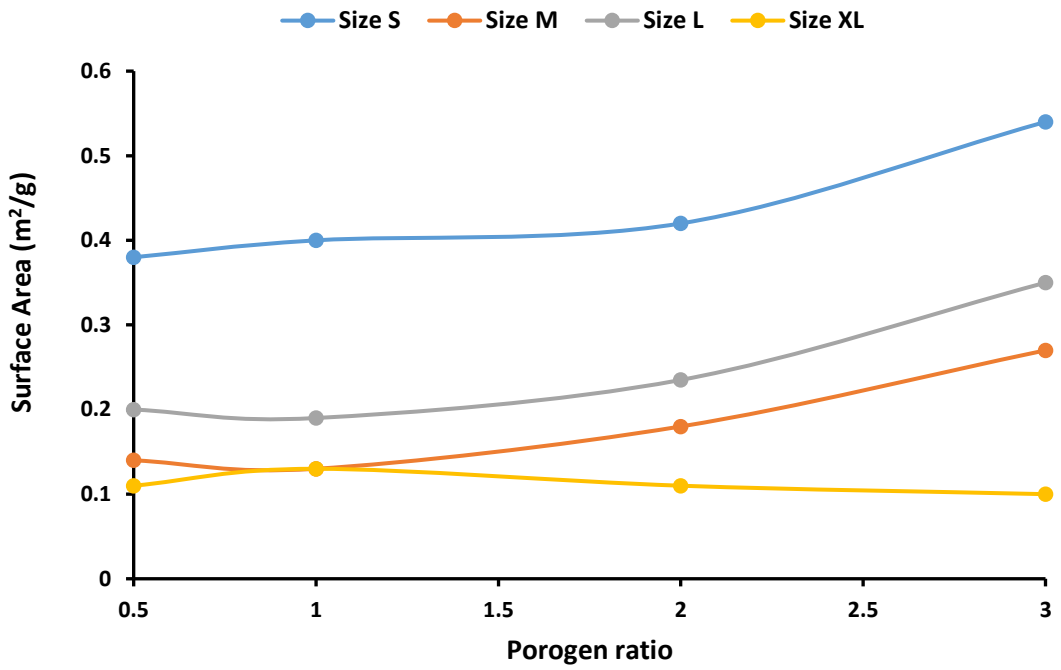



*Figure 3.10: Surface area measurement from BET analysis for the different size porous microspheres investigated.*

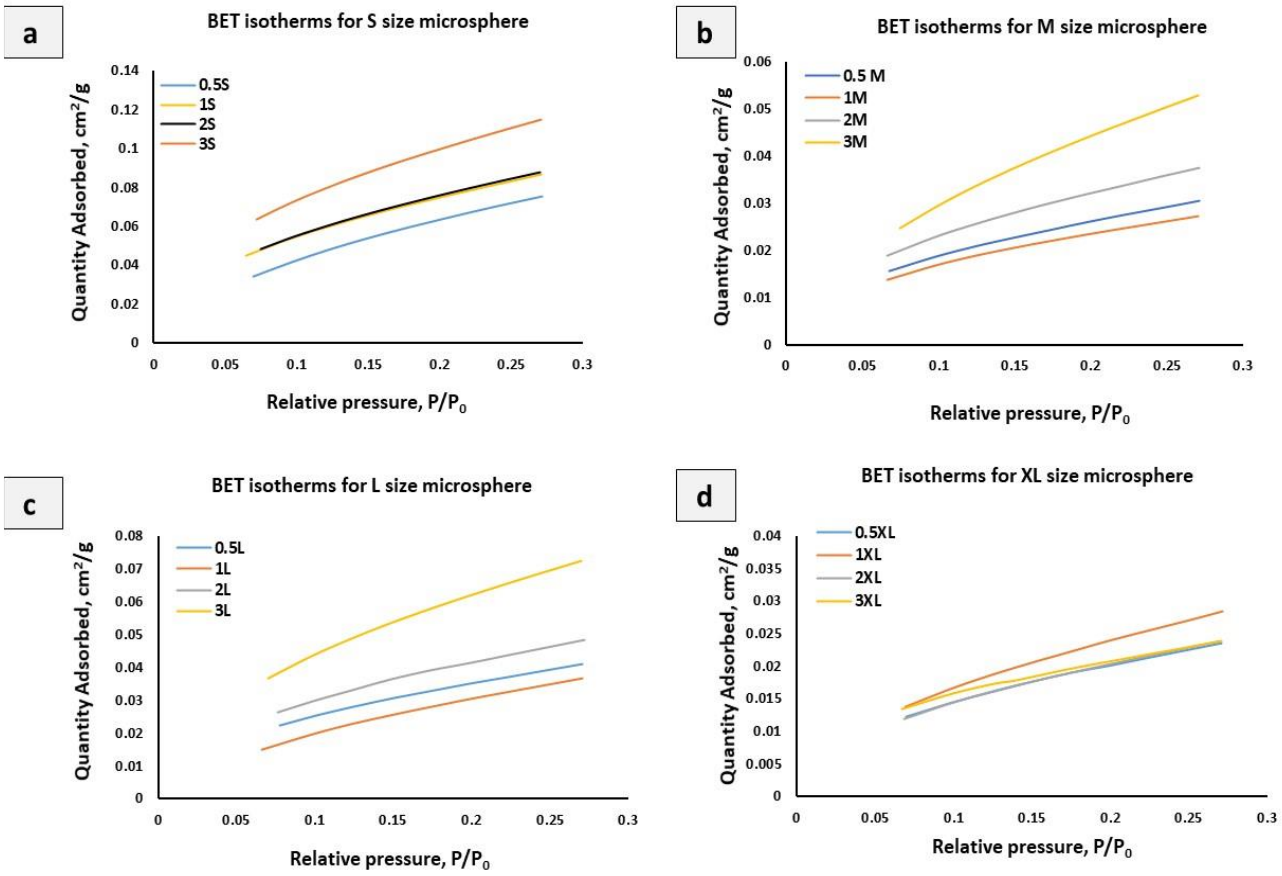



*Figure 3.11: BET isotherm for adsorption into a) S, b) M, c) L and d) XL sized porous glass microspheres.*

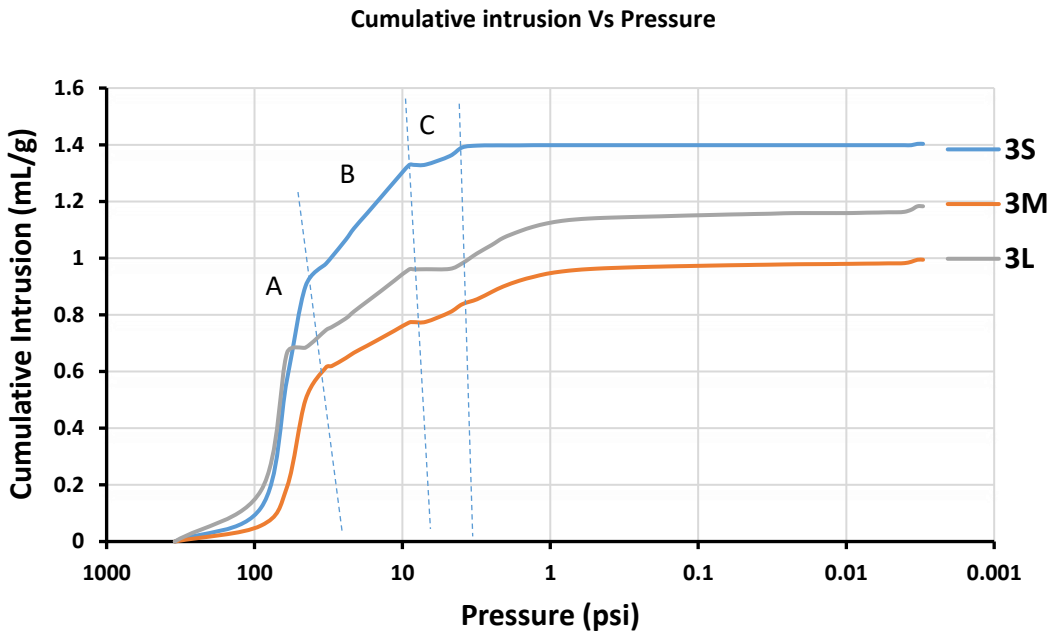



***Figure 3.12: Figure showing cumulative intrusion of mercury into different size microspheres. Zone A, B and C represents the interparticle space among microspheres, low pressure intrusion and high-pressure intrusion within the pores of microspheres, respectively.***

Figure 3.12 shows the cumulative intrusion of mercury into the different size microspheres investigated as a function of mercury pressure (obtained via mercury porosimetry analysis). With increasing pressure, mercury intrudes into the interparticle space (shown by zone A) and the pores of the microspheres (zone B and C). The intrusion within the microspheres follows the order 3S>3L>3M. From Figure 3.13, the inter particle gap ranges from 50-70 µm for 3S and 3M sized microspheres, whereas in the case of 3L this gap increased showing a range in between 50-85 µm. On the other hand, the pore diameter for these microspheres ranged from 5-45 µm. No abrupt changes were noticeable with further increases in pressure. The respective porosity profile was 70 %, 66 % and 68 % for 3S, 3M and 3L respectively.

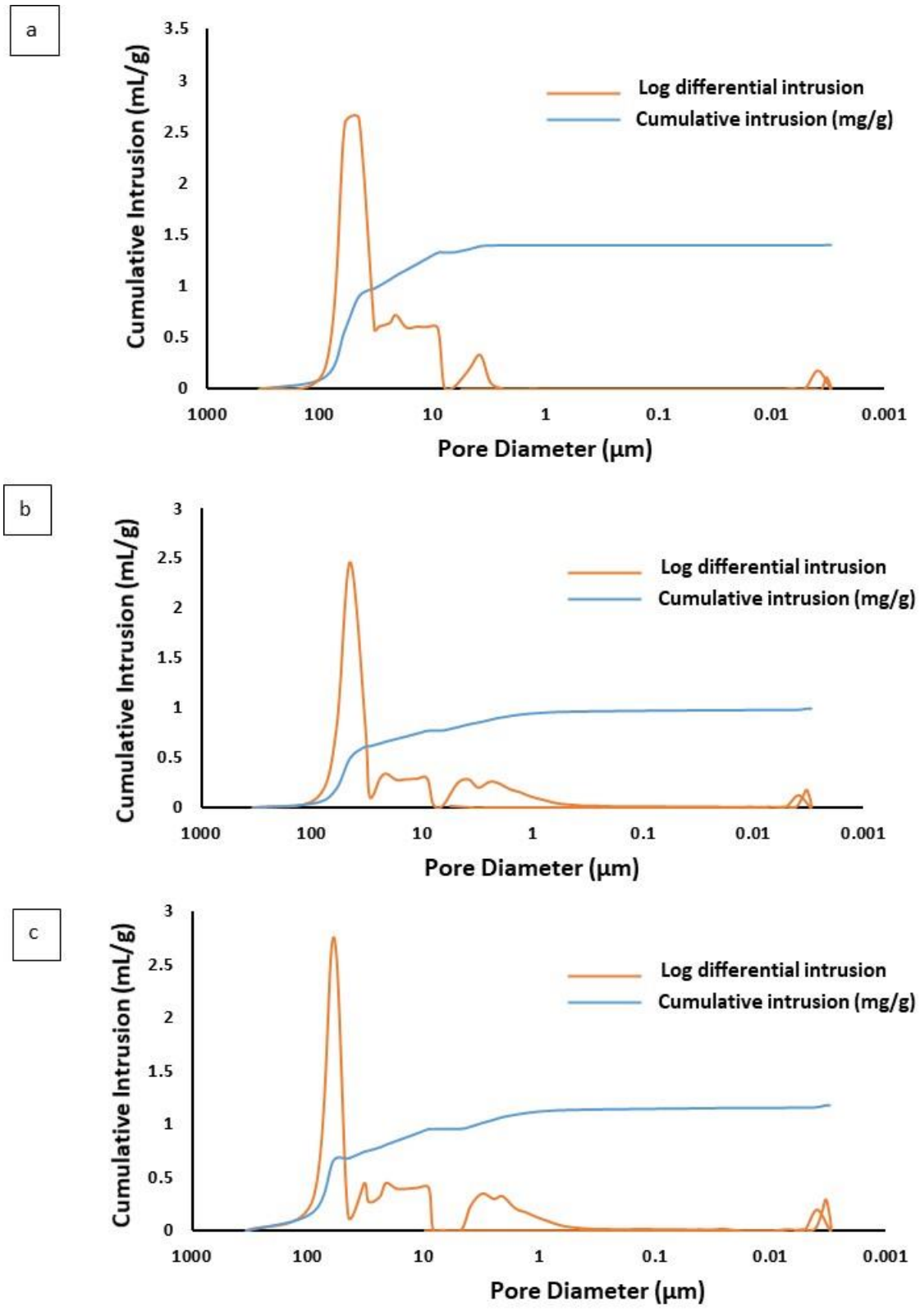
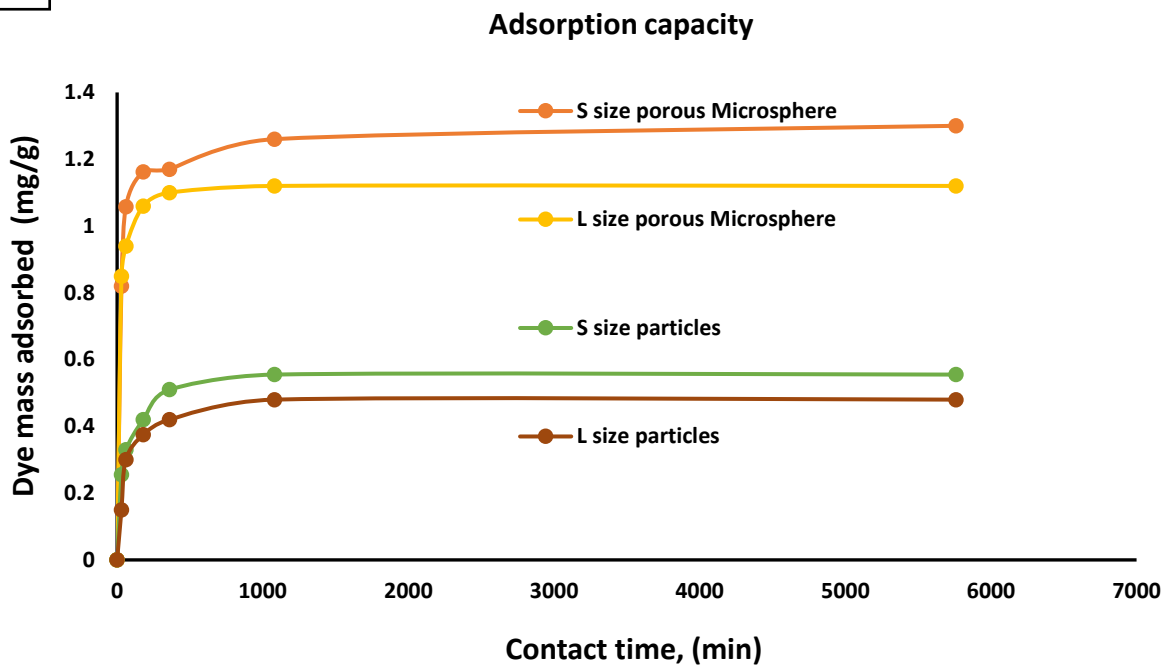



***Figure 3.13: Figure showing log differential intrusion and cumulative intrusion for different pore diameter for a) 3S microsphere with 70 % porosity b) 3M microsphere with 66 % porosity and c) 3L microsphere with 68 % porosity.***

### 3.2.7 Dye adsorption for batch studies

In batch dye adsorption experiment the effect of glass geometry and size are studied. Compared to the glass particles the porous glass microspheres showed highest dye removal capacity. From Figure 3.14, it was observed that the 125-150 µm microspheres achieved 87% dye removal with 1.3 mg/g dye adsorption. Glass particles of the same size achieved about 37% dye removal with only 0.58 mg/g dye adsorption. On the other hand, 200-355 µm microspheres (labelled L) achieved 70% dye removal with 1.1 mg/g dye removing capacity. This study also showed that the smaller size particles/microspheres of size 125-150 µm gave better adsorption profile compared to larger glass particles/microspheres of size 200-355 µm.

a



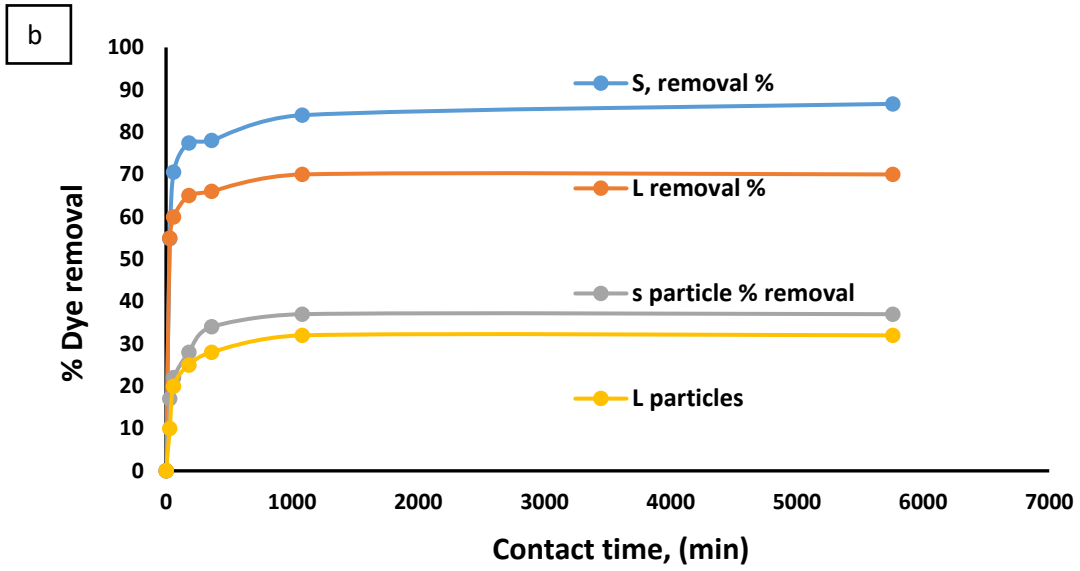



*Figure 3.14: Adsorption of dye by different size glass particles at different contact time in terms of a) amount of dye adsorbed per g of adsorbent and b) % dye removal.*

### 3.2.8 Dye adsorption for column studies

For the continuous dye adsorption studies, a glass pipette with 6 mm internal diameters was used was used for preliminary fixed bed column adsorption studies. The dye was gravity fed and a syringe pump was used maintain a uniform flow rate (see Figure 3.15). The experimental results were analysed, and a breakthrough curve (Figure 3.16) was drawn for bed weight of 170 mg under 100 mg/L initial concentration. The bed height for corresponding column was 2 cm. Having reviewed the experimental data, the critical bed length (cm), % Dye removal and Degree of column utilization (DOC %) were calculated.

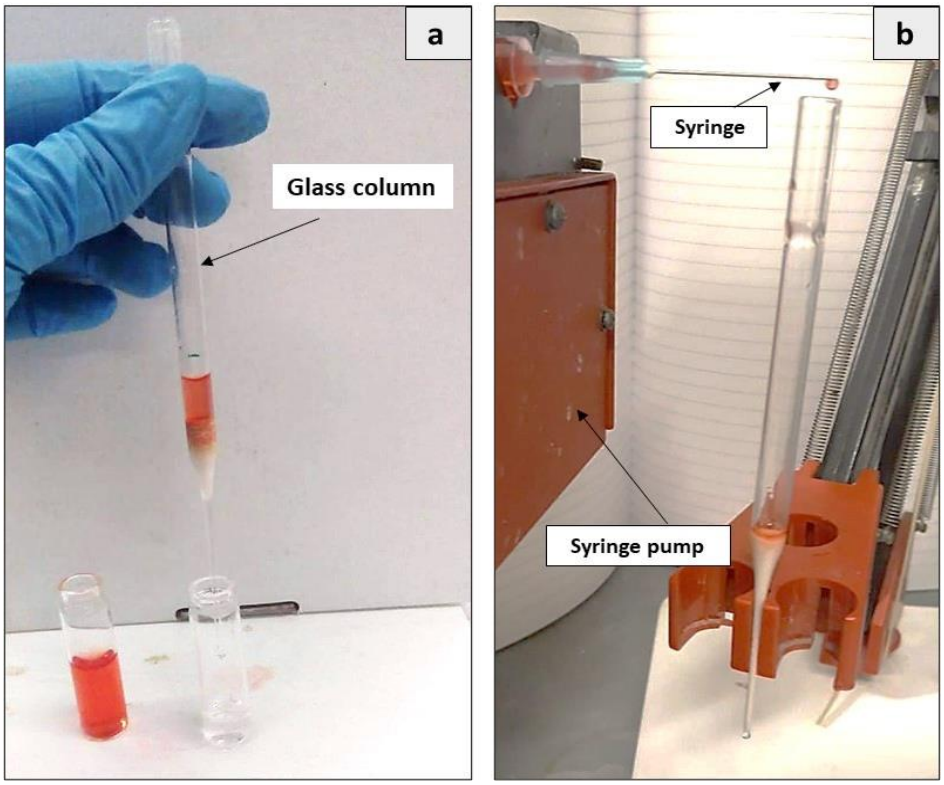



*Figure 3.15: Column adsorption using Acid red 88 on phosphate-based glass microsphere where image showing a) colourless solution coming out the tip of the column after getting adsorbed within the glass microsphere bed and b) instrument assembly.*

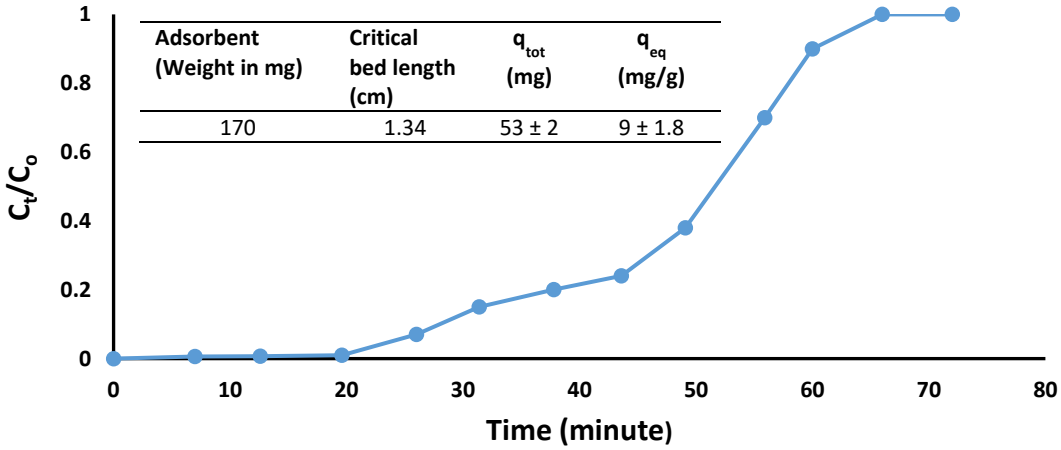



*Figure 3.16: Breakthrough curves for adsorption of Acid red 88 onto porous phosphate glass microspheres at 0.5 mL/min flow rate and 100 mg/L initial concentration with bed height 2 $cm^3$.*

## 3.3 Discussion

In this chapter, the studies conducted thus far focused on exploring porous phosphate-based glass (PBG) microspheres using flame spheroidisation (FS) process for dye removal as a proof of concept.

Existing porous materials for wastewater treatment are made via synthetic methods, which need the use of expensive and/or hazardous chemicals, lengthy processing periods, and costly manufacturing methods. Porous PBG microspheres were developed via FS within the Advance Materials Group at the UoN eliminates the use of toxic and hazardous chemicals during manufacturing. These glasses were selected for potential wastewater treatment studies as they are easy to manufacture into highly porous microspheres with interconnected porosities. However, the external pores were 55 ± 8 µm in diameter which were suitable for cell attachment and proliferation for bone implants. For wastewater treatment studies, porous structure with decrease in pore size is desired as most of the micro-pollutants are within size range of 10 µm-0.001 µm [370-372]. As a result, work was needed to identify the variables that would influence the pore dimeters with better dye removal efficacy. The ultimate goal was then to transfer this proof-of-concept processing methodology to manufacture porous microspheres with low-cost materials which are environmentally friendly.

The flame spheroidisation technique developed was investigated for phosphate-based glass ($40P_2O_5$-24MgO-16CaO-$20Na_2O$ in mol %) to tailor the level of porosity during the spheroidisation process via adopting various ratios of starting paticles/porogen. During spheroidisation of glass (mixed with various ratios of porogen), the heat induced shape change (for example, irregular shaped particles to regular shaped microspheres) without causing crystallisation which was confirmed via XRD analysis (see Figure 3.1). EDX analysis provided evidence of the final glass compositions of the glass prepared. The formulation investigated was close to actual values with 1–2 % error margin which is similar as previously reported by Hasan *et al* [258]. The EDX analysis showed 0.8-3 mole % increase of CaO for the microspheres from the target theoretical mole%. This discrepancy was suggested to be due to the presence of remnant amount of porogens that were either still clogged up within the pores or were remaining in the edges of the pores produced, giving an overall change in percentage composition.

The size distributions were broad for glass particles (Figure 3.3) which were due to the presence of coarse particles [373]. The distribution up to 50% volume for range 63-125 µm, 125-200 µm and 200-355 µm were below 104 µm, 172 µm, 255 µm respectively (see Table 3.1). This was identical to the distribution that fall in between 63-125 µm, 125-200 µm and 200-355 µm size range after manual sieving. The remaining 50- 90% volume particle size distribution was below 134 µm, 257 µm for 63-125 µm and 125-200 µm glass particles which was higher than expected. The glass particles are three-dimensional for which three parameters (the length, breadth, and height) are required. The higher size may be attributed to the random selection of any of these parameters that gave slightly higher particle distribution than expected [374]. By contrast, the microspheres gave a distribution below the

expected size distribution. This may be due to reflection from the pores of the microspheres resulting in anomalistic result [375].

The contact time of glass particles in the flame play a role in overall change in porosity and interconnectivity (see Figure 3.4, Figure 3.5, Figure 3.6, and Figure 3.7) that might resulted different size of microspheres. The microspheres generated from 63-125 µm particle had enough residence time within the flame for porogen to decompose and create pores that resulted 125-150 µm microspheres (size S) [376]. Moreover, this porosity level was seen to increase with increasing porogen ratios which was due to the higher levels of decomposed porogen within the molten glass particle [377]. Similar finding was reported by Dalai *et al.* for hollow amber glass microspheres using urea as porogen. They observed that that the number of pores increased when the percentage of urea increased from 0.3% to 2% [378]. The tapped density measurements provided evidence for increasing porosity that showed low tapped densities for size S with greater porogen ratios [379].

It was also observed that after spheroidising 200-355 µm particles, the microspheres obtained in the size range of 200-355 µm (XL size) were seen to be distorted (as not all were spherical) with a solid dense core having only surface porosity (see Figure 3.7). This could probably be attributed to the lack of gas diffusion capacity towards the centre of the higher size range molten glass particles. Bortot *et al.* studied the influence of contact time in the flame with particle size and the position were the particle entered the flame during glass spheroidization [307]. They reported that the large particles with greater mass, travelled at smaller trajectories in the flame and the heat exchange kinetics did not allow the particle to reach a temperature higher than the value of glass transition temperature. However, for small particles the effect was vice versa [307].

The morphological changes due to differences in porosity level can also be correlated with the variation of density (tapped and apparent) measurements [380]. The higher tapped density provided evidence for dense core with only surface porosity for size XL microspheres. Additionally, the 120-150 µm (size M) range microspheres showed an increase in tapped density compared to 200-300 µm (size L) range microspheres (see Figure 3.9). This was also suggested to be due to the microspheres having enough contact residence time in the flame to get expanded and to produce more pores within the microspheres [307, 379]. Small variation in apparent densities (see Figure 3.8) of microspheres was attributed to the presence of closed pores present within the microspheres [381]. During density measurement via helium gas pycnometry the interconnected open pores usually allowed the flow of helium gas through these pores to measure the pore volume, whereas if a number of closed pores existed within the porous microspheres restricted the flow of helium gas intrusion would result in a slight decrease in apparent density (2.5 g/cm$^3$) compared to actual density (2.6 g/cm$^3$). In addition,

the presence of some clogged porogen may also result in increase in apparent densities [382]. Semel *et al.* reported that the presence of closed porosity resulted change in apparent density for porous materials [383]. They illustrated that the closed porosity increased the density value of 6.4 g $cm^3$ (2.5% closed pores) to 7.2 g $cm^3$ (7% closed pores) for porous materials [383]. From mercury intrusion analysis the porosity for 3S, 3M and 3L was 70%, 66% and 68%, respectively, though the respective calculated porosity values were found to be 75%, 60%, 75% for 3S, 3M and 3L samples, respectively. The differences observed were suggested to be due to the presence of a number of closed pores within the microspheres.

The BET surface area analysis (using Kr gas) showed that the highest surface area (0.54 $m^2/g$) was obtained for 125-150 µm (size S) microspheres compared to other microspheres (see Figure 3.10), which was attributed to the increasing porosity level as observed via mercury intrusion analysis [378]. From the mercury intrusion analysis, the porosity of S size microspheres with high porogen ratio was found to be 69.92 %. A study showed by Yu *et al.* that the surface area of their hollow microspheres was 15.3 $m^2/g$ with 16.6 % porosity. However, under identical conditions in the absence of stabilising agent gave a surface area of 0.3 $m^2/g$ with only 0.001 % porosity [384]. Additionally, 150-200 µm (size M) gave 65.93% porosity where 200-355 µm (size L) size particles provided 68.12% porosity using same glass particle to porogen ratios as seen from Figure 3.12. This provided evidence that the surface area of size M were low surface area compared to the size L. By contrast, the smaller the particle size of an adsorbent, the greater the surface area [385]. Overall, the changes in porosity of the microspheres depend on two folds; one is the retention time in the flame spheroidisation zone [307] and the other one is the extent of porogen attachment on the surface of the glass particles which effected the porosity of the microspheres [376].

The batch dye adsorption (Acid red 88 dye) studies revealed that porous glass microspheres of 125-150 µm (labelled as S) were able to achieve 87% dye removal compared to same size glass particles which showed only 37% dye removal (see Figure 3.14). The dye adsorption capacity for glass particles could be attributed to the electrostatic interaction between acid red 88, which is an anionic dye, and partially charged glass surface [386]. On the other hand, the increased adsorption capacity of porous glass microspheres may also be due to increase in surface area generated within porous microspheres. As porosity and surface area are one of the parameters describing the properties of adsorbent materials [387]. The same reason implies for the 200-355 µm (labelled L) microspheres which achieved less adsorption capacity compared to the 125-150 µm (labelled as S) microspheres. The effect of surface area was reported by Chae *et al.* for crystalline $Zn_4O$ (1, 3, 5-benzenetribenzoate)$_2$ metal organic framework (MOF) as an adsorbent for dyes. They reported that the surface area of MOF is

related to open porosity and pores of MOFs which facilitated the adsorption of large amount of organic molecules [388].

The adsorption capacity of porous microspheres in fixed bed was higher than in batch adsorption studies. Adsorption capacity of the batch process revealed 1.3 mg/g removal whereas in fixed bed adsorption it was 9 mg/g. This represents that porous phosphate glass microspheres have equal potential for fixed bed and batch adsorption applications [389].

In general, higher porogen ratios provided with more interconnected porosity, although the behaviour was different regarding microspheres resulted from larger glass particles. The porous microspheres with greater surface area gave better adsorption profile compared to microspheres with less surface area. Regarding, adsorption studies both batch and fixed bed adsorption studies was suitable for the applicability of our porous phosphate glass microspheres prepared.

## 3.4 Summary

The present chapter investigated flame-spheroidised porous phosphate-based microspheres for potential wastewater treatment application. The effect of using specific sized ranged glass particle and varying porogen ratio in tailoring the pores, surface area and porosity of the microspheres was demonstrated. The investigated 125-150 µm (labelled S), 150-200 µm (labelled M) and 200-355 µm (labelled L) microspheres showed increase in surface area with increased interconnected porosity which was obtained with increasing glass particles to porogen ratios. By contrast, 200-355 µm size (labelled XL) microspheres revealed a porous surface along with a dense solid core with absence of interconnected porosity. The highest surface area values were measured 0.54 $m^2/g$, 0.35 $m^2/g$ and 0.27 $m^2/g$ for 125-150 µm (labelled S) with 70 % porosity, 200-355 µm (labelled L) with 68 % porosity and 150-200 µm (labelled M) with 66 % porosity respectively for higher porogen ratio. The average pore diameter for these microspheres were found to be 5-45 µm obtained via mercury intrusion analysis. In batch dye adsorption experiment, porous glass microspheres of 125-150 (labelled as S) achieved highest dye removal (87% dye removal with 1.3 mg/g adsorption capacity) capacity compared to the microspheres of 200-355 µm (labelled L) (70% dye removal with 1.1 mg/g adsorption capacity) and glass 69 particles of size 125-150 µm (37% with only 0.58 mg/g adsorption capacity). On the other hand, in fixed bed studies, the 125-150 (labelled as S) microspheres achieved higher adsorption capacity compared to batch adsorption. As a proof of concept, FS porous microspheres were investigated for dye removal, and the findings demonstrated that FS might be employed as a possible manufacturing approach for developing porous materials for wastewater treatment applications.

# Chapter 4: Effect of Heat-Treatment on Porous Glass Microspheres and Subsequent Dye Removal studies

## 4.1 Introduction

Pervious chapter demonstrated the effect of using specific staring glass particle size and porogen ration on tailoring the surface area and porosity profiles of the microspheres produced. This chapter investigates the effect of using smaller size porogen followed by heat-treatment for producing porous phosphate based (PBG) microspheres. Heat-treatment was applied at different temperatures between (510°-540°C) and dye separation studies were explored using anionic Acid Red 88 (AR 88), utilising batch and column adsorption experimental processes. Furthermore, the interaction of the dye with the surface of porous microspheres produced was also explained.

## 4.2 Results

### 4.2.1 Scanning Electron Microscopy (SEM) analysis

SEM images (Figure 4.1a) shows the uniform distribution of porous microspheres produced (labelled as UW-P40) with round-shaped pores and an average surface pore diameter ranging from few micrometres to 20 (±5) µm. After a brief acid wash step to remove excess of remanent porogen after spheroidisation, a distribution of more open pore morphologies with larger macro pore sizes from 7 (±4) µm to 26 (±4) µm compared with UW-P40 microspheres were achieved (see Figure 4.1b). Furthermore, highly interconnected porosity can be seen from the cross-sectional SEM image of the porous P40 microspheres as shown in Figure 4.1c.

Figure 4.1 d to i show SEM images of the microspheres heat-treated at 510°C. Whilst the heat-treatment process initially appeared to have closed the pores, closer inspection showed that the pores and pore size had significantly been reduced (see Figure 4.1h). The cross-sectional SEM image of these heat-treated microspheres (shown in Figure 4.1 f and i) revealed that the internal interconnected porosity was still present and remained similar to the initial non-heat-treated P40 porous microspheres.

Figure 4.1 j to o show microspheres heat-treated at 520°C. These microspheres exhibited similar surface pores compared to the 510-P40 microspheres. The cross-sectional images of these 520-P40 microspheres (presented in Figure 4.1l) also showed a distribution of microspheres with internal porosities similar to the initial porous and 510 heat treated microspheres. Figure 4.1o shows densely connected pores with a much narrower range of pores for these heat-treated 520-P40 microspheres whereas the pores remained larger for the 510-P40 microspheres (see Figure 4.1i). The morphology

of heat-treated microspheres at 530 and 540°C is shown in Figure 4.2 (a-d). The SEM images show further heat-treatment creates agglomerates due to the fusion of the microspheres with one another.

**Unwashed** **Acid washed** **Cross-section**

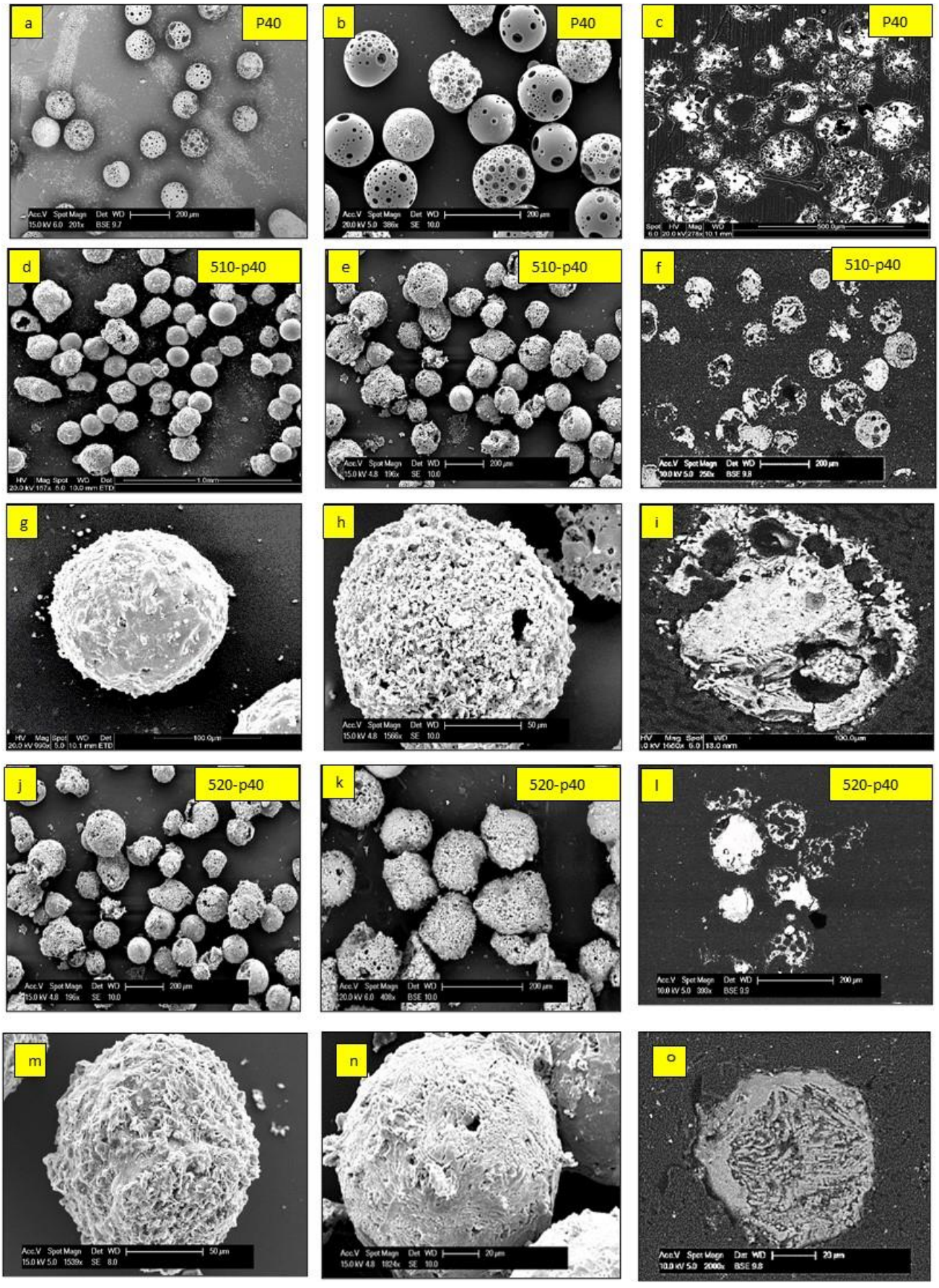


*Figure 4.1: Representative SEM images of heat-treated and untreated porous P40 microspheres: a) and b) shows the distribution and yield of unwashed and acid washed P40 microspheres respectively , c) cross-section of resin embedded washed porous P40 microspheres, d), g) and e), h) showing distribution and yield of heat-treated unwashed and acid washed 510-P40 microspheres at low ang high magnification respectively, j), m) and k), n) shows distribution of heat-treated unwashed and washed 520-P40 microspheres at low ang high magnification respectively, f), i) and l), o) shows cross-section of porous washed 510-P40 and 520-P40 microspheres at low ang high magnification respectively.*

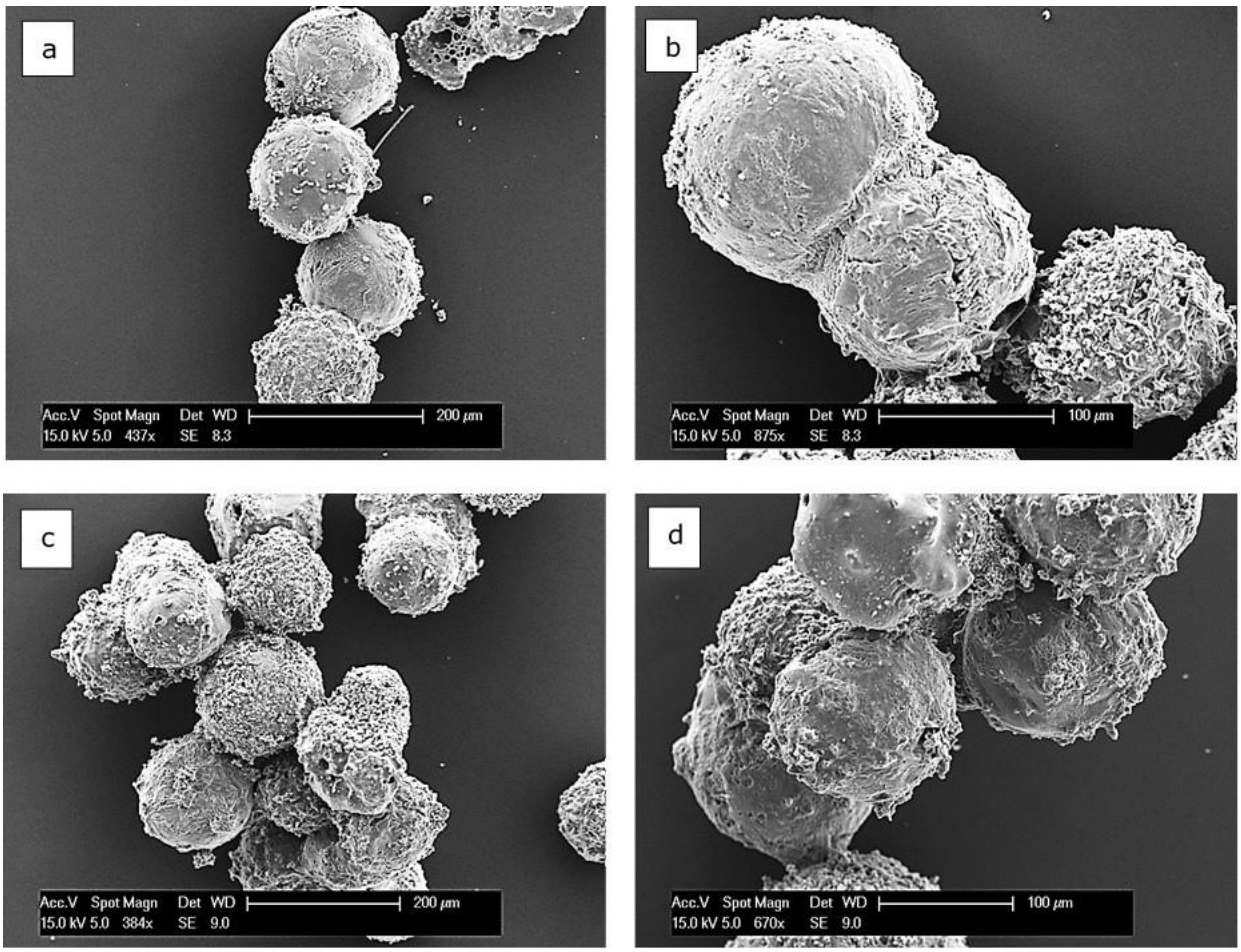



*Figure 4.2: (a and b) SEM images of P40 microspheres heat-treated at 530℃ and (c and d) SEM images of P40 microspheres heat-treated at 540℃.*

### 4.2.2 Surface area, pore size and pore volume analysis

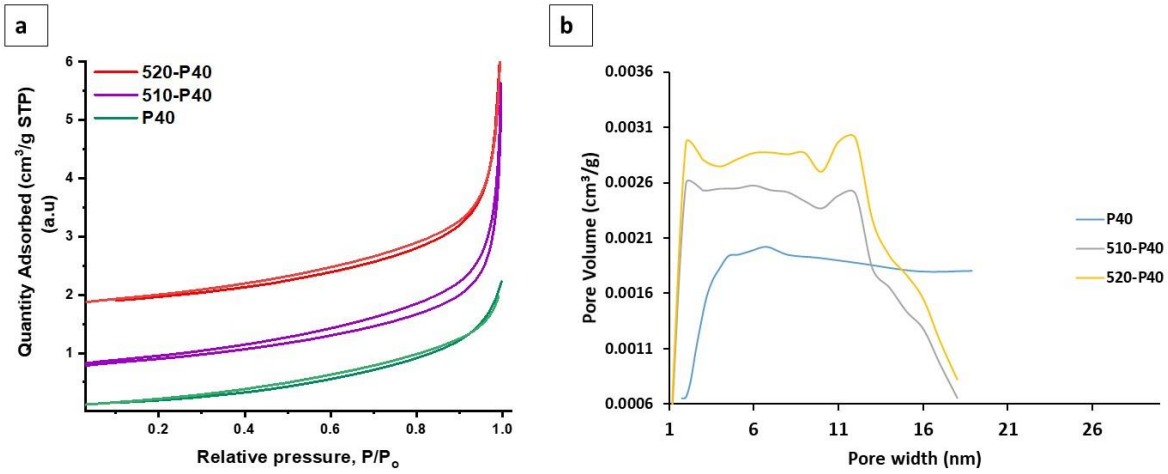



***Figure 4.3: Nitrogen adsorption-desorption Isotherm of a) P40, 510-P40, and 520-P40 microspheres and b) a comparison of pore size and pore volume analysis for P40 and heat-treated 510-P40 and 520-P40 porous microspheres.***

***Table 4.1: Specific surface area and pore volume of the porous microspheres prepared.***

| Sample | BET Specific surface area, ($m^2/g$) | Langmuir Surface Area ($m^2/g$) | Pore volume ($cm^3/g$) |
|---|---|---|---|
| **P40** | 0.50 | 2.96 | 0.0017 |
| **510-P40** | 1.05 | 3.72 | 0.0022 |
| **520-P40** | 1.23 | 4.36 | 0.0035 |

The surface area, pore size distribution and pore volume of the microspheres were analysed using nitrogen adsorption–desorption isotherms (BET). The porous P40 microspheres followed Type lll isotherm typical for macroporous materials (via the IUPAC classification) [390], as seen in Figure 4.3a. Isotherms for heat-treated 510-P40 and 520-P40 microspheres, exhibited a H3 hysteresis loop with a type IV isotherm which is a typical adsorption profile for mesoporous materials associated with slit shaped pores [391, 392]. Figure 4.3(b) depicts the pore size distribution obtained from BJH analysis and illustrates that a broad range of mesopores (2-50nm) were present in the heat-treated samples. Only macropores (>50nm) were observed for the P40 microspheres. In particular, heat-treated 510-P40 and 520-P40 produced a mesopore size distribution below 19 nm. The surface area for the porous 510-P40 and 520-P40 microspheres were found to be higher (1.05 to 1.33 $m^2/g$) compared to the porous P40 microspheres which was 0.50 $m^2/g$. The heat-treatment process led to an increase in pore volume by 22.7 % (0.0022 ± 0.003 $cm^3/g$) and 51.4 % (0.0035 ± 0.003 $cm^3/g$) for 510-P40 and 520-P40 microspheres respectively in comparison with non-heat-treated P40 (see Table 4.1).

### 4.2.3 X-Ray Diffraction analysis

XRD profiles for the microspheres are shown in Figure 4.4. Before heat-treatment, P40 porous microspheres revealed to be of an amorphous nature. However, sharp crystalline peaks were seen in the XRD pattern for the UW-P40 microspheres at 2θ ≈ 29.4° and 37.3° which correspond to the crystal planes (104) and (200) of calcium carbonate (used as porogen, JCPDS # 01-072-1652) and calcium oxide (JCPDS # 01-074-1226) respectively [393]. The same diffraction pattern with weaker intensities were also seen for the heat-treated porous microspheres. These peaks became sharper for acid washed heat-treated porous microspheres. However, they also exhibited weak crystalline diffraction pattern extending from 19 to 34°, indicating a glass-ceramic nature of the microspheres due to the presence of crystalline peaks for the porous heat-treated microspheres. The peaks at diffraction angle 2θ of ~ 32 ° and 21° were suggested to be due to the presence of crystal planes (031) and (201) that represent alpha calcium pyrophosphate ($Ca_2P_2O_7$, JCPDS # 09-0345) and sodium pyrophosphate ($Na_4P_2O_7$, JCPDS # 010-0187) respectively [394]. The cumulative percentage crystallinity calculated for unwashed heat-treated microspheres were 57% and 51%, respectively for 510-P40 and 520-P40. Although, the percentage crystallinity decreased slightly after acid wash for 510-P40 (from 57% to 52%) and 520-P40 (from 51% to 46%).

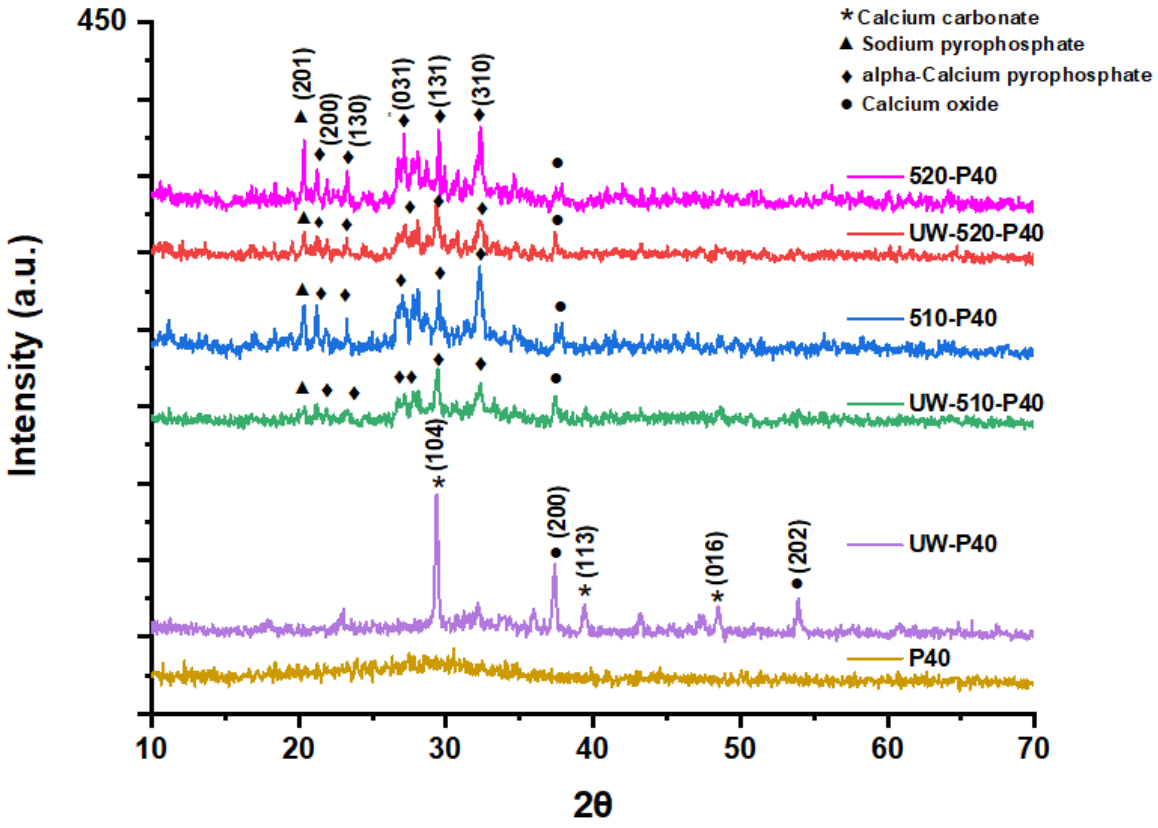



*Figure 4.4: XRD pattern for heat treated (before and after acid wash) and untreated P40 phosphate-based glass microspheres.*

### 4.2.4 Energy Dispersive X-Ray analysis

The composition of the porous microspheres and heat-treated porous microspheres were investigated via EDX analysis. Results showed (see Figure 4.5) that the composition of P40 porous microspheres revealed an increase in CaO content by 2-4 mol % in comparison with the expected composition. The heat-treated porous microspheres showed a decrease in $Na_2O$ content of (1-5 mol %) and an increase in CaO content (6-10 mol %). In either case, $P_2O_5$ showed approximately 1-2 mole% reduction with increase in $Na_2O$ and CaO compared to the expected values.

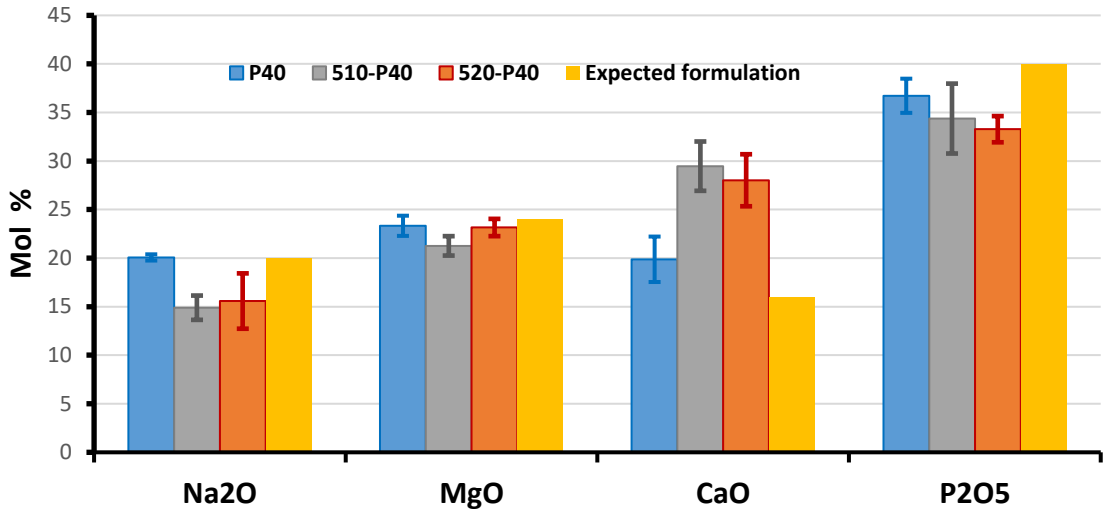



***Figure 4.5: Elemental compositional analysis of the porous microspheres produced as measured by EDX.***

## 4.2.5 Batch dye adsorption studies

### *4.2.5.1 Adsorption Isotherms studies*

The adsorption capacity and the interactive behaviour between dye and microspheres were investigated by conducting equilibrium batch adsorption experiments. Equilibrium isotherm studies were conducted using different initial concentrations of AR88 dye in distilled water (20–500 mg/L) at 25°C and without changing the pH of dye solution. The data was then fitted to the Langmuir, Freundlich and Temkin adsorption isotherm models [395]. Dye adsorption for the microspheres was poor at lower concentrations (below 100 mg/L). However, at higher concentrations (when the initial dye concentration was 300 mg/L) the maximum adsorption ($q_{eq}$) of the AR88 dye was 70 ± 4, 98 ± 4, 110 ± 2, and 120 ± 2 mg/g for P40, UW-P40, 510-P40 and 520-P40, respectively (see Figure 4.6). The theoretical adsorption capacities ($q_e$) were predicted using all three isotherm models (Langmuir, Freundlich, and Temkin) and the corresponding parameters along with the regression coefficients are listed in Table 4.2. According to Langmuir isotherm the surface of an adsorbent is homogeneous, assuming that there is no lateral interaction between adjacent adsorbed molecules. The maximum adsorption capacity based on Langmuir isotherm consists of a monolayer adsorption [396-398]. Freundlich adsorption isotherms are based on the assumption that adsorption is heterogeneous and multilayer [398, 399]. A favourable adsorption process from Freundlich isotherm can be deduced when the value of $1/n < 1$ [398, 399]. Temkin isotherm considers the effects of indirect adsorbate/adsorbate interactions on the adsorption process. As the adsorbent–adsorbate interaction increase, the heat of adsorption would decrease [396-398]. As observed in Table 4.2 that the experimental data fit was better with the Temkin isotherm as compared to the Freundlich with $R^2$>0.92 for all the microspheres tested and applicability follows the order; Temkin > Freundlich > Langmuir

adsorption model. The Temkin constant, bT, linked to the heat of adsorption for P40, UW-P40, 510-P40 and 520-P40 were 33.12 J/mol, 32.75 J/mol, 20.72 J/mol and 26.52 J/mol, respectively. From Freundlich isotherm parameter 1/n were found to be less than unity (0.3–0.9) indicating that the isotherms can be characterized as a favourable isotherm [400]. The Langmuir monolayer maximum adsorption capacities were 3 mg/g, 8 mg/g, 22 mg/g and 28 mg/g for, P40, UW-P40, 510-P40 and 520-P40 respectively.

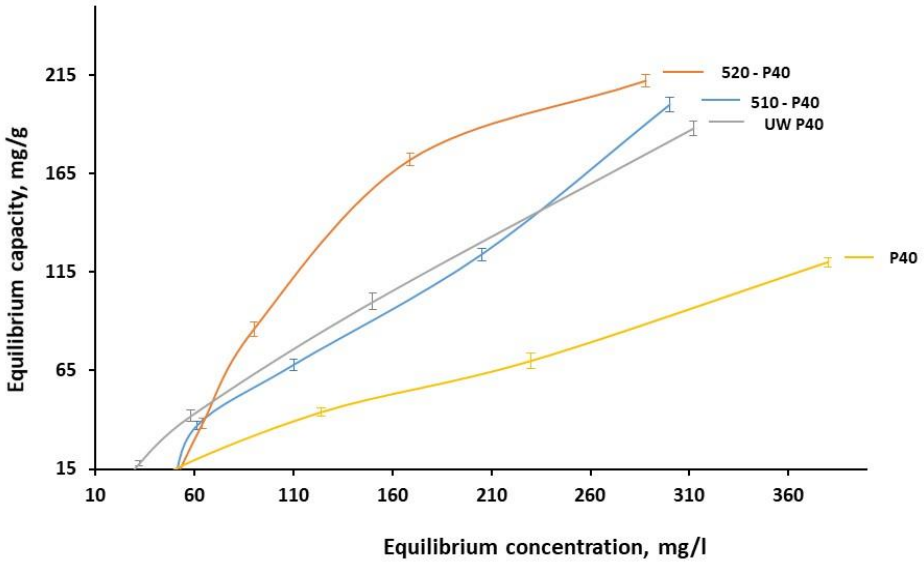



***Figure 4.6: Isotherm plots for adsorption of AR88 dye on P40 and heat-treated porous microspheres (the conditions of the isotherm adsorption experiment are as follows: microsphere dose 1 g/L, pH 7, temperature 22 ± 2 °C and stirring time 24 h).***

### 3.6.2 Adsorption kinetics studies

The effect of the initial AR88 concentration on the adsorption rate by washed and unwashed P40 and heat-treated microspheres is shown in Figure 4.7. The dye adsorption increased initially followed by a plateau towards equilibrium. For UW-P40 microspheres, the increase in initial dye concentration led to an increase in adsorption capacity. A similar trend was also observed for P40, 510-P40 and 520-P40 microspheres (see Figure 4.7). It was also observed that the adsorption capacity of UW-P40 microspheres were higher than the P40 microspheres alone. Pseudo 1$^{st}$ and 2$^{nd}$ order rate constants

*Table 4.2: Parameters of fitting the adsorption isotherm data using Langmuir, Freundlich, Temkin equations for P40, UW-P40, 510-P40 and 520-P40 (The conditions of the isotherm adsorption experiment are as follows: microsphere dose 1 g/L, pH 7, temperature 22 ± 2 ℃ and stirring time 24 hr).*

| | Langmuir Isotherm | | | | Freundlich Isotherm | | | | Temkin Isotherm | | | | |
|---|---|---|---|---|---|---|---|---|---|---|---|---|---|
| **Sample** | **$Q_m$ (mg/g)** | **$R^2$** | **$X^2$** | **$q_e$ (mg/g)** | **$K_f$ (ml/g)** | **1/n** | **$R^2$** | **$X^2$** | **$q_e$ (mg/g)** | **$A_T$ (L/g)** | ***$b_T$* (J/mol)** | **$R^2$** | **$X^2$** |
| **P40** | 3 | 0.97 | 0.58 | 84 | 0.50 | 0.90 | 0.973 | 0.61 | 83 | 0.01 | 33.12 | 0.97 | 0.44 |
| **UW- P40** | 8 | 0.94 | 0.37 | 178 | 1.05 | 0.91 | 0.932 | 0.20 | 90 | 0.01 | 32.75 | 0.95 | 0.20 |
| **510-P40** | 22 | 0.86 | 0.30 | 192 | 22.08 | 0.38 | 0.897 | 0.38 | 104 | 0.01 | 20.72 | 0.98 | 0.25 |
| **520-P40** | 28 | 0.84 | 0.39 | 230 | 22.19 | 0.41 | 0.854 | 0.52 | 125 | 0.01 | 26.52 | 0.92 | 0.33 |

*(The adsorption capacity $q_e$ based on Freundlich Isotherm and Temkin Isotherm models were calculated when initial concentration $C_0$= 450 mg/l)

and the calculated adsorption capacities $q_{ecal}$ were determined from the models presented in Table 4.3 along with the corresponding correlation coefficients. It was also observed that the adsorption capacity of the heat-treated 510-P40 and 520-P40 followed 1st order kinetics. However, the washed and unwashed P40 microspheres followed 2nd order kinetics. Although washed P40 microspheres followed a 1st order kinetics for higher concentrations (500 mg/L). For all types of microspheres, the calculated $q_e$ values agreed well with the experimental values and a regression coefficient of above 0.92 showed that the model is applicable applied for the entire adsorption process.

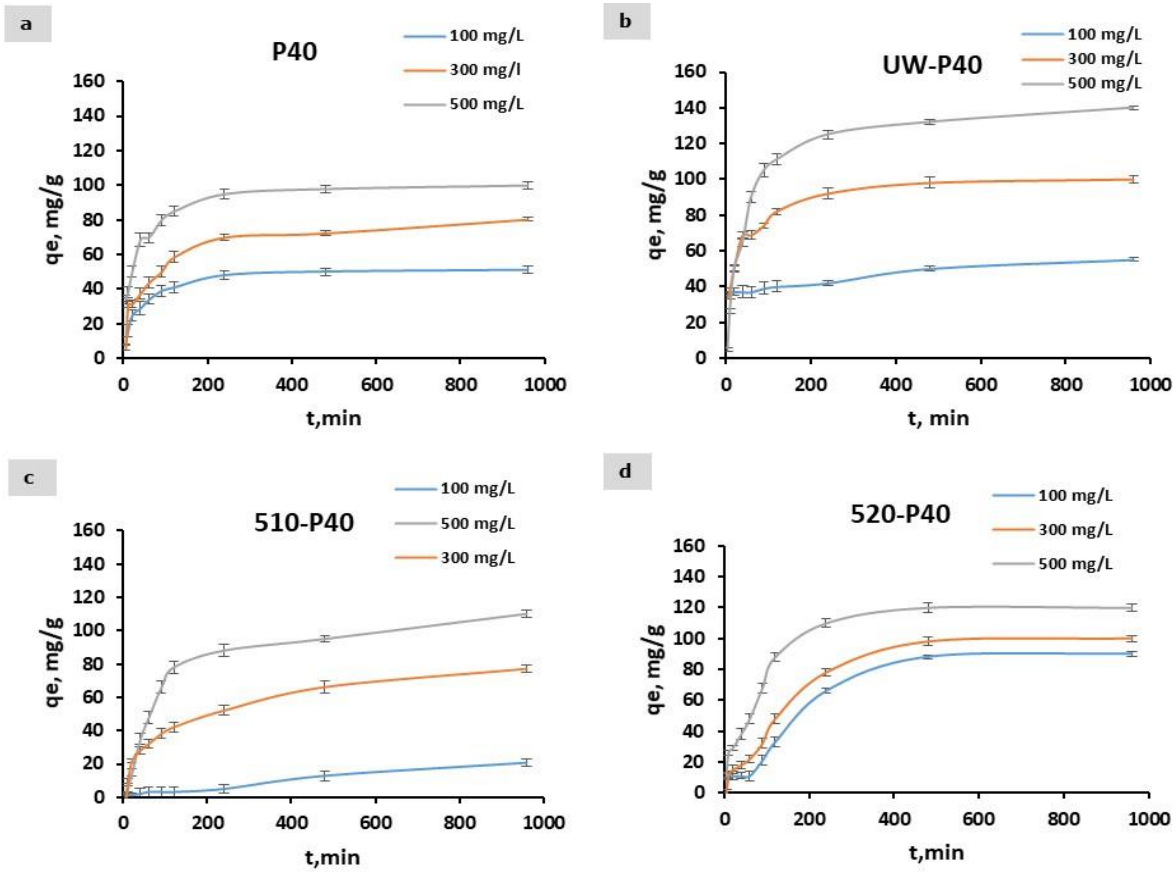



*Figure 4.7: Effect of dye concentration on adsorption in a) P40, b) UW-P40, c) 510-P40, and d) 520-P40 microspheres at the microsphere dose of 1g/L, pH 7 and temperature of 22 ± 2℃.*

*Table 4.3: Comparison of the pseudo-first-order, pseudo-second-order adsorption rate constants and calculated and experimental $q_e$ values obtained at different initial AR88 concentrations at the microsphere dose of 1g/L, pH 7 and temperature of 22 ± 2 ℃.*

| | | Pseudo 1st order | | | | | Pseudo 2nd order | | | | |
|---|---|---|---|---|---|---|---|---|---|---|---|
| **Sample with different dye concentrations** | | **$q_{e\ exp}$ (mg/g)** | **$q_{e\ cal}$ (mg/g)** | **$K_1$ ($min^{-1}$)** | **$R^2$** | **$X^2$** | **$q_{e\ exp}$ (mg/g)** | **$q_{e\ cal}$ (mg/g)** | **$K_2$ (g /mg /min)** | **$R^2$** | **$X^2$** |
| **UW-P40** | 100 mg/l | 50 | 27 | 0.022 | 0.807 | *0.51* | 50 | 52 | 0.0016 | 0.996 | *0.31* |
| | 250 mg/l | 81 | 65 | 0.009 | 0.916 | *0.21* | 81 | 85 | 0.0023 | 0.941 | *0.32* |
| | 450 mg/l | 118 | 207 | 0.013 | 0.903 | *0.01* | 118 | 115 | 0.002 | 0.872 | *0.6* |
| **P40** | 100 mg/l | 14 | 7 | 0.023 | 0.925 | *0.42* | 14 | 14 | 0.013 | 0.998 | 0.32 |
| | 250 mg/l | 42 | 67 | 0.034 | 0.904 | *0.53* | 42 | 43 | 0.001 | 0.998 | *0.33* |
| | 450 mg/l | *93* | *96* | 0.042 | *0.920* | 0.36 | 98 | 105 | 0.003 | 0.999 | *0.21* |
| **510-P40** | 100 mg/l | 21 | 21 | 0.016 | 0.951 | 0.0009 | 21 | 30 | 0.00005 | 0.446 | *0.32* |
| | 250 mg/l | 110 | 112 | 0.002 | 0.961 | 0.0004 | 110 | 131 | 0.00006 | 0.331 | *0.32* |
| | 450 mg/l | 77 | 70 | 0.003 | 0.926 | 0.0013 | 77 | 86 | 0.016 | 0.967 | *0.45* |
| **520-P40** | 100 mg/l | 32 | 33 | 0.001 | 0.952 | 0.000009 | 32 | 128 | 0.000002 | 0.017 | *0.44* |
| | 250 mg/l | 88 | 89 | 0.002 | 0.954 | 0.0009 | 88 | 136 | 0.000001 | 0.603 | *0.31* |
| | 450 mg/l | 176 | 174 | 0.002 | 0.982 | 0.027 | 176 | 217 | 0.000015 | 0.861 | *0.34* |

### 4.2.6 Fixed bed adsorption studies

The amount of dye adsorbed and equilibrium adsorption of AR88 into the microspheres are shown in Table 4.4. At both flow rates, an incomplete "S" shape of the breakthrough curve is obtained (see Figure 4.8). The adsorption capacity of the P40 and 510-P40 microspheres was also significantly lower in the column adsorption studies (see Table 4.4 and Figure 4.8) in comparison to batch studies (81±4 mg/g for P40 and 110±1.8 mg/g for 510-P40). Moreover, the heat-treated 520-P40 showed a slight discrepancy from the batch adsorption studies (120 ± 2.3 mg/g for batch adsorption studies and 138.4 ± 0.53 at flow rate 2.2 ml/min for column adsorption studies). However, the adsorption capacity of 520-P40 decreased to 83.5 ± 0.53 mg/g at 0.5 ml/min flow rate. Comparing the column adsorption performance of P40, 510-P40 and 520-P40 microspheres under the same flow rate conditions (2.2.ml/min or 0.5 ml/min) indicated better AR88 adsorption by 520-P40 microspheres with adsorption follows the order P40 < 510-P40 < 520-P40 (see Table 4.4).

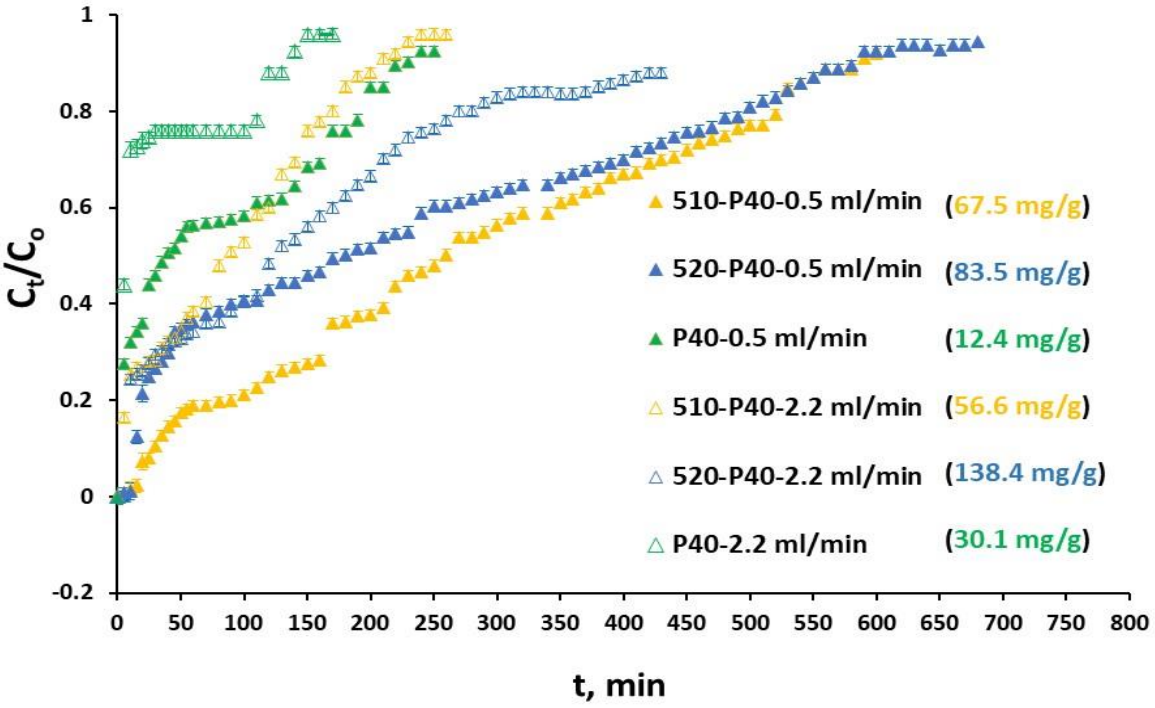



*Figure 4.8: Breakthrough curve of AR88 dye adsorption for P40, 510-P40 and 520-P40 microspheres at 2.2 ml/min and 0.5 ml/min flow rates with starting dye concentration of 300 mg/L, pH 7 and temperature at 22 ± 2 ℃.*

*Table 4.4: Total adsorption and equilibrium adsorption capacity of AR88 at different flow rates for P40 and heat-treated microspheres. (Starting dye concentration of 300 mg/L, pH 7 and temperature at 22 ± 2 °C)*

| Sample | Flow rate, (mL/min) | EBCT, min | $q_{tot}$, mg (±0.53) | $q_{eq}$, mg/g (±0.53) |
|---|---|---|---|---|
| **P40** | 2.2 | 1 | 50.3 | 30.1 |
| **P40** | 0.5 | 5 | 20.1 | 12.4 |
| **510-P40** | 2.2 | 1 | 93.9 | 56.6 |
| **510-P40** | 0.5 | 5 | 112.3 | 67.5 |
| **520-P40** | 2.2 | 1 | 260.1 | 138.4 |
| **520-P40** | 0.5 | 5 | 157.6 | 83.5 |

#### *4.2.6.1 Modelling of breakthrough curves*

The data obtained from the column adsorption studies was fitted using the Thomas model, Adams-Bohart model and Yoon-Nelson model to generate the breakthrough curve data [162]. The Thomas and Yoon-Nelson models provided more appropriate fits to the experimental data (Table 4.5) for heat-treated microspheres. The regression coefficients were above or equal to 0.85 for two of the different flow rates. Based on the Thomas model, the calculated adsorption capacities for 510-P40 microspheres were found to be 97 mg/g and 89 mg/g for flow rates 2.2 ml/min and 0.5 ml/min respectively. For the 520-P40 microspheres, the calculated adsorption capacities were 153 mg/g and 76 mg/g for flow rates 2.2 ml/min and 0.5 ml/min respectively. Other than 520-P40 microspheres at flow rate of 0.5 ml/min, all the microspheres showed slightly higher adsorption capacity than the experimental values (see Table 4.5). The values of $\tau_{cal}$ and $\tau_{exp}$ obtained from Yoon-Nelson model (where $\tau$ indicates the time required to reach 50% exhaustion of the entire column) decreased with increasing flow rate. The $\tau_{cal}$ values were modelled (regression value above ≥ 0.90) for the heat-treated microspheres with discrepancies (of approximately 8-15 %) from the calculated values.

*Table 4.5: Breakthrough curve models with their parameters. (At 2.2 ml/min and 0.5 ml/min flow rates with starting dye concentration of 300 mg/L at 22 ± 2 °C).*

| Experimental | | | Thomas model | | | Adams-Bohart model | | Yoon-Nelson model | | |
|---|---|---|---|---|---|---|---|---|---|---|
| **Sample** | **Flow Rate, mL/min** | **$q_{e\ exp}$, mg/g** | **$q_{th}$, mg/g** | **$K_{th}$ (mL/min/mg)** | **$R^2$** | **$K_{AB}$ (mL/min/mg)** | **$R^2$** | **$\tau_{cal}$ min** | **$\tau_{exp}$ min** | **$R^2$** |
| **P40** | 2.2 | 30 | 34 | 0.014 | 0.767 | 0.0018 | 0.312 | 30 | 75 | 0.767 |
| | 0.5 | 12 | 15 | 0.013 | 0.919 | 0.003 | 0.634 | 47 | 125 | 0.772 |
| **510-P40** | 2.2 | 67 | 97 | 0.008 | 0.968 | 0.005 | 0.727 | 87 | 115 | 0.968 |
| | 0.5 | 56 | 89 | 0.007 | 0.854 | 0.001 | 0.609 | 295 | 300 | 0.901 |
| **520-P40** | 2.2 | 138 | 153 | 0.018 | 0.969 | 0.002 | 0.628 | 128 | 140 | 0.950 |
| | 0.5 | 83 | 76 | 0.005 | 0.855 | 0.002 | 0.415 | 232 | 240 | 0.910 |

### 4.2.7 FTIR and SEM analysis of microspheres after adsorption

SEM images of the microspheres tested post dye adsorption are shown in Figure 4.9(a). FTIR analysis of P40, 510-P40, and 520-P40 before and after adsorption are represented in Figure 4.9(b). The microspheres (only) showed common peaks at 721 $cm^{-1}$ (stretching vibration $P_2O_7^{4-}$), 890 $cm^{-1}$ (asymmetric stretching of $P_3O_9^{2-}$), 1096 $cm^{-1}$ ($PO_3^{2-}$ asymmetric stretching), 1205 $cm^{-1}$ ($PO_2^-$ asymmetric stretching), and 1399 $cm^{-1}$ (bending vibrations of $CO_3^{2-}$) characteristic for phosphate glasses [401-403]. Conversely, after the AR88 dye adsorption experiments the peaks associated with asymmetrically substituted -N=N- at 1475 $cm^{-1}$ and bands assigned to S=O groups at 1146 $cm^{-1}$ were observed, which were characteristic peaks for AR88 [404, 405]. Furthermore, the peak at 793 $cm^{-1}$

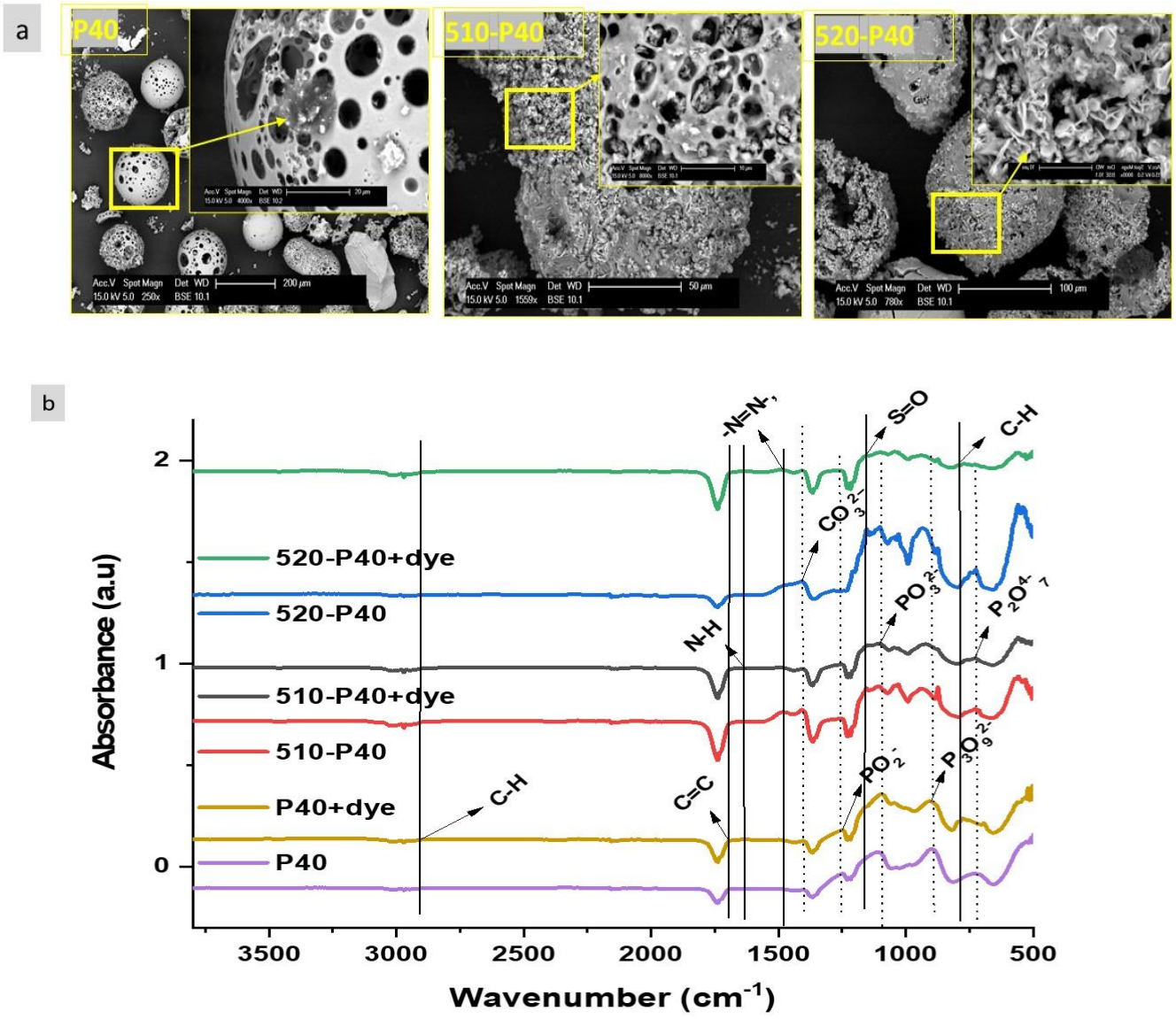



*Figure 4.9: Figure showing a) SEM images after dye adsorption and b) FTIR spectra (before and after dye adsorption).*

and 2900 $cm^{-1}$ associated with aromatic C-H bending vibrations and C-H asymmetric stretching vibrations (from dye AR88), respectively were also observed only after the adsorption experiment [404-406]. An intense band at 1630 $cm^{-1}$ was also identified which was associated to the aromatic skeletal stretching (C=C) [407]. Besides, the intensities of adsorption bands associated with stretching vibration of $P_3O_9^{2-}$ and $PO_3^{2-}$ for the heat-treated microspheres after dye adsorption, were seen to have decreased. For P40 microspheres adsorption band for $PO_3^{2-}$ only showed decrease in intensity after adsorption. These observations suggested that some of the AR88 dye remained on the surface of P40 microspheres, whilst for 510-P40 and 520-P40 microspheres which exhibited a rougher surface with smaller pores, the dye may also have blocked some of their pores (see Figure 4.9a).

## 4.3 Discussion

Chapter 3 demonstrated that microspheres produced using porogen sizes of between 45 – 63 µm possessed large surface pores from 5-45 µm with highly interconnected porosities. In this chapter, we utilised significantly smaller sized porogen material (i.e., below 5 µm) which resulted in porous glass microspheres with much smaller pore sizes ranging from between 7 (±4) to 26 (±4) µm. This significant reduction in pore size was associated with the size of porogen itself as reported by Hossain *et al*. [309]. The heat-treatment process caused further changes resulting in even further decreased pore sizes and changes in internal porosity, as observed in the SEM images (see Figure 4.1). This result showed that the pore sizes obtained could be tailored via careful selection of the porogen powder used and via subsequent heat-treatment processes.

### 4.3.1 Influence of smaller size porogen (≤5 µm) and heat-treatment

The surface pores of the heat-treated 510-P40 and 520-P40 microsphere were significantly smaller than the starting porous P40 glass microsphere pores. During the spheroidisation process, glass particles reach a temperature at which the viscosity of glass becomes sufficiently low to allow $CO_2$ gas formed during decomposition of the porogen to escape from the molten particle. Then as the particles are ejected out of the flame, this results in surface tension induced particle sphericity and thus porous microspheres with a size range 125-200 µm are formed [309]. The initial glass particle size was between 63-125 µm while the final microsphere size achieved was between 125-200 µm. This has been attributed to the interaction of molten particles colliding together and how much porogen they come into in contact with [309].

Heat-treatment of UW-P40 microspheres (see Figure 4.1) at 510°C and 520°C (i.e. above their $T_g$, 432 ± 1°C) [258]) for 3 hours resulted in the pores becoming smaller and narrower which would have also trapped any residual porogen inside the microsphere pores (see Figure 4.1 g and Figure 4.1m). During

the acid wash step, the enclosed/entrapped porogen was anticipated to dissolve and wash away leading to opening of the pores. Figure 4.10 highlights a schematic representation of the proposed underlying mechanisms to produce heat-treated open pore microspheres. Heat-treating the microspheres with 10°C increase at 520°C led to further increases in shrinkage kinetics of the pores resulting ultimately in much smaller surface pores [408].

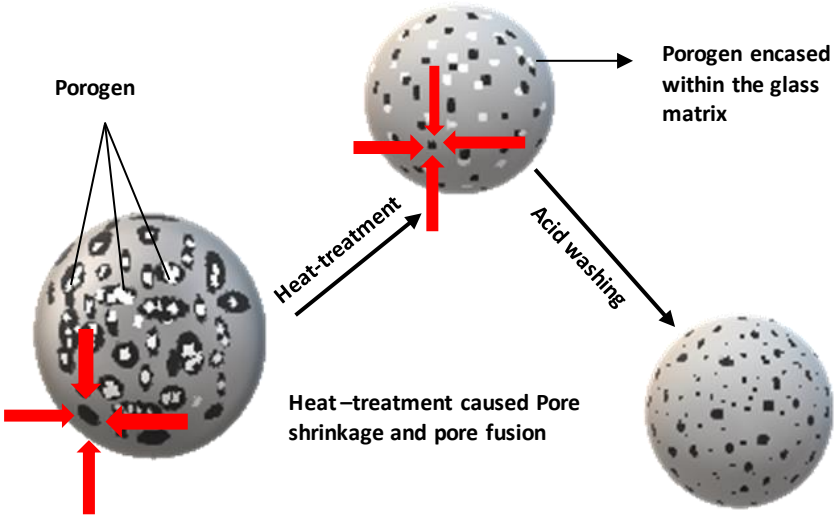



***Figure 4.10: Schematic representation of the proposed mechanism for changing the textural property of the heat-treated glass porous microspheres during the heat-treatment process.***

The surface area of the P40 glass microspheres was recorded as 0.49 $m^2/g$ whereas the surface area of heat treated 510-P40 and 520-P40 were 1.05 $m^2/g$ and 1.33 $m^2/g$, respectively. The heat-treatment process revealed a 22.7 % and 51.4 % increase in pore volume compared to the non-heat-treated P40 microspheres (see Figure 4.3). This increase in surface area and pore volume was probably assisted due to a heat induced densification process [409]. As a result of the heat treatment, the open spaces (i.e. pores) in UW-P40 microspheres started to shrink due to material (glass matrix) flow driven by heat energy. Accumulation of glassy material at pores caused pore narrowing and this was supported with the pore size distribution analysis revealing a shift from macropore to mesopores (See Figure 4.3 b) in the heat-treated microspheres. Similar observations were reported by Conzone *et al.* for heat-treated Dysprosium lithium-borate glass microspheres where they observed pore shrinkage with increasing temperature [410].

It was also observed that increasing the heat-treatment temperature led to an increase in the crystallinity of the glass microspheres. XRD results showed that the starting porous P40 microspheres were amorphous. The heat-treatment temperatures were chosen to be between the glass transition temperature and the onset of crystallisation temperature to minimise glass crystallisation tendency

of the microspheres [411]. Following heat treatment of the P40 microspheres, formation of crystals within an amorphous matrix was observed from XRD analysis. The presence of the crystal planes (104) and (200) observed represented calcium carbonate and calcium oxide respectively, which was probably due to residual porogen material. The same peaks were also observed for unwashed porous P40 microspheres. However, the major crystalline peaks located at 32° and 21° 2θ referred to the presence of calcium pyrophosphate and sodium pyrophosphate respectively. The presence of crystalline peaks, suggesting the formation of a glass-ceramic structure [412]. It is suggested that presence of the porogen during heat-treatment may have induced a partial transformation of the porogen used (calcium carbonate) into a crystalline calcium pyrophosphate ($Ca_2P_2O_7$) phase. Moreover, as the microspheres were heat-treated above $T_g$ there was possible chance of crystallisation. Heat-treating P40 microspheres without porogen could be explored further to fully understand the crystallisation behaviour of P40. Combes *et al*. reported presence of crystalline pyrophosphate phases from mixing calcium carbonate and calcium phosphate cement while investigating phosphates for bone reconstruction [413].

The compositional analysis for porous P40 microspheres showed slight increases in mole% (2-4%) of calcium content. Hossain *et al.* suggested this was due to the presence of Ca-based porogen remaining after the flame-spheroidisation process [309]. However, an increase (6-10 mole %) mole% of CaO was observed for the heat-treated microspheres. This increased amount may be attributed to the excess porogen fused onto the glass matrix due to the heat-treatment process which led to partially transformed calcium pyrophosphate ($Ca_2P_2O_7$).

### 4.3.2 Dye removal study of heat-treated microspheres in batch process

The effect of heat-treatment also resulted in significant differences in the adsorption studies. In the batch adsorption process the adsorption property of heat-treated and non-heat treated porous P40 microspheres were studied. The results showed improved adsorption capacities (83 mg/g to 125 mg/g based on Temkin isotherm) of the heat-treated microspheres compared to non-heat-treated microspheres. This improved adsorption capacity could be ascribed to several factors such as increased surface area, open and interconnected porosities, surface charge, presence of porogen and presence of crystalline phases. As reported in the literature, increased surface area has also been attributed to increased adsorption capacities [414]. The surface area for heat-treated microspheres was higher than the initial porous P40 microspheres. Results also demonstrated presence of mesopores in the heat-treated microspheres which have been reported to lead to enhanced absorbability [415, 416]. The adsorption property of P40 microspheres could also be attributed to the electrostatic interaction between the dye molecule (negatively charged) and the partially charged

glass microspheres [386]. The UW-P40 microspheres showed significantly higher adsorption capacity than washed P40 microspheres (as shown in Table 4.2). This was attributed to the UW-P40 microspheres containing remnant amounts of the porogen used (as observed from XRD, EDX and density analysis). Calcium carbonate itself can act as an adsorbent, as demonstrated in several studies investigating anionic dyes [417, 418]. Studies have also demonstrated that calcium pyrophosphate ($Ca_2P_2O_7$) revealed an enhancement in dye removing capabilities [419]. The partial transformation into alpha calcium phosphate ($Ca_2P_2O_7$) after heat-treatment may also be considered for the improved dye adsorption capacities for the heat-treated microspheres.

The kinetic studies suggested that the heat-treated microspheres followed a pseudo 1$^{st}$ order model, which which describe dye adsorption occurring through mass transfer or physisorption (physical adsorption) process [366]. Physisorption process relies on the assumption that the initial concentration of adsorbate (dye) is higher compared to sites available for adsorption on the adsorbent [366]. The driving force for mass transfer of the dye could be referred to higher initial dye concentration that would overcome the surface resistance allowing dye diffusion into the microsphere pores [369]. In addition, heat-treatment induced pore narrowing in 520-P40 and 510-40 microspheres that would allow capillary forces to draw in fluids thereby promoting dye molecule diffusion. Kinetic studies for the UW-P40 and washed P40 microspheres (dye concentrations up to 300 mg/L) speculate that were fitted with Pseudo 2$^{nd}$ order kinetics suggesting that chemical interactions took place [420]. This may be correlated with dye-porogen interaction as well as with the suggested dye–microsphere electrostatic interaction. However, further higher concentrations (500 mg/L) were fitted with Pseudo 1$^{st}$ order model. Through it must be noted that the adsorption mechanism for the washed and unwashed P40 microspheres is not fully understood yet considering their low surface areas profiles.
Overall, surface charge determination of the microspheres is important to understand the entire dye adsorption mechanism. In such regard, isoelectrical point measurement could be considered. However, investigation of surface charge properties of the porous microspheres is difficult considering the large size of the particles (125-200 µm).

### 4.3.3 Dye removal study of heat-treated microspheres in column setup

Column dye adsorption tests were also conducted which are a dynamic process representing industrial and point-of-use applications [421]. It was observed that non-heat treated P40 microspheres showed poor adsorption capacity (30 mg/g at flow rate 2.2 ml/min) in column adsorption experiments. Whereas the heat-treated microspheres showed improved dye adsorption capacity and overall column experiment performance. The highest dye adsorption capacity was found to be 153 mg/g at a

flow rate of 2.2 ml/min for the 520-P40 microspheres. The maximum adsorption capacity ($q_e$) of the microspheres using the column process increased with increasing flow rate indicating that the mass transport resistance decreased. The values obtained from the Thomas constant ($K_{th}$) model were similar to published studies where the $K_{th}$ value decreased with decreasing flow rates [422]. This may account for the packing process of the microspheres in the column. At higher flow rates, the microspheres would be more packed and in contact with each other which would act as a multi-pass system due to their interconnected porosity (see proposed mechanism highlighted in Figure 4.11). The higher flow rates not only favoured creating channels inside the column but also reduced the interparticle space between the microspheres. It has also been reported that mass transfer/diffusion through inter- pore (inside microspheres) was achievable when the microspheres were more closely packed together [423]. However, the pore diameters for the porous P40 microspheres were larger, which would have allowed the dye molecules to enter and perhaps escape more easily. As such, the time required to achieve equilibrium was not sufficient for dye adsorption.

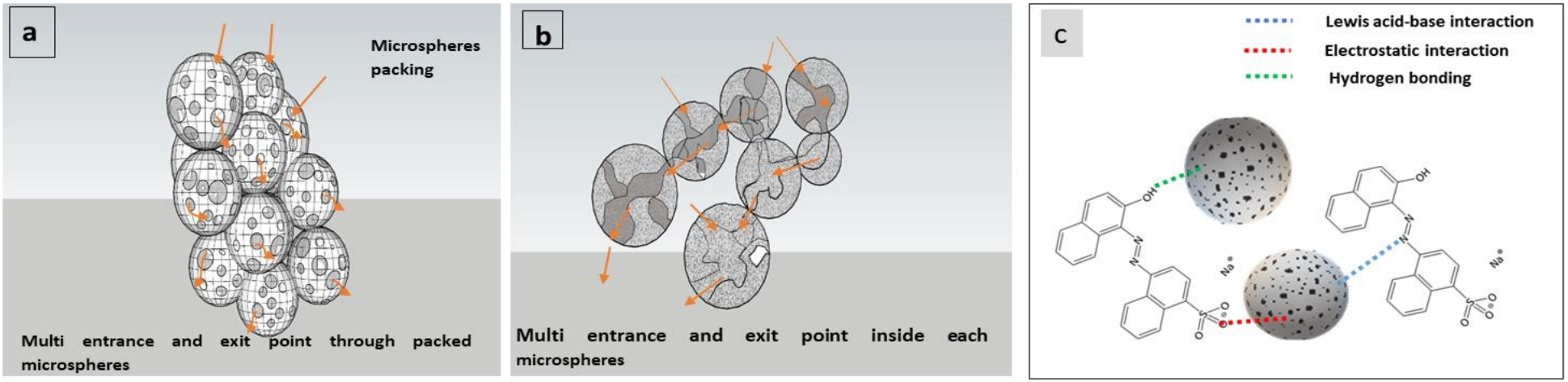



*Figure 4.11: Schematic diagram showing a) packing of the microsphere, b) dye diffusion inside multichannel created by interconnected porosity in column adsorption and c) Possible interactions of AR88 dye with different sites on the surface of microspheres. The arrows show flow direction.*

### 4.3.4 Factors influencing dye interaction and high adsorption efficacy of heat-treated microspheres

The values of dye adsorption capacity achieved from batch adsorption studies were consistent with the column adsorption tests. This was suggested to be due to the unique geometry and microstructure of the microspheres produced, which provided sufficient residence time for the dye molecules to diffuse into their structure. Inside the porous microspheres the dye molecules have to find their way out using the internal interconnected porosity which offered sufficient contact time between adsorbent (microspheres) and the adsorbate (dye molecule). The SEM images (see in Figure 4.9) show that the microspheres present a well-developed porous structure and thus could be used for uptake of dye molecules either through a physical mechanism via diffusion, and/or a chemical mechanism via bonding at the active sites located within the pores of the microspheres. FTIR analysis suggested a variety of the functional groups on 520-P40, 510-P40 and P40 microspheres that would act as binding sites for potential attachment of AR88 dye molecules. The existence of dye molecule was confirmed by the presence of characteristic bands of AR88 dye. The dye molecules could be adsorbed by the outer exposed pores via electrostatic interaction (see Figure 4.9) as no shift in adsorption bands were observed after dye adsorption [405]. The decrease in intensities of stretching vibration of $P_3O_9^{2-}$ and $PO_3^{2-}$ in all the heat-treated microspheres could be attributed to hydrogen bonding and/or Lewis acid-base interaction between the $Ca^{2+}$(from porogen and calcium based crystalline phases) and basic components (N=N, and OH groups) of AR88 dye which may have occurred on their surface (see proposed mechanism highlighted in Figure 4.11) [405]. Based on these results it is suggested that adsorption of AR88 onto microspheres depends on both their unique morphology and surface chemical properties of the microspheres.

Although higher surface area is one of the important parameters for an adsorbent, studies have reported that adsorption efficiency of an adsorbent is not only predominated by its surface area but also other factors such as surface chemistry and morphological features [424-427]. Yan *et al.* studied successful adsorption of acid dyes by cetyltrimethyl ammonium bromide (CTMAB) modified organo-bentonite which had a surface area of 4.4 $m^2/g$ [428]. Deng *et al.* reported removal of methylene blue dye using sulphuric acid treated cotton stalk (SCS) and phosphoric acid treated cotton stalk (PCS) with surface areas of 2.8 and 7.2 $m^2/g$ respectively [429]. Ehrampoush *et al.* reported adsorption of reactive red 123 using eggshell featuring surface area of 1.2 $m^2/g$ [430]. The surface area of these reported adsorbents were very low compared to higher surface area materials such as activated carbon or MOFs [431, 432]. All these studies reported that surface functionality and pore morphology played a dominant role for adsorption other than surface area.

In summary, this chapter demonstrated that simple use of smaller porogen materials and subsequent heat-treatment processes could be employed to control the pore sizes. Based on these findings, it is suggested that porous glass microspheres with similar unique morphology could be utilised as potential adsorbents for dye removal from water.

## 4.4. Summary

This study highlighted the manufacture of a single-step flame spheroidised process for producing porous glass microspheres and their non-heat-treated and post heat-treated effects. The heat-treatment led to significant increase in the surface area (from 0.49 to 1.33 $m^2/g$) and decrease in the pore sizes (from 55 ± 8 µm to ≤19 nm). The heat-treated microspheres showed the highest dye adsorption capacity (125 mg/g) in comparison with the non-heat treated P40 microspheres (83 mg/g). Kinetic studies highlighted that the dye adsorption of heat-treated microspheres followed physisorption (physical adsorption) process by fitting pseudo $1^{st}$ order kinetic models. Furthermore, the column adsorption capacity measured for the 520-P40 microspheres were found to be higher than 510-P40 and P40 microspheres which were 138 mg/g for 520-P40 and 67 mg/g and 30 mg/g for 510-P40 and P40 microspheres, respectively. This enhanced column adsorption capacity was attributed to the unique geometry (large and small pore) and interconnected microstructure of heat-treated microspheres that provided sufficient residence time for the dye molecules to diffuse into their structure. Electrostatic interaction, hydrogen bonding and Lewis acid-base interaction were determined as the possible mechanisms of adsorption of AR88 onto porous microspheres.

# Chapter 5: Developing porous microspheres from recycled glass

## 5.1 Introduction

The previous chapter demonstrated the manufacturing of porous non-heat-treated and heat-treated microspheres from phosphate glasses with the potential of removing dyes from water. In this chapter recycled glasses (RG) were used to develop porous recycled glass microspheres (PRGMs) since they could be regarded as a low-cost, sustainable waste material resource compared to phosphate glasses (which were initially used to explore proof-of-concept for dye separation). This chapter demonstrated that RG have higher viscosity profiles and melt temperatures therefore it was difficult to process them into PRGMs via our conventional processing route (as outlined in, section 5.4). As a result, this research developed a revised methodology, and the process was termed as the 'granular method'. The structural, morphological, surface area and porosity profiles of PRGMs were influenced by changing manufacturing parameters such as particle milling time and speed, alongside varying porogen ratios. The PRGMs manufactured were then tested for dye separation studies using anionic Acid red 88 (AR88) dye and cationic Methylene blue (MB) dye. Furthermore, the regeneration process and potential of reusing PRGMs were also demonstrated.

## 5.2 Structural and Compositional analysis of starting recycled glass particles

SEM images of irregular shaped as received recycled glass (RG) particles (≤ 63 µm) are presented in Figure 5.1a. An X-ray diffraction pattern of the starting RG materials (see inset Figure) revealed a single broad halo shaped peak between 15° to 39° of the diffraction angles. The absence of any sharp crystalline peaks suggested the amorphous nature of RG. EDX spectra indicated that RG were

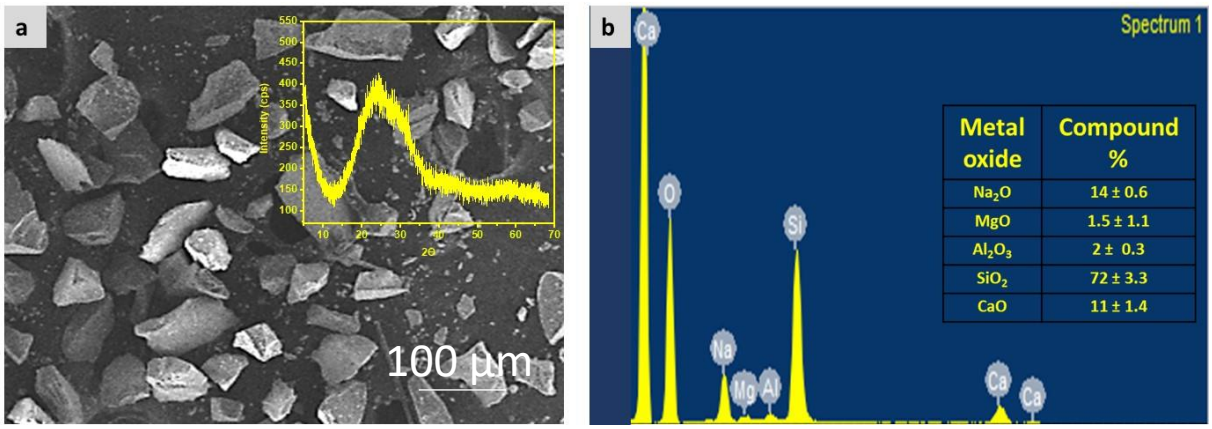



*Figure 5.1: a) SEM image with inset showing XRD pattern & b) EDX spectrum of recycled glass (RG) as received (particle size ≤63 um).*

composed of Si, Na, Ca, Al and Mg with oxide weight percentages of approximately 72%, 14%, 11%, 2% and 1.5%, respectively (see Figure 5.1b).

## 5.3 Processing of RG materials into Solid microspheres

The SEM image and XRD profile of solid recycled glass microspheres (SRGM) prepared via flame spheroidisation process are presented in Figure 5.2. The morphologies of the SRGM revealed mostly spherical morphology with a few non-spheroidised particles with a size range between 34 (±10) µm and 90 (±10) µm (see Figure 5.2a). XRD analysis did not detect any sharp crystalline peak for SRGM which confirmed the amorphous nature of SRGM (see Figure 5.2b). A single broad halo shaped peak was observed for SRGM which was similar to the XRD profiles of un-spheroidised starting RG.

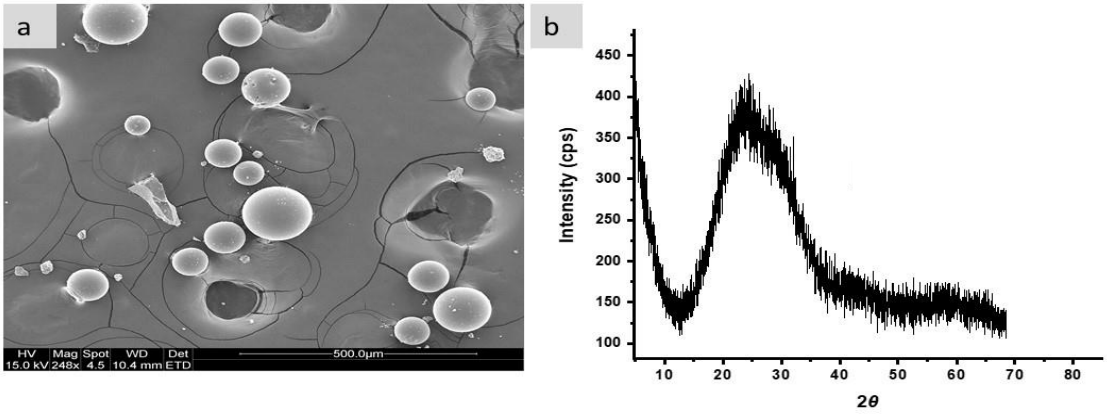



***Figure 5.2: a) Representative SEM image and b) X-ray diffraction of solid recycled glass microspheres (SRGM) obtained via flame spheroidisation.***

## 5.4 Porous recycled glass microsphere manufacture using a 'conventional process'

Initial trials to manufacture PRGMs were explored via the conventional flame spheroidisation processing route using varying porogen ratios i.e., particle to porogen ($CaCO_3$) ratio (2:1, 1:1 and 1:3), utilizing a smaller size (≤5 µm) and larger size (≤ 63 µm) porogen particles and gas flow rate ratio (3:3). Using the conventional method, the mixture of RG and porogen were introduced into the flame directly and the outcomes are presented in Figure 5.3 (a-f). However, as can be seen, these trials were unsuccessful in terms of producing any PRGMs. It was apparent that the conventional spheroidisation process was not suitable for manufacturing PRGMs although phosphate-based glasses were spheroidised into porous microspheres using the same conventional processing. In order to explore the melt behaviour of RG, the particles were investigated via thermal analysis, ash fusion tests and viscosity profile analysis and compared with phosphate glass particles (P40).

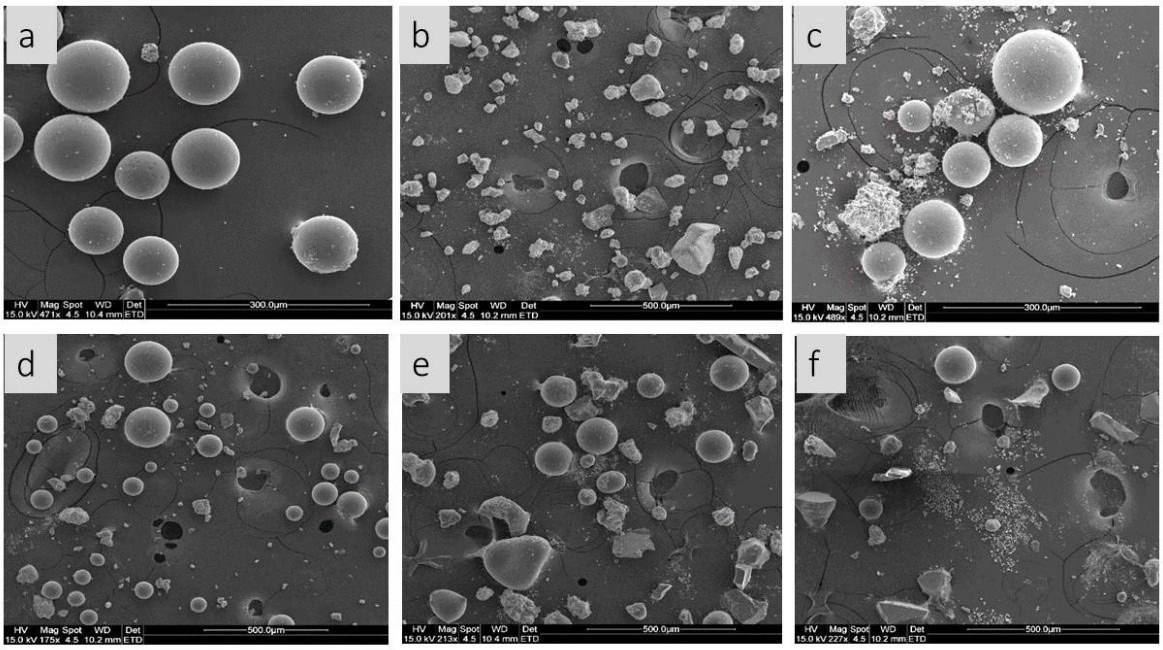



*Figure 5.3: Initial attempts to prepare PRGMs using conventional process a) 2:1, b) 1:1 and c) 1:3 porogen ratio using below 5µm porogen and d) 1:0.5, e) 1:1 and f) 1:3 porogen ratio using below 63 µm porogen.*

## 5.5 Structural characterisation of RG particles

### 5.5.1 Thermal analysis of RG

The RG utilised was composed of a mixture of different coloured glasses. The glass particles were separated into brown, green and transparent glasses and coded as brown, green, and white glass. DSC profiles for the separate-coloured glasses, bulk RG (mixture of brown, green and white glasses) and compared to the successful P40 glasses (explored in Chapter 3) are shown in Figure 5.4. The glass transition temperature ($T_g$), onset crystallisation temperature ($T_x$), crystallisation temperature ($T_c$) and melting temperature ($T_m$ ) for the five different glasses (i.e., brown, green, white, RG and P40) are summarised in Table 5.1 . The $T_g$ values for brown glass, green glass and white glass were observed at temperatures in the vicinity of 555 °C to 575 °C while a $T_c$ was observed between 930-1063 °C (see Figure 5.4 and Table 5.1). Moreover, the melting temperature of brown, green and white glasses were observed to be between 1164 °C to 1251°C.

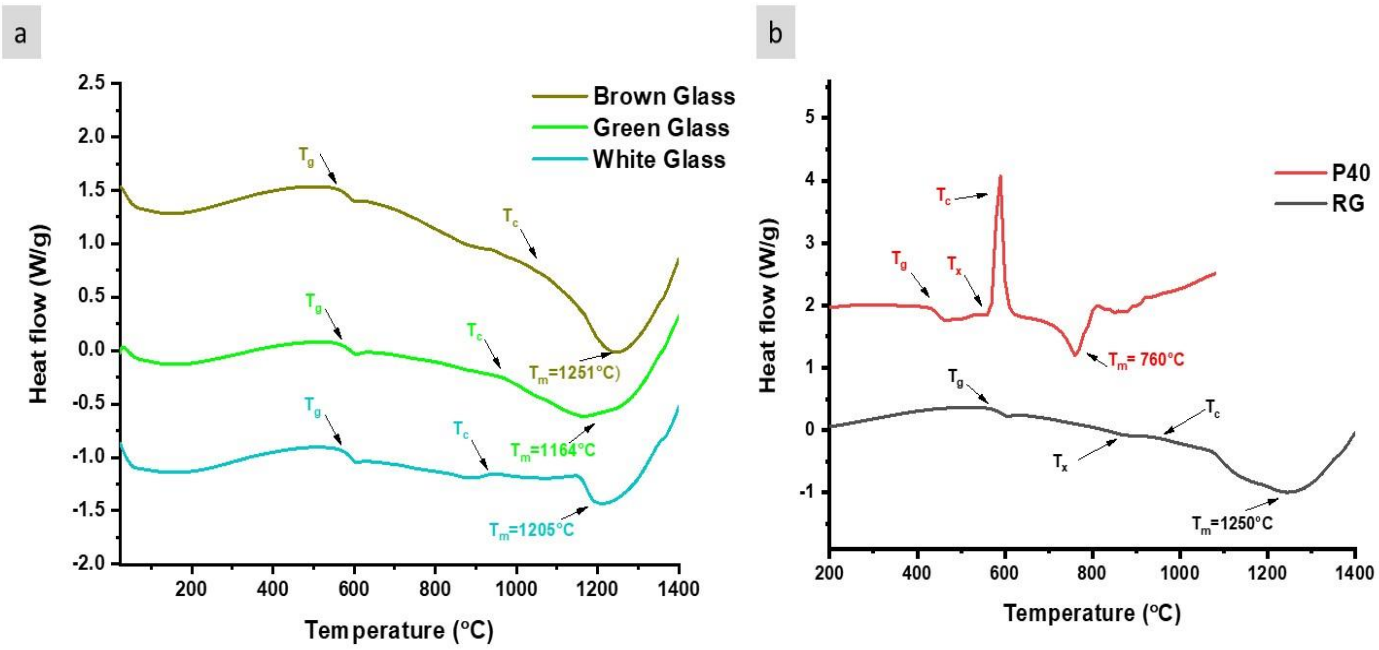



*Figure 5.4: DSC analysis of a) colour sorted RG and b) bulk RG and P40.*

According to Figure 5.4b, lower $T_g$ value (~436°C) was observed for P40 glass particles compared to bulk RG (~566°C). Furthermore, lower $T_x$ and $T_c$ values were also found for the P40 (see Figure 5.4 b) as compared to bulk RG (see Table 5.1). It can be seen from Figure 5.4(b) that, the melting temperature for bulk RG (1250 °C) was 490°C higher in comparison to P40 (760 °C). Overall, it was found that the P40 glasses had lower $T_g$, $T_x$, $T_c$, and processing window ($\Delta T = T_c - T_g$) compared to the rest of the separate-coloured glasses.

*Table 5.1: Summary of DSC analyses (±SD) conducted on colour coded glasses, bulk RG and P40 having particle size ≤ 63 µm.*

| | Glass transition $T_g$ (°C) | Onset crystallisation $T_x$ (°C) | Processing window $\Delta T = (T_x - T_g)$ (°C) | Crystallisation temperature $T_c$ (°C) | Melting temperature $T_m$ (°C) |
|---|---|---|---|---|---|
| **Brown glass** | 557 ± 3 | 894 ± 5 | 337 ± 3 | 1057 ± 5 | 1251 ± 4 |
| **Green glass** | 568 ± 4 | 869 ± 5 | 301 ± 4 | 965 ± 4 | 1164 ± 4 |
| **White glass** | 570 ± 3 | 884 ± 2 | 314 ± 3 | 935 ± 2 | 1205 ± 3 |
| **RG** | 566 ± 7 | 870 ± 6 | 304 ± 7 | 948 ± 5 | 1250 ± 6 |
| **P40** | 436 ± 1 | 555 ± 2 | 119 ± 1 | 589 ± 1 | 760 ± 2 |

## 5.5.2 Compositional analysis of RG

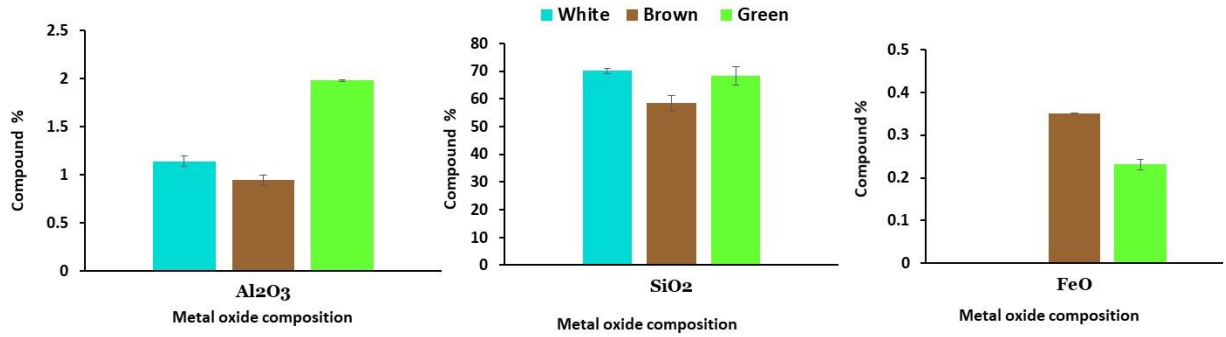



***Figure 5.5: EDX analysis of white, brown, and green glasses investigated for $Al_2O_3$, $SiO_2$ and FeO content.***

EDX analysis were performed to determine the compositions of individual oxide components of white, brown and green glasses (see Figure 5.5). Higher percentage of $Al_2O_3$ (2%) content was observed for green glasses compared to white and brown glasses which showed approximately 1% of $Al_2O_3$ content. The lowest $SiO_2$ content was identified for Brown glasses (approximately 62%). Beside these traces amount of $K_2O$, $SnO_2$, FeO were identified in brown and green glasses (see Table 5.2). Furthermore, higher percentage of FeO content was identified for brown glasses compared to green glasses.

***Table 5.2: EDX analyses (±SD) conducted on colour coded glasses.***

| | Compound % | | |
|---|---|---|---|
| **Glass component** | **White glass** | **Brown glass** | **Green glass** |
| **$Na_2O$** | 13 ± 0.3 | 15 ± 0.2 | 14 ± 0.2 |
| **MgO** | 2 ± 0.5 | 2 ± 0.04 | 2 ± 0.3 |
| **$Al_2O_3$** | 1 ± 0.008 | 0.9 ± 0.02 | 2 ± 0.2 |
| **$SiO_2$** | 72 ± 3.5 | 62 ± 3 | 68 ± 4 |
| **CaO** | 11 ± 1 | 14 ± 2 | 11 ± 1 |
| **$K_2O$** | -- | 0.9 ± 0.02 | 1 ± 0.2 |
| **SnO** | -- | 0.3 ± 0.3 | 0.3 ± 0.2 |
| **FeO** | -- | 0.3 ± 0.03 | 0.2 ± 0.04 |
| **Other** | 1 ± 0.7 | 4.6 ± 2.5 | 1.5 ± 1 |

## 5.5.3 Ash fusion test (AFT)

The Ash fusion test (AFT) is considered as one of the most popular methods used for studying fuels in terms of ash behaviour (detailed methodology described in **Chapter 2**, **Section 2.2.6**). In this study, AFT was conducted to understand the melting profile of RG (≤63 µm) with or without porogen and later compared with P40 (≤63 µm). Porogen (≤5 µm) were mixed with RG and P40 glass particles at a

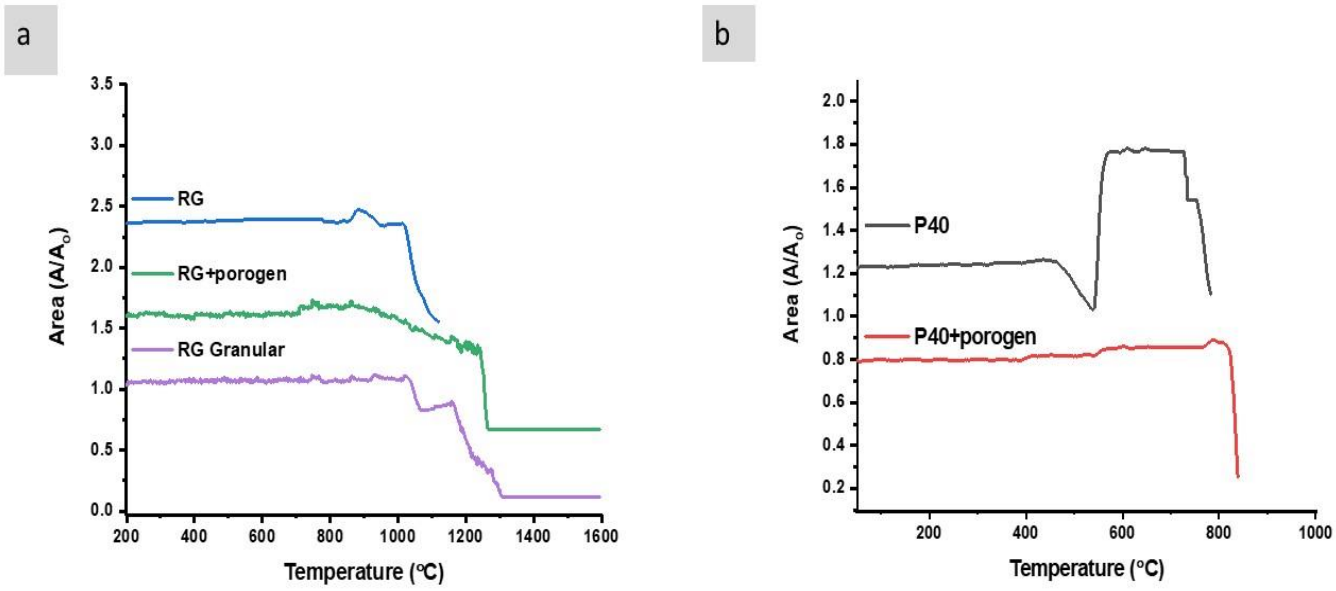



*Figure 5.6: Plots demonstrating the change in area with temperature based AFT instrument for a) RG with and without porogen and RG made into granules and b) P40 glass with and without porogen.*

ratio 1:1. RG were also made into granules by grinding RG (≤45 µm) with porogen (1:1 and grinded for 5 mins) and later mixed together using 2% PVA coded as 'RG-Granular'. Figure 5.6 displays the AFT curves for each sample tested. It was clearly observed that the melting profile for RG (1125°C to 1250°C) and P40 (787°C to 835°C) shifted to higher temperature with addition of porogen. Moreover, the P40 samples exhibited the lowest temperature profiles compared to RG samples (as expected). P40 and P40+porogen experienced single expansion during melting between the region 543-570 °C and double thermal expansion at region 543-570 °C and 766-800 °C, respectively. During AFT, three

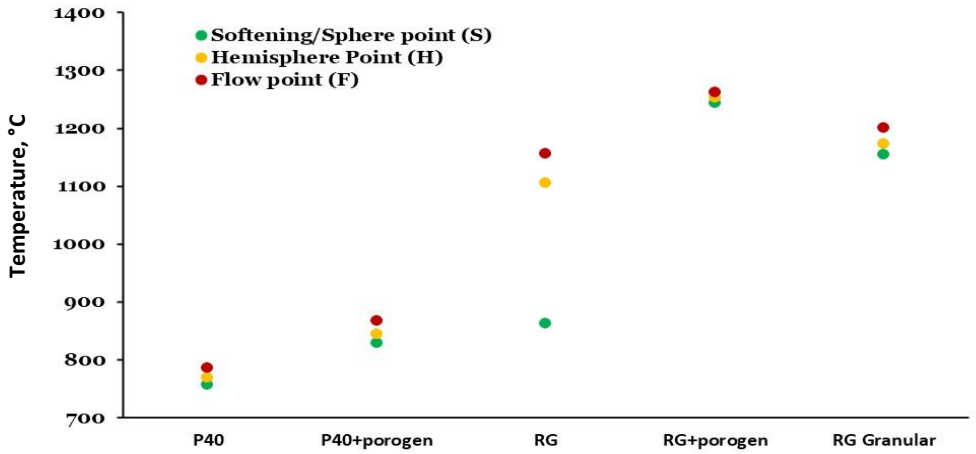



*Figure 5.7: Temperature difference among flow, hemisphere, and sphere point for RG and P40 based samples explored by ash fusion test (AFT).*

discrete temperatures were noted; softening point/sphere temperature (ST), hemisphere temperature (HT), and flow temperature (FT), which are represented in Figure 5.7. The change from hemisphere to flow point occurred very rapidly for the P40 (without porogen) whilst a large difference was noticed for the RG samples (without porogen). A temperature difference between HT to FT were

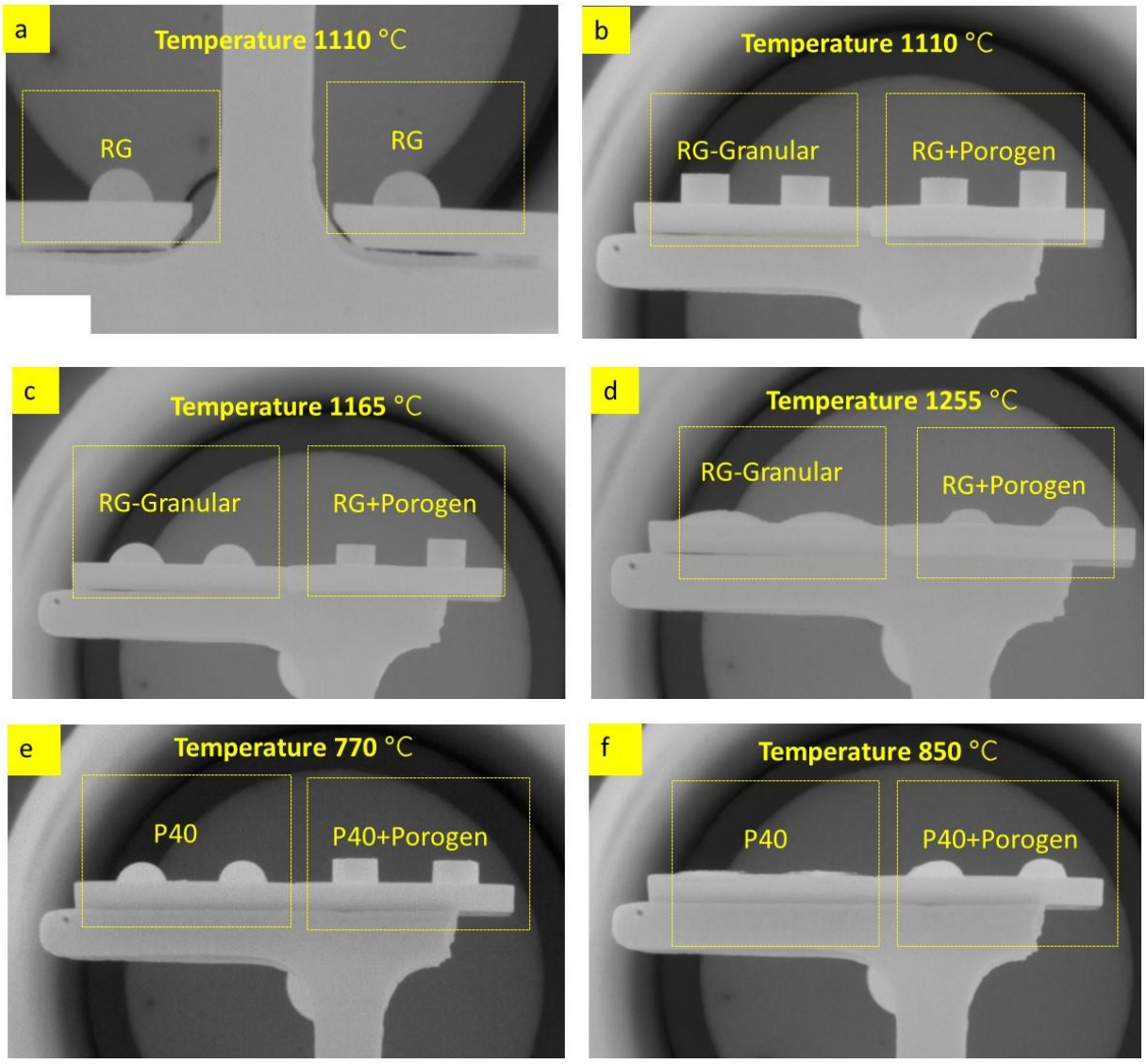



***Figure 5.8: Images of hemisphere for a) RG without porogen, b), c) and d) RG granules, e) and f) P40 with and without porogen at temperature 770 °C and 850 °C, respectively obtained by HD camera inside AFT furnace.***

recorded 41°C ± 1°C, 10°C ± 1°C and 60°C ± 1°C for P40+Porogen, RG+Porogen and Granular RG samples (RG-Granular), respectively.

The hemisphere configuration for P40, P40+porogen, RG, RG+porogen and GR-Granular are shown in Figure 5.8. It was seen that at 1110 °C, RG formed a hemisphere while RG with porogen (RG+porogen) and granular RG (RG-Granular) retained their cylindrical morphology (based on area change).

RG+porogen and RG-Granular transformed into a hemisphere at temperature 1255°C and 1165°C, respectively. P40 glass particles without porogen formed into hemisphere at 770 °C which was approximately 80 °C lower compared to P40 glass particles with porogen.

### 5.5.4 Viscosity analysis

Viscosity of bulk RG and P40 glass particles were measured directly via rotating cylinder (High temperature viscometer) and the respective viscosity at softening point/sphere temperature (ST), hemisphere temperature (HT), and flow temperature (FT) were measured using Avramov–Milchev (AM) model [360] (see Figure 5.10). It was apparent that the viscosity of P40 glass was much lower as compared to RG. For example, the log viscosity at 1190 °C for P40 were -0.4 P which is 88% lower than RG. The respective viscosity (in cP) at FT, HT and ST using AM model is presented in Figure 5.9. The viscosity at FT/melting temperature of RG was 5175 cP which is ~2.5 times higher than P40 glass. Moreover, the viscosity changes from hemisphere point (H) to flow point (F) was ~3 times higher for RG compared to P40.

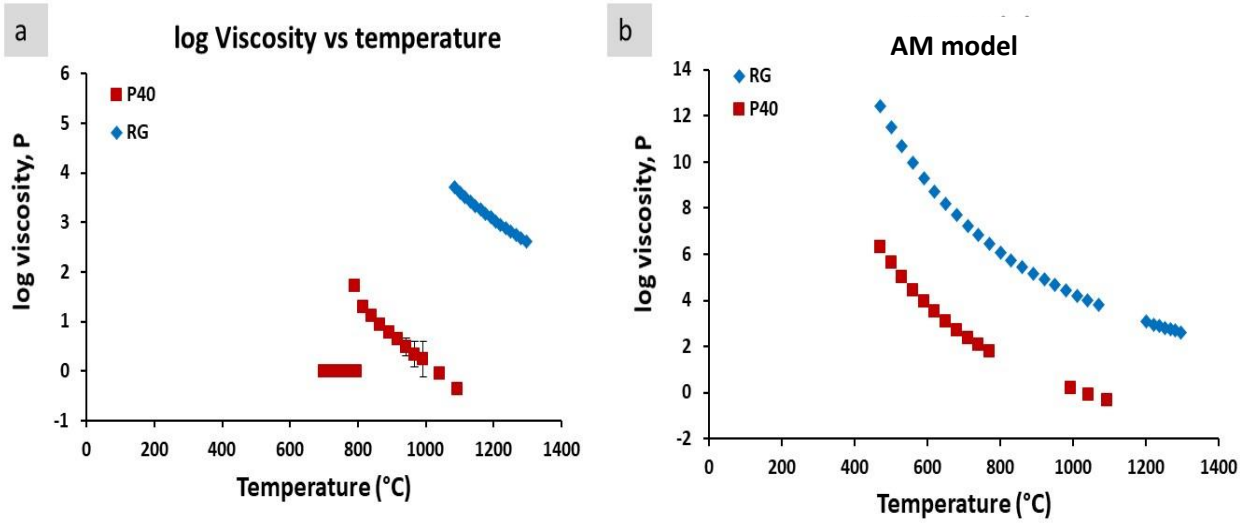



*Figure 5.9: Viscosity curve for P40 and RG glass particles from a) high temperature viscometer and b) Avramov-Milchev (AM) model.*

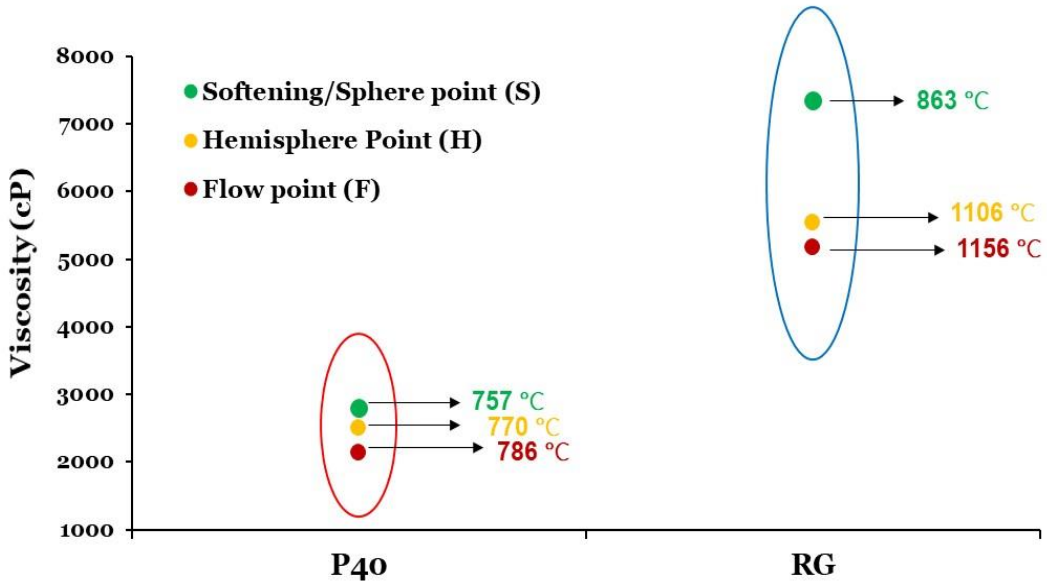



*Figure 5.10: Rate of viscosity change at softening temperature, hemisphere temperature and flow temperature for P40 and RG.*

Considering the difficulty of processing RG particles into porous microspheres using the conventional process, an alternate granular process was developed pre-flame spheroidisation where porogen/RG glass mixtures were ground together and mixed with 2% poly vinyl alcohol (PVA) and made into 3D globules for spheroidisation. Parameters such as grinding time, grinding speed, and porogen ratios were varied to improve the porosity and surface area of PRGMs for further exploration and suitability for separation experiments.

## 5.6 Optimising PRGMs manufacture

### 5.6.1 Effect of grinding time and grinding speed

The morphologies of the PRGMs manufactured maintaining 1 min, 5 min and 15 min grinding time using 300 rpm and 500 rpm grinding speed in a ball-mill were evaluated using SEM analysis.

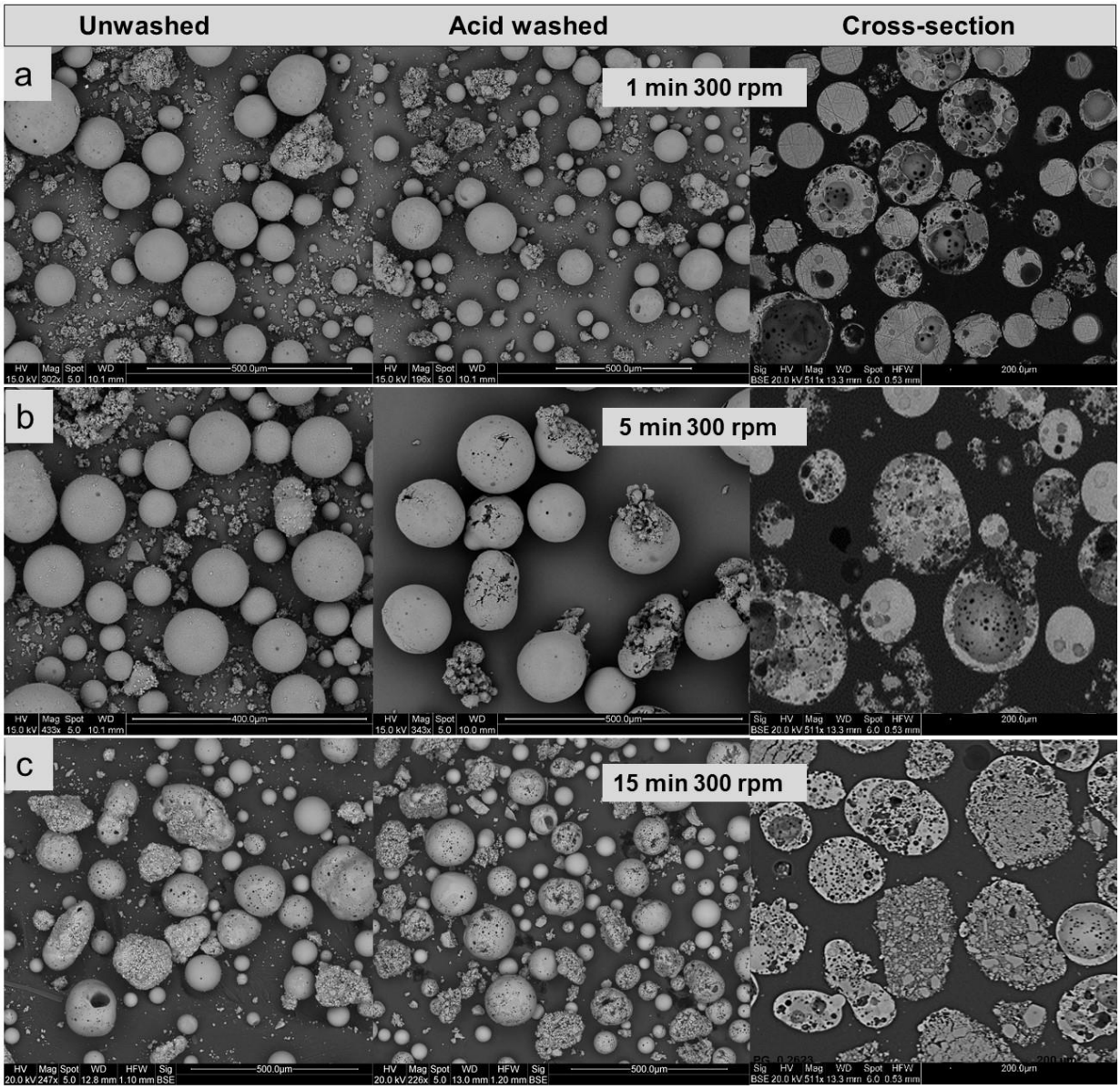



*Figure 5.11: SEM images from (a-c) displaying the effect of grinding time in a ball-mill on manufacturing PRGMs for various time points a) 1 min, b) 5 min and c) 15 min grinding time at 300 rpm.*

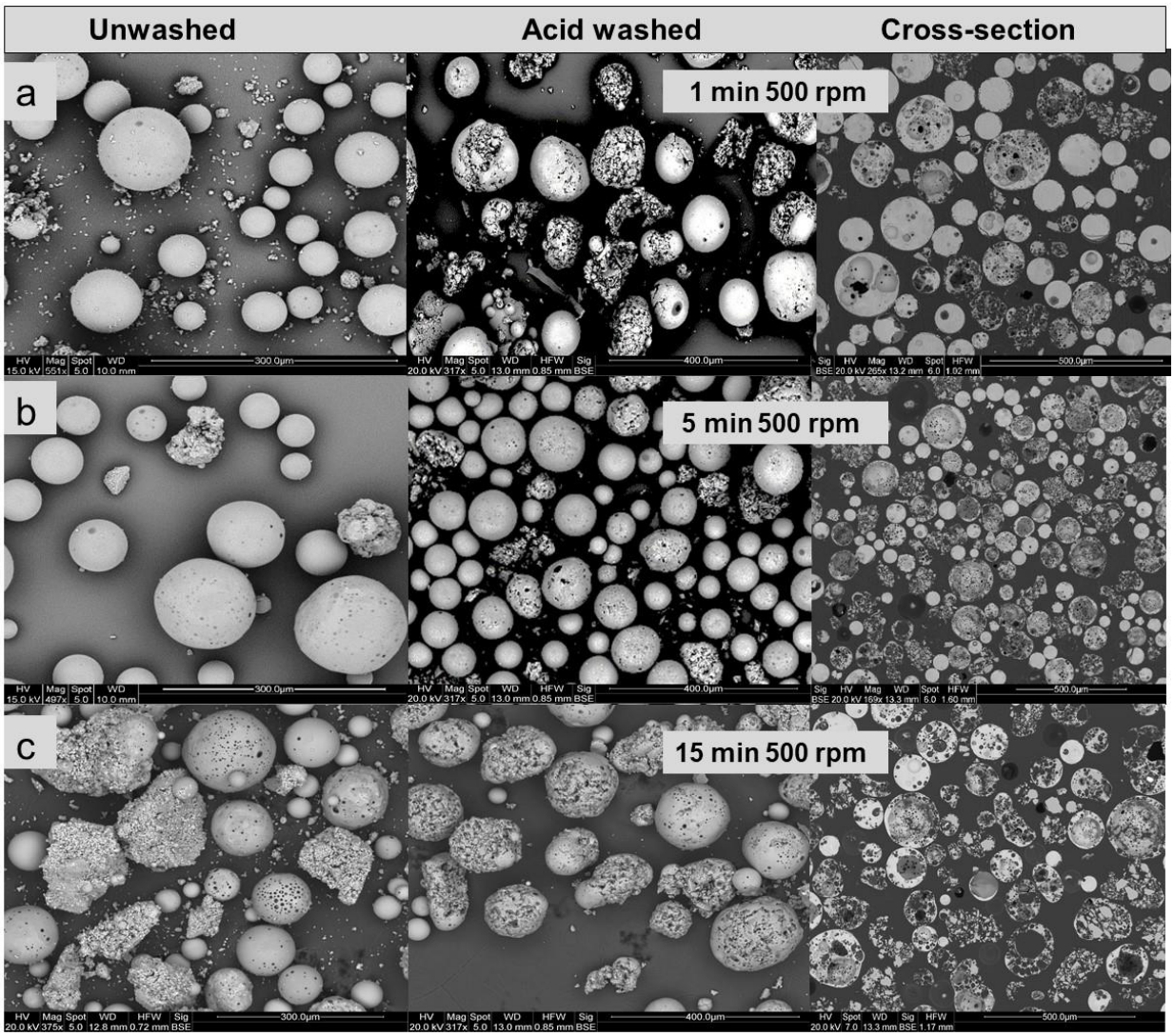



***Figure 5.12: SEM images from a-c displaying the effect of grinding time in a ball-mill on manufacturing PRGMs for various time point a) 1 min grinding, b) 5 min grinding and c) 15 min grinding at 500 rpm.***

A mixture of large porous (125 - 180 µm) and smaller dense (55 - 80 µm) microspheres were produced. The external pores of large PRGMs (125 - 180 µm) exhibited a pore size distribution (PSD) of 0-8 µm (analysed using Image J) for 1min, 5 min and 15 min grinding time. However, increasing grinding speed to 500 rpm decreased external pore to 0-3.5 µm. Moreover, the number of pores increased with increasing grinding time and grinding speed as can be seen from Figure 5.12. The resin embedded cross-sections revealed the internal porosity of the PRGMs produced. An increase in internal porosity was observed with increasing grinding time (from 1 min to 15 min). On contrary, dense microspheres (55 - 80 µm) exhibited few/no pores on the surface and the cross-sections revealed they had dense cores with absence of internal porosity.

### 5.6.2 Effect of porogen

PRGMs were also prepared with varying glass particle and porogen ratios (i.e., 2:1, 1:1 and 1:3) to investigate if any changes of pore size and porosity of the microspheres could be influenced. Figure 5.13 represents the surface morphology of unwashed and acid washed PRGMs with their respective elemental mapping. It can be seen that the pore size decreased with increasing porogen content. Upon acid washing, the number of broken microspheres increased with higher porogen ratio (i.e., 1:3). Moreover, elemental mapping of UW-PRGMs revealed that the surface of the microspheres mostly consisted of Ca whilst a small amount of Ca was found for W-PRGMs. Furthermore, the surface porosity of UW-PRGMs were higher compared to W-PRGMs as shown in Figure 5.13. Cross-sectional analysis as presented in Figure 5.14 revealed interconnected pores with increased porosities. Furthermore, the number of dense (55 - 80 µm) microspheres decreased with increasing amount of porogen ratio. However, any insight regarding micropores, mesopores were not possible to detect, using SEM analysis. As a result, $N_2$ adsorption desorption analysis was conducted to give further insight into the surface area, pore volume etc.

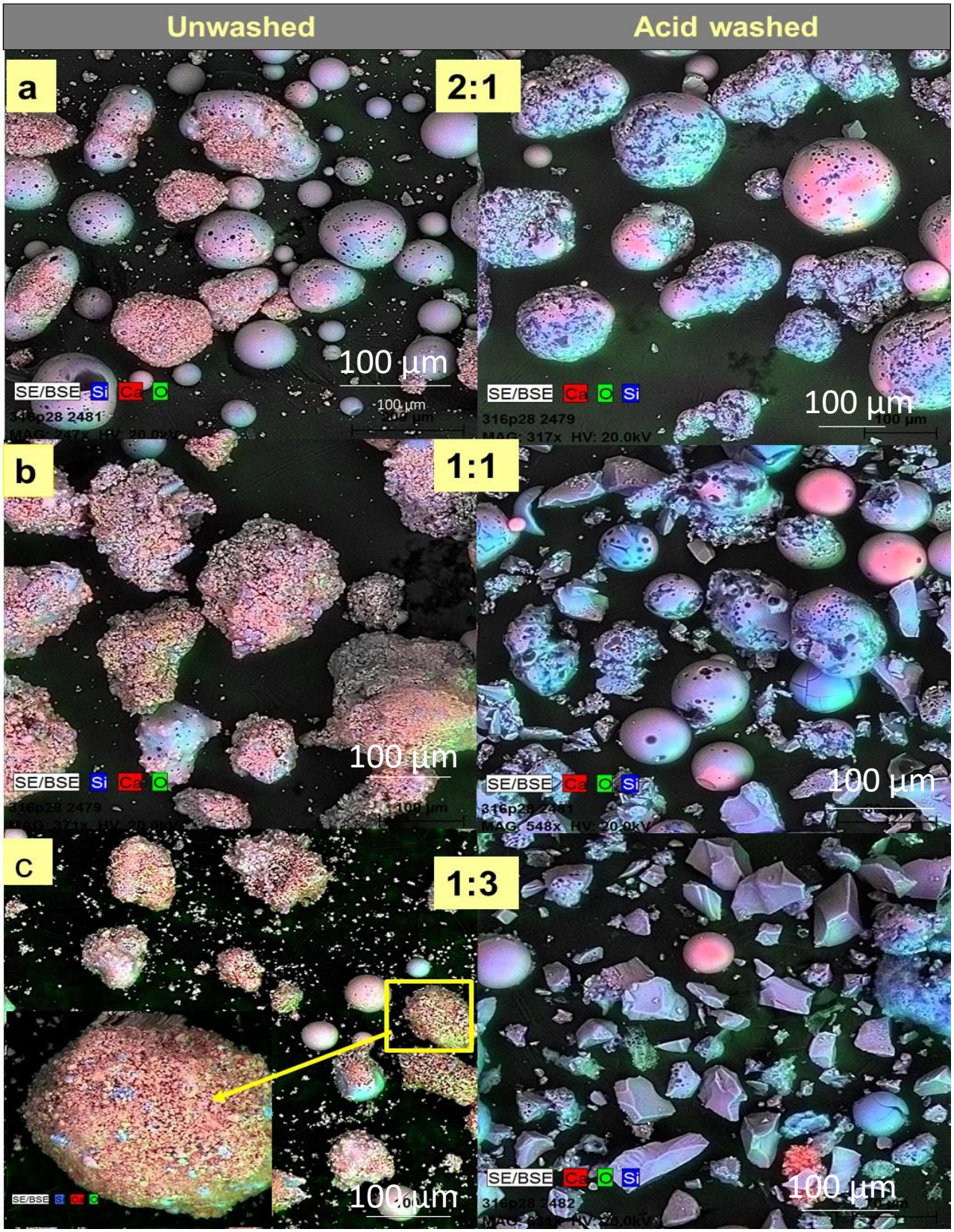



*Figure 5.13: SEM images showing elemental mapping of unwashed, and acid washed PRGMs a) 2:1, b) 1:1 and c) 1:3 glass to porogen ratios.*

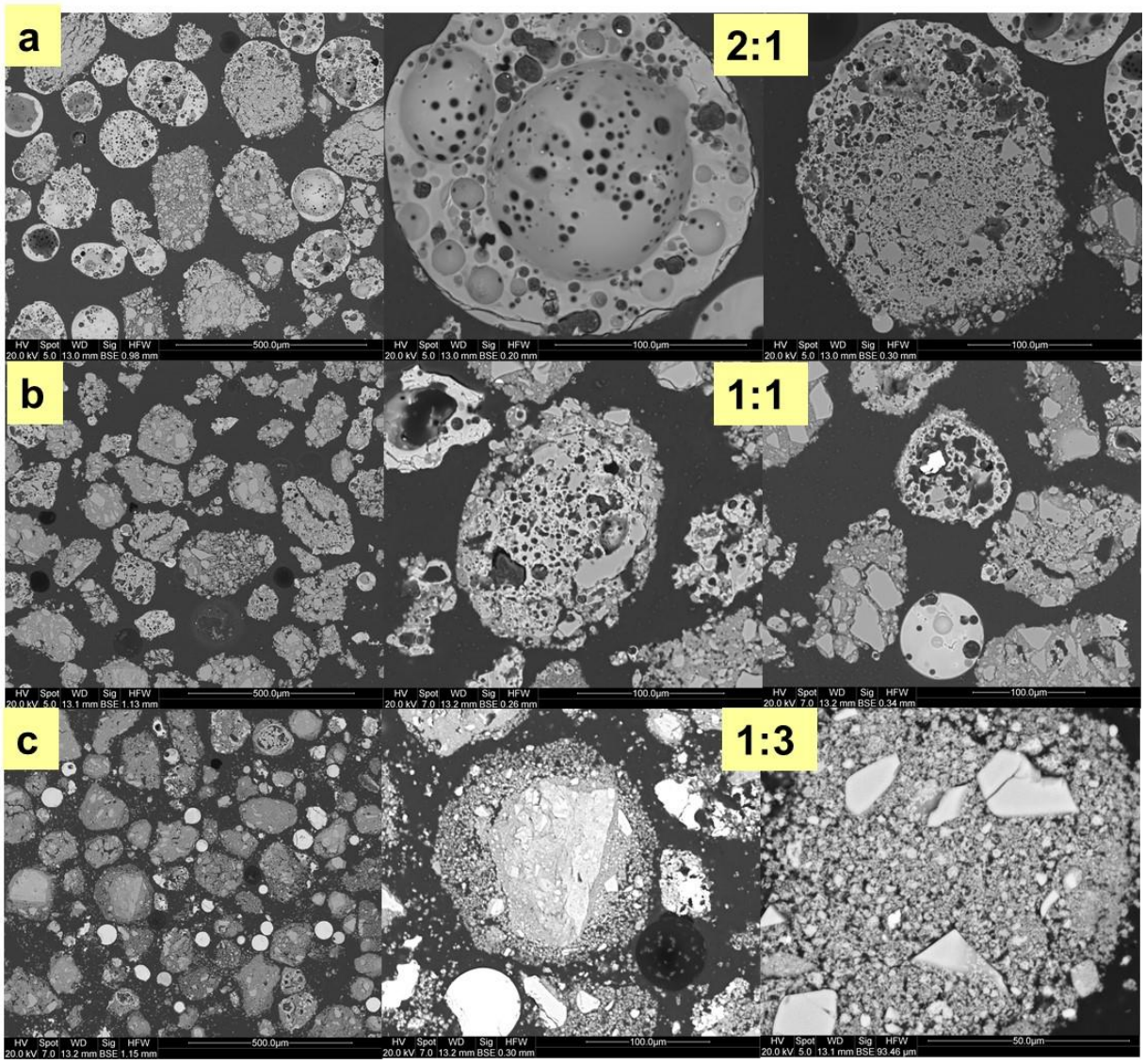



*Figure 5.14: Cross-sectional SEM images showing unwashed PRGMs with a) 2:1, b) 1:1 and c) 1:3 glass to porogen ratios.*

## 5.7 Surface area, porosity, and structural analysis of PRGMs

### 5.7.1 Surface area and pore volume analysis PRGMs

Figure 5.15 (a) represents the surface area of the microspheres analysed using BET analysis. It was apparent that the surface area of PRGMs increased with increasing grinding time and porogen ratio. For example, the highest BET specific surface area of 3.379 and 7.651 $m^2/g$ were found for PRGMs with 1:1 and PRGMs with 1:3 ratios, respectively. The sorption isotherms in Figure 5.15(a-inset) exhibited a Type IV (a) isotherm associated with mesoporous and macroporous materials with cylindrical pore geometries [368, 369].

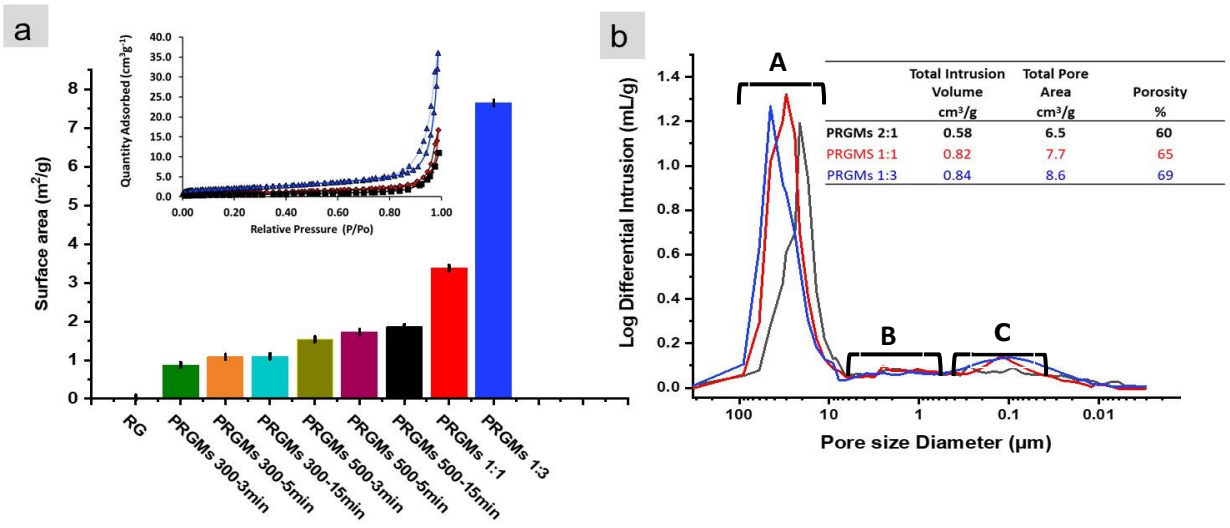



***Figure 5.15: a) surface area analysis using BET method with inset showing nitrogen sorption isotherms of microsphere samples and b) macropore volume and porosity analysis using mercury porosimetry analysis of PRGMs.***

The sorption isotherms (see Figure 5.15 a-inset) did not reveal a plateau indicating macropores existed which are beyond the pressure limits of the $N_2$ adsorption-desorption instrument. Also, the desorption branch of the isotherms showed H3 hysteresis indicating a high degree of macropores were not filled with $N_2$ condensate. As a result, it was necessary to carry out Mercury Intrusion Porosimetry (MIP) analysis for macropore volume and size distribution to determine an accurate total pore volume as well as porosity of the PRGMs.

*Table 5.3: Pore size and pore volume analysis using t-plot and BJH method by nitrogen adsorption desorption analysis.*

| Sample | Amicro, ($m^2$/g) | Vmicro, ($cm^3$/g) | Vmeso, ($cm^3$/g) | Vtotal, ($cm^3$/g) | D, (nm) |
|---|---|---|---|---|---|
| **RG** | 0.006 | 0.000002 | 0.00014 | 0.00023 | 27.76 |
| **PRGMs 300-3 min** | 0.082 | 0.000028 | 0.00268 | 0.00547 | 24.98 |
| **PRGMs 300-5min** | 0.038 | 0.000008 | 0.00318 | 0.00639 | 23.59 |
| **PRGMs 300-15 min** | 0.145 | 0.000051 | 0.00289 | 0.00768 | 27.93 |
| **PRGMs 500-3min** | 0.301 | 0.000122 | 0.00455 | 0.01214 | 31.54 |
| **PRGMs 500-5 min** | 0.236 | 0.000092 | 0.00514 | 0.01251 | 29.00 |
| **PRGMs 500-15 min** | 0.331 | 0.000138 | 0.00611 | 0.01712 | 36.88 |
| **PRGMs 1:1** | 0.635 | 0.000264 | 0.00808 | 0.02598 | 30.75 |
| **PRGMs 1:3** | 1.485 | 0.000633 | 0.02102 | 0.05622 | 29.39 |

Figure 5.15 (b) displays the pore diameters of the measured samples against the log differential pore volume using MIP. It should be noted that mercury porosimetry also determines the inter particular gap as a pore size which is not the actual "pore size" [433]. A trimodal behaviour was observed for all PRGMs. The first prominent peak (see Figure 5.15 b denoted zone A) showing a modal value of c.a. 21 µm, 28 µm and 42 µm for PRGMs with 2:1, 1:1 and 1:3 porogen ratios respectively. These values represent the inter-microsphere gaps between the PRGMs including macropores within PRGMs. The second and third peak (see Figure 5.15 b, denoted by zone B and C) revealed the inner pore features with large and small pores respectively. The large and smaller pores were recorded to have pore diameter ranges from 5- 0.450 µm and 0.450- 0.017 µm, respectively. The corresponding porosity profiles found 60%, 65% and 69% for PRGMs with 2:1, 1:1 and 1:3 porogen ratios, respectively. Furthermore, total intrusion volume (overall pore volume) and pore area of PRGMs increased with increasing porogen ratio with maximum pore volume (intrusion volume) of 0.84 $cm^3$/g and a pore area of 8.6 $cm^3$/g were observed for PRGMs produced using a 1:3 ratio.

$N_2$ sorption instrument provided detailed insights for micropores (≤2 nm), mesopores (2 - 50 nm), and macropores (0 - 140 nm). In Table 5.3, $A_{micro}$ and $V_{micro}$ represents pore area and pore volume respectively for micropores using t-plot model (Harkins/Jura correction [359]). $V_{meso}$ and $V_{total}$ represents pore volume of mesopores and total volume of macropores respectively using t-plot + BJH model (Harkins/Jura correction) [359]. It was observed that increasing grinding time and porogen ratio increased micro, meso and macro pore volume of the PRGMs. For example, greater micro and mesopore volumes were found 0.000264 and 0.00808 $cm^3$/g respectively for PRGMs 1:1 and 0.000633

and 0.02102 $cm^3/g$ respectively for PRGMs 1:3. Moreover, pore diameter (D) was recorded to be between ~23 - 36 nm for the PRGMs.

### 5.7.2 X-ray diffraction analysis

XRD profiles of UW-PRGMs at different porogen ratios are presented in Figure 5.16. All diffraction patterns revealed peaks corresponding to calcium carbonate ($CaCO_3$) and calcium oxide (CaO) phases. The peak intensity of $CaCO_3$ and CaO increased with increasing porogen ratios. The overall percentage of $CaCO_3$ and CaO phases combinedly represents the crystallinity of UW-PRGMs calculated by origin software (version 2020) which is summarised in Table 5.4. Crystallinity can be calculated semi-quantitively from the ratio of the integrated area of all crystalline peaks to the total integrated area under the XRD peaks. The % crystallinity were found 24%, 39% and 55% for 2:1, 1:1 and 1:3 porogen ratios, respectively.

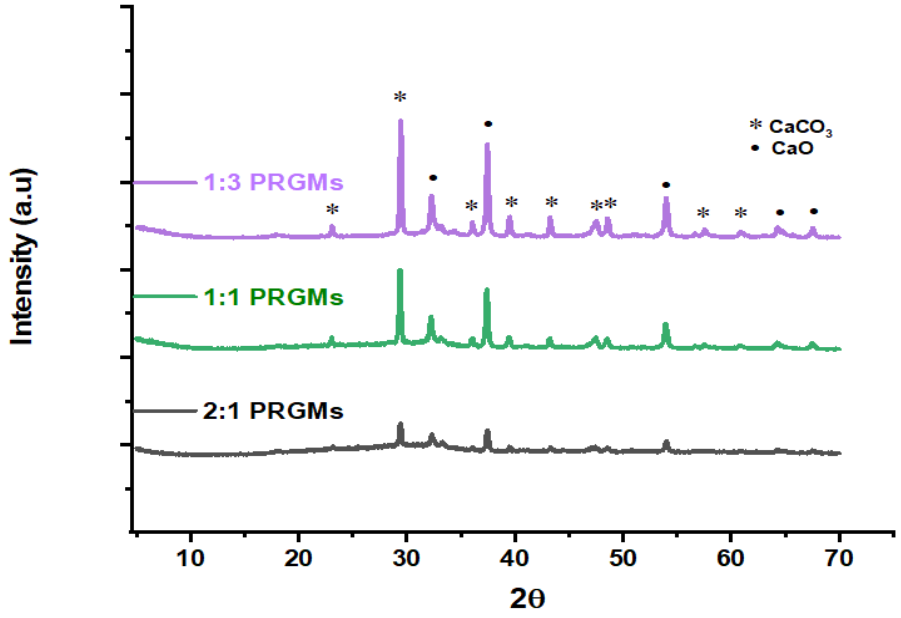



*Figure 5.16: XRD of UW-PRGMs with porogen ratio 2:1, 1:1 and 1:3.*

*Table 5.4: Summery of % crystalline phase in UW-PRGMs*

| Sample Name | Area of Crystalline peaks | Area of all peaks | % Crystallinity |
|---|---|---|---|
| **2:1 PRGMs** | 31 | 129 | 24 ± 2 |
| **1:1 PRGMs** | 62 | 159 | 39± 3 |
| **1:3 PRGMs** | 92 | 166 | 55± 3 |

## 5.8 Adsorption studies

### 5.8.1 Effect of Initial pH

The initial pH of the solution can significantly influence adsorption of dyes; thus, the effects of solution pH on dye adsorption using the PRGMs was studied first. A range of pH conditions were investigated to explore the effects of alkaline and acidic conditions on adsorption performance of PRGMs manufactured with varying porogen ratios. The adsorption performance was examined across the pH range from 2-12, utilising both an anionic dye AR88 and a cationic dye methylene blue (MB) was also explored.

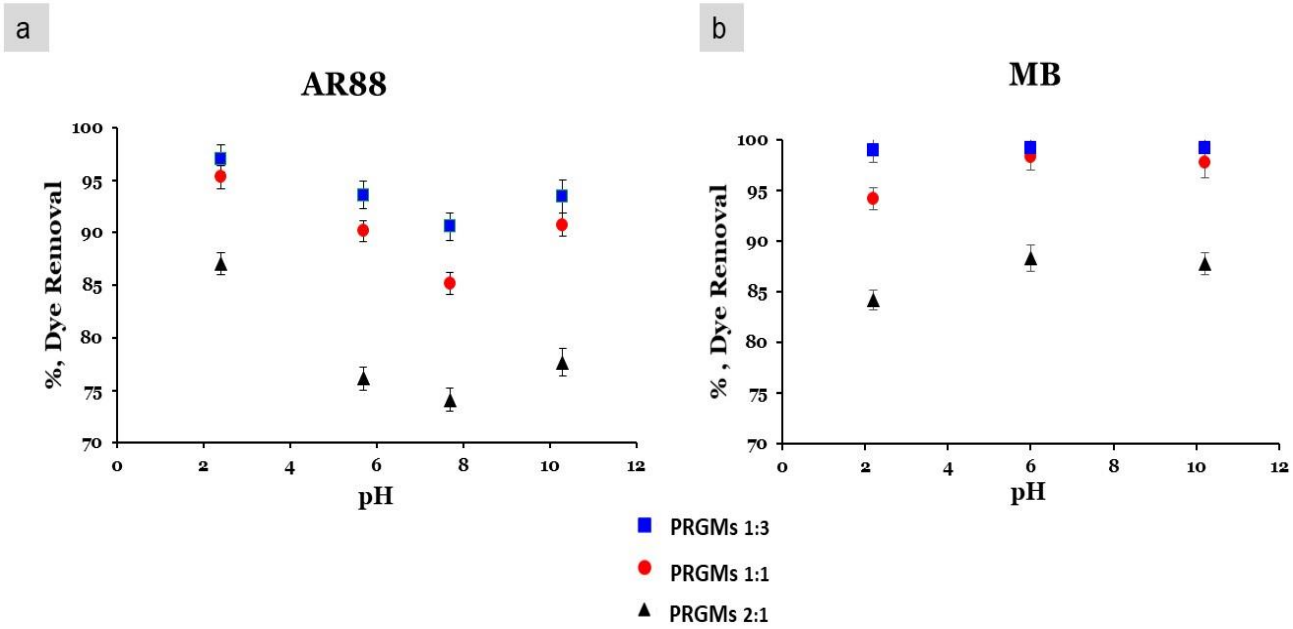



*Figure 5.17: Impact of the initial pH of solution on the adsorption of a) AR88 and b)MB by PRGMs with varying porogen ratios after equilibrium ($C_0$=200mg/L for AR88 and 25mg/L for MB; dye volume=10mL; adsorbent loading=10 g/L; T=22 ± 2 ℃).*

For the AR88 dye, maximum dye removal (~100%) was observed at the initial pH ~2.5 for PRGMs with porogen ratio 1:3 and 1:1 whilst the maximum dye removal was recorded ~87% for PRGMs with porogen ration 2:1. The dye removal percentage decreased by approximately 10% as the initial pH increased from 2 to 8 and increased by approximately 4% beyond pH 8 (see Figure 5.17a).

Dye removal percentage for MB showed a slight increase in adsorption of approximately 4% as pH increased from 2 to 6 for PRGMs with porogen ratio 1:1 and 2:1. The removal percentage was constant beyond pH 6. On the contrary, no significant change in adsorption capacity was noticed for PRGMs with 1:3 ratio (see Figure 5.17b).

## 5.8.2 Effect of Adsorbent Dose

The effect of PRGMS (unwashed and washed) and porogen dose on adsorption of AR88 and MB is detailed in Figure 5.18. The adsorbent dose was varied from 1 g/L to 20 g/L in order to investigate a wide range of PRGMs mass loadings and the effect that this has in terms of dye removal %. The solution pH was adjusted to 2 and 7 for AR88 and MB, respectively.

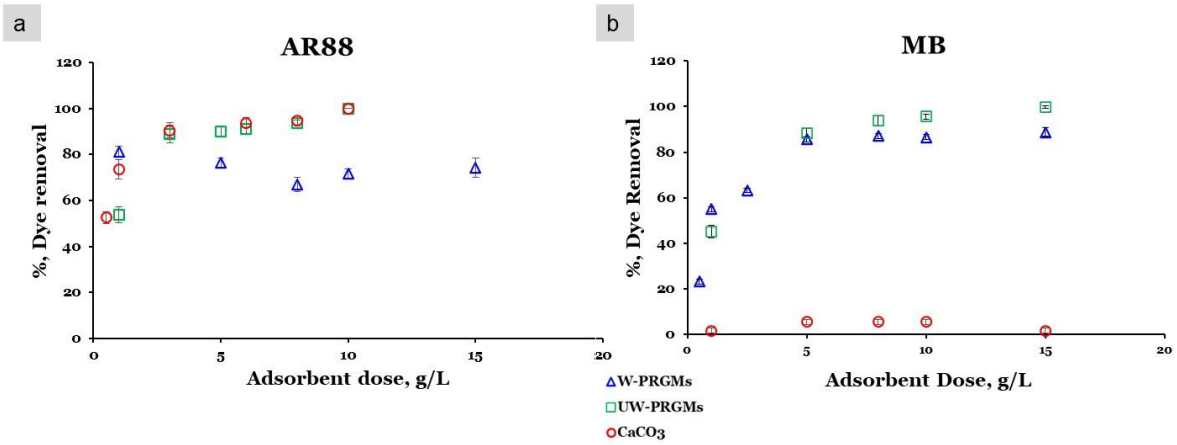



***Figure 5.18: Influence of the PRGMs loading on the adsorption of a) AR88 and b) MB after equilibrium ($C_0$=200mg/L for AR88 and 25 mg/L for MB, pH= 2.5 for AR88 and 20mg/L, pH=7 for MB; dye volume= 10mL; T= 22 ± 2 ℃).***

With increasing adsorbent dose, the dye removal % increased with increasing UW-PRGMs and porogen ($CaCO_3$) dose from 1 g/L to 10 g/L for AR88 dye. The AR88 dye removal % for 1 g/L of UW-PRGMs and porogen alone was 54 ± 2.1 % and 53 ± 2.8 % respectively, whereas for an adsorbent loading of 10 g/L values of 98.5 ± 1.5 % mg/g and 98 ± 2 % respectively, were obtained. For W-PRGMs the dye removal % was nearly the same for 2-5 g/L dosing which then decreased by 10% with increasing the dose to 8 g/L. However on further increase in W-PRGMss dose from 8 to 10 mg/L, the dye removal percentage increased slightly by 5%.

For MB, the dye removal percentage increased from 1g/L to 6 g/L and then reached a plateau with no significant change in dye removal for UW-PRGMs and W-PRGMs. For both dyes (AR88 and MB), the dye removal percentage of UW-PMMs was higher compared to W-PRGMs (see Figure 5.18 b). No noticable dye removal was observed by varying porogen dose for MB dye adsorption.

### 5.8.3 Effect of concentration on Reaction Kinetics

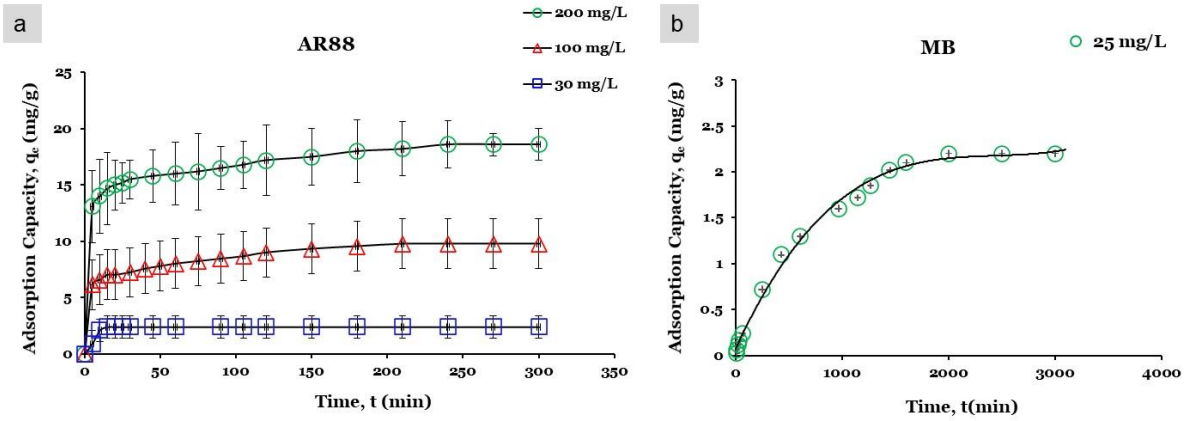



*Figure 5.19: Effect of dye concentration on adsorption into UW-PRGMs for a) AR88 and, b) MB. (PRGMs dose= 10 g/L and 6 g/L with pH 2.5 and pH 7 for AR88 and MB respectively and temperature of 22 ± 2 ℃).*

The effects of the initial concentration of AR88 and MB dyes on the adsorption rate by UW-PRGMs are shown in Figure 5.19. It was clear that the equilibrium adsorption capacity ($q_e$) increased with increasing dye concentration (See Figure 5.19 a). Complete adsorption of AR88 was observed for dye concentrations of 100 mg/L and 200 mg/L which took place within 120 mins of contact time (see Figure 5.19 a) whilst complete adsorption for 30 mg/L occurred within 30 mins. However, adsorption of 25 mg/L MB by UW-PRGMS followed a slower adsorption (5 times slower compared to AR88 dye adsorption) and reached a plateau towards equilibrium (at 1500 mins) as shown in Figure 5.19 b.

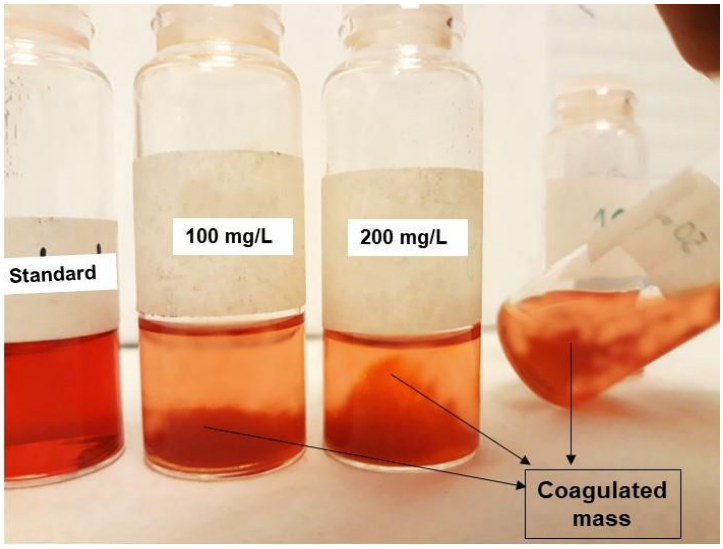



*Figure 5.20: Effect of dye concentration on adsorption into UW-PRGMs for AR88 (PRGMs dose= 10 g/L with pH 2.5 and temperature of 22 ± 2 ℃).*

On the contrary, it was not possible to carry out similar kinetics study for W-PRGMs for adsorption of AR88 due to formation of a coagulated mass, which was within 30 mins (see Figure 5.20).

The data from adsorption experiments at different concentrations were modelled against the pseudo 1st order and pseudo 2nd order models, these are the most common kinetic models in the published literature [366] applied to studying the dynamics of the adsorption process in terms of the order of rate constant.

The plots of the linear pseudo 1st and 2nd order model for adsorption of AR88 are presented in Figure 5.21. Values of the rate constant ($k_1$), equilibrium adsorption capacity ($q_e$), calculated equilibrium adsorption capacities ($q_{ecal}$), and correlation coefficient ($R^2$) were calculated from the plots of log ($q_e - q_t$) versus t for each individual dye and are presented in Table 5.5. The best fit among the kinetic models was assessed by linear coefficient of determination ($R^2$) and Chi-square ($\chi 2$) test. It was observed that the $q_{ecal}$ values did not agree with experimental values ($q_e$) for AR88 and MB dye adsorption into UW-PRGMs. These data indicated that the pseudo 1st order reaction equation was not ideal to model the adsorption data. The linear equation, with a correlation coefficient $R^2$ is ≥0.98, fitted better to pseudo 2nd order model than the pseudo 1st order model. The pseudo 2nd order rate constant ($k_2$) decreased with increasing initial concentrations of AR88 dye (see Table 5.5).

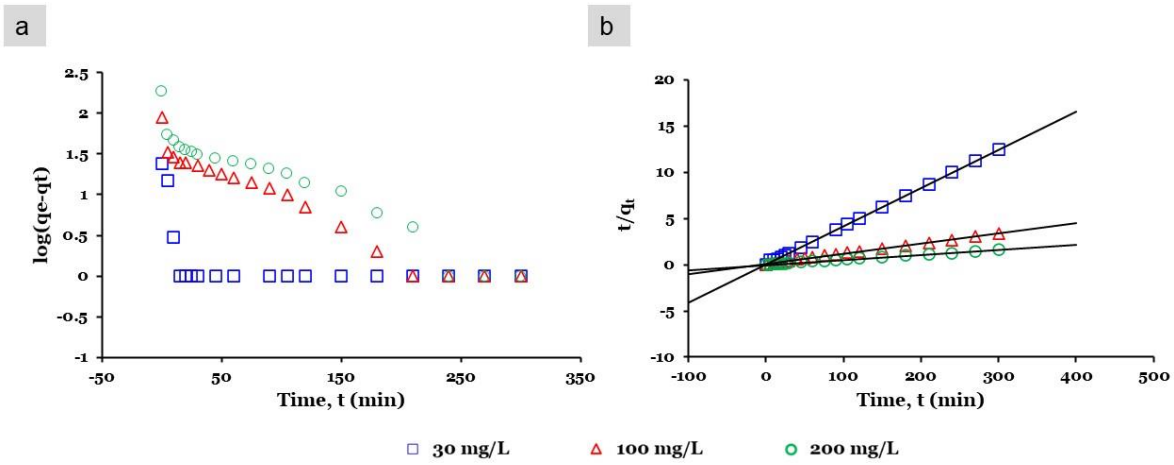



*Figure 5.21: a) Linear pseudo 1st order kinetic model and b) Linear pseudo 2nd order for the adsorption of AR88 (Volume of dye= 10mL; adsorbent loading= 10 g/L, pH= 2.5 for AR88).*

*Table 5.5: Kinetic rates for the adsorption of AR88 and MB on UW-PRGMs.*

| UW-PRGMs with different dye concentrations | | Pseudo 1st order | | | | | Pseudo 2nd order | | | | |
|---|---|---|---|---|---|---|---|---|---|---|---|
| | | $q_{e\ exp}$ (mg/g) | $q_{e\ cal}$ (mg/g) | $K_1$ ($min^{-1}$) | $R^2$ | $X^2$ | $q_{e\ exp}$ (mg/g) | $q_{e\ cal}$ (mg/g) | $K_2$ (g/mg/min) | $R^2$ | $X^2$ |
| **MB** | **25 mg/L** | 2.2 | 2.8 | 0.0004 | 0.236 | 0.45 | 2.2 | 2.3 | 0.0007 | 0.983 | 0.21 |
| **AR88** | **50 mg/L** | 2.4 | 2.2 | 0.0018 | 0.20 | 0.24 | 2.4 | 2.4 | 0.03 | 0.999 | 0.0001 |
| | **100 mg/L** | 8.9 | 4.8 | 0.0062 | 0.94 | 0.31 | 8.9 | 9 | 0.001 | 0.997 | 0.0002 |
| | **200 mg/L** | 18.6 | 6.6 | 0.0063 | 0.93 | 0.21 | 18.6 | 18.8 | 0.0007 | 0.998 | 0.0001 |

### 5.8.4 Adsorption Isotherms

The adsorption isotherms are used to assess adsorbent-adsorbate (dye) surface interactions, particularly to estimate distribution of the dye molecules (maximum uptake capacity ($q_m$)) at the adsorption sites. The isotherms for adsorption of AR88 and MB were calculated from experiments with varying dye concentration from 300 mg/L to 100 mg/L and 50 mg/L to 10 mg/L for AR88 and MB respectively (see Figure 5.22 a, and b) with a PRGMs dose 5 g/L. These parameters were chosen to ensure that PRGMs would be saturated so the maximum capacity of PRGMs from the isotherm experiments could be appropriately determined. The Langmuir and Freundlich models for AR88 and MB are illustrated in Figure 5.22. The parameters obtained from the models are outlined in Table 5.6 and Table 5.7.

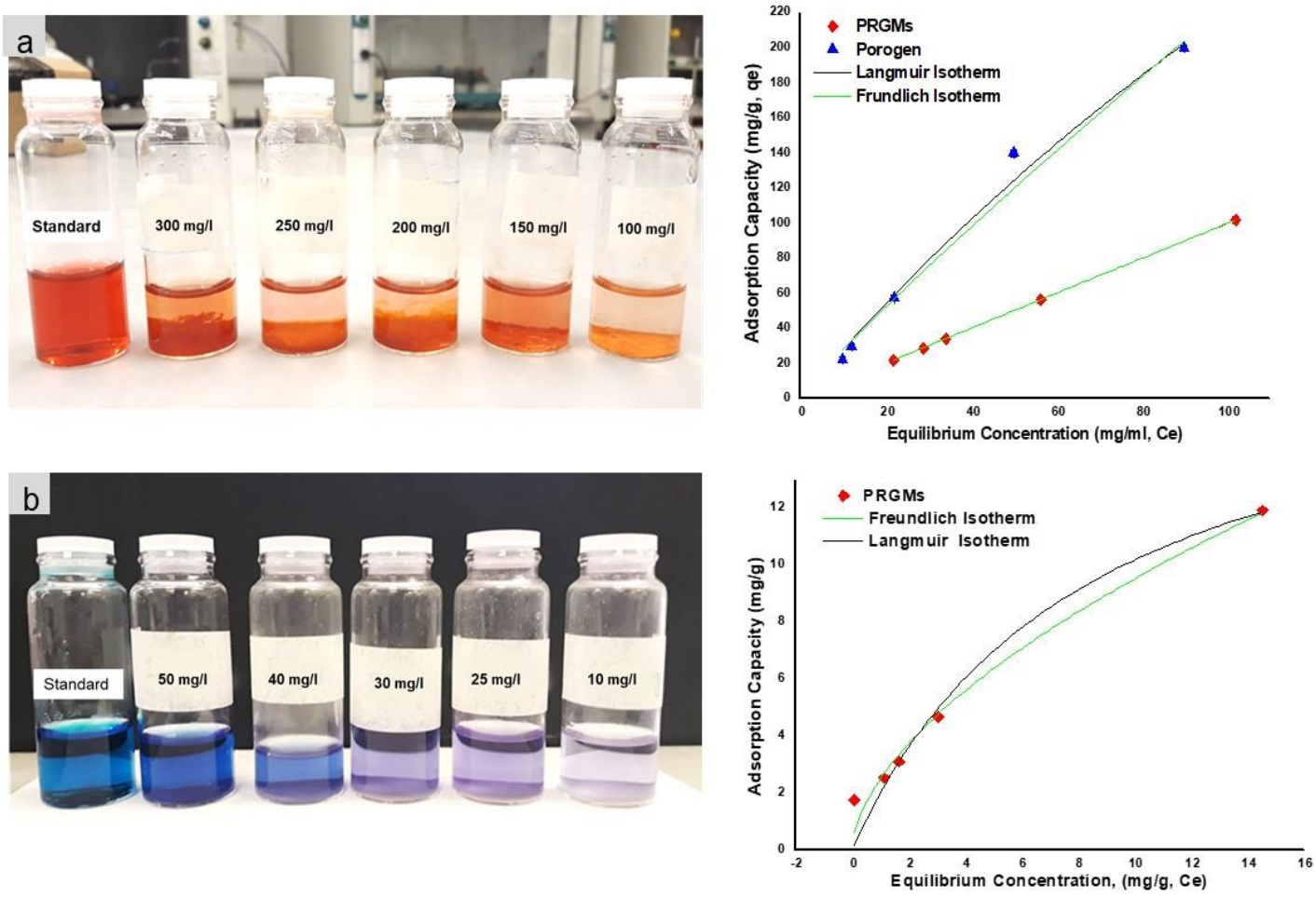



***Figure 5.22: Isotherm data fitted with Langmuir and Freundlich models for a) AR88 and b) MB dye (PRGMs dose= 5 g/L, pH 2.5 and pH 7 for AR88 and MB respectively and temperature of 22 ± 2 ℃, equilibrium time 24 hrs).***

*Table 5.6: Isotherm constants for adsorption of AR88.*

| | Langmuir isotherm | | | | Freundlich isotherm | | | |
|---|---|---|---|---|---|---|---|---|
| **Sample** | **$q_m$ (mg/g)** | **$R^2$** | **$X^2$** | **$q_e$ (mg/g)** | **$K_f$ (ml/g)** | **1/n** | **$R^2$** | **$X^2$** |
| **PRGMs** | 78 ± 4 | 0.99 | 2.1 | 98.26 | 3.42 ± 0.01 | 0.71 ± 0.1 | 0.99 | 1.2 |
| **RG** | -- | -- | -- | --- | -- | -- | -- | -- |
| **Porogen** | 227 ± 5 | 0.99 | 3.07 | 200 | 2.2 ± 0.001 | 1±0.2 | 0.99 | 5.3 |

*(The adsorption capacity $q_e$ based on Freundlich isotherm model was calculated when adsorbent dose= 10 g/L)

*Table 5.7: Isotherm constants for adsorption of MB.*

| | Langmuir isotherm | | | Freundlich isotherm | | | | |
|---|---|---|---|---|---|---|---|---|
| **Sample** | **$q_m$ (mg/g)** | **$R^2$** | **$X^2$** | **$q_e$ (mg/g)** | **$K_f$ (ml/g)** | **1/n** | **$R^2$** | **$X^2$** |
| **PRGMs** | 20 | 0.97 | 0.37 | 13.70 | 2.93 | 0.58 | 0.98 | 1.2 |
| **RG and Porogen** | - | - | - | - | - | - | - | - |

*(The adsorption capacity $q_e$ based on Freundlich isotherm model was calculated when adsorbent dose= 10 g/L)

From Table 5.6, comparing both Langmuir and Freundlich models, data for adsorption of AR88 on PRGMs fitted well to Freundlich's model obtaining a higher correlation coefficient ($R^2_{Freundlich}$ =0.99) closer to unity and smaller values of $\chi^2$ compared with those using Langmuir's model. The maximum monolayer adsorption capacity ($q_m$) calculated for PRGMs and porogen were 78 mg/g and 227 mg/g respectively. The isotherm studies were also conducted for unprocessed RG particles; however, no noticeable adsorption was observed during this experiment for AR88 dye.

In contrast, adsorption of MB data fitted well with the Langmuir model ($R^2_{Langmuir}$ =0.99). The maximum monolayer adsorption capacity ($q_m$) estimated for PRGMs were found to be 20 mg/g (see Table 5.7). The unprocessed RG or porogen alone did not show any MB dye adsorption.

## 5.9 Coagulation study

It is apperent that W-PRGMs showed evidance of forming an agglomarated / coagulated mass which hindered conducting kinetic studies (see Figure 5.20). To simulate coagulation/agglormeration of AR88 dye, PRGMs with different doses were investigated using the commonly used 'jar test' method. During the jar test process, PRGMs were simultaneously mixed with dye at a constant rapid mixing time (600 rpm for 3 mins) and then under slow agitation (≈100 rpm) for 30 min. Samples were collected after 2 hrs settling-time. The microfloc formed after coagulation during rapid mixing further underwent flocculation during slow agitation and is allowed to settle.

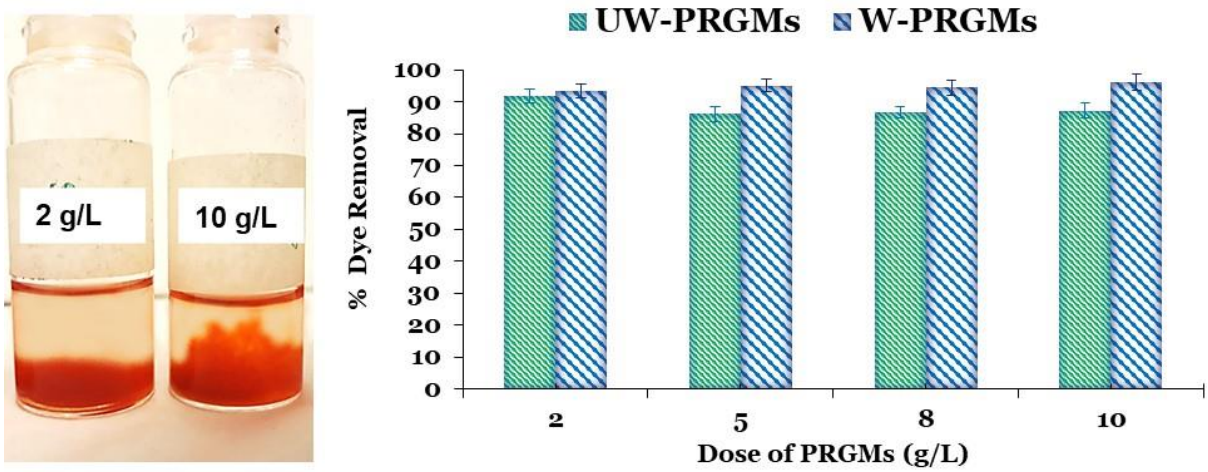



***Figure 5.23: Effect of UW-PRGMs and W-PRGMs dose on removing AR88 dye by coagulation. ($C_0$= 200mg/L, pH= 2.5, dye volume=10mL; T= 22 ± 2 ℃).***

It was observed that for different PRGMs dosing, the dye removal percentage were higher for W-PRGMs compared to UW-PRGMs. For example, the maximum dye removal was observed as 91 % ±

1.2 and 96 % ± 1.6 for UW-PRGMs and W-PRGMs, respectively. With increasing PRGMs doses the dye removal percentage values had not significantly changed for UW-PRGMs and W-PRGMs.

## 5.10 Fixed bed adsorption studies

Fixed-bed column is a more desirable and industrially practical for contaminants removal from wastewater [434, 435]. The performance of fixed-bed column is studied using breakthrough curves. Figure 5.24 shows the concentration-time profiles obtained in a fixed-bed column experiments at flowrates of 2.2 ml/L and 0.5 ml/L. The total amount of dye adsorbed and equilibrium adsorption of AR88 is outlined in Table 5.8.

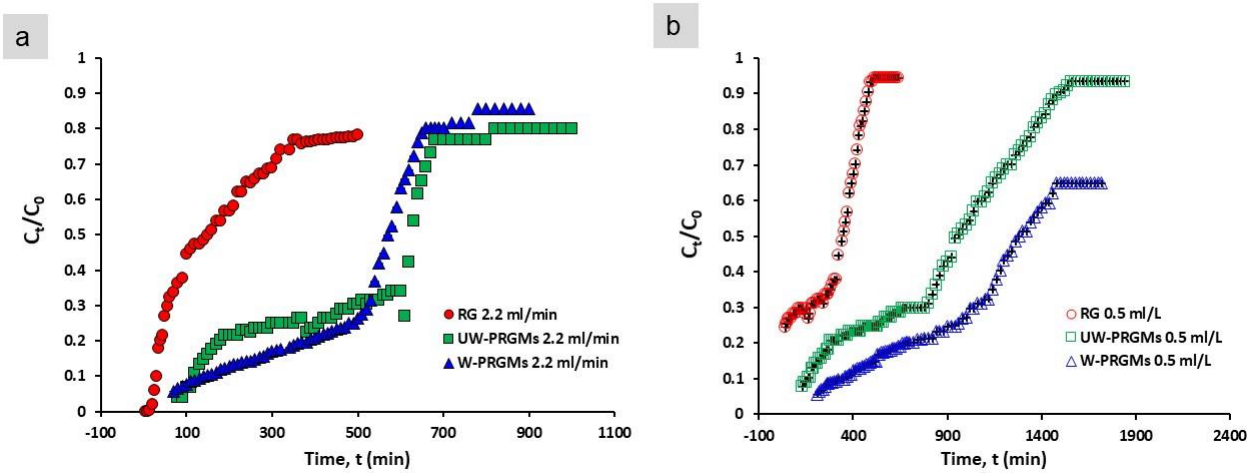



***Figure 5.24: Breakthrough curve of AR88 dye adsorption for RG, UW-PRGMs and W-PRGMs microspheres at a) 2.2 ml/min and b) 0.5 ml/min flow rates with starting dye concentration of 100 mg/L at 22 ± 2 ℃.***

From the data, it can be seen that there is an increase in adsorption compared to the batch process (adsorption capacity obtained from Langmuir isotherm) for UW-PRGMs. Furthermore, the adsorption of unwashed and washed microspheres was higher than as received RG. the Thomas, Adams-Bohart and Yoon-Nelson models were applied to fit the experimental data to describe the fixed-bed column behaviour as shown in Figure 5.25. Between the Thomas and Adams-Bohart models, Adams-Bohart model was the least appropriate equation for modelling the adsorption in column experiment (see Table 5.9). The Thomas model provided the best fit for the experimental data at both flowrates ($R^2 > 0.80$), suggesting its suitability for the design and scale-up purpose. Although the calculated adsorption capacity ($\mathbf{q_{th}}$) of microspheres were slightly lower than the experimental values ($\mathbf{Q_{e\ exp}}$).

*Table 5.8: Total adsorption and equilibrium adsorption capacity of AR88 at different flow rates for RG, UW-PRGMs and W-PRGMs.*

| | Column study | | | | Batch study |
|---|---|---|---|---|---|
| **Sample** | **Flow rate, (mL/min)** | **EBCT, (min)** | **$q_{tot}$ (mg) (±3)** | **$q_{eq}$ (mg/g) (±3)** | **$q_e$ (mg/g) (±4)** |
| **RG** | 2.2 | 1 | 235 | 84 | -- |
| **RG** | 0.5 | 5 | 89 | 42 | |
| **UW-PRGMs** | 2.2 | 1 | 763 | 381 | 98 |
| **UW-PRGMs** | 0.5 | 5 | 425 | 202 | |
| **W-PRGMs** | 2.2 | 1 | 611 | 305 | -- |
| **W-PRGMs** | 0.5 | 5 | 282 | 157 | |

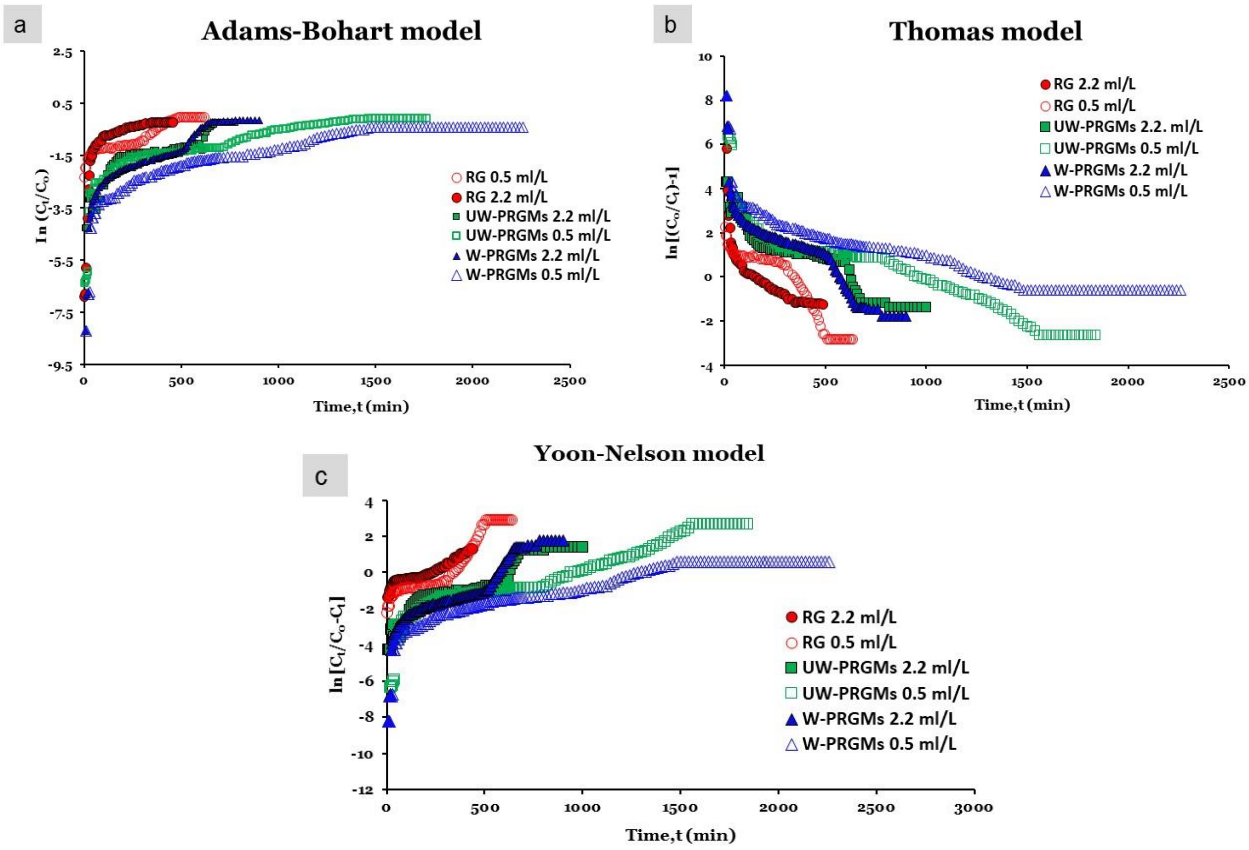



*Figure 5.25: a) Adams-Bohart model, b) Thomas model, and c) Yoon-Nelson model at different flowrates ($C_0$= 100mg/L).*

*Table 5.9: Breakthrough curve models with their parameters.*

| | | | Thomas model | | | Adams-Bohart model | | | Yoon-Nelson model | | |
|---|---|---|---|---|---|---|---|---|---|---|---|
| **Sample** | **Flow Rate, (mL/min)** | **$Q_{e\ exp,}$ mg/g** | **$q_{th,}$ mg/g** | **$K_{th}$ (mL/ min/mg)** | **$R^2$** | **$N_0$ (mg/L)** | **$K_{AB}$ (mL/ min/mg)** | **$R^2$** | **$\tau_{cal}$ (min)** | **$\tau_{exp}$ (min)** | **$R^2$** |
| **RG** | **2.2** | 84 | 12 | 0.001 | 0.64 | 39 | $4x10^{-5}$ | 0.92 | 175 | 204 | 0.94 |
| | **0.5** | 42 | 33 | 0.001 | 0.94 | 25 | $9x10^{-5}$ | 0.4 | 245 | 255 | 0.9 |
| **UW-PRGMs** | **2.2** | 381 | 250 | $6.8x10^{-5}$ | 0.88 | 193 | $5.4x10^{-5}$ | 0.77 | 420 | 622 | 0.88 |
| | **0.5** | 202 | 231 | $3.1x10^{-5}$ | 0.80 | 135 | $2.2x10^{-5}$ | 0.61 | 800 | 914 | 0.86 |
| **W-PRGMs** | **2.2** | 305 | 244 | $9.5x10^{-5}$ | 0.83 | 222 | $5.4x10^{-5}$ | 0.7 | 400 | 549 | 0.83 |
| | **0.5** | 157 | 168 | $4.5x10^{-5}$ | 0.86 | 95 | $2.5x10^{-5}$ | 0.61 | 750 | 1285 | 0.80 |

Based on the Thomas model, the calculated adsorption ($q_{th}$) capacities for UW-PRGMs and W-PRGMs at flow rate 2.2 ml/min were found to be 250 mg/g and 244 mg/g, respectively and at flow rate 0.5 ml/min were 231 mg/g and 168 mg/g, respectively. The Thomas model rate constants increased with increasing flow rate; however, the equilibrium uptake capacity ($Q_{e\ exp}$) decreased with decreasing flowrates. The Yoon-Nelson model decribes the half life of PRGMs before exhaustion i.e half life before regeneration [162]. It was observed that increased flowrate reduced the value of $\tau_{cal}$. However the $\tau_{cal}$ value was lower than the experimental $\tau_{exp}$ obtained from Yoon-Nelson model for both experimental flowrates.

## 5.11 Interaction of Dye with PRGMs

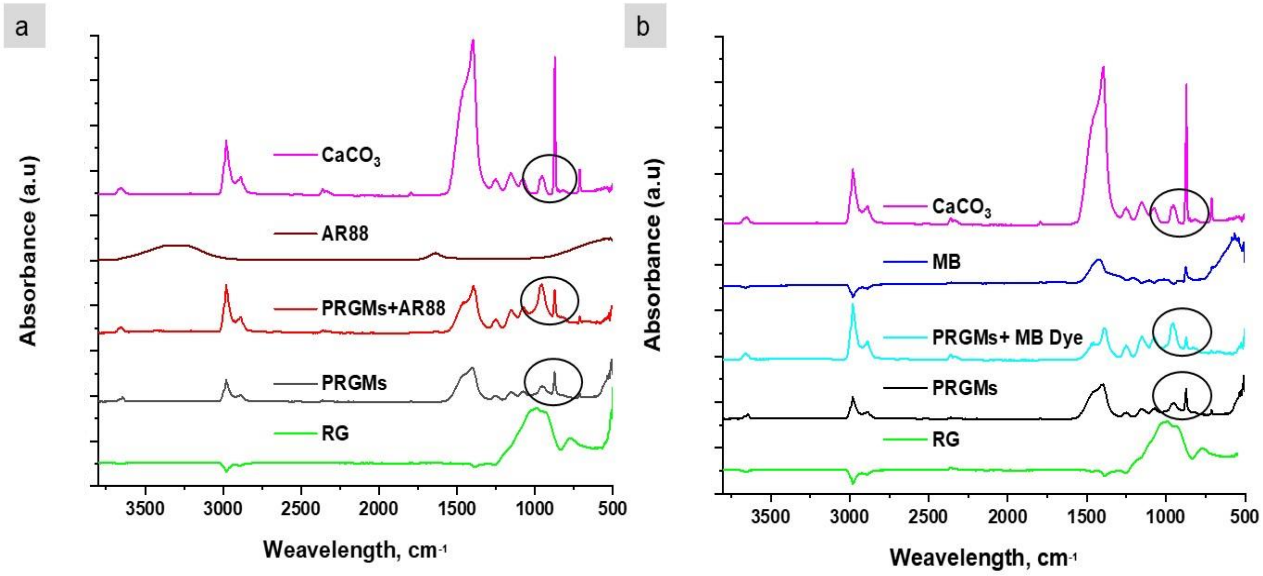



*Figure 5.26: FTIR spectra for PRGMs before and after a) AR88 and b) MB dye adsorption.*

To examine the mechanism of dye interaction with PRGMs, analytical techniques such as FTIR and XPS studies were conducted. Figure 5.26 shows the FTIR spectrum of PRGMs (unwashed) before and after AR88 and MB dye adsorption in batch studies.

An intense absorption at 1400–1500 $cm^{-1}$ along with an adsorption peak at 874 $cm^{-1}$ and 710 $cm^{-1}$ were observed for porogen ($CaCO_3$). These adsorption bands were assigned to stretching of C=O in $CaCO_3$ and $CO_3^{2-}$[436]. These peaks were also present in PRGMs before and after AR88 and MB dye adsorption. However, after dye adsorption a major change in relative absorption intensity at ~ 874 $cm^{-1}$ was observed for PRGMs+AR88 dye and PRGMs+MB dye (see Figure 5.26 a and b) [436]. No noticeable peak shift or change in relative intensity was observed in the rest of the spectrum. The

characteristic adsorption band for AR88 and MB dye were not detected in PRGMs+AR88 dye and PRGMs+ MB dye as a result XPS studies were performed for further investigation.

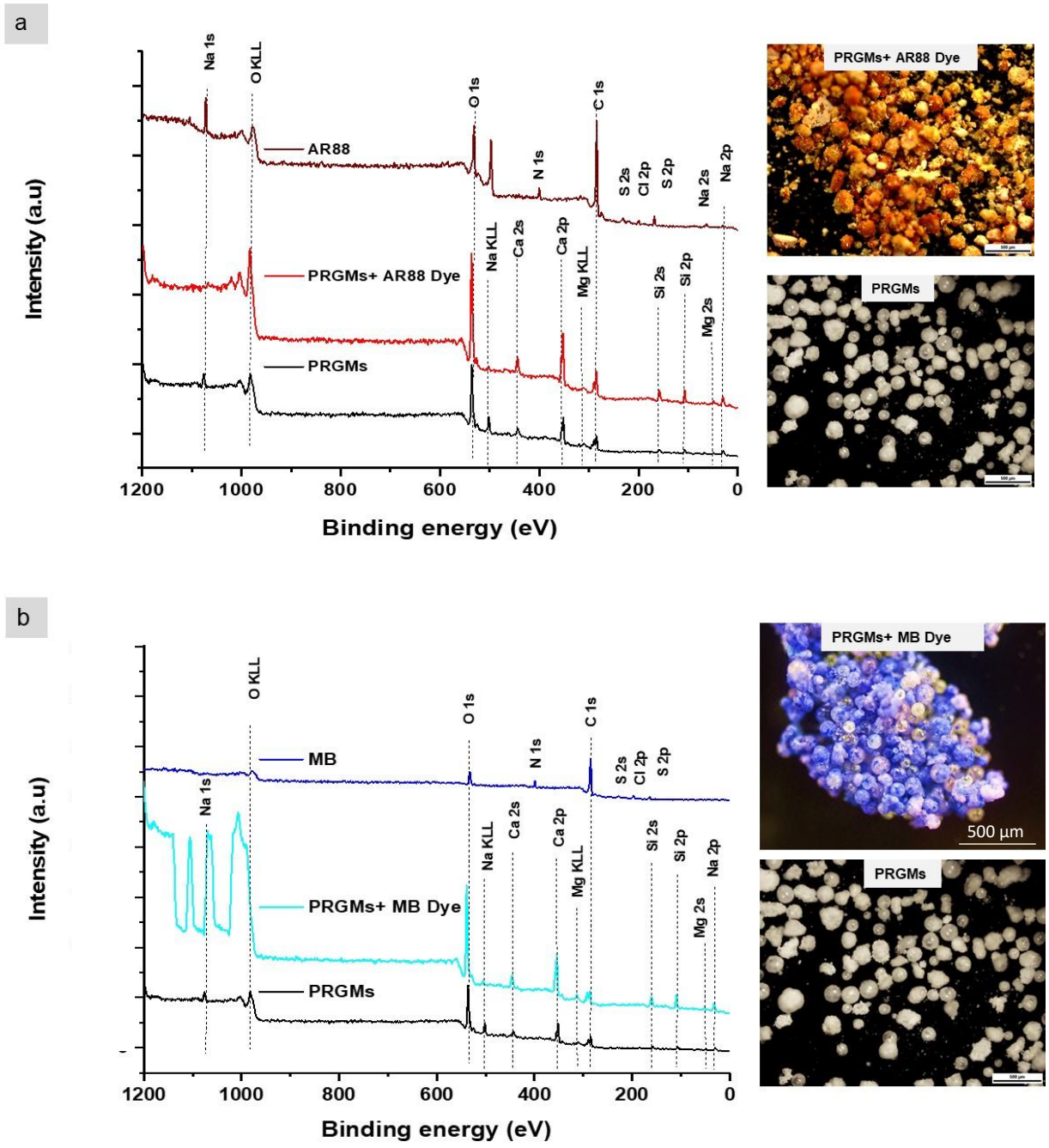



***Figure 5.27: XPS survey scan and optical microscope images for PRGMs before and after a) AR88 and b) MB dye adsorption.***

XPS analysis was performed to investigate dye interaction on the surface of the PRGMs before and after dye adsorption. As shown in Figure 5.27, peaks corresponding to Si 2p, O 1s, C 1s and Ca 2p can be clearly identified in the survey scan spectrum for PRGMs before and after dye adsorption. No

characteristic peak (N 1s, S 2s and S 2p) for AR88 and MB dye were identified on PRGMs after dye interaction. For more detailed analysis, high resolution scan run for UW-PRGMs before and after dye adsorption for each signature characteristic peaks (for C 1s, O 1s, Ca 2p and Si 2p).

Figure 5.28 shows there were two carbon species present in C1s spectra for PRGMs with the

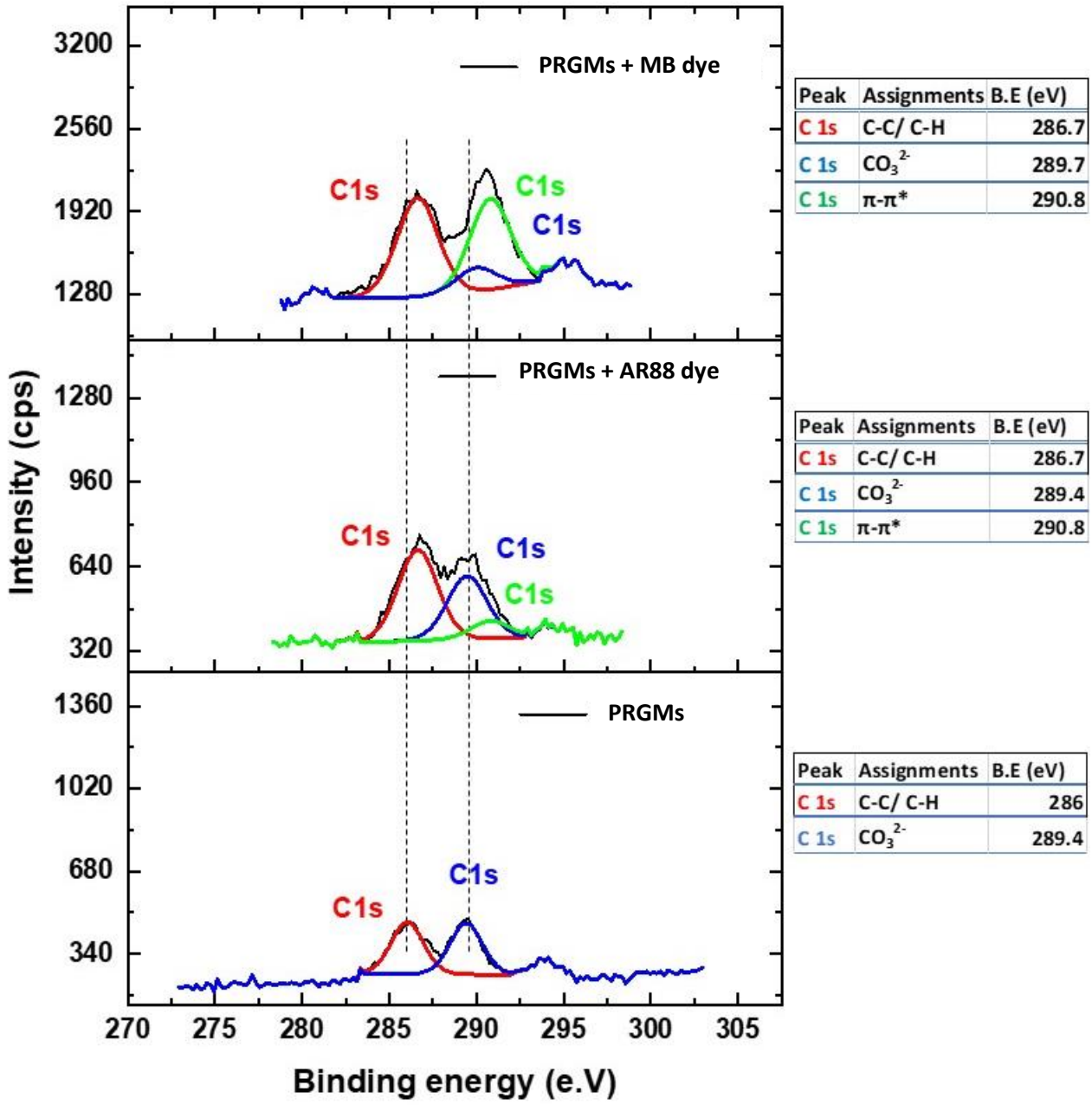



*Figure 5.28: High resolution XPS spectra of C 1s for PRGMs before and after AR88 and MB adsorption.*

corresponding binding energies centred at 286 eV and 289.4 eV. The lowest binding energy represents the carbon on the carbon tab or carbon contamination, whilst the highest binding energy is assigned to carbonate ion from the remnant porogen [437-439]. After dye adsorption one new component of

C 1s appeared at 290.8 eV which corresponds to π–π* transition in aromatic ring for the dyes [440, 441]. Moreover, the peak at binding energy 286 eV and 289.4 eV showed deviation to higher binding energy after interaction of PRGMs with AR88 and MB dye.

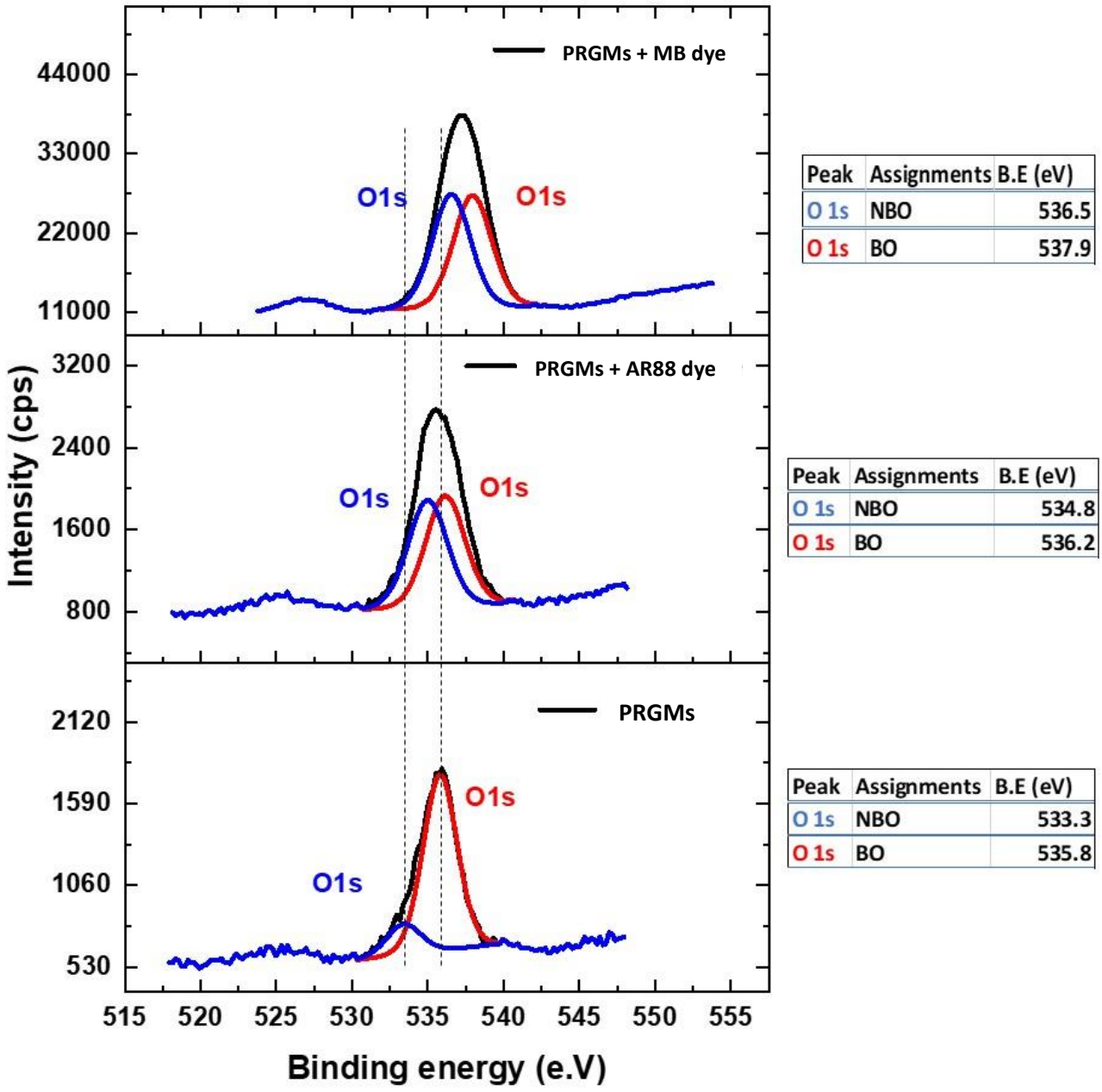
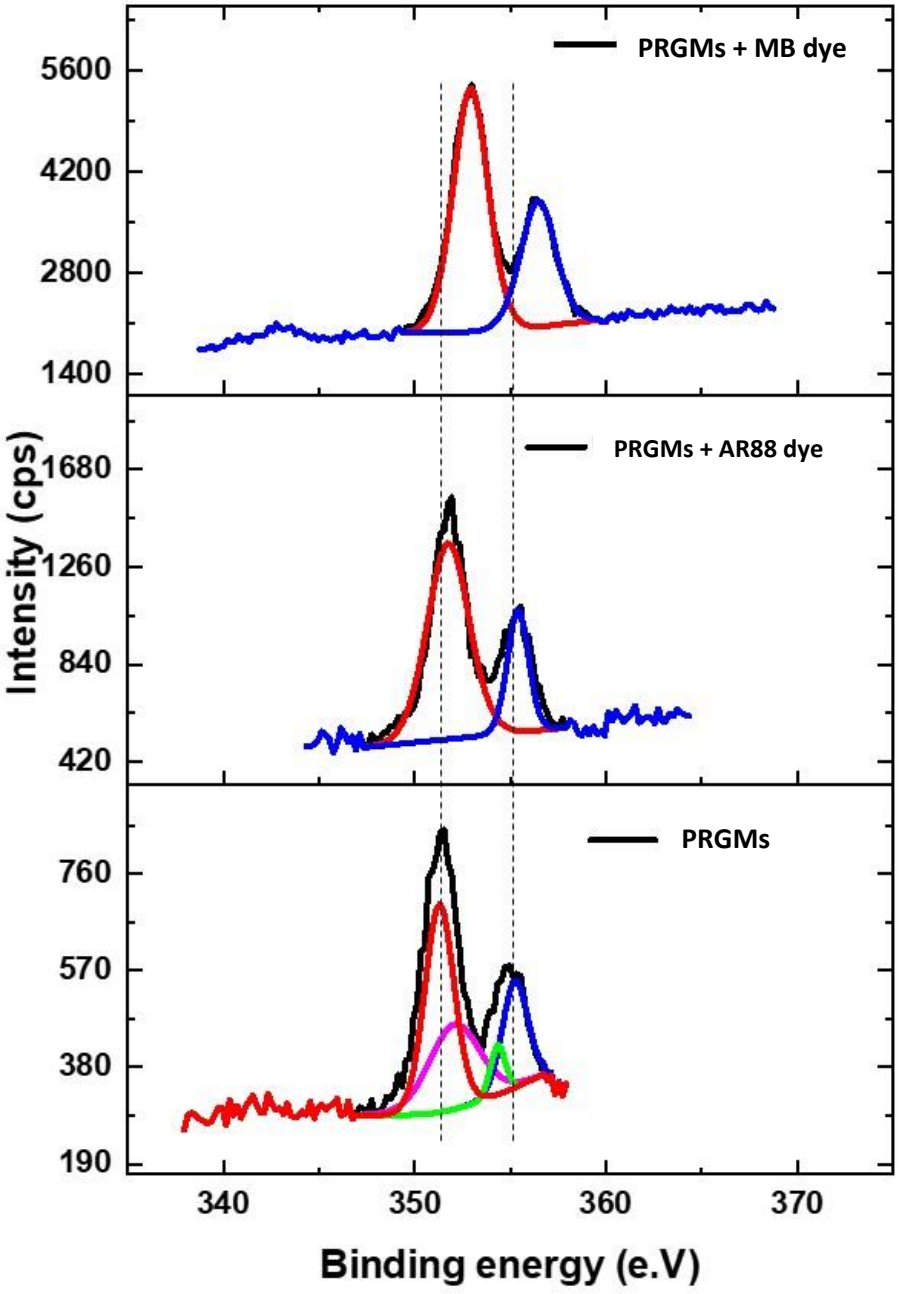



*Figure 5.29 :High resolution XPS spectra of O 1s for PRGMs before and after AR88 and MB adsorption.*

O 1s spectra revealed characteristic peak for PRGMs at 535.8 eV and 533.3 eV for covalently bonded bridging oxygen (BO) atoms that connect two $SiO_4$ tetrahedra; and non-bridging oxygen (NBO) atoms that covalently bonded to one $SiO_4$ tetrahedron and ionically bonded to one alkali (or alkaline earth) ion surface oxygen and lattice oxygen, respectively [439, 442]. A shift to higher binding energy of O 1s

spectrum was observed in PRGMs after AR88 and MB dye interaction. Furthermore, Figure 5.29 showed that the relative peak intensity of NBO increased (with the BO component kept constant) after AR88 and MB dye interaction.

Ca 2p spectra of PRGMs before adsorption (Figure 5.30) was deconvoluted into four peaks: two peaks from Ca $2p_{3/2}$ and another two peaks from Ca $2p_{1/2}$. Ca $2p_{3/2}$ and Ca $2p_{1/2}$ with binding energy at 351.3 eV and 354.3 eV corresponds to Ca in $CaCO_3$ and binding energy at 352.4 eV and 355.3 eV corresponds Ca in PRGMs. After AR88 and MB dye adsorption the central peak for Ca $2p_{3/2}$ and Ca $2p_{1/2}$ also showed a peak shift to higher binding energy.




| Peak | Assignmei | B.E (eV) |
|---|---|---|
| Ca $2P_{3/2}$ | Ca in RG | 352.9 |
| Ca $2P_{1/2}$ | Ca in RG | 356.4 |

| Peak | Assignments | B.E (eV) |
|---|---|---|
| Ca $2P_{3/2}$ | Ca in RG | 351.5 |
| Ca $2P_{1/2}$ | Ca in RG | 355.5 |

| Peak | Assignments | B.E (eV) |
|---|---|---|
| Ca $2P_{3/2}$ | Ca in $CaCO_3$ | 351.3 |
| Ca $2P_{3/3}$ | Ca in RG | 352.4 |
| Ca $2P_{1/2}$ | Ca in $CaCO_3$ | 354.3 |
| Ca $2P_{1/3}$ | Ca in RG | 355.3 |

*Figure 5.30: High resolution XPS spectra of Ca 2p for PRGMs before and after AR88 and MB adsorption.*

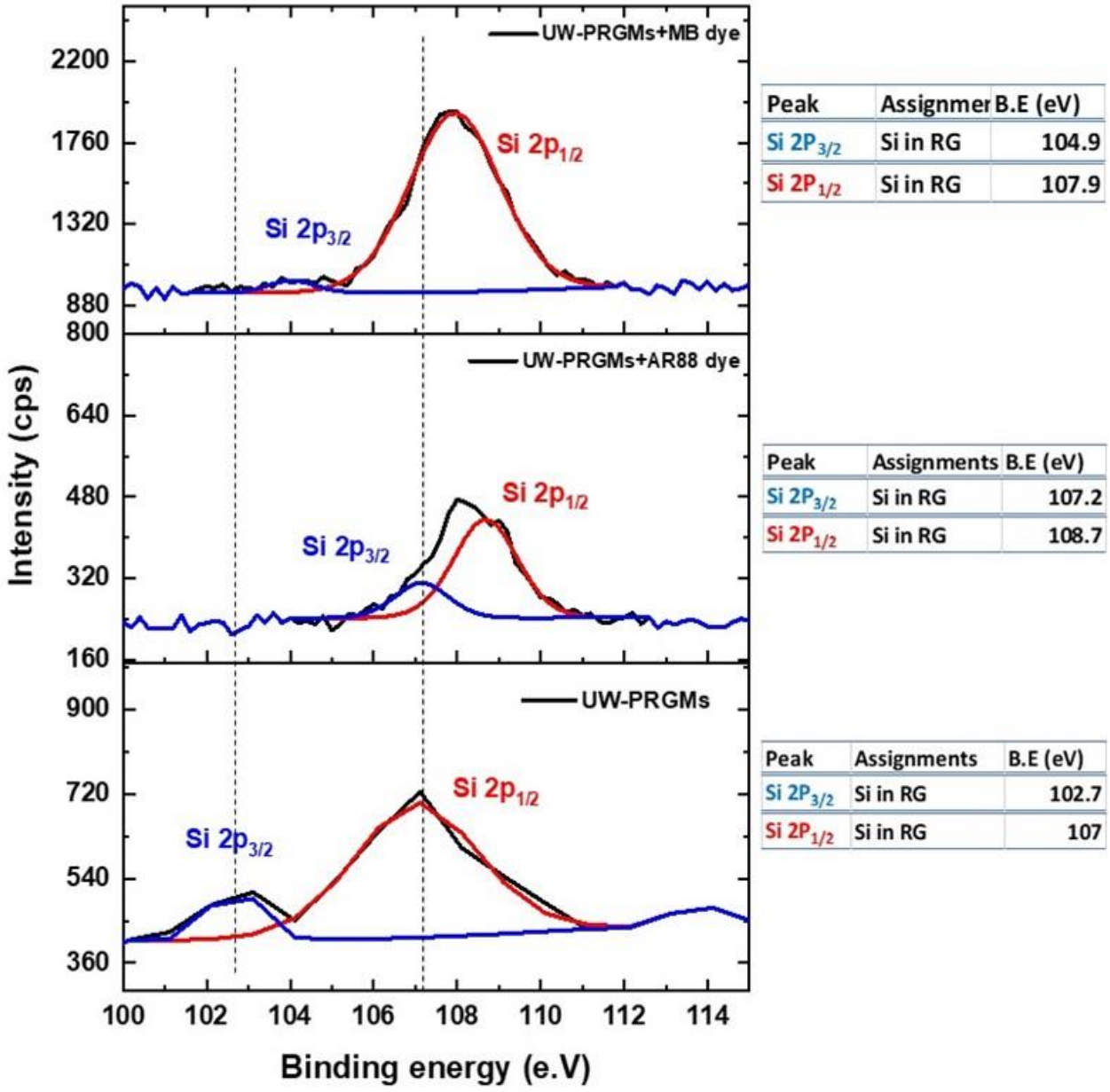



***Figure 5.31: High resolution XPS spectra of Si 2p for PRGMs before and after AR88 and MB adsorption.***

The Si 2p spectra in Figure 5.31 shows two main features assigned to Si $2p_{3/2}$ at 102.7 eV assigned to Si–$O^-$ bond (silicon bonded with NBO) and Si $2p_{1/2}$ at 107 eV for to Si–O–Si bond (silicon bonded with BO) [442, 443]. A closer look into Si $2p_{3/2}$ spectra and Si $2p_{1/2}$ spectra revealed a shift of around 2.2-4.5 eV and 0.9-1.7 eV, respectively toward higher binding energy for PRGMs after dye adsorption.

## 5.12 Reusability of PRGMs

If the adsorbents could be regenerated and recycled after the adsorption process, then this would be highly beneficial for potential sustainable material applications. The reusability of the PRGMs were investigated by repeating 5 cycles of the adsorption–desorption process in our study (Figure 5.32). Adsorbent regeneration was investigated only for AR88 dye as the dye was not the main focus of the experiment, instead establishing a suitable solvent free regeneration process and investigating subsequent performance of PRGMs was the key outcome.

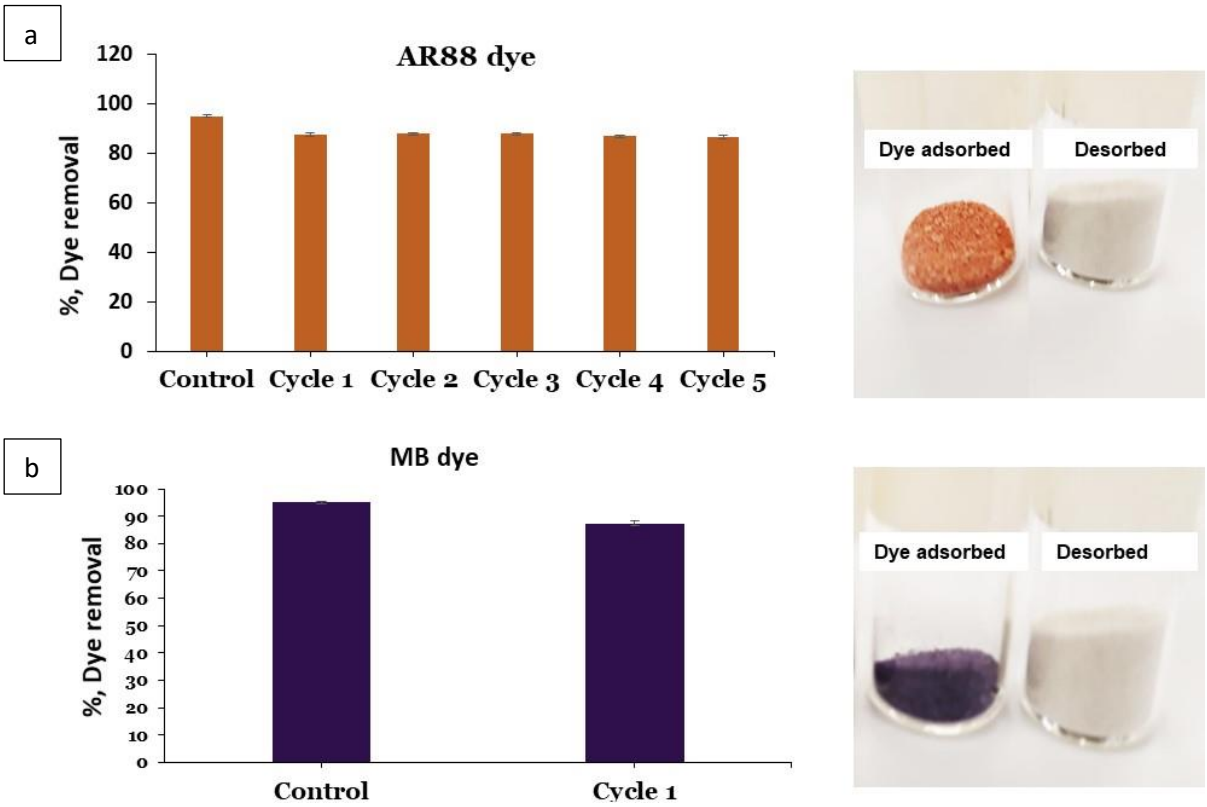



***Figure 5.32: Recycling of the PRGMs for the removal of a) AR88 upto 6$^{th}$ cycle and b) MB upto 1$^{st}$ cycle. (For AR88 $C_0$ = 180 mg/L, Adsorbent dose = 5g/L and pH = 2.5; MB, $C_0$= 25 mg/L, Adsorbent dose = 5g/L and pH =7) with photograph showing microspheres after regeneration.***

For regeneration-reuse/recycling study, a solution of AR88 (180 mg/L) was stirred with 5g /L of porous microspheres until equilibrium was reached. A 1 mL aliquot was taken for analysis and the adsorption capacity was calculated. The dye adsorbed microspheres were heated in a furnace at 400°C for 1hrs to burn off the dyes from the microspheres. DTG and XRD analysis were performed after heating in furnace to confirm the dye was completely removed (see Figure 5.33 and Figure 5.34). These potentially desorbed microspheres were then reused. This process of adsorption-desorption/recycling was repeated with up to 5 cycles.

Initial PRGMs (control) showed AR88 dye removal percentage was 95% ± 0.8 %. After 1st cycle the dye removal % decreased slightly to 87% ± 0.6%. For rest of cycles the dye removal percentage were fairly constant (86-87%). Similarly, PRGMs (control) showed MB dye removal percentage of 92% ± 1 %. After 1st cycle the dye removal was 85% ± 0.6%. These results suggested that heating dye adsorbed PRGMs were an effective process for desorption. The DTG profile in Figure 5.33 revealed that AR88 and MB dyes were volatilized below 400°C. No traces of AR88 or MB were identified after dye desorption. The XRD patterns of desorbed PRGMs were found same as the control PRGMs. However, a decreased peak intensity characteristic for $CaCO_3$ and CaO were observed after desorption (see Figure 5.34 a). Moreover, SEM images revealed that the pores of the PRGMs were closed after dye adsorption which then re-opened after the dye desorption process (see Figure 5.34b).

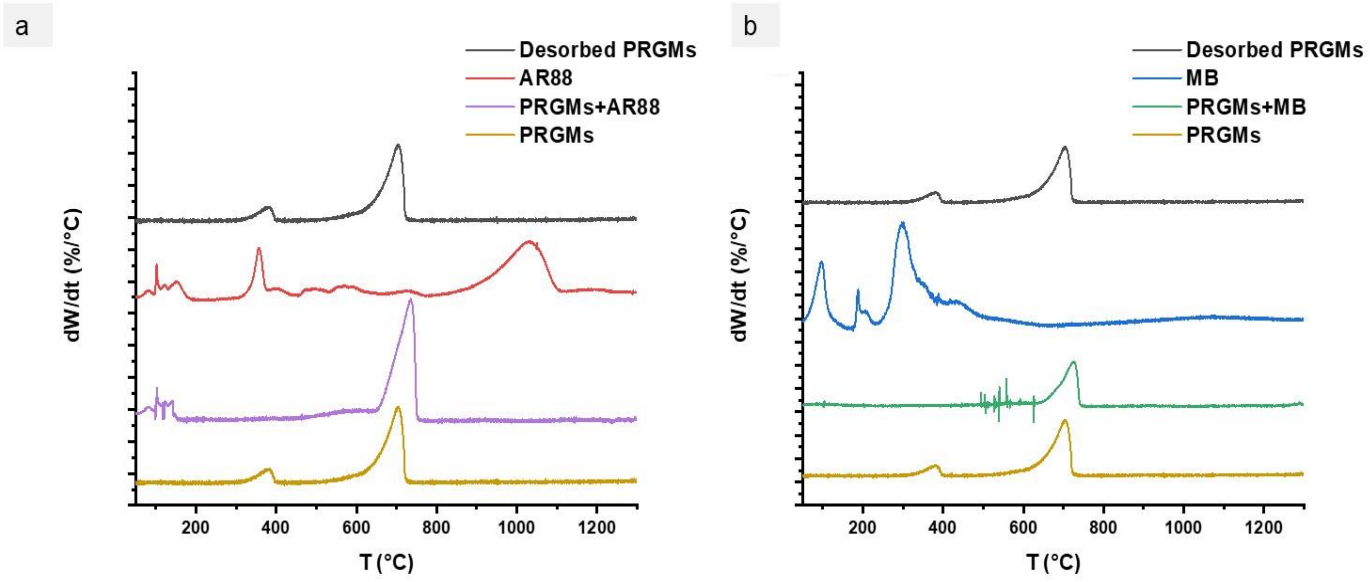



***Figure 5.33: DTG graph of PRGMs with a) AR88 dye and b) MB dye before and after dye adsorption and desorption.***

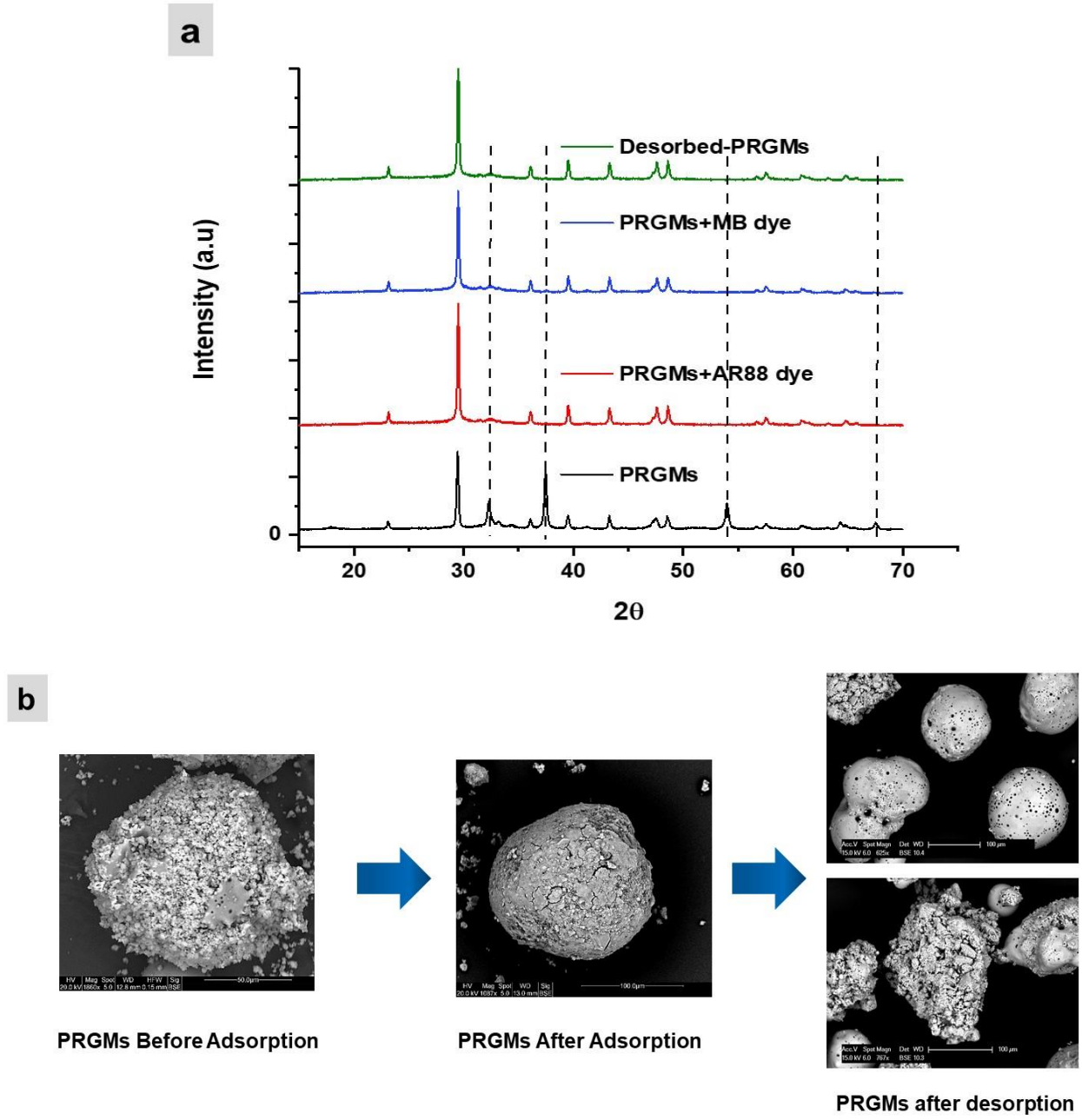



*Figure 5.34: a) XRD patterns and b) SEM images of PRGMs before dye adsorption, after dye adsorption and desorption.*

## 5.13 Discussion

A key goal of circular economy approach is to initiate sustainable manufacturing through conserving energy and natural resources [444-446]. This is plausible by minimising resource consumption, recycling, reclaiming and reusing or upcycling materials [447, 448]. Environmental protection agency (EPA) published in 2018 that glasses alone contributes in 12.3 million tons of municipal solid waste (MSW) generation of which 3.1 million tons recycled, 1.6 million tons were combusted and rest (approximately 7.6 million tons) were landfilled [449, 450]. It is estimated that within 2050, MSW glass will increase by 13% [445]. This chapter aims to demonstrate the reusing and/or recycling waste glass materials (particles) known as recycled glass (RG) particles for alternate applications, in this case we explore wastewater treatment. The manufacturing process of producing porous recycled glass microspheres (PRGMs) has been demonstrated and its potential for removing dyes from water is evaluated.

### 5.13.1 Initial processing trials of RG particles into microspheres using conventional process

RG mainly consists of a silica backbone with alkaline earth oxide glass former and/ or modifiers (as seen Figure 5.5). The SEM images revealed successful manufacture of solid recycled glass microspheres (SRGMs). The glass particles were transformed into solid microspheres due to surface tension during the cooling stage as the molten glass globules were ejected from the flame. However, initial attempts to make PRGMs using our 'Conventional method', following the same parameters for making porous phosphate glass microspheres were unsuccessful. According to Hossain *et al.,* manufacture of porous microspheres via conventional method relies on various factors [309]. These included chemical and physical interaction of the porogen with the glass formulations, glass viscosity, along with both components (porogen and glass particles) being delivered within a suitable thermal processing window and a sufficient residence time within the flame [309, 310]. These initial unsuccessful attempts to develop PRGMs by 'conventional method' are suggested to be due to several factors as seen by comparing RG particles with P40 glass particles. These were

a) RG particles were mixture of colour coded glasses (green, brown and transparent) as can be seen from EDX analysis. Regardless of CaO, MgO, $Na_2O$, $SiO_2$ content; RG contained 0.9-2 % of $Al_2O_3$, 0-0.3% FeO. Variation in metal oxides content influenced the melting point, glass transition temperature and processing window of RG (see Figure 5.4). Several studies have shown that, the melting temperature and glass transition temperature increases with increasing $Al_2O_3$ and FeO content [451-453]. It can therefore be assumed that RG would not have a specific meting point depending on various % content of metal oxides. Whereas, P40

glass particles had uniform glass formulation having a specific melting temperature and glass transition temperature unlike RG.

b) Thermal analysis revealed that RG had higher melting temperature ($T_m$=1250 ± 6°C), compared to P40 glass particles ($T_m$=760 ± 2°C). High melting temperature of RG was attributed to increased silicate content (would increase silicate chain length) and aluminium, iron content (would cause cross linking effect [454, 455]) within glass formulation. This large difference in melting temperature would require utilisation of high temperature flame with longer residence time for the RG particles. Furthermore, the decomposition temperature of the $CaCO_3$ porogen were ~800 °C. This also indicated a larger melting temperature difference between RG particles with porogen whilst this difference was much smaller for P40 glass particles.

c) The interaction of porogen with glass particles were studied by ash fusion test (AFT) study. It was clearly seen that the melting temperature shifted to higher temperature with addition of porogen (at 1:1 ratio) to RG and P40 glass particles compared to RG and P40 without porogen. This could be attributed to the added porogen. However, further studies required to understand the influence of porogen on melt profile by varying the porogen to glass particle ratio. Moreover, while comparing the Softening point temperature (ST), Hemisphere point temperature (HT) and Flow point temperature (FT) for RG+porogen, it appeared that these points were much higher than P40+porogen. This was expected and attributed to the higher melting temperature of RG particles. Furthermore, the temperature difference between HT and FT was 30°C higher for P40+porogen compared to RG+porogen. It is thus be suggested that the temperature difference may be an important consideration for pore formation.

d) It is also suggested that successful development of porous glass microsphere is strongly influenced by material viscosity profile [309]. Viscosity depends on the chemical glass composition and subsequently influences the melting conditions of the glass. It was observed that the viscosity profile for RG (see Figure 5.10) were higher than P40 at equivalent temperatures. This indicated that silicate network has a greater effect on the viscosity than phosphate network. The viscosity profiles for RG and P40 followed similar trends with P45 glasses and silicate glasses investigated by Parsons *et al.* [455]. Additionally, the rate of change of viscosity at FT were ~5175 cP for RG whereas is for P40 this was only ~2136 cP. It is therefore suggested that high viscosity at FT for RG would impede $CO_2$ bubbles escaping from the molten glass particles whilst porogen decomposes and thus hinder pore formation upon cooling. Although, bubbles growth are controlled by a variety of other parameters, such as the

pressure within flame, temperature of the flame, surface tension of glass melt, diffusion coefficient of the gas through glass melt and amounts of porogen etc [456].

e) The unsuccessful formation of PRGMs was initially thought to be due to unsuccessful/insufficient interaction of glass particles with porogen along with secondary factors such as viscosity, high melting temperature of RG etc. In order to improve sufficient porogen particle interaction, the mixture of RG and porogen were ground and mixed with 2% poly vinyl alcohol (PVA) and made into 3D globules (RG-Granular). It was hypothesised that using PVA would help the glass particles to fuse together with the porogen and form porous microspheres by decomposition of the porogen (formation of $CO_2$ gas) inside the granules during flame spheroidisation. The AFT studies showed that RG-Granular samples formed a hemisphere at 1165°C which is 90°C lower than RG+porogen. This suggested earlier melt kinetics due to milling and combining of particles during granulation. König *et al.* investigated waste cathode ray tubes (CRTs) glasses-calcium carbonate using heated-microscope for porous foam preparation [457]. This study also showed that milling of the glass–$CaCO_3$ mixture resulted shifting of the decomposition temperature of carbonate to lower temperature [457]. By milling/grinding the contact area of glass-$CaCO_3$ mixture increased as the particle size decreased [457]. Hence, it could be hypothesised that granulation process allows earlier melting profiles compared to non-granular (conventional process). The RG-Granular samples (prepared using 5 min grinding at 300 rpm for AFT studies) were then spheroidised which revealed successful manufacture of porous microspheres (see SEM images, Figure 5.11).

To optimise the manufacturing process (using alternate granular method) with enhanced separation capability of PRGMs, RG particles were ground with porogen (in ratio 2:1, 1:1 and 1:3) for 1, 5 and 15 mins using 300 rpm and 500 rpm.

### 5.13.2 Processing of RG into PRGMs via alternate granular method

During flame-spheroidisation (FS), the prepared granules were fed into the high-temperature flame (~3100 °C) where rapid melting and some melted glass droplet coalescence occurred. The molten particles spheroidised post exiting the flame due to surface tension. It is considered that porous structures formed due to decomposition of porogen in the form of gas bubbles rapidly escaping at the point of solidification which led to the production of PRGMs exhibiting high levels of interconnected porosity (see Figure 5.11 and Figure 5.12).

SEM images in Figure 5.11 shown that with increasing grinding time (from 1min to 15 mins) and grinding speed (300 rpm to 500 rpm) increased the number of pores and decreased the pore size (PSD

≤ 8 µm at 300 rpm to PSD ≤ 3.5 µm at 500 rpm) while keeping the porogen to particle ratio 2:1. The pore size determined using $N_2$ adsorption desorption analysis showed PRGMs had a pore diameter in a range 23-36 nm. This suggested that PRGMs formed with mesopores (i.e. pore diameter within 2-50 nm). Furthermore, using the t-plot and BJH model, greater micro (≥50 nm) and mesopore sizes for increased grinding time and speed were obtained. This indicated increasing grinding time and speed influenced the pore diameter, pore number and pore volume. For wastewater treatment studies, porous structure with decease in pore size is desired as most of the micro-pollutants are within size range of 10 µm-0.001 µm [370-372]. Moreover, it was reported that pore size could also influence the rate of diffusion of pollutant molecules into the active site of an adsorbent [458]. Furthermore, increase number of pores will allow more separation, or size exclusion to separate micro pollutants from wastewater [459].

The BET surface area of the PRGMs were found to be greater with increasing grinding time and grinding speed with same amount of porogen (at porogen ratio 2:1, BET surface area was 0.03 $m^2/g$ for RG and increased to 1.9 $m^2/g$ for 15 min grinding at 500 rpm). Increasing grinding time and speed would generate particles with smaller size that would have smaller interparticular gaps. These particles would then fuse together during spheroidisation resulting in increased number of pores, hence increase in surface area (see Figure 5.35).

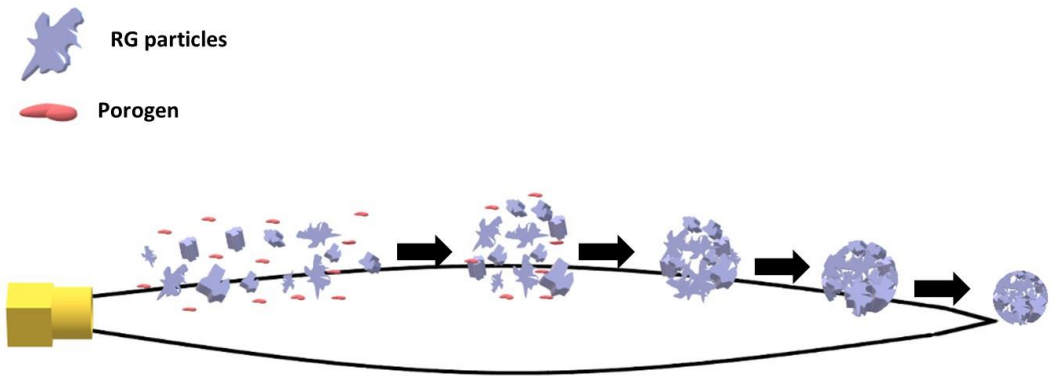



*Figure 5.35: Schematic representation of PRGMs formation via FS processing.*

It was observed that number of external and internal pores of PRGMs increased with increasing porogen ratio. This could be attributed to larger quantity of porogen entrapment leading to higher amounts of $CO_2$ release, forming more pores within the microspheres. Simultaneously, increasing porogen ratio also increased BET surface area of PRGMs (1.9 $m^2/g$ for 2:1 to 7.6 $m^2/g$ for 1:3 porogen ratio). The t-plot and BJH model revealed PRGMs to having greater micro and mesopore volumes as can be seen from nitrogen sorption analysis (see Figure 5.15). This also confirmed that increasing

porogen ratio is associated with increased micro and meso pore volumes. On the other hand, as received RG has shown the lowest BET specific surface area of 0.033 $m^2/g$.

In SEM analysis, smaller dense (55 - 80 µm) microspheres were observed with few/no external pores having dense internal core. These dense microspheres could be produced due to inadequate amount of porogen or due to longer residence time of smaller granules (sieved granules had a size of ≤200 µm before FS) within the flame resulting in complete fusion of the pores.

Mercury Intrusion Porosimetry (MIP) used to accurately determine the large pores and smaller pores which were recorded to have a pore diameter ranged from 5-0.450 µm and 0.450- 0.017 µm, respectively for PRGMs manufactured using 2:1, 1:1, and 1:3 with porosity profile ranging between 65-69%. Greater macropore volume and pore area was observed for PRGMs with porogen ratio 1:3 compared to PRGMs with 1:1 and 2:1 porogen ratio.

Overall, these results clearly demonstrated that processing of RG particles using FS technique generated pores in macropores, microporous and mesoporous range with addition of porogen. Furthermore, generation of porosity and pore sizes of PRGMs depends on several factors such as glass melt profiles, glass viscosity, particle residence time, the grinding time, grinding speed of glass particle with porogen and glass powder to porogen ratio.

### 5.13.3 Factors influencing dye removal by PRGMs

Unwashed PRGMs manufactured using porogen ratio 2:1, 1:1 and 1:3 had greater surface area and porosity, thus were considered for initial dye removal studies. Results have shown that removal of acid red 88 (AR88) and methylene blue (MB) by PRGMs is influenced by dye solution pH, porogen ratio, PRGMs dose, and dye concentrations.

It was observed that increasing porogen ratio favours increased % of AR88 and MB dye removal (see Figure 5.17). This could be attributed either to added porogen to UW-PRGMs and/or to increasing surface area of PRGMs. The XRD traces shown in see Figure 5.16 indicated the presence of residual porogen and CaO in UW-PRGMs. CaO generated due to decomposition of $CaCO_3$ during FS [460]. The % of remnant porogen (as CaO and $CaCO_3$) present in PRGMs was 34%, 39% and 55%, respectively. The adsorption capacity of porogen for AR88 dye estimated in this study was 227 ± 5 mg/g. However, as indicated in isothermal studies that porogen itself does not have any affinity to adsorb MB (see Table 5.7). This is suggesting that the increased removal of dye cannot be solely attributed to porogen rather than as a result of combined effect of porogen content and surface area of PRGMs.

Moreover, the dye removal of PRGMs changed with changing pH for both dyes. Adsorption of AR88 by PRGMs showed an increased adsorption when the pH decreased (≤6) while adsorption of MB showed favourable adsorption at higher pH (≥6). AR88 is anionic dye that contains one sulfonic acid group (R-$SO_3Na$). In aqueous solution, the AR88 dye dissociates to the sodium ion ($Na^+$) and the sulfonate anion (R-$SO_3^-$) [362, 461]. At acidic pH, the sulfonate groups of dye is negatively charged due to their $pK_a$ values lower than zero [362, 461]. This negatively charged AR88 dye which might have electrostatically interacted with positively charged PRGMs (due to protonation, see Reaction 5.1 and 5.2) in acidic pH. When the pH of the dye solution increased, the number of positively charged sites on surface of PRGMs decreases. As in higher pH values, additional $OH^-$anions compete with the anionic AR88 for available active sites on PRGMs [462]. Therefore, there is an increased repulsive electrostatic force between the negatively charged surface of the PRGMs and negatively charged AR88 dye molecules. As a result, % AR88 dye removal decreases with increasing pH. Conversely, MB is a positively charged dye that could have electrostatically interacted with negatively charged PRGMs (due to de-protonation, see Reaction 5.3 and 5.4) in a basic pH.

**For the AR88 sorption in acidic medium**

$PRGMs + H^+ \rightarrow PRGMs–H^+$ ……(Protonation of PRGMs) ***Reaction 5.1***

$PRGMs–H^+ + AR88^- \rightarrow PRGMs–H–AR88$ ***Reaction 5.2***

**For the MB sorption in basic medium**

$PRGMs + OH^- \rightarrow PRGMs–OH^-$……(de-protonation of PRGMs) ***Reaction 5.3***

$PRGMs–OH^- + MB^+ \rightarrow PRGMs–OH–MB$ ***Reaction 5.4***

Although surface charge analysis for PRGMs with varying pH would be considered suitable to understand the influence of pH on dye adsorption. The PZC point / zeta potential of PRGMs was not determined considering the size of the PRGMs and the availability of the analysing equipment.

The dosage of PRGMs was also an important parameter to optimize the adsorption behaviour for removing dyes. The % dye removal efficacy of AR88 and MB dye increased from 1 g/L to 10 g/L with increasing PRGMs dose, and then reached a plateau with no significant change. The removal efficiency of dyes improved by increasing PRGMs loading due to the increased active sites within the PRGMs [462]. The dye removal reached plateau when the available adsorption sites were greater than the adsorbate level (dye concentration) [463].

Adsorption kinetics is an important factor that predicts the adsorption rate of the PRGMs towards dyes. The adsorption kinetics of AR88 on UW- PRGMs revealed complete adsorption within 120 mins for dye concentration 100 mg/L and 200 mg/L. However, at lower dye concentration (50 mg/L) the AR88 dye adsorption was rapid (within 30 mins). A rapid adsorption suggesting active sites with PRGMs were more compared to AR88 dye molecules in solution. With increasing dye concentrations, the number of dye molecules increases compared to number of active sites on PRGMs. Moreover, the equilibrium adsorption capacity ($q_e$) of PRGMs increased with increased dye concentration. This was attributed to the driving force of the concentration gradient increased with increasing the initial dye concentration [464].

The data indicated (see Table 5.5) that the pseudo 1$^{st}$ order reaction equation was not ideal to model the adsorption data of AR88 in UW-PRGMs. Thus, it is hypothesised that the rate-limiting step of the adsorption on PRGMs is mainly chemical process (as fitted to pseudo 2$^{nd}$ order) which could involve electron sharing or exchange via electrostatic attraction, hydrogen bonding, covalent bond, ionic bond formation, between the adsorbate and the active site of an adsorbent surface [465]. Additionally, pseudo 2$^{nd}$ order rate constant ($k_2$) decreased with increasing initial concentrations of AR88 dye. This again was related to the availability of active adsorption sites decreasing with increasing dye concentrations [464, 466].

In isothermal studies, the $R^2$ values of the Freundlich model was higher than Langmuir model for adsorption of AR88 dye. This indicated multilayer adsorption for the AR88 dye on the active sites within PRGMs [467, 468]. Isothermal study indicated that porogen itself had an affinity to adsorb AR88 dye (see Chapter 4, result 4.2). UW-PRGMs consists of approximately 55% of remnant porogen based on XRD analysis (see Figure 5.16). This suggests that adsorption of AR88 could be due to porogen. However, it was seen that AR88 dyes were coagulated by W-PRGMs (PRGMs without remnant porogen) during isothermal studies. To simulate coagulation, Jar tests were conducted for W-PRGMs and UW-PRGMs at same pH that was used for isothermal studies. It was observed after coagulation that the % dye removal for W-PRGMs and UW-PRGMs were ~96% and ~91% respectively. Hence, PRGMs act as a coagulant and presence of porogen in PRGMs slightly decreased the coagulation process. Hence, the dye removal of AR88 dye by PRGMs were not solely attributed to porogen only.

In contrast, the $R^2$ values of the Langmuir model was higher than Freundlich model for adsorption of MB dye. This indicated homogeneous adsorption for the MB dye on the active sites within PRGMs [467, 468]. Furthermore, isothermal studies showed that porogen has no affinity to adsorb MB dye. Thus, it could be suggested that adsorption of MB dye (see Table 5.7) was due to surface properties of PRGMs. The maximum monolayer adsorption capacity ($q_m$) calculated for UW-PRGMs was 78 mg/g

and 20 mg/g for AR88 and MB dye, respectively. The adsorption capacity of AR88 was much higher than that of MB. The greater affinity of AR88 onto PRGMs than that of MB can be attributed to the chemical structure, surface charge as well as solubility of the dyes. In general, adsorption capacity on an adsorbent is influenced by molecular size and aromaticity, and by solubility, polarity and carbon chain branching in dyes [3]. Whilst both dyes are water soluble, AR88 has larger molecular size than MB and the smaller molecules would find more accessible pores for adsorption. However, AR88 is negatively charged dye contains more benzene rings and accessible oxygen groups (see Figure 5.36), which might increase the adsorption capacity on PRGMs. In such regard, considering dyes of similar surface charge having different dye molecule size and surface groups for adsorption on PRGMs would be considered for future studies.

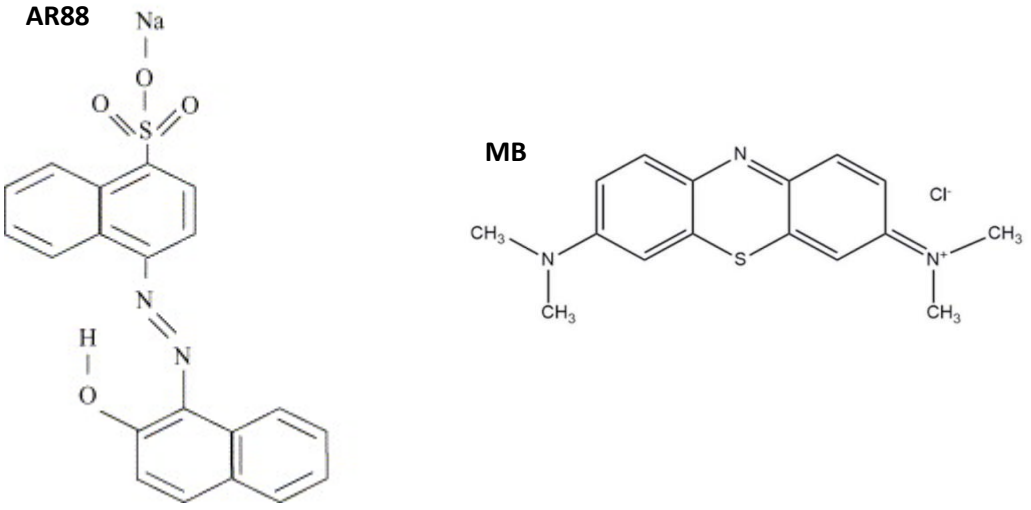



*Figure 5.36: Structure of AR88 [469, 470] and MB [470].*

Column adsorption process requires prediction of the breakthrough curve for the experimental data through mathematical models for describing and analysing the lab-scale column studies for the purpose of industrial applications [471-473]. In this study, the breakthrough curves were fit by linear regression to the Thomas, Adams-Bohart and Yoon-Nelson adsorption models for predicting dynamic behaviour of the fixed-bed column [474-476]. The Adams-Bohart model was the least appropriate equation for modelling the adsorption in these column experiments based on $R^2$ values (see Table 5.9). This is primarily due to the fact that the Adams-Bohart model is best used for modelling early stages of adsorption and the lower end of the ideal breakthrough curve [477]. Therefore, the Adams-Bohart model cannot be considered useful for modelling the adsorption data in this research.

The Thomas model assumes a reversible pseudo 2$^{nd}$ order reaction and Langmuir adsorption characteristics and found more appropriate fit to the experimental data [478]. Based on Thomas model it is possible to predict that adsorption would not be controlled by the chemical reaction, but by mass transfer at the interface [479, 480].

Flow rate determines the sufficient contact between adsorbate and adsorbent. Hence considered as an important factor affecting the efficiency of fixed bed column [478, 481]. The maximum adsorption capacity ($q_{eq}$) of the microspheres using the column process increased with increasing flow rate as seen from the Thomas model. However, in most literatures the adsorption capacity of a column decreased with increasing flow rate [478, 482, 483]. Only few authors reported increased column adsorption with increasing flowrate [484-486]. Column adsorption is based on complex phenomena such as axial dispersion, film diffusion resistance, intraparticle diffusion resistance (both pore and surface diffusion) and adsorption equilibrium with the adsorbent [487, 488]. In a column process an adsorbate molecule must diffuse through the fluid film surrounding the adsorbent, travel by diffusion along the length of a pore until it finds a vacant active site for adsorption. In general, increasing the flow rate will decrease the film thickness and film resistance around adsorbent. Aroonwilas *et.al.* reported increased adsorption contributes to by hydrodynamics of the column, which reflects the effective mass-transfer area (surface area) provided by packing [489]. Furthermore, Yu *et.al.* while studying ammonia gas adsorption reported that the effective surface area of the column increases with increasing solvent flow rate [490]. It is expected that at a high flowrate creates more turbulence within the column [491]. Under the turbulence mixing, the film around PRGMs would be thinner and more dyes could be transported to the surface [492]. Thus, there would be an increase in contact area for mass transfer process with increasing flowrates. Moreover, increased mass transfer/diffusion through inter- pore (inside microspheres) was achievable when the microspheres were more closely packed together [423]. Consequently, the overall adsorption capacity would increase with increasing flowrates, despite decreasing empty bed contact time (EBCT) or residence time. However, it is worth mentioning that the HPLC pump used for the experiment could not operate below 0.5 ml/min for a EBCT of 5 min. In this study only two different flowrates were explored. To understand more, it would be necessary to operate adsorption column with varied flowrates to explore the influence of mixing rate more detail.

The Yoon–Nelson model presented the 50% exhaustion time *τ decreased* with the increase in the flow rate as the saturation of the column occurred more rapidly. Moreover, from the Thomas model, the Thomas rate constant ($k_{th}$) increased with increased flowrate indicating the column reached equilibrium more quickly. However, implications of the kinetics parameters identified from the

Thomas model and Yoon–Nelson model are inconclusive due to the fact that none of the models fit well with the experimental data (<0.80). There were significant discrepancies observed between the calculated data and experimental data for column adsorption process. The Yoon-Nelson and Thomas models only provided an indication that increased flowrate and reduced EBCT could affect adsorption of AR88 onto PRGMs.

However, from the accumulated evidence, the proposed mechanism is column process is thought to be complex and could involve combination of several mechanisms including, adsorption and coagulation/ filtration process.[493] Netpradit *et.al.* reported while studying adsorption of reactive dye in a column system that in a down-flow system (where dye is flown in the direction of gravity), the adsorbent can serve for adsorption and filtration of wastewater [494]. Qi *et.al.* studied graphene oxide/chitosan sponge for column performance and stated the material acted as a filtering material for removing MB from water while an adsorbent in batch process [495]. In another study reported by Dimitrova *et al.* mentioned coagulation effect of granular slag in column for lead removal [496]. PRGMs were explored as a coagulant for AR88. However, the coagulation kinetics is much slower than the adsorption process. Thus, dye removal mechanism cannot result solely via coagulation. Furthermore, an increase in adsorption capacity was observed while comparing the batch adsorption process (Table 5.6, Table 5.7 and Table 5.9), i.e., $q_e$ at batch study was 98 ± 4 mg/g, whereas in column testing $q_{eq}$ was <200 mg/g for UW-PRGMs. In column process the PRGMs are packed in the column providing more area of contact (interfacial area) for adsorption. Hence, more mass transfer/diffusion through interconnected pores (inside microspheres) would be achieved when the microspheres were more closely packed. Such packing will account for more accessible pores with increase in effective surface area of contact for adsorption/filtration. Overall, it can be assumed that a synergistic effect of adsorption/coagulation followed by filtration process is responsible for showing discrepancy from the experimental value in column process.

### 5.13.4 Dye removal mechanism and desorption study

Batch adsorption process involves three main steps:

1. Migration of solute molecules (dye) from the solution to the boundary layer of adsorbent particle (known as external mass transfer).
2. Diffusion of adsorbate molecules to the surface and interior pores of adsorbent particles (intra-particle diffusion).
3. Physical or chemical attachment of these penetrated molecules to the active sites (adsorption) [497, 498].

Depending on the adsorbent-adsorbate type, interaction with the active sites could be explained by the hydrophobic and hydrophilic interaction theory, molecular polarity theory, electrostatic interaction theory, the electron donor-acceptor interaction theory, π-π dispersion theory [499, 500]. Besides active site interactions, adsorbent surface area, pore size distribution and pore structure of the adsorbent material also plays a decisive role to its adsorption properties [500, 501]. In this study, to explore the interaction mechanisms of AR88 and MB dye with PRGMs, FTIR and XPS analysis of UW-PRGMs post adsorption were conducted.

XPS high resolution scan for C1s of UW-PRGMs after AR88 and MB dye adsorption revealed presence of new peak corresponded to C-O for AR88 and either C-N or C-S for MB. Moreover, the centre of C1s peak deviated to higher binding energy after adsorption. This would indicate possible dye interaction with the surface of PRGMs through C-OH linkers for AR88 and C-N/C-S terminal for MB dye (see Figure 5.28). Moreover, high resolution O1s spectra revealed a peak shift to higher binding energy with increased relative peak intensity of a non-bridging oxygen (NBO) after dye adsorption. Suzuki *et. al.* reported hydroxyl group involved in the silicate network structure (Si–OH) can be classified as a NBO while studying low temperature porous glass fabrication by hydrothermal reaction [502]. As highlighted earlier, dye adsorption was influenced by change in pH. With an acidic pH, protonation ($H^+$) of PRGMs might occur due to ionic exchange between the $H^+$ of the solution and the modifying ions ($Na^+$ and $Ca^{+2}$) present in the glass network. It could be suggested due to protonation of PRGMs the intensity of NBO increased according to Reaction 5.5. As such, AR88 dye was adsorbed through hydrogen bonding via electro negative oxygen terminal of the dye and hydrogen on PRGMs.

$$\text{-SiO- + } H^+ \rightleftharpoons \text{-SiOH} \qquad \textit{Reaction 5.5}$$

At basic pH the surface of the PRGMs deprotonate which could result in possible hydrogen bonding via MB dye and the surface of PRGMs is enhanced based on the following Reaction 5.6:

$$\text{-SiOH + } OH^- \rightleftharpoons \text{-}SiO^- + H_2O \qquad \textit{Reaction 5.6}$$

In high resolution Ca 2p spectra of PRGMs after AR88 and MB dye adsorption shown peak shift to higher binding energy for the central peak for Ca $2p^{3/2}$ and Ca $2p^{1/2}$. As illustrated in FTIR analysis that after dye adsorption a major change in relative absorption intensity at ~874 $cm^{-1}$ was observed for PRGMs + AR88 dye and PRGMs + MB dye (see Figure 5.26). Both XPS and FTIR results indicated possible interactions of dyes with the porogen or Ca withing silicate glass. However, it was evident that porogen does not have any affinity to adsorb MB. O 1s spectra showed possible hydrogen bonding via Si-NBO site with MB dye. Thus, it is suggested that deviation to higher binding energy for Ca 2p was due to hydrogen bond formation with MB.

Furthermore, the Si 2p spectra revealed that there is a shift of around 0.9-1.7 eV and 2.2- 4.5 eV, Si $2p_{1/2}$ and Si $2p_{3/2}$, respectively. Furthermore, the deviation for Si $2p_{1/2}$ (silicon bonded with BO) was higher than Si $2p_{3/2}$ (silicon bonded with NBO). This indicates possible electrostatic dye interaction with the surface of PRGMs.

Overall, the selective adsorption of AR88 and MB dye on PRGMs depends on its surface charge for electrostatic attraction. The mechanism of adsorption of dyes on PRGMs surface can be summarised in the following steps: in the first step, the $H^+$/ $OH^-$ ions (pH dependent) interacts with PRGMs and forms charged monolayer. Therefore, electrostatic attraction between oppositely charged surfaces were primarily responsible for adsorption of dyes. Besides electrostatic interaction, XPS studies also revealed possible Hydrogen bonding with the dye molecules. Furthermore, the interaction of porogen with AR88 could be suggested while the adsorption. However, for MB dye adsorption could have been a combination of many factors, such as surface area, surface hydroxyl density for possible hydrogen bonding, surface charge for electrostatic interaction.

Reuse of PRGMs is necessary to reduce costs as well as to preserve the environment. For this purpose, to recycle PRGMs, desorption of the dye and the reuse of the spent PRGMs (after desorption) in consecutive cycles were studied. It was apparent that desorption via heating were proved effective for desorbing AR88 and MB dye. For both dyes PRGMs were heated in the furnace for 1 hr at 400 °C. TGA/DTA analysis revealed that MB and AR88 dye completely decomposed after 350°C (see Figure 5.33). The adsorption efficiency decreased after 2$^{nd}$ cycle (% dye removal reduced to 87% from 95%) and remained constant for rest of the cycles (experiment conducted up to 5$^{th}$ cycle). This decrease in dye removal efficiency could be related to the decrease in adsorbent sites, the blockage of pores and loss of adsorbent after each adsorption recovery cycle [503]. However, SEM images revealed opening of blocked pores after desorption. In such regards one possibility would be reduced content of porogen after 1$^{st}$ adsorption cycle. As the desorption studies conducted for UW-PRGMs which contained remnants of porogen. Hence, 1$^{st}$ cycle adsorption process could have lost some remnant porogen. Moreover, PRGMs exhibited a melting temperature of ~1250°C. Therefore, there is no possibility of losing PRGMs after heating. XRD results showed that after desorption no change of phases were visible. In general, heating adsorbed PRGMs indicated that PRGMs can be successfully reused several times. In such regard, as an alternative dye desorption/regeneration process, re-spheroidisation could be considered for PRGMs with having the advantage of re-processing these materials withing milli seconds.

## 5.14 Summary

This research was undertaken to manufacture porous recycle glass microspheres (PRGMs) from recycled glass (RG) using flame spheroidisation technique and to evaluate its applicability for water treatment applications. According to SEM imaging, the conventional manufacturing process was not suitable to manufacture PRGMs. EDX, AFT, thermal and viscosity analyses demonstrated that development of PRGMs were influenced by factors such as high melting temperature of RG, high viscosity of RG at melting point, large difference between melting point of porogen and RG and insufficient interaction between porogen and RG. The investigation of AFT study has shown that RG-Granular samples formed a hemisphere at 1165°C which was 90°C lower than RG+porogen samples. Taken together, these findings suggested that conventional process was unsuitable and alternate granular method was applied for manufacturing PRGMs.

In granular method, porogen/RG glass mixtures were ground at different time and speed (300 and 500 rpm, for 1 to 15 min.) and mixed with 2% poly vinyl alcohol (PVA) and made into 3D globules (RG-Granular) for spheroidisation. The surface area, porosity and pore size distribution were influenced by the grinding time, grinding speed and porogen to glass particle ratio. Increasing grinding time and porogen ratio revealed an increased specific surface area (from 0.03 to 7.6 $m^2/g$) of PRGMs. Mercury intrusion analysis revealed PRGMs with 63-65 % porosity having large and smaller pore diameter ranged from from 5- 0.450 µm and 0.450- 0.017 µm, respectively.

The dye removal capability of PRGMs for two types of dye (AR88 and MB) from water were investigated. A range of factors such as pH, adsorbent dose, dye concentration influenced the adsorption kinetics and efficacy of the PRGMs. The optimum PRGMs (Unwashed) dose used were 10 g/L and 6 g/L and pH were 2.5 and 7 for AR88 and MB dye, respectively. Adsorption kinetics and isotherm models (including the pseudo-first-order, Langmuir and Freundlich models) were used to fit the experimental data, and to help with the mechanistic discussions. The maximum monolayer adsorption capacity ($q_m$) calculated for UW-PRGMs were 78 mg/g and 20 mg/g for AR88 and MB dye, respectively. In batch adsorption and coagulation was observed for AR88 dye removal whilst MB dye removal capacity was attributed to only adsorption process. XPS and FTIR study further confirmed that the adsorption process was due to electrostatic interaction and hydrogen bond formation.

The column adsorption study for RG, washed and unwashed PRGMs demonstrated successful removal of AR88 dye. The adsorption capacity increased with increasing flowrate which were 381 (±3) mg/g, 305 (±3) mg/g and 42(±3) mg/g for unwashed, washed PRGMs and RG respectively. The breakthrough Adams-Bohart and Yoon-Nelson adsorption models indicated that increased flowrate and reduced

EBCT could affect adsorption of AR88 onto PRGMs. However, the results have shown significant discrepancy between calculated and experimental data. Thus, a synergistic effect of adsorption/coagulation followed by filtration process had been considered responsible for column adsorption process.

The reusability of the PRGMs were investigated by repeating $5^{th}$ cycles of the adsorption–desorption process. The PRGMs loaded with dye could be regenerated efficiently using 1 hr of heating in the furnace at 400 °C. After desorption, TGA analysis confirmed that MB and AR88 dye were completely decomposed after 350°C. PRGMs showed good recovery with almost stable efficiency (86-87%) for the second to fifth adsorption/desorption cycles.

# Chapter 6: Developing porous microspheres from natural magnetite

## 6.1 Introduction

Magnetite ($Fe_3O_4$) is a natural magnetic material found in nature, has many advantages such as availability, low cost, ecological friendliness and non-flammability [504, 505]. In this context, the use of natural substances represents a good contribution for sustainable manufacturing. This chapter demonstrates a novel manufacturing method for synthesis of $Ca_2Fe_2O_5$ from a mixture of $Fe_3O_4$ powder/$CaCO_3$ porogen with potential for wastewater treatment applications. The structural, morphological, surface area and porosity profile of microspheres were tailored by varying manufacturing parameters such as effect of particle milling and varying porogen ratios. Furthermore, the adsorption property of microspheres was investigated using anionic acid red 88 (AR88) dye and cationic methylene blue (MB) dye.

## 6.2 Results

### 6.2.1 Structural and Compositional analysis of initial (as received) magnetite particles

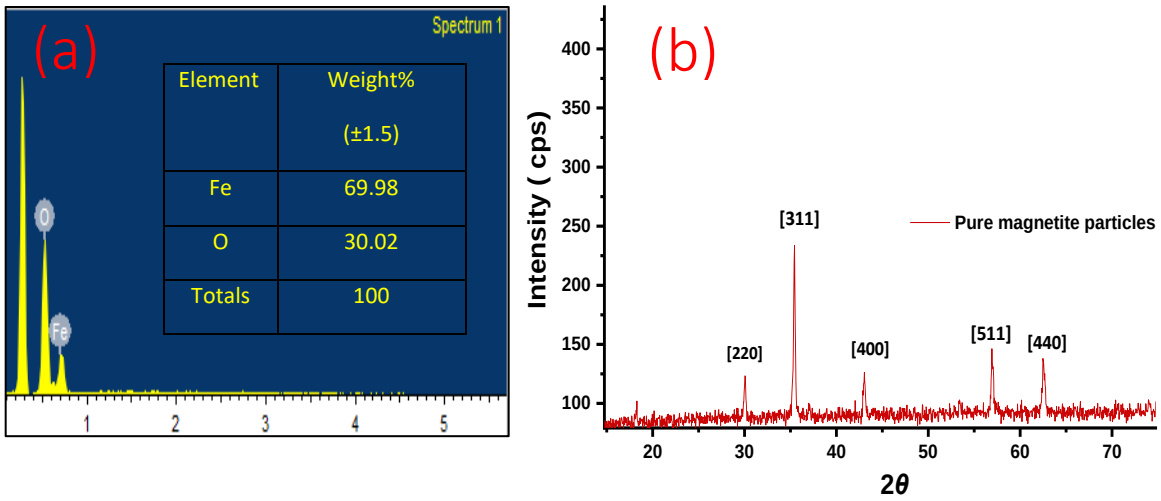



***Figure 6.1: a) EDX spectrum & b) XRD analysis of irregular shaped as received magnetite ($Fe_3O_4$) particles (size <45um).***

EDX and XRD analysis was conducted to investigate the composition and structure of as received magnetite particles. EDX spectrum (see Figure 6.1a) showed that the magnetite contained 69.98% (±1.5) of iron (Fe) and 30.02% (±1.5) of oxygen (O) with no noticeable impurities. A sharp dominant crystallographic peak was observed in the XRD pattern at $2\theta \approx 35.5°$ which corresponded to the crystal plane [311] characteristics for $Fe_3O_4$ (magnetite) (see Figure 6.1b). All other diffraction peaks with

crystal plane [220], [400], [511] and [440] also matched well with the normal characteristic diffractions pattern of the $Fe_3O_4$, magnetite (JCPDF No. 89-0691).

### 6.2.2 Solid magnetite microsphere manufacture

The SEM images and the size distribution of magnetite solid microspheres (MSM) prepared via flame spheroidisation process are presented in Figure 6.2. The morphologies of the MSM evaluated revealed spherical morphology. Upon closer inspection, some of the surfaces of MSMs exhibited either a smooth surface and others with grooves which looked like a series of small particles had agglomerated and fused together into spherical shape (see Figure 6.2). A broad size distribution of MSM with sizes ranging between 30 (±10) µm and 50 (±10) µm were obtained. Semi-quantitative analysis from XRD showed ~ 87% magnetite and ~13% hematite ($Fe_2O_3$) from the MSM produced.

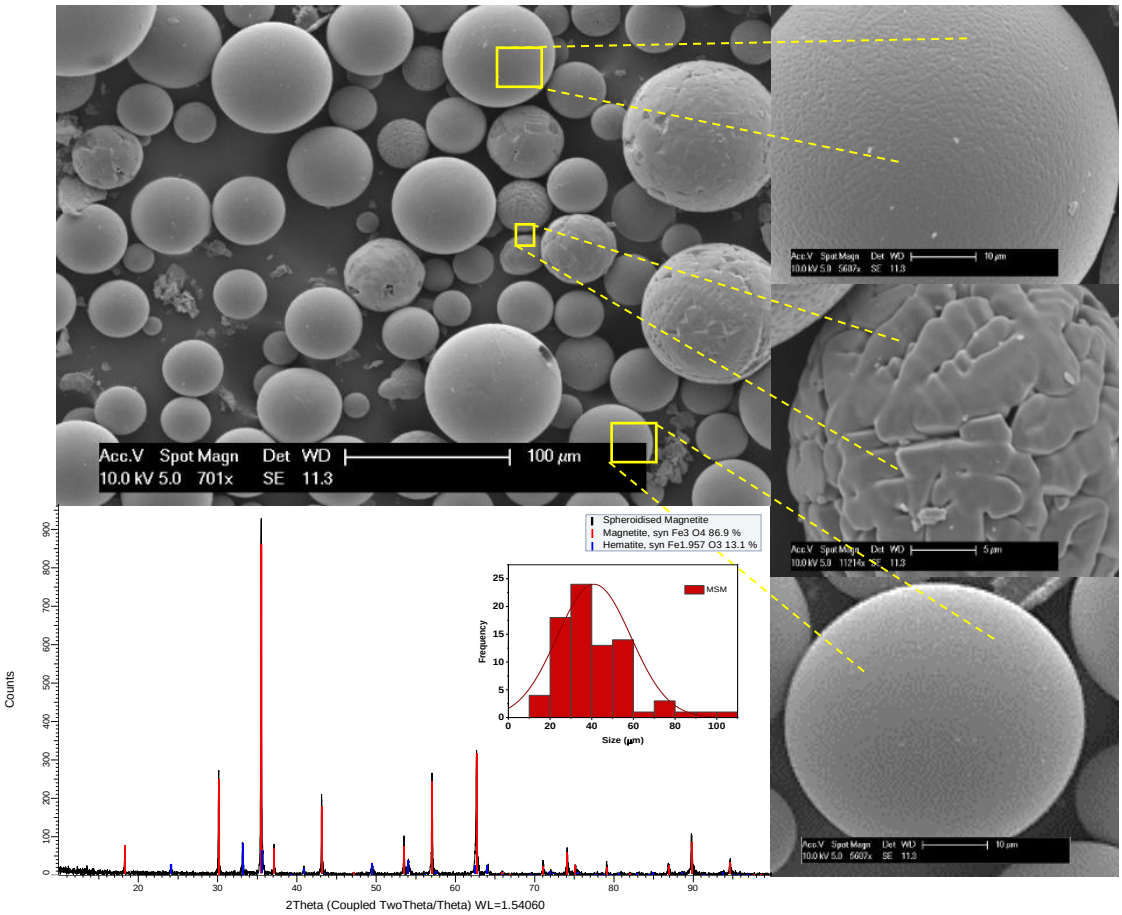



***Figure 6.2: SEM images, XRD profile and particle size distribution histogram for MSM.***

### 6.2.3 Developing porous magnetite microspheres

Manufacture of porous magnetite microspheres (PMMs) were initially investigated via conventional flame spheroidisation processing route using the same parameters i.e. particle to porogen ($CaCO_3$)

ratio (1:3) and gas flow rate ratio (3:3) as used for making porous phosphate glass microspheres. However, the initial trials using this process were unsuccessful (see Figure 6.3). To introduce porosity, novel granular processing method was then explored to prepare PMMs by modifying the initial conventional processing route. Initial feasibility studies using granular (150-200 µm) particles were carried out by grinding magnetite (<45 µm) with porogen (< 5 µm) using 2 % polyvinyl alcohol (PVA) solution to aid binding of the particles. Figure 6.4 (a and b) shows the SEM and cross-sectional images for the samples prepared using 5 min ball milling. Open surface pores with internal porosities were observed for PMMs as presented in Figure 6.4. However, some of the microspheres remained solid with dense solid cores.

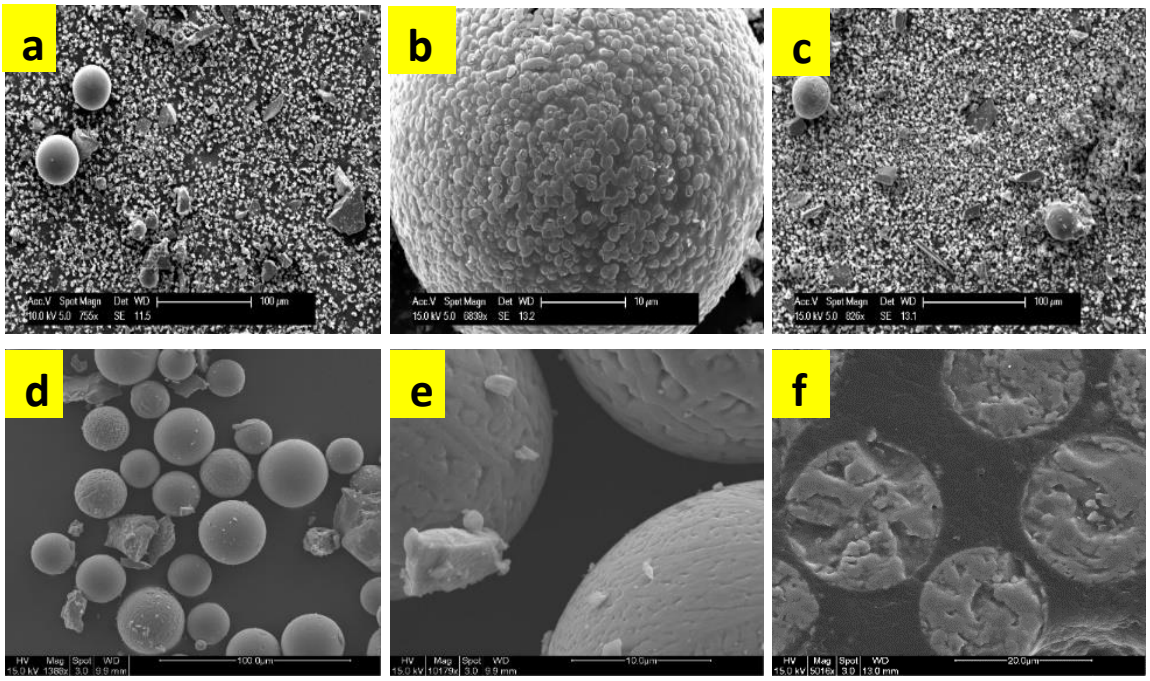



*Figure 6.3: Initial attempts to prepare PMMs using conventional process a), b) and c) unwashed samples and d) and e) magnetite samples after acid wash and f) cross section of acid washed magnetite sample.*

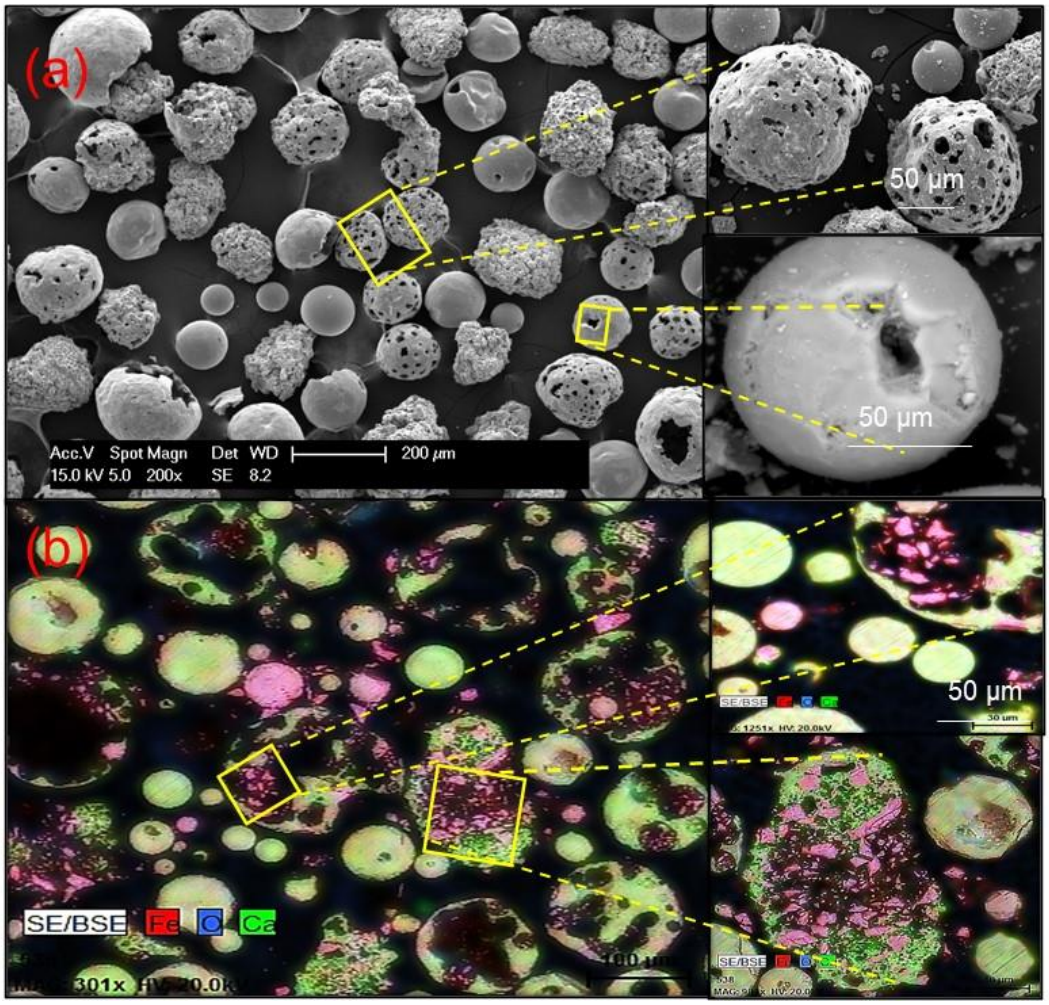



***Figure 6.4: Initial trial to prepare PMMS using granular method (5 min ball milled at 500 rpm) via flame spheroidisation process. a) SEM images of washed samples and b) elemental mapping showing distribution of Fe, O and Ca in pink, blue and green colour within the cross-sectioned samples.***

Elemental mapping of the cross-sectioned samples show that the elements were not homogeneously distributed within the samples.

For initial trials, magnetite particles and porogen were ground using ball mill at 500 rpm for 5 min with 1:0.5 porogen ratio. However, 15 min grinding protocol (as optimised for manufacturing porous recycled glass microspheres, PRGMs) was not possible due high heat generation and difficulty in recovering the ground samples from the ball mill pot. Further studies used a ring-milling process instead of ball milling. Also, to improve yield and porosity, the granulation process was optimised further by varying the grinding time, re-spheroidisation of PMMs and varying porogen ratios (i.e. 1:1 and 1:3).

### *6.2.3.1 Effect of grinding time*

#### 6.2.3.1.1 Morphology of the PMMs

The morphologies of the PMMs manufactured using 1 min, 5 min and 15 min grinding time were evaluated using SEM. The images revealed that microspheres with the size of 110 ± 27 µm had open surface pores. However, for 15 min grinding time smaller microspheres with size 50 ± 10 µm revealed smooth surfaces. The pore sizes of PMMs demonstrated a decreasing trend from 1 min to 15 min grinding time. Elemental mapping shown the presence and distribution of calcium, iron, and oxygen within PMMs (see Figure 6.5 (a-c)). Furthermore, the cross-sectional SEM images showed the PMMs also had internal porosity and with increasing grinding time (from 1 min to 15 min) where the microspheres were more spherical, with uniform interconnected porosity.

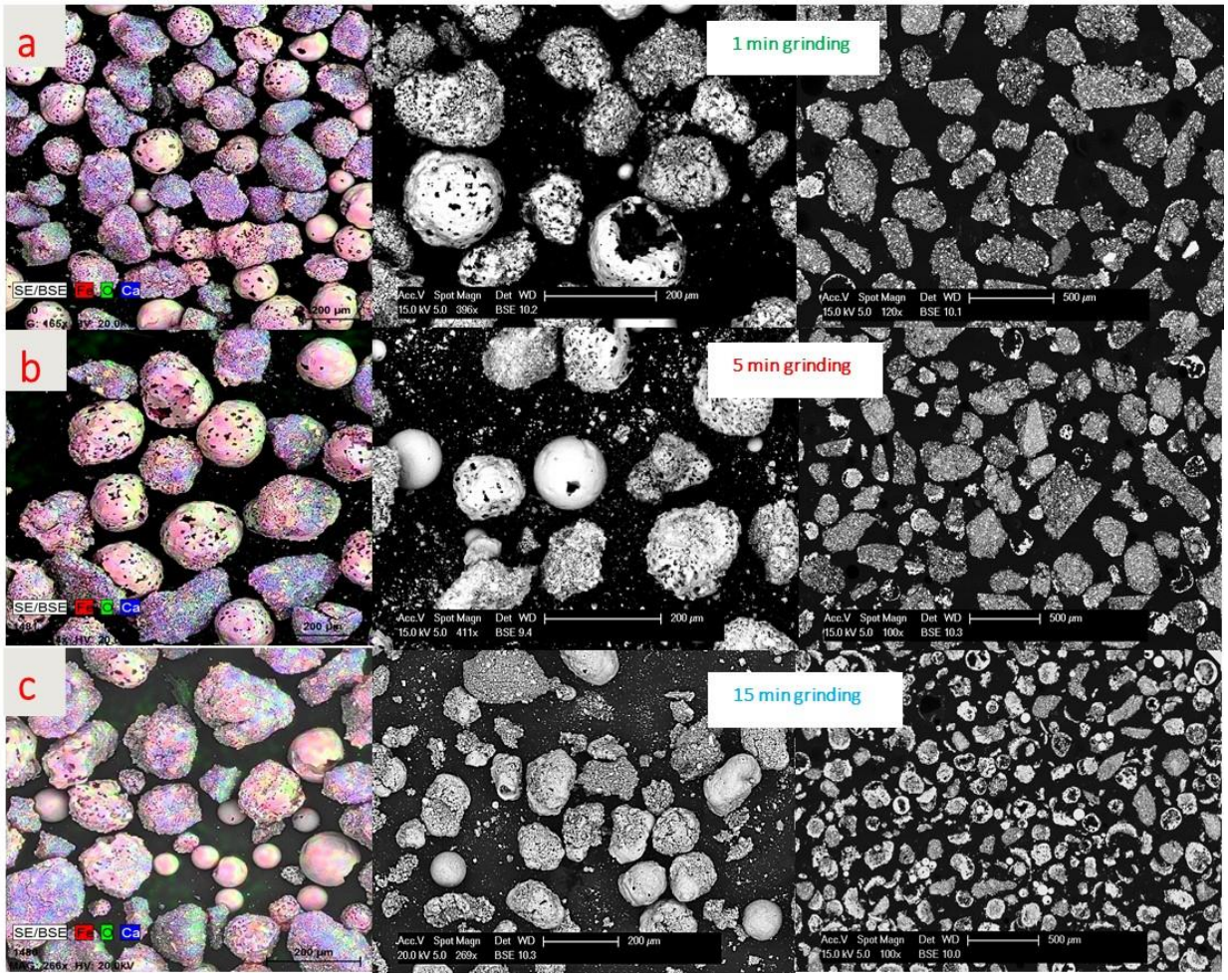



***Figure 6.5: SEM images from a-c displaying the effect of grinding time in a ring-mill on manufacturing PMMs for various time point a) 1 min grinding, b) 5 min grinding and c) 15 min grinding.***

#### 6.2.3.1.2 Structural analysis

Post-spheroidised PMMs (acid washed) samples were characterised by XRD analysis. Sharp crystalline peaks were observed (see Figure 6.6 a). Highlighting characteristics peaks for magnetite along with a new mineral $Ca_2Fe_2O_5$ brownmillerite (also referred to as Srebrodolskite). The sharp major crystalline peaks at 2θ ≈ 32-34° corresponds to the crystal planes (002), (200) and (141) characteristics of $Ca_2Fe_2O_5$. The semi-quantitative analysis revealed that increasing grinding time decreased the content of $Ca_2Fe_2O_5$ brownmillerite which subsequently led to an increase in the magnetite content (see Figure 6.6 c). The percentage of magnetite phase obtained were 41 (±2.3) %, 61 (±1.8) % and 70 (±1.1) % for 1min, 5 min and 15 min, respectively. However, the ground samples before spheroidisation were also analysed to investigate the presence of $Ca_2Fe_2O_5$ brownmillerite mineral. The results confirmed that the ground samples did not contain any $Ca_2Fe_2O_5$ brownmillerite phase, only $CaCO_3$ and $Fe_3O_4$ as starting minerals were found. Furthermore, increasing grinding time also decreased the $CaCO_3$ content, although the same volume of starting samples was used for XRD analysis. The $CaCO_3$ content of the ground samples were found to be 35 (±1.3) %, 18 (±1.1)% and 11 (±1.3)% for 1 min, 5 min and 15 min grinding, respectively (see Figure 6.6 b) whilst the percentage of magnetite phase was 65 (±1.3) %, 78 (±1.1) % and 89 (±1.3) % (see Figure 6.6 b). In order to address the effect of residual porogen, the unwashed PMMs prepared by 1:0.5 weight % porogen ratio were re-spheroidised and investigated.

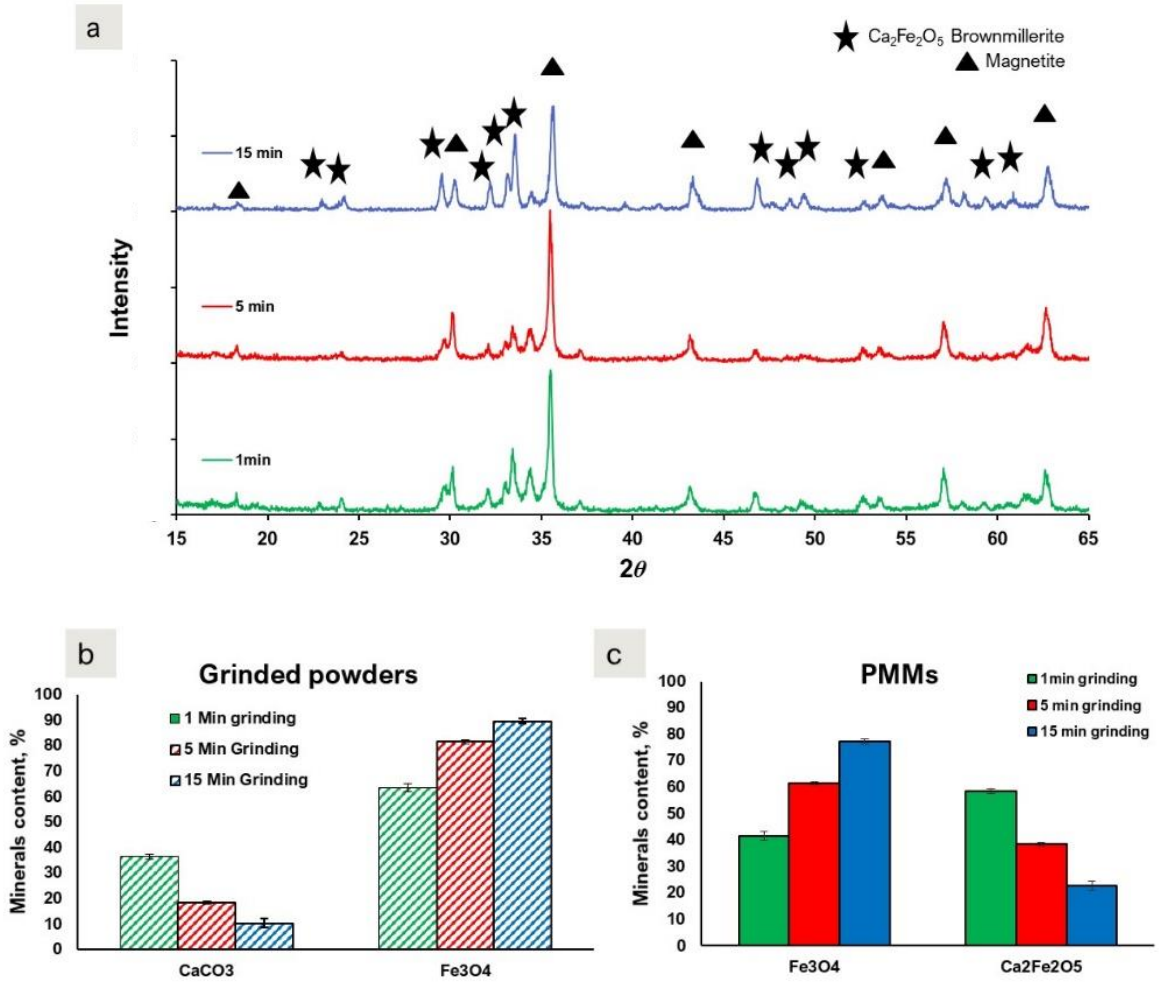



***Figure 6.6: a) X-Ray diffractograms for PMMs produced at 1 min, 5 min and 15 min grinding time, b) semi-quantitative analysis of minerals for grinded powders before spheroidisation and c) PMMs after spheroidisation.***

### *6.2.3.2 Effect of re-spheroidisation*

#### 6.2.3.2.1 Morphology of re-spheroidised PMMs

The PMMs prepared from 15 min grinding protocol (1:0.5 by weight porogen ratio) were re-spheroidised up four times and their morphology investigated by SEM (see Figure 6.7). After spray 4, the microspheres were more spherical with significantly narrowed pores compared to spray 1. The cross-sectional SEM images further shown that repeating spheroidisation progressively (from spray 1 to spray 4) densified the internal cores reducing interconnected porosities.

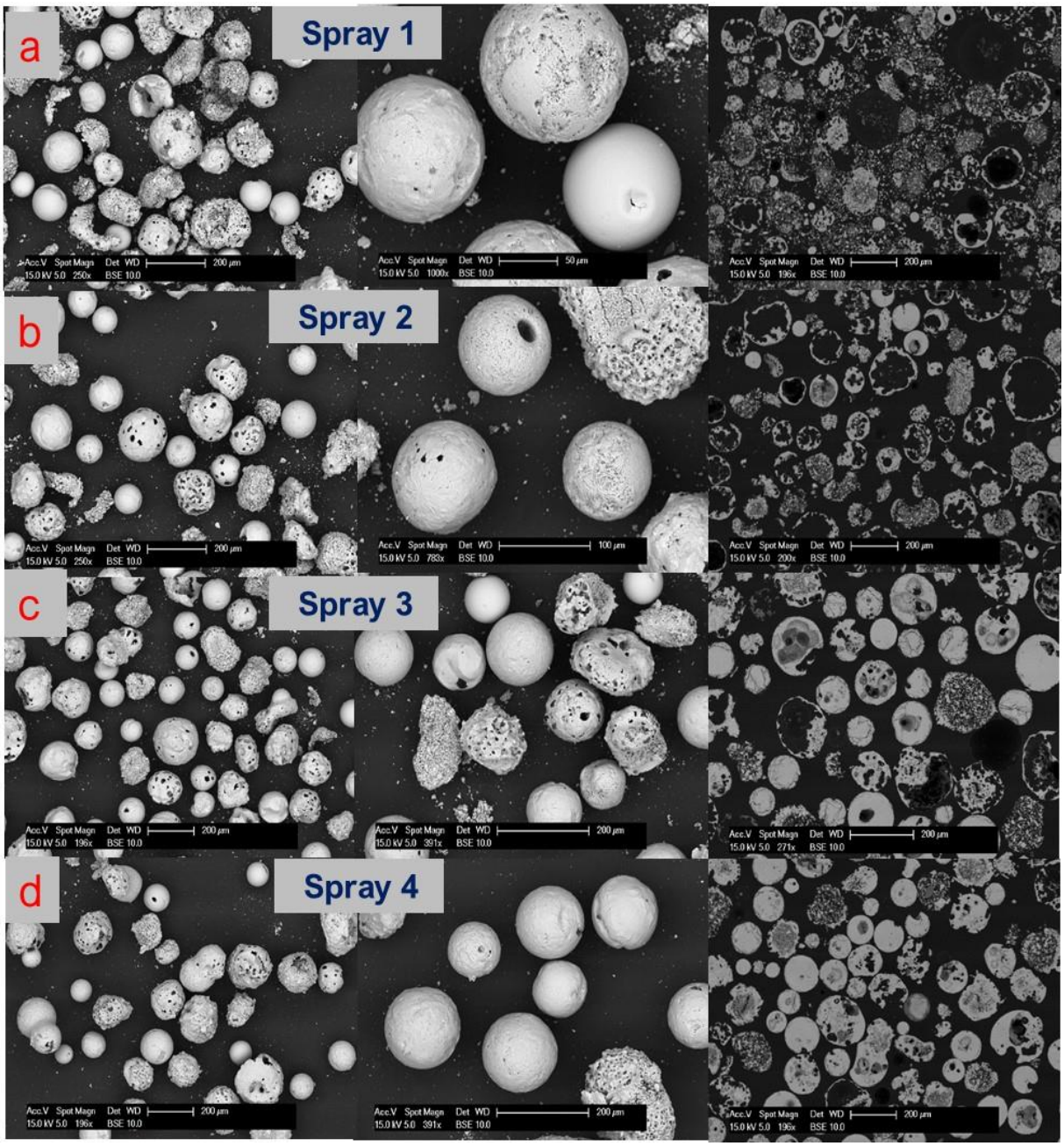



***Figure 6.7: SEM images of PMMs (manufactured with 1:0.5 porogen ratio and 15 min grinding time) after a) 1st spray, b) 2nd spray, c) 3rd spray and d) 4th spray.***

#### 6.2.3.2.2 Thermal and structural analysis of re-spheroidised PMMs

The re-spheroidised PMMs after 1st, 2nd and 4th spray were further investigated by TGA and XRD as presented in Figure 6.8 (a-c). Ground sample, spray 1 and spray 2 showed major weight loss at 730 °C (see Figure 6.8 a). The weight % of porogen ($CaCO_3$) calculated from first derivative of the TGA curve (inset) presented in Figure 6.8(b). The initial ground sample shown 8% weight loss and spray 1 to spray 4 shown a weight loss of 6.5 % to 1% when PMMs were re-spheroidised. Semi-quantitative XRD

analysis indicated (Figure 6.8 c) that the PMMs samples post acid wash contained only magnetite and $Ca_2Fe_2O_5$ brownmillerite mineral. Spray 1, 2 and 4 also showed slight changes in phase % (30%, 31% and 33% unreacted magnetite for spray 1, spray 2 and spray 4 respectively). However, these were not statistically significant ($P > 0.05$). To further explore the effect of porogen on magnetite, the porogen ratios were varied from 1:0.5 to 1:3.

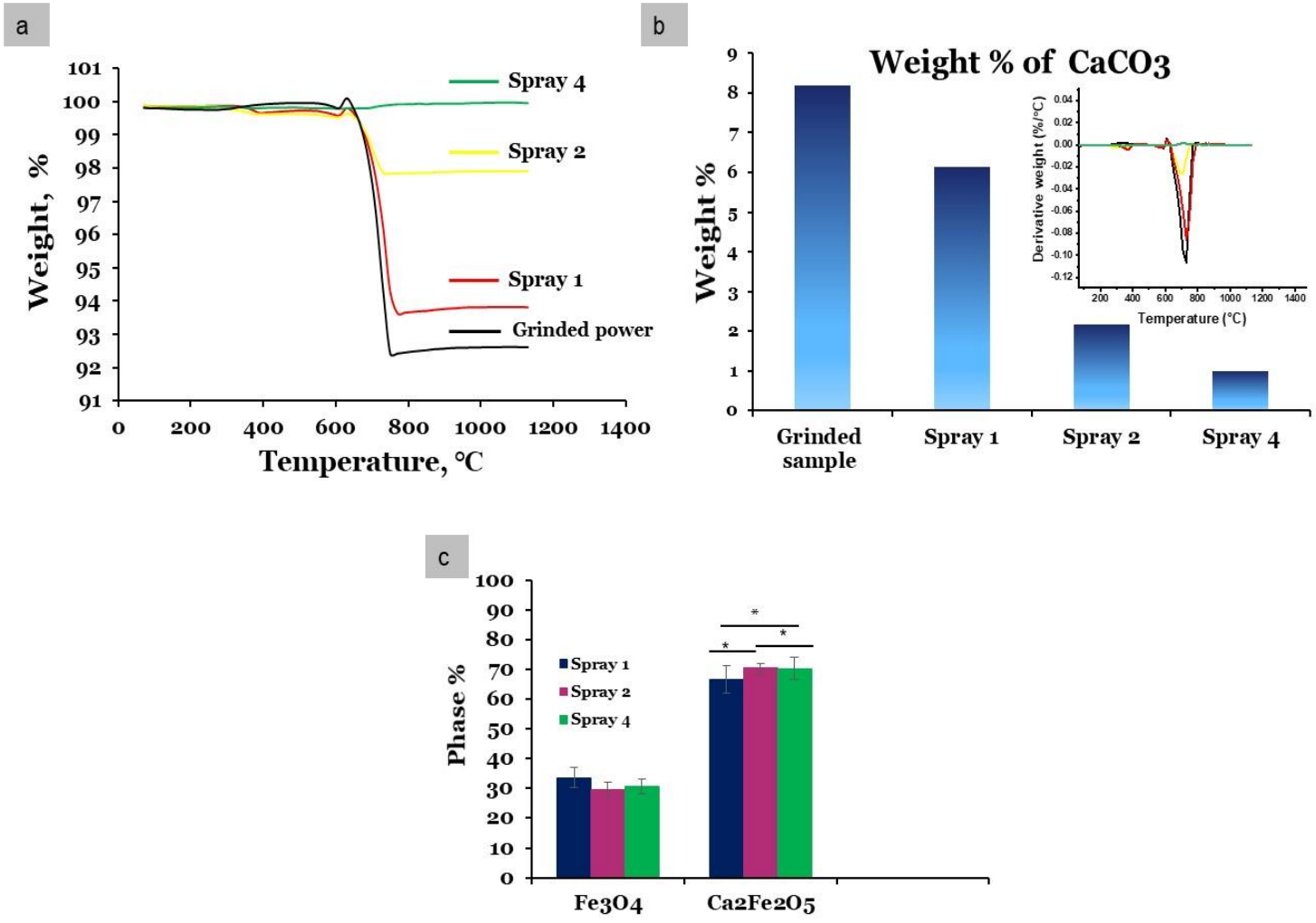



*Figure 6.8: a) TGA analysis of grinded and re-spheroidised PMMS after 1st, 2nd and 4th spray. b) Graph showing weight % of $CaCO_3$ with inset showing the derivative weight of PMMS after 1st, 2nd and 4th spray and c) semi-quantitative analysis by XRD after 1st, 2nd, and 4th spray (acid washed).*

### *6.2.3.3 Effect of porogen*

#### 6.2.3.3.1 Effect of porogen on the morphology of PMMs

Increasing porogen ratio demonstrated substantial effect on the final morphology of the PMMs. As shown in, Figure 6.9 increasing porogen ratio (from 0.5 to 3) produced some irregular shaped particles (length-diameter ratio not close to 1:1). However, they were still porous. The pore sizes varied a lot and composed of small (circled in red) and large pores (circled in blue) for 1:0.5 and 1:1 porogen ratios. However, some microspheres with smooth surfaces and large pores (circled in yellow) were also observed (see Figure 6.9 a), whilst open interconnected pores were visible in PMMs with porogen ratio samples of 1:1 and 1:3 (Figure 6.9 b, c). Furthermore, the number of pores increased, and pore sizes were seen to be decreased with an increase in porogen ratio.

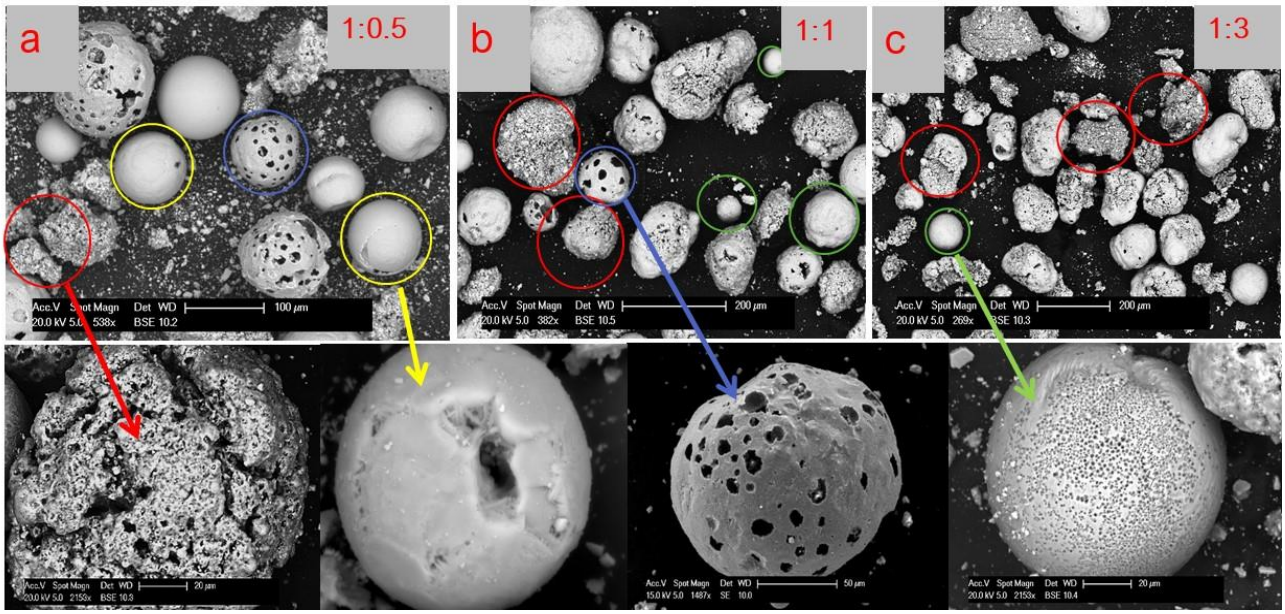



***Figure 6.9: SEM images of PMMs (unwashed) a) 1:0.5, b) 1:1 and c) 1:3 magnetite to porogen ratios.***

The granulation process without any porogen were also investigated by SEM (see Figure 6.11). These microspheres exhibited more spherical shape with smooth surfaces and with few pores on the surface. Few microspheres were also observed with corrugated surfaces having closed pores. The cross-sectional SEM image revealed mostly dense solid cores with a few microspheres exhibiting hollow cores and no interconnected internal porosity.

The morphology of acid washed PMMs (W-PMMs) with varying porogen ratios are shown in Figure 6.10. After acid wash the surface of PMMs prepared using 1:0.5 became smooth and pores were narrowed. Moreover, agglomeration of microspheres was also observed. The PMMs prepared using

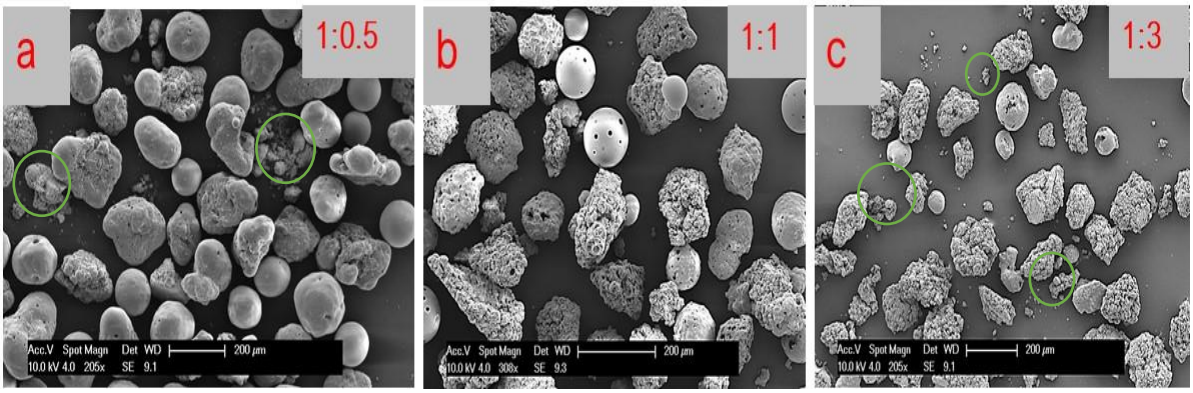



*Figure 6.10: SEM images of W-PMMs a) 1: 0.5, b) 1:1 and c) 1:3 magnetite to porogen ratios.*

1:1 and 1:3 on the other hand revealed mixed morphologies. Microspheres with wrinkled surfaces and narrow pores and smooth surface with larger pores were visible. Broken microspheres after acid wash were only seen for porogen 1:0.5 and 1:3 (shown in green circles in Figure 6.10).

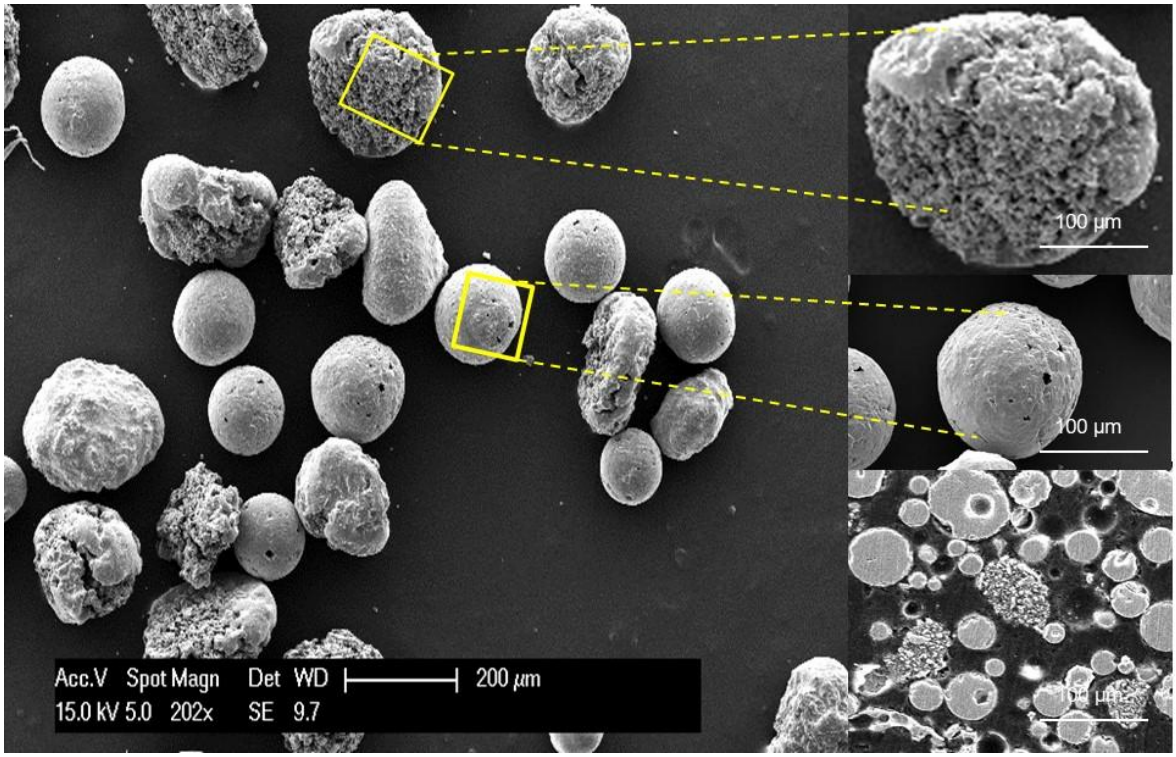



*Figure 6.11: SEM images with cross-section of magnetite microspheres prepared using granular method without any porogen.*

#### 6.2.3.3.2 Structural analysis of PMMs prepared with varying porogen ratios.

Figure 6.12 (a) represents XRD profiles for unwashed and acid washed PMMs with 0.5, 1 and 3 porogen ratios. The unwashed spheres contained residual porogen as evident by the presence of calcite ($CaCO_3$) and lime (CaO) mineral. Few traces of porogen were found in acid washed PMMs prepared using 1:3 magnetite to porogen ratio. Moreover, the peak intensities of $Ca_2Fe_2O_5$ Brownmillerite mineral increased with increasing porogen ratio. The semi-quantitative analysis revealed that acid washed PMMs prepared with 1:1 and 1:3 porogen rations had nearly same amount of $Ca_2Fe_2O_5$ Brownmillerite mineral (60% ±4). However, the amount of unreacted porogen was higher in PMMs prepared with 1:3 porogen ratio (50 % ± 2) compared to 1:1 porogen ratio (30 % ± 2).

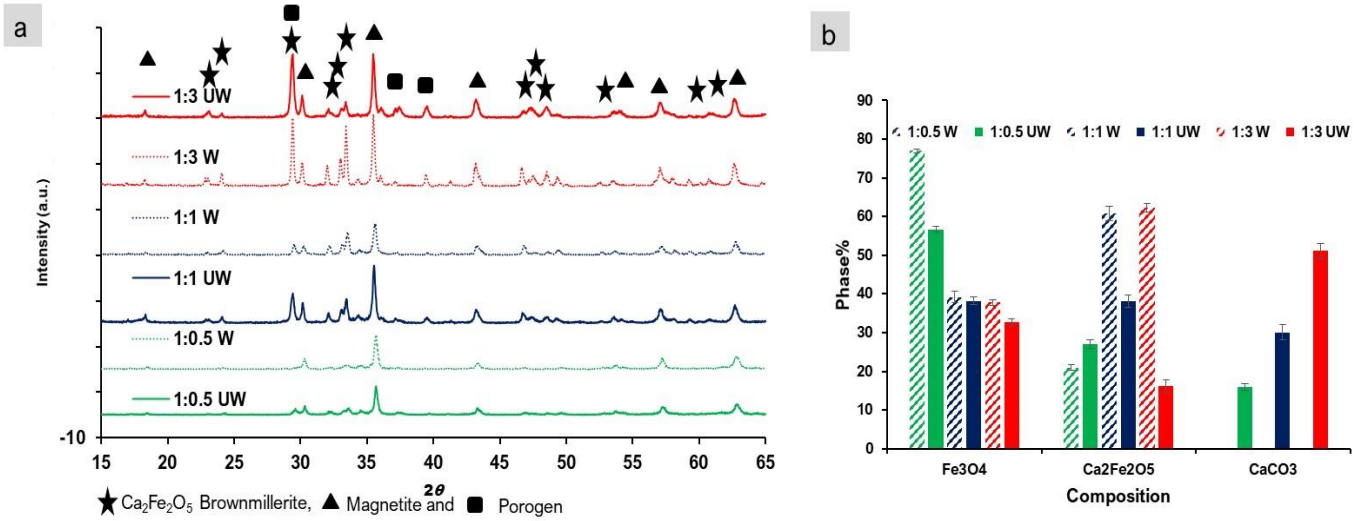



***Figure 6.12: a) X-Ray diffractograms for unwashed (UW) and acid washed(W) PMMs produced with varying porogen ratios, b) semi-quantitative analysis of minerals for PMMs with varying porogen ratios.***

## 6.2.4 PMMs characterisation

### *6.2.4.1 Mineral liberation analysis (MLA)*

Figure 6.13 (a-c) and Figure 6.14 (a-c) shows the cross-sectional SEM images and mineral distribution mapping of UW-PMMs and W-PMMs samples with varying porogen ratios. UW-PMMs prepared using 0.5 porogen ratio were ~80% $Ca_2Fe_2O_5$ brownmillerite (see Figure 6.15 a). Spherical $Ca_2Fe_2O_5$ brownmillerite microspheres with large internal pores were identified with size ranges of 150-250µm, while smaller microspheres (diameter below 150 µm) displayed dense solid cores (see Figure 6.13 a). Moreover, irregular shaped $Ca_2Fe_2O_5$ microspheres were observed with entrapped magnetite particles exhibiting internal porosities. Only small traces (below 2%) of porogen were found.

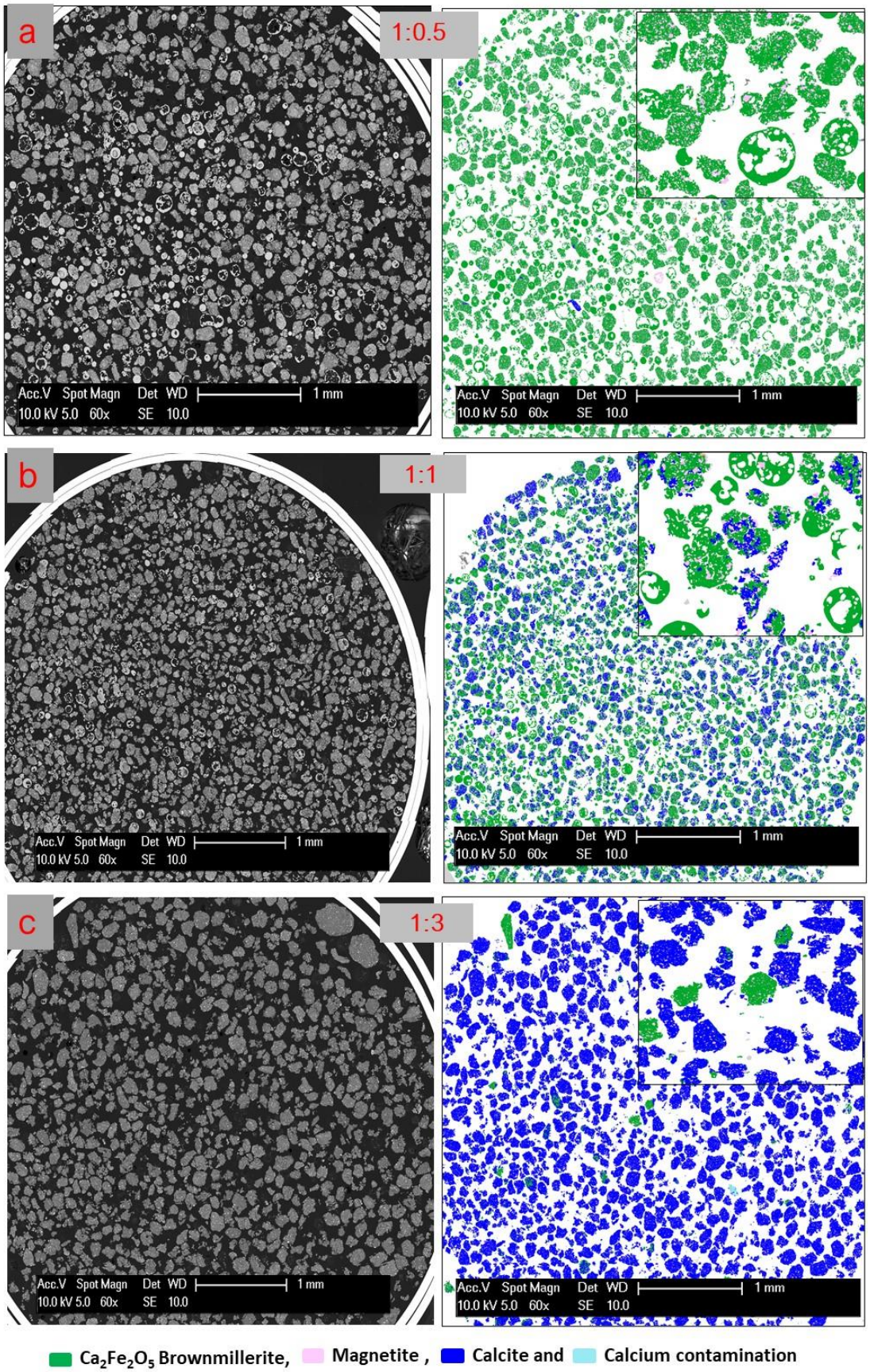



*Figure 6.13: SEM image and mineral distribution map of UW-PMMs with a) 1:0.5 porogen ratio, b) 1:1 porogen ratio and c) 1:3 porogen ratio.*

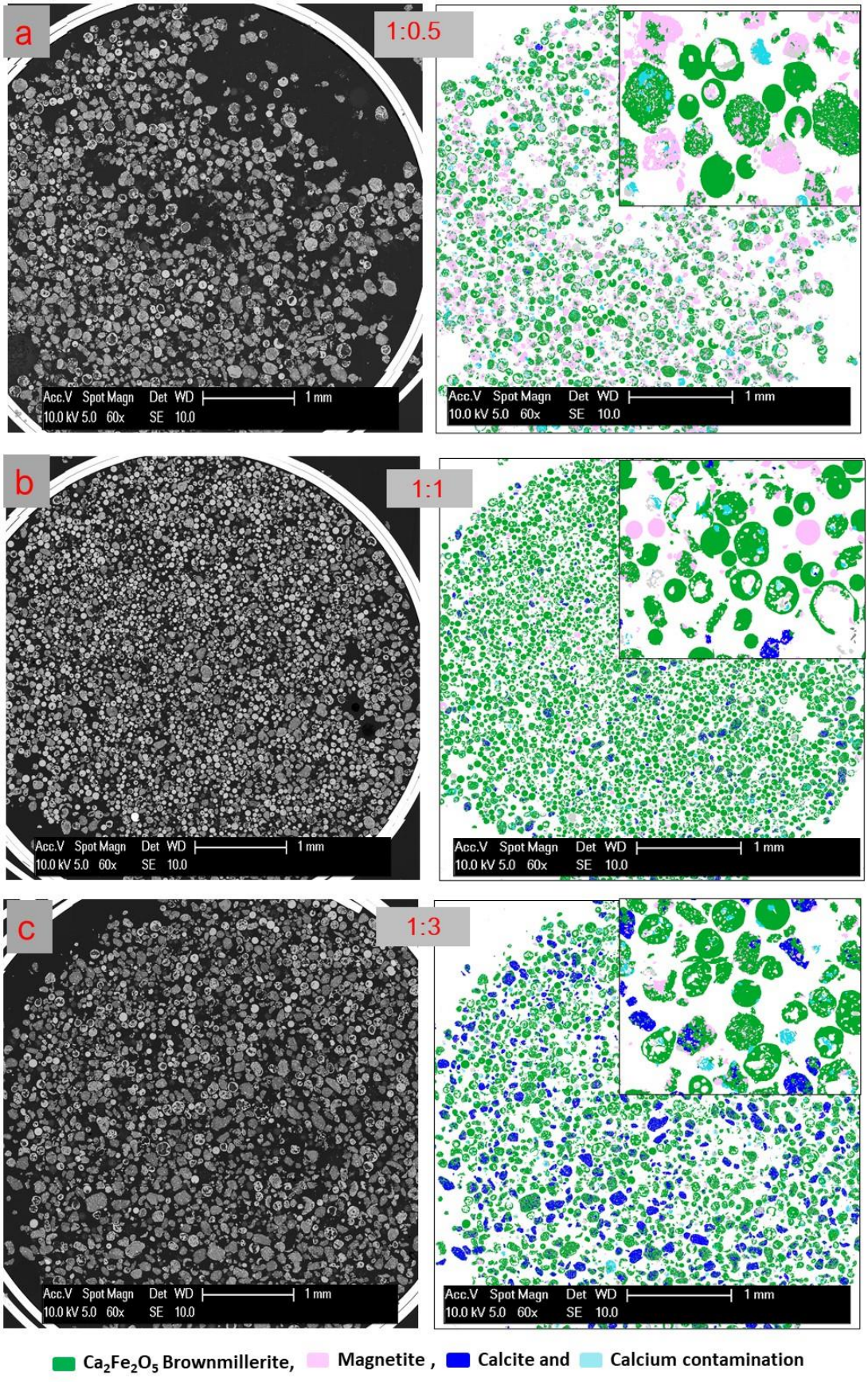



*Figure 6.14: SEM image and mineral distribution map of W-PMMs with a) 1:0.5 porogen ratio, b) 1:1 porogen ratio and c) 1:3 porogen ratio.*

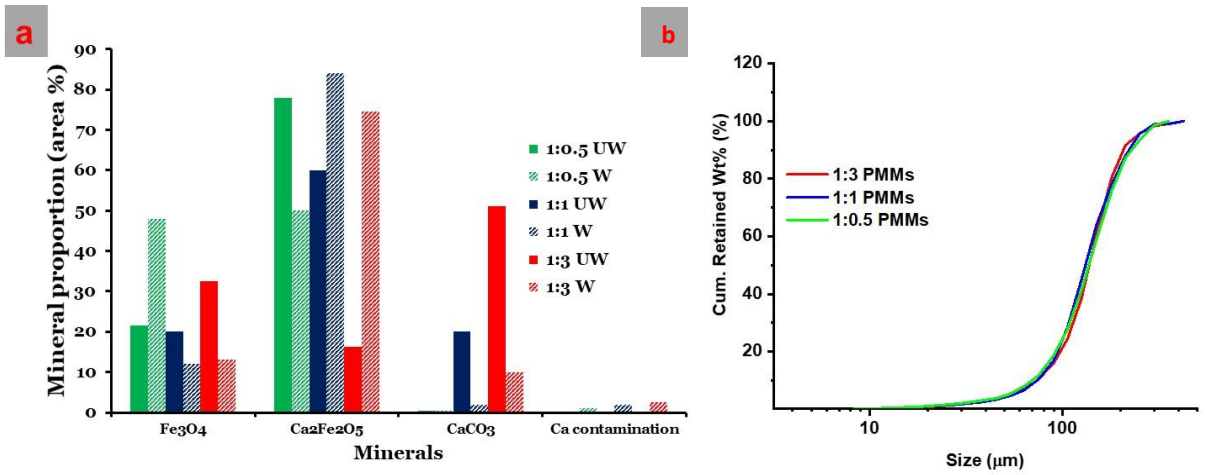



*Figure 6.15: Graph showing a) mineral proportions in unwashed and acid washed PMMs with varying porogen ratio and b) size distribution of PMMs with varying porogen ratio.*

After acid washing the number of pores inside the W-PMMs increased (see Figure 6.14 a cross-sectional SEM image). However, the content of $Ca_2Fe_2O_5$ brownmillerite in W-PMMs decreased significantly from 80 to 50% as observed in Figure 6.15 a.

The cross-sectional image of UW-PMMs with 1:1 porogen ratio presented spherical microspheres with increased no. of pores and pore sizes compared to UW-PMMs prepared by 1:0.5 porogen ratio. These spherical microspheres were comprised of $Ca_2Fe_2O_5$ mineral (see Figure 6.14 b), whilst irregular microspheres were composed of porogen and $Ca_2Fe_2O_5$ with traces of magnetite. The UW-PMMs (1:1) samples contained 20% unreacted porogen, while the amount of magnetite content was nearly same (~21%) for UW-PMMs prepared by 1:0.5 and 1:1 porogen ratio (see Figure 6.15 a). After acid washing more spherical $Ca_2Fe_2O_5$ microspheres (85%) either with increased small and large pore sizes or solid dense core were observed (see Figure 6.14 b). Very few traces of porogen (below 2%) were found after acid washing. Both washed and unwashed samples were found to show internal porosities.

The cross-sectional SEM image for UW-PMMs (1:3) were observed with irregular shaped microspheres with internal porosities. These microspheres exhibited ~51% porogen with~ 32% magnetite and the balance as $Ca_2Fe_2O_5$, as shown in Figure 6.15 a. After acid washing microspheres with spherical and irregular shape with increased pore size and porosity were observed (see Figure 6.14 c). Furthermore, both W- PMMs (1:1 and 1:3) had ~13% magnetite. However, the amount of $Ca_2Fe_2O_5$ mineral in W-PMMs with 1:1 was higher (~85%) compared to W-PMMs with 1:3 (~74%) (see Figure 6.15 a). The resulting particle size distribution of PMMs with 1:0.5, 1:1 and 1:3 porogen ratio are represented in Figure 6.15(b) where 80% of the particle were found to be 180 ± 10 µm.

### *6.2.4.2 Surface area and porosity analysis*

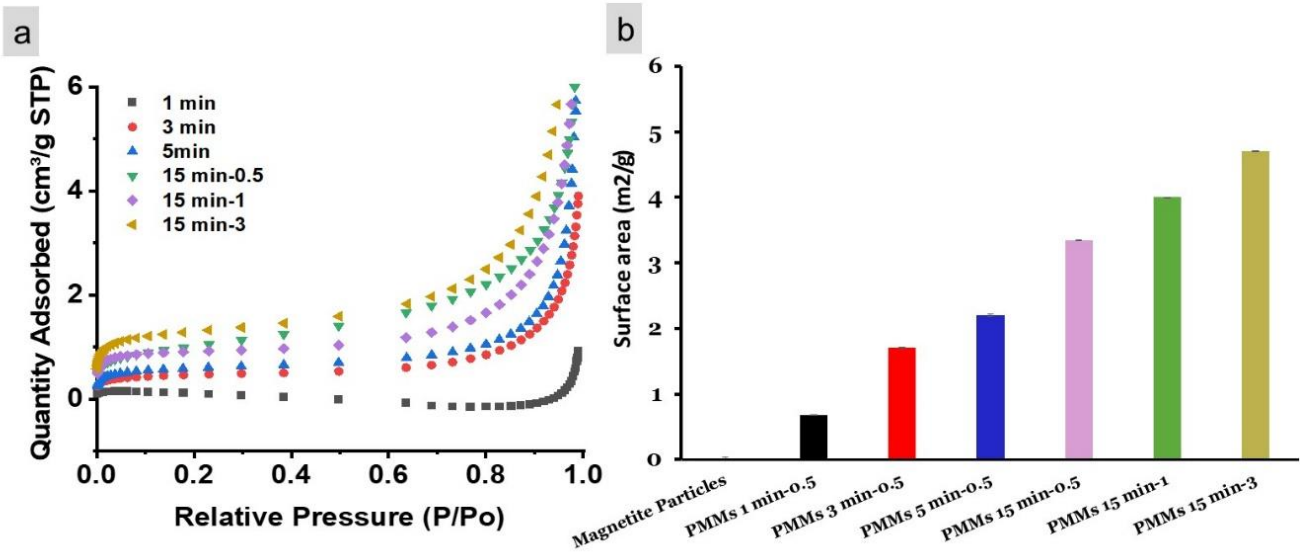



***Figure 6.16: a) Nitrogen adsorption isotherms and b) surface area of PMMs with varying grinding time and porogen ratios.***

The nitrogen adsorption isotherms are detailed in Figure 6.16 a for PMMs manufactured at varying grinding time and porogen ratios. Increasing grinding time (1 to 15 mins) and increasing porogen ratio (0.5 to 3) results in an increase in nitrogen adsorption. Increasing grinding time (from 1 min to 15 mins using 1:0.5 porogen ratio) resulted in an increase in surface area (see Figure 6.16 b). The surface area calculated for PMMs 1min-0.5 was 0.68 ± 0.01 $m^2/g$, whilst for PMMs 15 min-0.5 was 3.35 ± 0.01. In addition, it was also evident that increasing porogen ratio led to an increase in surface area by 19 % (4.00 ± 0.01 $m^2/g$) and 40 % (4.70 ± 0.01 $m^2/g$) for sample PMMs 15 min-1 and PMMs 15 min-3, respectively in comparison with PMMs 1, 3, 5 and 15 min-0.5 porogen ratio. The Surface area of unprocessed magnetite particles were found to be 0.03 $m^2/g$. Whereas, PMMs prepared with 1 min grinding 1:0.5 porogen ratio showed 92 % increase in surface area when compared to unprocessed magnetite particles.

Porosity and pore size distribution measurements were determined using mercury porosimetry. The cumulative intrusion curves are displayed in Figure 6.17 a showing PMMs with 1:1 and 1:3 porogen ration follow the same trend. With increasing pressure, mercury intrudes into the interparticle space (shown by zone A) and the pores of the microspheres (larger pores, zone B and smaller pores, zone C). The samples also did not show signs of compression (denoted by zone D) before 750 psi. Figure 6.17 b displays the pore diameters of the measured samples against the log differential pore volume. The inter particle gaps ranged from 60-30 µm with larger pores and smaller pore with diameter ranging from 2-25 µm and 0.43-2 µm, respectively were identified. The intrusion within the PMMs

followed the order PMMs with 1:3 > PMMs with 1:1. The respective porosity profiles were measured as 65% and 63% for PMMs with 1:1 and 1:3 porogen, respectively.

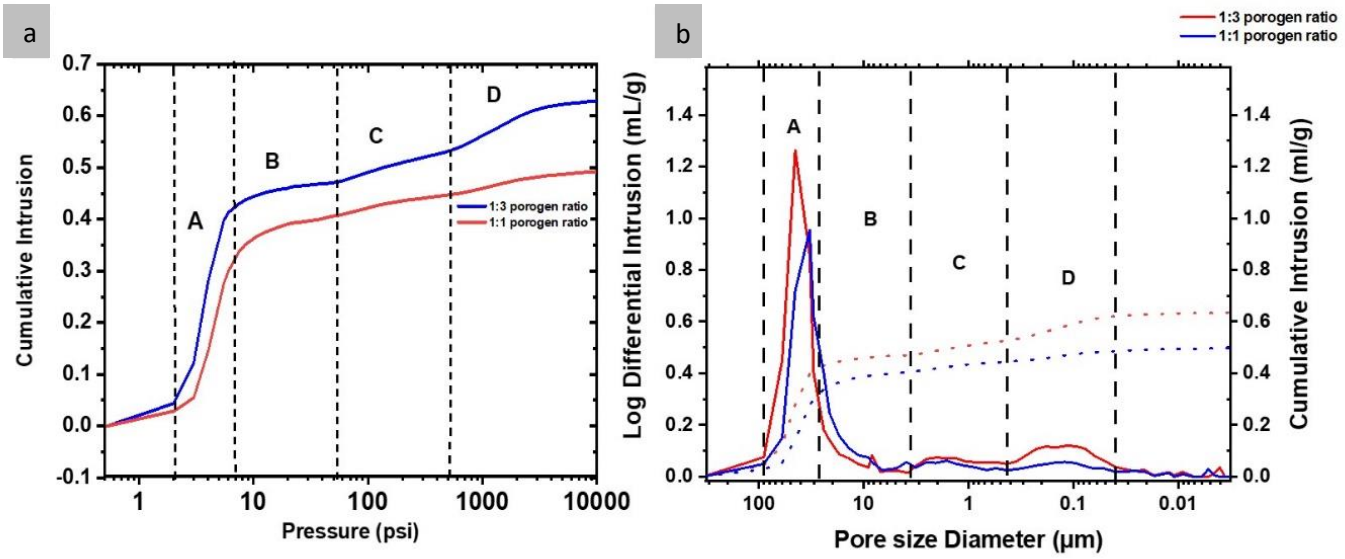



*Figure 6.17: a) Displaying the cumulative intrusion and their possible corresponding intrusion points and b) Pore diameter against Log differential pore volume of PMMs with1:1 and 1:3 porogen ratio as obtained from mercury porosimetry.*

### 6.2.5 Adsorption studies

To demonstrate the applicability of PMMs as adsorbents for water treatment applications, anionic acid red 88 (AR88) dyes was used as test molecules to study the adsorption activity. Table 6.1 shows that UW-PMMs showed increased % dye removal (57% to 78%) at neutral flame with increasing flowrates (2:2-3:3).

*Table 6.1: Yield (%) and Dye removal (%) of unwashed PMMs prepared using varying flowrates, grinding time and porogen ratios.*

| Sample | Flame type | Flowrates Oxygen/Acetylene | Porogen ratio | Yield, % | %, Dye removal |
|---|---|---|---|---|---|
| **A** | Neutral flame | 2:2 | 1:0.5 | 73±2 | 57 |
| **B** | Neutral flame | 2.5:2.5 | 1:0.5 | 68±4 | 62 |
| **C** | Neutral flame | 3:3 | 1:0.5 | 63±2 | 78 |
| **D** | Oxidising flame | 3.3-3 | 1:0.5 | 58 ±3 | 100 |
| **E** | Reducing flame | 3:2.7 | 1:0.5 | 13±4 | 48 |
| **F** | Oxidising flame | 3.3:3 | 1:1 | 52±2 | 100 |
| **G** | Oxidising flame | 3.3:3 | 1:3 | 48±6 | 100 |

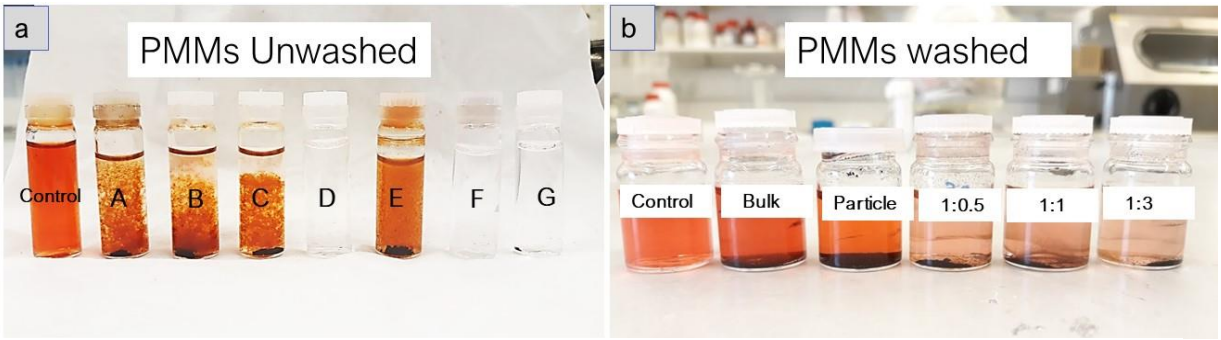



***Figure 6.18: Adsorption using Acid red 88 on a) unwashed PMMs prepared using different flowrates, grinding time and porogen ratio and b) washed PMMs prepared using different porogen ratio using oxidising flame. Each vial contained 50 mg/L AR88 and 5 g/L of PMMs at pH 7 and temperature 22 ± 2 ℃.***

The adsorption of AR88 dye at the solid-liquid interface of UW-PMMs displayed specific selectivity with 100% dye removal when using PMMs produced with 15 min grinding time (using oxidising flame) (see Figure 6.18a). The % dye removal for W-PMMs prepared using 1:0.5, 1:1 and 1:3 porogen ratio is also presented in Table 6.2. Adsorption of W-PMMs decreased as the maximum dye removal (%) achieved was 83%, 80% and 74% with 1:3, 1:1 and 1:0.5 porogen ratio, respectively. However, the SMS and as received magnetite particles did not remove any AR88 dye (see Table 6.2 and Figure 6.18b). The yield % of UW-PMMs prepared with increasing flowrates (from 2:2 to 3:3) decreased from 73±2 to 63±2 %. The yield % also decreased (58% to 48%) with varying porogen ratio.

***Table 6.2: Dye removal (%) of SMS, magnetite particles and washed PMMs prepared using varying porogen ratios.***

| Sample | Flame type Oxygen/Acetylene | Flowrates | Porogen ratio | %, Dye removal |
|---|---|---|---|---|
| **SMS (bulk)** | - | 3:3.3 | - | 0 |
| **Magnetite Particles** | - | - | - | 0 |
| **W- PMMs** | Oxidising flame | 3:3.3 | 1:0.5 | 74 |
| **W- PMMs** | Oxidising flame | 3.3:3 | 1:1 | 80 |
| **W- PMMs** | Oxidising flame | 3.3:3 | 1:3 | 83 |

Based on results of initial adsorption experiment and surface area profiles, UW-PMMs and W-PMMs prepared using 1:3 porogen ratio (oxidising flame, flowrate 3:3.3) were used to carry out the entire dye adsorption experiment.

### *6.2.5.1 Effect of Initial pH*

The initial solution pH can significantly influence dye adsorption, thus the effects of pH on dye adsorption by the PMMs was investigated. A range of pH conditions were investigated to explore the effects that alkaline and acidic conditions have on adsorption performance of PMMs. The adsorption

performance was examined across the pH range from 2-12. Furthermore, in addition to the anionic dye AR88, a cationic dye methylene blue (MB) was also explored.

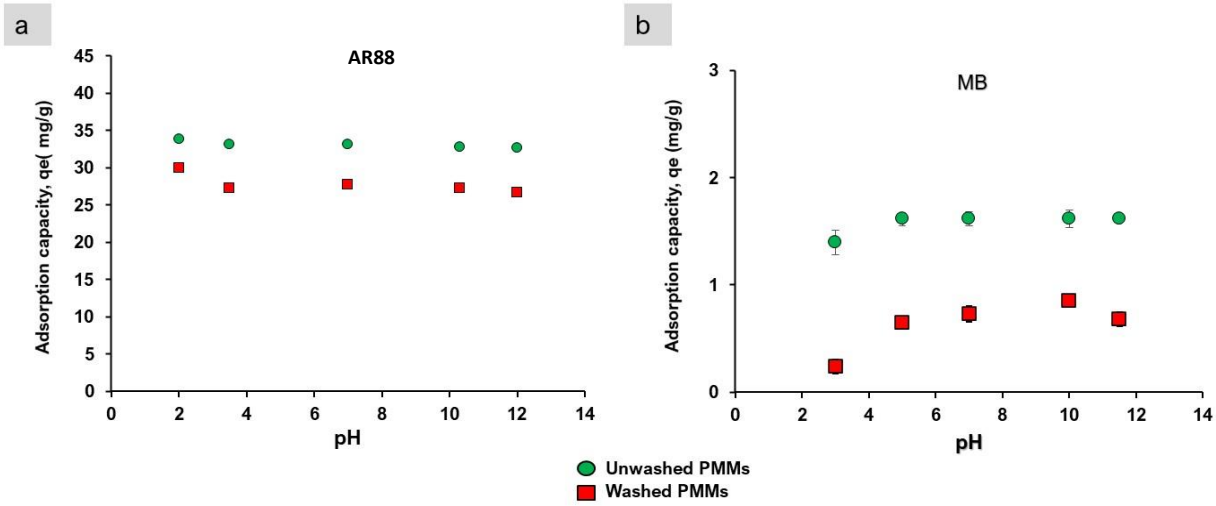



***Figure 6.19: Impact of the initial pH of solution on the adsorption of a) AR88 and b) MB after equilibrium ($C_0$ = 300mg/L for AR88 and 50mg/L for MB; dye volume= 10mL; adsorbent loading = 5 g/L; T= 22 ± 2 °C).***

For AR88 dye maximum dye adsorption capacity was found 30 mg/g at an initial pH of 2 for W-PMMs. The dyes adsorption capacity slightly decreased (adsorption capacity 27 mg/g) as the pH was then increased from 2 to 4, and the adsorption capacity was constant above pH 4. There was no significant trend observable in adsorption performance of UW-PMMs across the pH range tested (2-12) for AR88 dye as detailed in Figure 6.19 a.

Adsorption capacity of W-PMMs for MB dye showed an increase in adsorption at alkaline region (8-10) and then decreased after pH 10. No significant change in adsorption capacity was noticed for UW-PMMs (see Figure 6.19 b). The adsorption capacity of UW-PMMs for both dyes (AR88 and MB) were higher compared to W-PMMs over the entire pH range of (2-12).

### *6.2.5.2 Effect of Adsorbent Dose*

The effect of PMMs (unwashed and washed) dose on adsorption of AR88 and MB is presented in Figure 6.20. The adsorbent dose was varied from 1 g/L to 10 g/L in order to investigate a wide range of mass loadings in terms of % dye removal. The solution pH was adjusted to 2 and 10 for AR88 and MB, respectively based on previous findings. With increasing adsorbent dose (from 1g/L to 6 g/L) the % dye removal increased reaching a plateau with no significant change in % dye removal for AR88 dye.

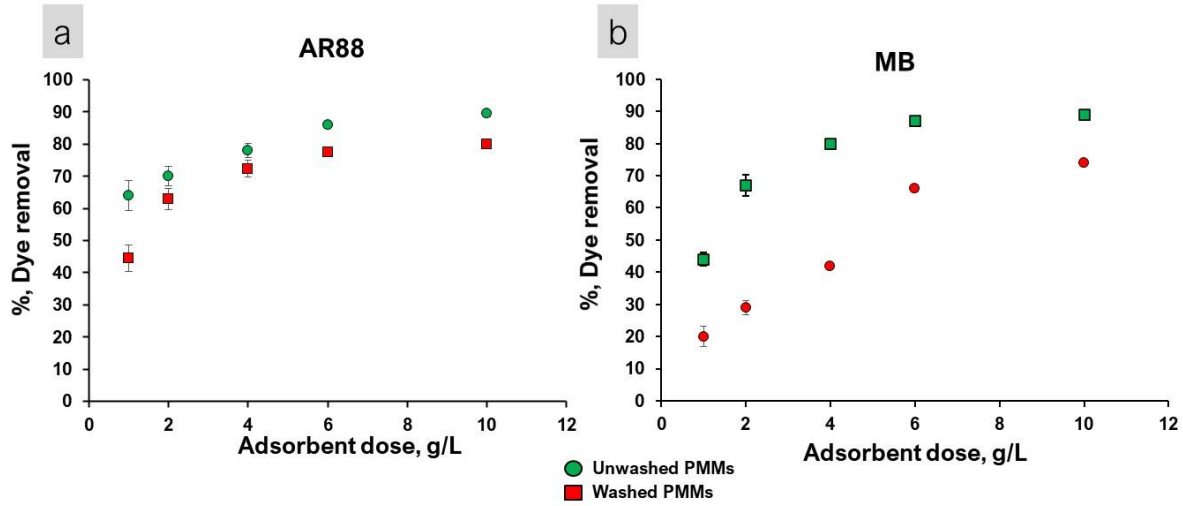



***Figure 6.20: Influence of the PMMs loading on the adsorption of a) AR88 and b) MB after equilibrium ($C_0$ = 300mg/L for AR88 and 50 mg/L for MB, pH= 2 for AR88 and 20 mg/L, pH = 10 for MB; dye volume = 10mL; T = 22 ± 2 °C).***

The % dye removal for 1 g/L of UW-PMMs and W-PMMs was 64 ± 3 % and 44 ± 3 % respectively, whereas for an adsorbent loading 6 times greater (6 g/L) showed 90 ± 0.5 % and 77 ± 1 %, for AR88 dye (see Figure 6.20 a) respectively. Similar profiles were observed for adsorption of MB on both unwashed and acid washed PMMs. The % dye removal for 1 g/L of unwashed and acid washed PMMs on MB was estimated at 44 ± 3 % and 20 ± 2.5 % respectively, whereas % dye removal for 6 g/L was estimated 87± 4 % and 87 ± 2 %for unwashed and acid washed PMMs, respectively as shown in Figure 6.20 b.

### *6.2.5.3 Effect of concentration on Reaction Kinetics*

The effect of the initial AR88 and MB dye concentrations on the adsorption rate by acid washed and unwashed PMMs are shown in Figure 6.21. For both dyes, the equilibrium adsorption capacity ($q_e$) increased with increasing dye concentration. However, complete adsorption of AR88 was observed using UW-PMMs for dye concentration of 50 mg/L and 100 mg/L which took place within 40 mins of contact time (see Figure 6.21a) with complete adsorption for W-PMMs occurred within 90 mins. However, adsorption of 200 mg/L AR88 by UW-PMMs was initially very rapid (first 10 min) followed by slower adsorption until a plateau was observed (360 mins). Similar profiles were noticed for adsorption of 200 mg/L AR88 dye by W-PMMs. The increase in initial dye concentration led to an increase in adsorption capacity. Adsorption rate of MB on UW-PMMs and W-PMMs as illustrated in Figure 6.21 b was also very rapid during the initial stages (first 30 mins) of the adsorption processes. After a very rapid adsorption, dye uptake capacities reached equilibrium values after 300 mins for all dye concentrations.

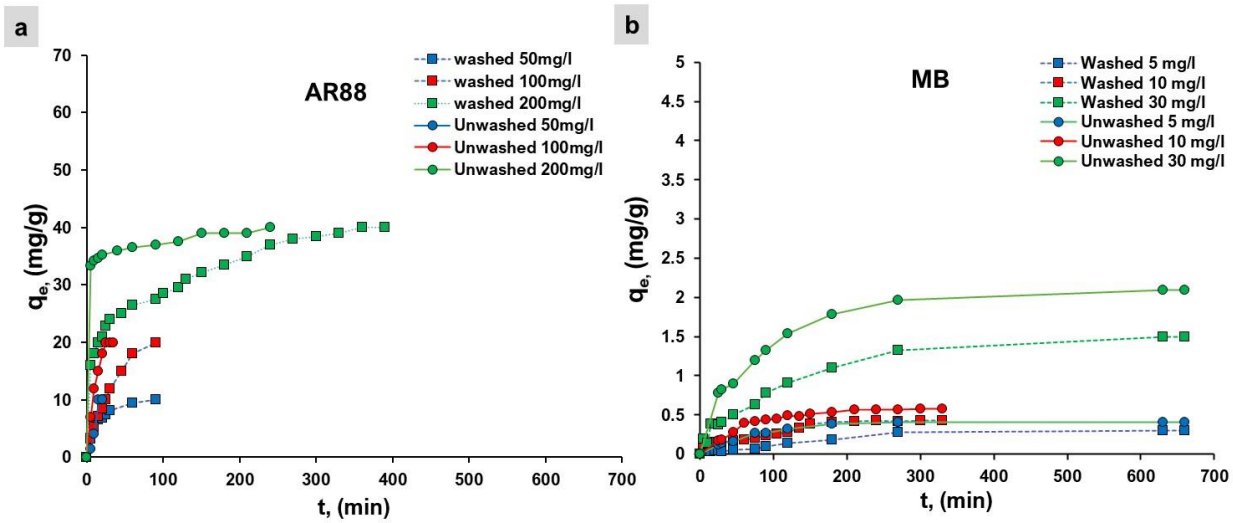



*Figure 6.21: Effect of dye concentration on adsorption into UW-PMMs and W-PMMs for a) AR88 and, b) MB (PMMs dose= 6 g/L, pH 2 and pH 10 for AR88 and MB respectively and temperature of 22 ± 2 °C).*

The data from adsorption experiments at different concentration were modelled against pseudo 1$^{st}$ order and pseudo 2$^{nd}$ order models, as these are the most common kinetic models applied to study the dynamics of the adsorption process in terms of the order of rate constant in literature [366].

The plot of the linear pseudo 1$^{st}$ order model for adsorption of AR88 and MB are presented in Figure 6.22. Values of the rate constant ($k_1$), equilibrium adsorption capacity ($q_e$), calculated equilibrium adsorption capacities ($q_{ecal}$), the correlation coefficient ($R^2$) calculated from the plots of log ($q_e - q_t$) versus t for each of the dyes are presented in Table 6.3. The best fit among the kinetic models is assessed by linear coefficient of determination ($R^2$) and Chi-square ($\chi 2$). It was observed that the calculated value $q_{ecal}$ did not agree with experimental values ($q_e$) for AR88 dye adsorption into UW-PMMs and W-PMMs and MB for UW-PMMs. The data indicated that the pseudo 1$^{st}$ order reaction equation was not ideal to model the adsorption data. However, adsorption of MB on W-PMMs with concentration 5 mg/L and 10 mg/L indicated the closest relationship to a pseudo 1$^{st}$ order model (with a small discrepancy seen between $q_{ecal}$ and $q_e$). Adsorption of 5 mg/L and 10 mg/L MB occurred at a similar rate ($k_1$=0.002 min $^{1}$) (Table 6.3).

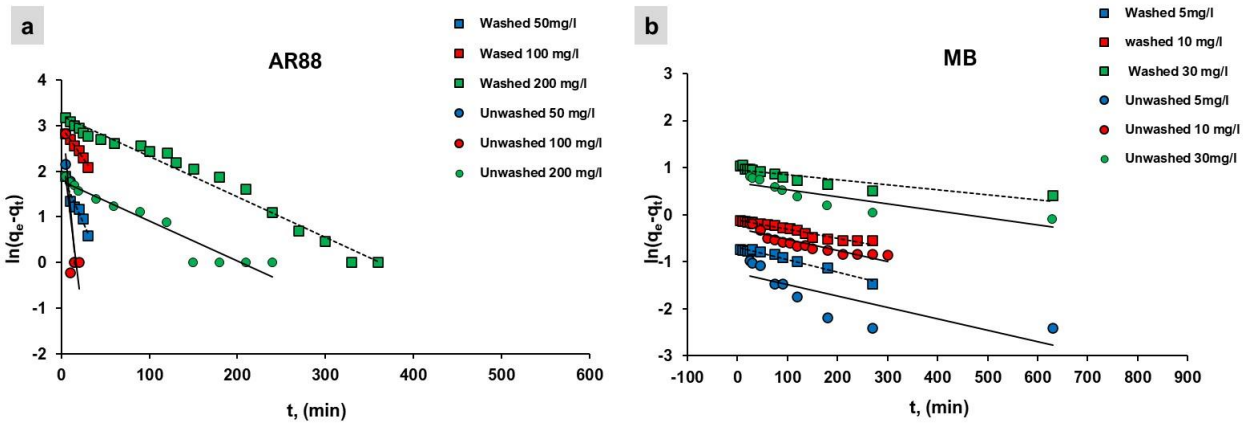



*Figure 6.22: Linear pseudo 1st order kinetic model for the adsorption of a) AR88 and b) MB (V of the dye=10mL; adsorbent loading=6 g/L, pH= 2 for AR88 and pH=10 for MB).*

The linear fit of the pseudo 2nd order model with the data is outlined in Figure 6.23. The linear equation showed a better fit to pseudo 2nd order model than the pseudo 1st order model with a correlation coefficient $R^2$ of ≥098, except MB dye adsorption with concentration 5 mg/L and 10 mg/L on W-PMMs. The pseudo 2nd order rate constant ($k_2$) decreased with increasing initial concentrations of AR88 dye for both unwashed and acid washed PMMs (Table 6.3). For MB dye adsorption on UW-PMMs the rate constant $k_2$ increased from 0.003 g/mg/min to 0.02 g/mg/min with increasing dye concentration (from 5 mg/L to 10 mg/L). With further increase of dye concentration to 30 mg/L the rate constant decreased to 0.007 g/mg/min. Moreover, the pseudo 2nd order rate constants ($k_2$) for AR88 adsorption on W-PMMs appeared to be higher for all three dye concentrations when compared to UW-PMMs.

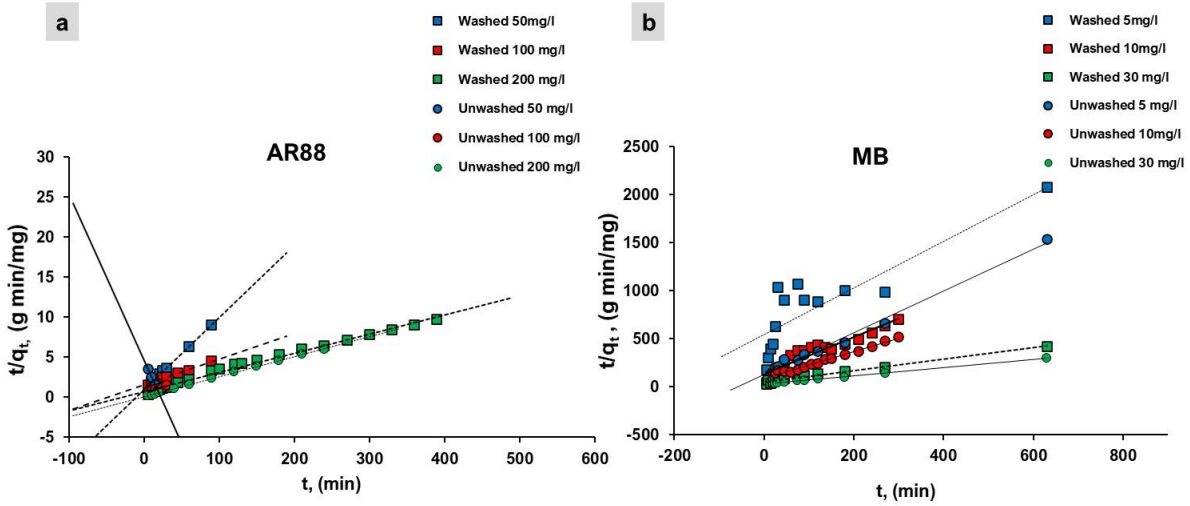



*Figure 6.23: Linear pseudo 2nd order kinetic model for the adsorption of a) AR88 and b) MB (V of the dye=10mL; adsorbent loading=6 g/L, pH= 2 for AR88 and pH=10 for MB).*

*Table 6.3: Kinetic rates for the adsorption of AR88 and MB on UW-PMMs and W-PMMs.*

| PMMs with different dye concentrations | | | Pseudo 1st order | | | | | Pseudo 2nd order | | | | |
|---|---|---|---|---|---|---|---|---|---|---|---|---|
| | | | $q_{e\ exp}$ (mg/g) | $q_{e\ cal}$ (mg/g) | $K_1$ ($min^{-1}$) | $R^2$ | $X^2$ | $q_{e\ exp}$ (mg/g) | $q_{e\ cal}$ (mg/g) | $K_2$ (g/mg/min) | $R^2$ | $X^2$ |
| MB | UW-PMMs | 5 mg/L | 0.5 | 0.28 | 0.0024 | 0.64 | 0.32 | 0.5 | 0.47 | 0.003 | 0.99 | 0.31 |
| | | 10 mg/L | 1 | 0.74 | 0.0023 | 0.82 | 0.32 | 1 | 0.98 | 0.021 | 0.99 | 0.32 |
| | | 30 mg/L | 3 | 1.9 | 0.0015 | 0.76 | 0.45 | 3 | 2.9 | 0.007 | 0.99 | 0.6 |
| | W-PMMs | 5 mg/L | 0.3 | 0.33 | 0.002 | 0.89 | 0.44 | 0.5 | 0.41 | 0.010 | 0.75 | 0.32 |
| | | 10 mg/L | 0.8 | 0.79 | 0.002 | 0.95 | 0.31 | 1 | 0.52 | 0.027 | 0.90 | 0.33 |
| | | 30 mg/L | 2.6 | 2.5 | 0.0011 | 0.82 | 0.34 | 2.6 | 2.68 | 0.002 | 0.98 | 0.21 |
| AR88 | UW-PMMs | 50 mg/L | 10 | 9.9 | 0.215 | 0.87 | 0.0009 | 10 | 10 | 0.19 | 0.99 | 0.32 |
| | | 100 mg/L | 20 | 8.8 | 0.168 | 0.53 | 0.0004 | 20 | 20 | 0.001 | 0.98 | 0.32 |
| | | 200 mg/L | 40 | 6 | 0.008 | 0.93 | 0.0013 | 40 | 40 | 0.0005 | 0.99 | 0.45 |
| | W-PMMs | 50 mg/L | 10 | 8.2 | 0.041 | 0.75 | 0.000009 | 10 | 10.1 | 0.25 | 0.99 | 0.44 |
| | | 100 mg/L | 20 | 22.6 | 0.04 | 0.89 | 0.0009 | 20 | 20.8 | 0.002 | 0.98 | 0.31 |
| | | 200 mg/L | 40 | 24.5 | 0.0089 | 0.97 | 0.027 | 40 | 40 | 0.0006 | 0.99 | 0.34 |

### *6.2.5.4 Adsorption Isotherms*

The adsorption isotherms are used to assess adsorbent-adsorbate (dye) surface interactions, particularly to estimate distribution of the dye molecules (maximum uptake capacity ($q_m$)) at the adsorption sites. The Isotherms for adsorption of AR88 and MB were calculated from experiments with varying adsorbent dose from 1 g/L to 12 g/L with an initial dye concentration of 300 mg/L. These parameters were chosen to ensure that PMMs would be saturated so the maximum concentration of the isotherm experiments could be appropriately determined. The Langmuir and Freundlich models for AR88 and MB are illustrated in Figure 6.24. The parameters from models are given in Table 6.4 and Table 6.5.

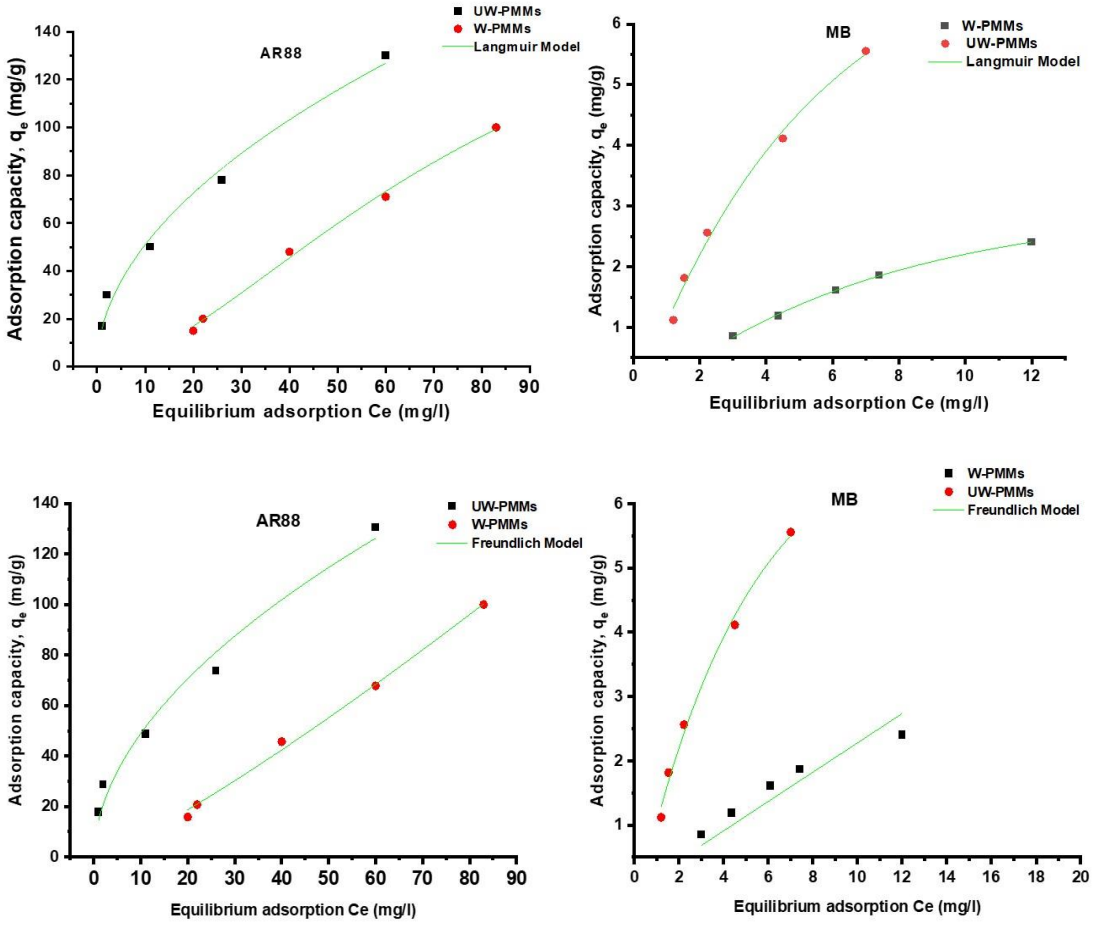



***Figure 6.24: AR88 and MB dye isotherm data fitted with Langmuir and Freundlich models (PMMs dose = 6 g/L, pH 2 and pH 10 for AR88 and MB respectively and temperature of 22±2 °C).***

*Table 6.4: Isotherm constants for adsorption of AR88.*

| | Langmuir isotherm | | | | Freundlich isotherm | | | |
|---|---|---|---|---|---|---|---|---|
| **Sample** | **$q_m$ (mg/g)** | **$R^2$** | **$X^2$** | **$q_e$ (mg/g)** | **$K_f$ (mL/g)** | **1/n** | **$R^2$** | **$X^2$** |
| **UW-PMMs** | 80 | 0.90 | 0.002 | 69 | 19 | 0.40 | 0.99 | 0.12 |
| **W-PMMs** | 50 | 0.98 | 0.012 | 56 | 14 | 0.56 | 0.99 | 0.31 |
| **Unprocessed magnetite** | -- | -- | -- | --- | -- | -- | -- | -- |

*(The adsorption capacity $q_e$ based on Freundlich isotherm model was calculated when adsorbent dose= 6 g/l)

*Table 6.5: Isotherm constants for adsorption of MB.*

| | Langmuir isotherm | | | | Freundlich isotherm | | | |
|---|---|---|---|---|---|---|---|---|
| **Sample** | **$q_m$ (mg/g)** | **$R^2$** | **$X^2$** | **$q_e$ (mg/g)** | **$K_f$ (mL/g)** | **1/n** | **$R^2$** | **$X^2$** |
| **UW-PMMs** | 14.5 | 0.99 | 0.32 | 8 | 2.10 | 0.53 | 0.91 | 0.31 |
| **W-PMMs** | 6 | 0.99 | 0.51 | 3 | 1.14 | 0.71 | 0.76 | 0.22 |
| **Unprocessed magnetite** | 1 | 0.76 | 0.62 | 1.5 | 0.58 | 0.90 | 0.52 | 0.53 |

*(The adsorption capacity $q_e$ based on Freundlich isotherm model was calculated when adsorbent dose= 6 g/l)

From Table 6.4, comparing Langmuir and Freundlich models, adsorption of AR88 on UW-PMMs and W-PMMs data fitted well using Freundlich's model revealing a high correlation coefficient ($R^2_{Freundlich}$ = 0.99) closer to unity and smaller values of $\chi^2$ compared with those using Langmuir's model. The 1/n value for UW-PMMs were smaller than W-PMMs. The maximum monolayer adsorption capacity ($q_m$) calculated for UW-PMMs and W-PMMs were 80 mg/g and 50 mg/g respectively. Isotherm studies were also conducted for unprocessed as received magnetite particles, and no noticeable sign of adsorption was observed using the AR88 dye.

In contrast, adsorption of MB data fitted well with the Langmuir model ($R^2_{Langmuir}$ = 0.99). The maximum monolayer adsorption capacity ($q_m$) estimated for UW-PMMs and W-PMMs were found to be 14.5 mg/g and 6 mg/g respectively (see Table 6.5). The as received magnetite interestingly also showed slight adsorption for MB dye. The investigated adsorption capacity ($q_m$) for as received magnetite was 1 mg/g according to Langmuir isotherm (with the best fit $R^2_{Langmuir}$ = 0.76 and $R^2_{Freundlich}$ = 0.52).

#### *6.2.5.5 Characterisation of PMMs post adsorption*

XPS analysis was performed to investigate the chemical bonding and structures on the surface of PMMs before and after dye adsorption. As shown in Figure 6.25, the peaks corresponding to Fe 2p, O 1s, C 1s and Fe 3p can clearly be identified in the survey scan spectrum for pure magnetite, UW-PMMs and W-PMMs before and after dye adsorption. No characteristic peak for Ca (Ca 2s, Ca 2p and Ca 3p) was seen for pure magnetite.

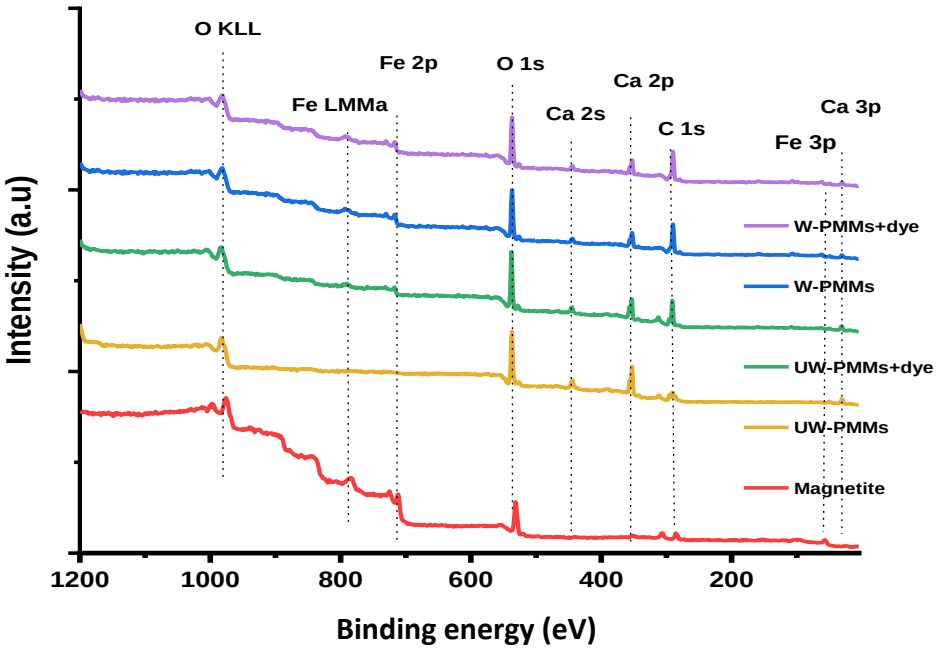



*Figure 6.25: XPS survey scan for Magnetite, UW-PMMs and W-PMMS before and after dye adsorption.*

Further, high resolution scans were carried out on UW-PMMs and W-PMMs before and after adsorption for each signature characteristic peaks (for C 1s, O 1s, Ca2p and Fe 2p). There are mainly two carbon species (see Figure 6.26 a) present in C 1s spectra for W-PMMs and the corresponding binding energies of 284.8 eV and 289.8 eV. The lowest binding energy represents the carbon from the carbon tab used or from carbon contamination, whilst the highest binding energy was assigned to carbonate ion most likely from remaining porogen remnants [437, 438, 506]. After dye adsorption two new components of C 1s appeared at 286.2eV and 288.5 eV which corresponded to either C-N or C-S and C-N-C bonds from the MB dye [507, 508]. From Figure 6.26 (b) it was observed that C 1s peak for MB had six components at binding energies 283.8 eV for C-C bond in the aromatic ring [509], 285 eV for aliphatic C-H/C-C bond, 286 eV for aliphatic C-N bond, 286.8 eV for C-S-C bond in aromatic ring [510, 511] , 288.4 eV for C-N-C bond in aromatic ring [508] and 289.5 eV for $C=N^{+}$ bond or $\pi$–$\pi^*$ transition in aromatic ring [438, 440]. Similar binding energies were also recorded for UW-PMMs before and after MB adsorption as shown in Figure 6.27.

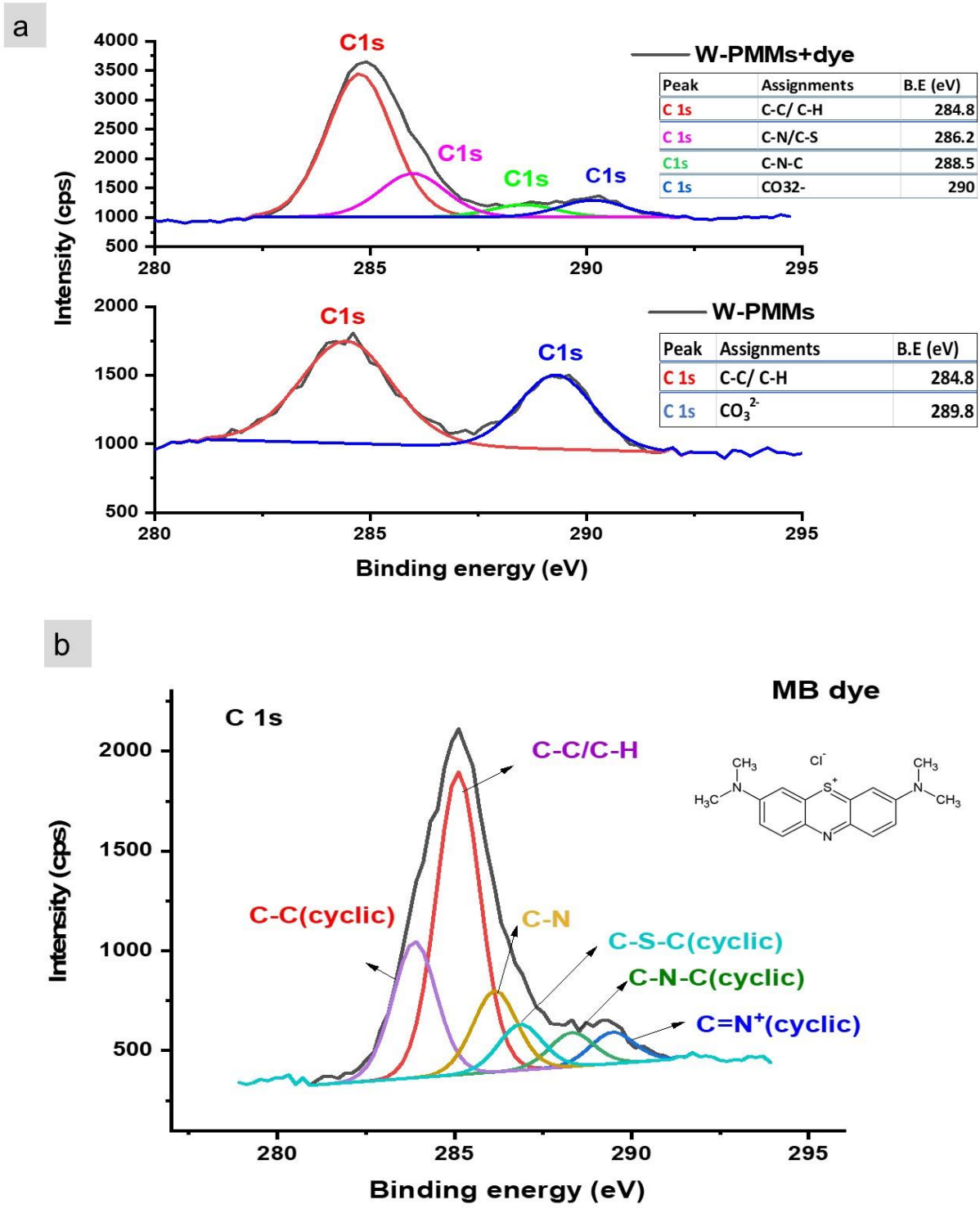



*Figure 6.26: High resolution XPS spectra of C 1s in a) W-PMMs before and after MB adsorption b) MB dye.*

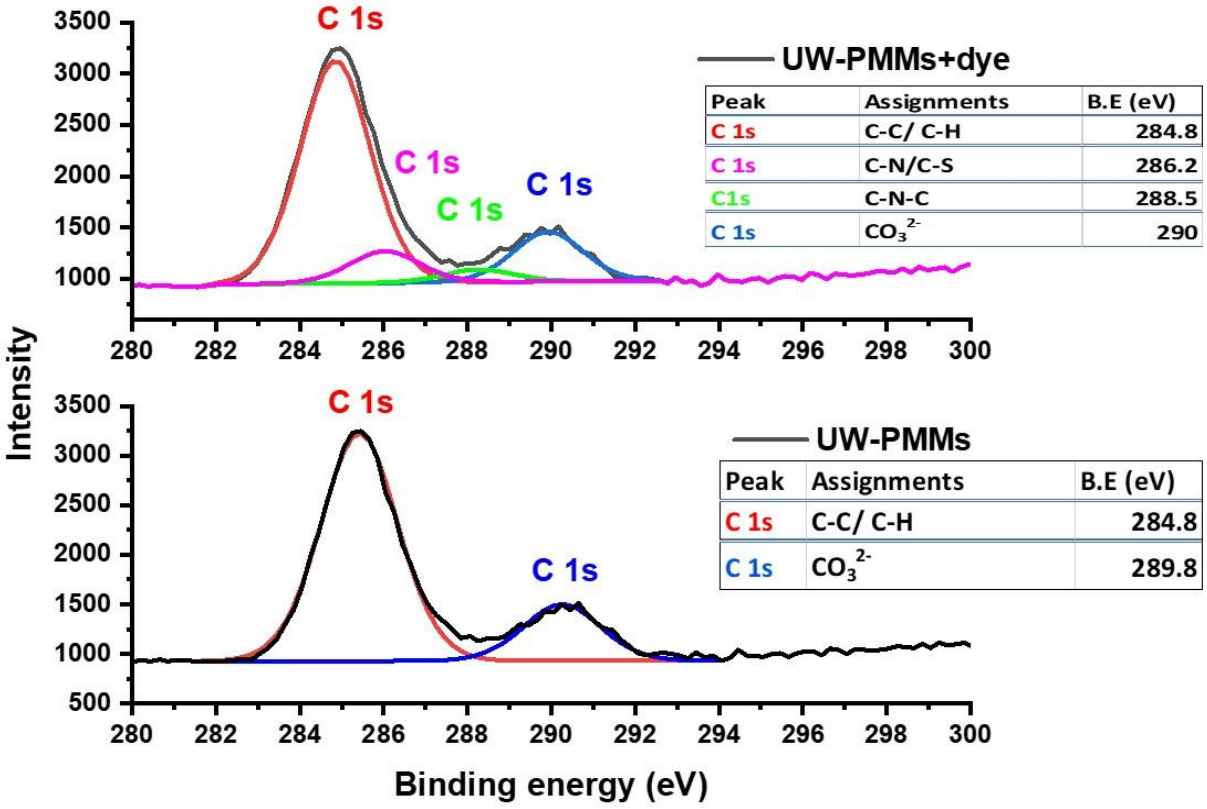



*Figure 6.27: High resolution XPS spectra of C 1s for UW-PMMs before and after MB adsorption.*

O 1s spectra of W-PMMs revealed characteristic peak for $Ca_2Fe_2O_5$ brownmillerite at 530.5 eV and 5291 eV for surface oxygen and lattice oxygen, respectively [512-515]. The other two peaks corresponded to oxygen in the porogen at 531.6 eV and the -OH functional group on the surface at 532.2 eV binding energies [512, 513]. After dye adsorption the O 1s peak at binding energy 529 eV and 530.5 eV revealed a deviation of 0.5 eV and 0.3 eV. Similar deviations were observed for UW-PMMs (see Figure 6.28). A new peak appeared at 533.4 eV which corresponded to either -OH group which may have been generated due to dissociation of water on metal surface or water molecule adsorbed on the surface [437].

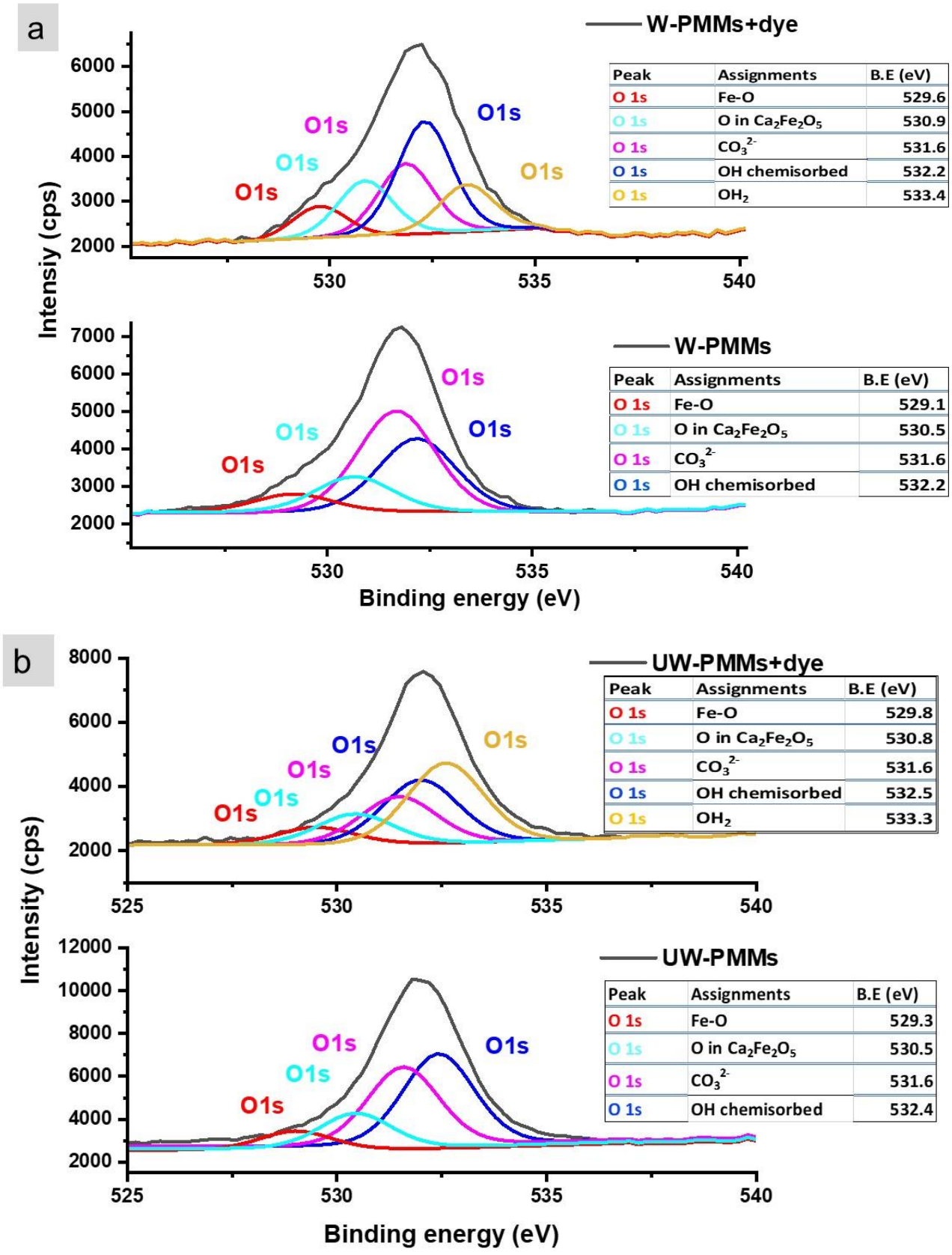



*Figure 6.28: O 1s spectra for a) W-PMMs and b) UW-PMMs before and after dye adsorption.*

Ca 2p spectra of W-PMMs and UW-PMM before adsorption (Figure 6.29) split into doublet due to spin-orbit coupling of Ca $2p_{3/2}$ and Ca $2p_{1/2}$ with binding energy difference approximately 3.5 eV which corresponding to Ca in $Ca_2Fe_2O_5$ [506]. W-PMMs and UW-PMMs revealed a peak shift to higher binding energy by ~0.6 eV and ~0.2 eV, respectively after dye adsorption.

The Fe 2p spectra in Figure 6.30 shows two main features assigned to Fe $2p_{3/2}$ at 710−713.2 eV for $Fe^{3+}$ in tetrahedral chain ($FeO_4$) and Fe $2p_{1/2}$ at 722.6−728.2 eV for $Fe^{3+}$ in octahedral chains ($FeO_6$) most likely from the $Ca_2Fe_2O_5$ mineral [515]. A closer look into Fe $2p_{3/2}$ spectra and Fe $2p_{1/2}$ spectra revealed that there was a shift of around 0.6-0.9 eV for $Fe^{3+}$ in tetrahedral chain ($FeO_4$) and 0.4-1.7 eV for $Fe^{3+}$ in octahedral chains ($FeO_6$), respectively toward higher binding energy for UW-PMMs and W-PMMs after dye adsorption.

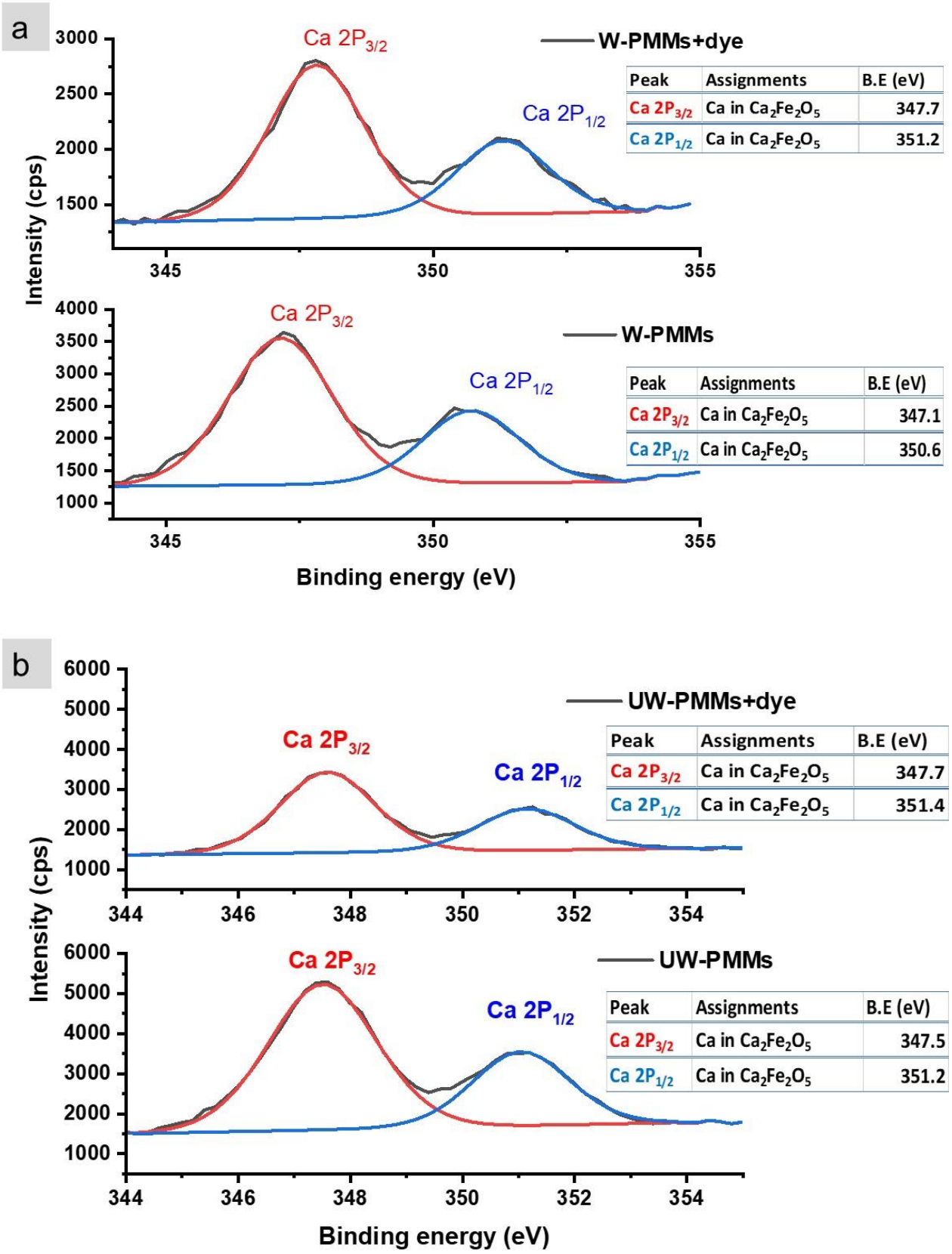
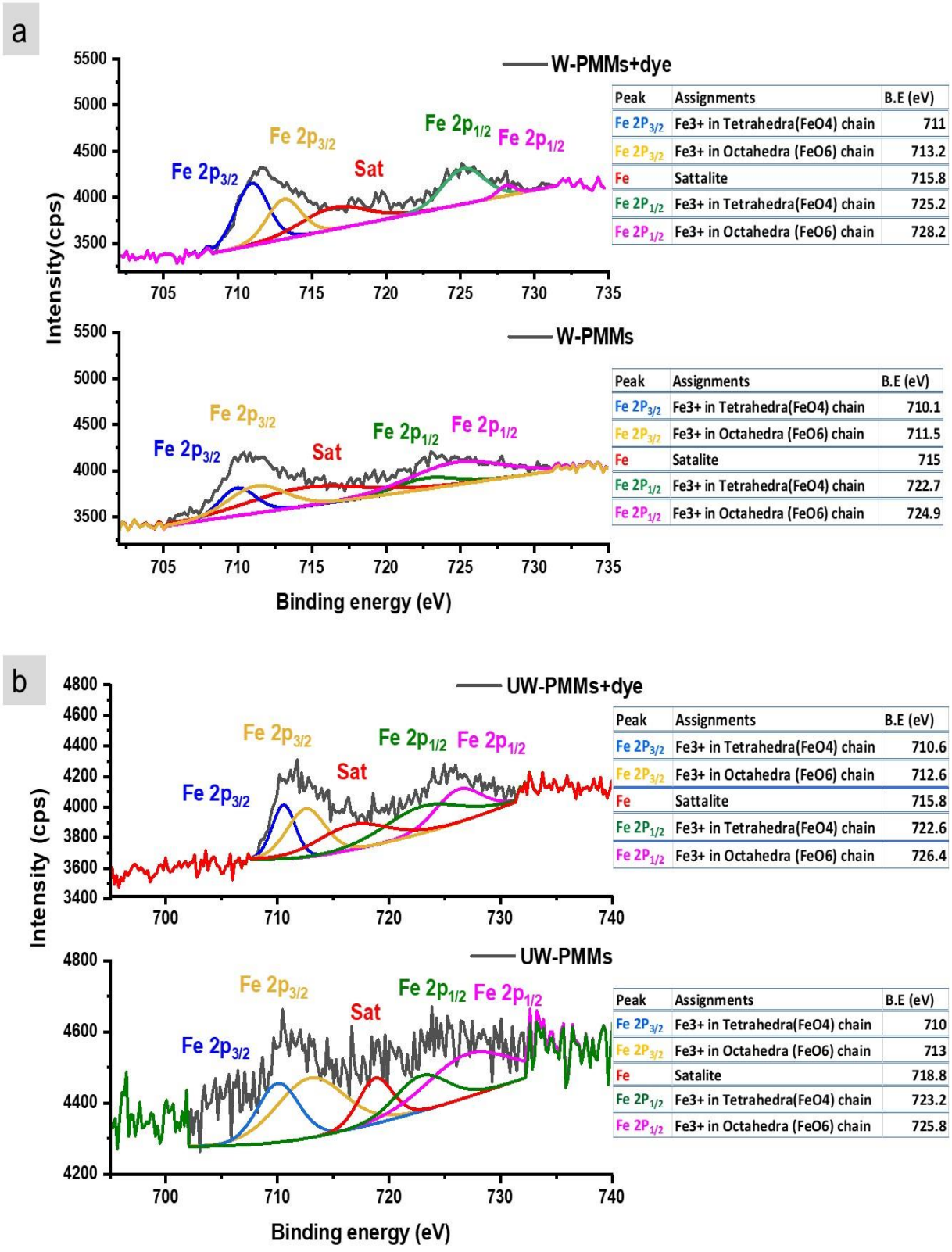



*Figure 6.29: Ca 2p spectra for a) W-PMMs and b) UW-PMMs before and after dye adsorption.*




| Peak | Assignments | B.E (eV) |
|---|---|---|
| Fe $2P_{3/2}$ | Fe3+ in Tetrahedra(FeO4) chain | 711 |
| Fe $2P_{3/2}$ | Fe3+ in Octahedra (FeO6) chain | 713.2 |
| Fe | Sattalite | 715.8 |
| Fe $2P_{1/2}$ | Fe3+ in Tetrahedra(FeO4) chain | 725.2 |
| Fe $2P_{1/2}$ | Fe3+ in Octahedra (FeO6) chain | 728.2 |

| Peak | Assignments | B.E (eV) |
|---|---|---|
| Fe $2P_{3/2}$ | Fe3+ in Tetrahedra(FeO4) chain | 710.1 |
| Fe $2P_{3/2}$ | Fe3+ in Octahedra (FeO6) chain | 711.5 |
| Fe | Satalite | 715 |
| Fe $2P_{1/2}$ | Fe3+ in Tetrahedra(FeO4) chain | 722.7 |
| Fe $2P_{1/2}$ | Fe3+ in Octahedra (FeO6) chain | 724.9 |

| Peak | Assignments | B.E (eV) |
|---|---|---|
| Fe $2P_{3/2}$ | Fe3+ in Tetrahedra(FeO4) chain | 710.6 |
| Fe $2P_{3/2}$ | Fe3+ in Octahedra (FeO6) chain | 712.6 |
| Fe | Sattalite | 715.8 |
| Fe $2P_{1/2}$ | Fe3+ in Tetrahedra(FeO4) chain | 722.6 |
| Fe $2P_{1/2}$ | Fe3+ in Octahedra (FeO6) chain | 726.4 |

| Peak | Assignments | B.E (eV) |
|---|---|---|
| Fe $2P_{3/2}$ | Fe3+ in Tetrahedra(FeO4) chain | 710 |
| Fe $2P_{3/2}$ | Fe3+ in Octahedra (FeO6) chain | 713 |
| Fe | Satalite | 718.8 |
| Fe $2P_{1/2}$ | Fe3+ in Tetrahedra(FeO4) chain | 723.2 |
| Fe $2P_{1/2}$ | Fe3+ in Octahedra (FeO6) chain | 725.8 |

*Figure 6.30: Ca 2p spectra for a) W-PMMs and b) UW-PMMs before and after dye adsorption.*

An intense absorption peak at 1400–1500 $cm^{-1}$ was observed in the PMMs samples from the FTIR-spectroscopic data (Figure 6.31). This peak was assigned to a symmetrical carbonate ion along with an adsorption at 874 $cm^{-1}$ and 710 $cm^{-1}$ for stretching of C=O in $CaCO_3$ and $CO_3^{2-}$, respectively [516]. The adsorption band from 554-583 $cm^{-1}$ are corresponded to the Fe–O-Fe stretching vibration [517, 518]. The peaks at ~ 525–580 $cm^{-1}$ was assigned to the stretching vibrations (v1) of the tetrahedral chain and the other low frequency band at ~500–522 $cm^{-1}$ was assigned to the stretching vibrations (v2) of the octahedral chain in $Ca_2Fe_2O_5$. Furthermore, FTIR band observed at 913 $cm^{-1}$, 1106 $cm^{-1}$ and 1203 $cm^{-1}$ could be attributed to Fe–Ca system [519, 520]. For MB dye vibrational peaks at 3211-3366 $cm^{-1}$ and 1638 $cm^{-1}$ are related to-NH/-OH overlapped stretching vibrations and stretching band of C=O, C-N from the amide II, respectively [521]. Post dye adsorption the Intensities (within adsorption band 554-583 $cm^{-1}$) of UW-PMMs and W-PMMs decreased and shifted to lower wave number without appearance of any new peak (see Figure 6.32b).

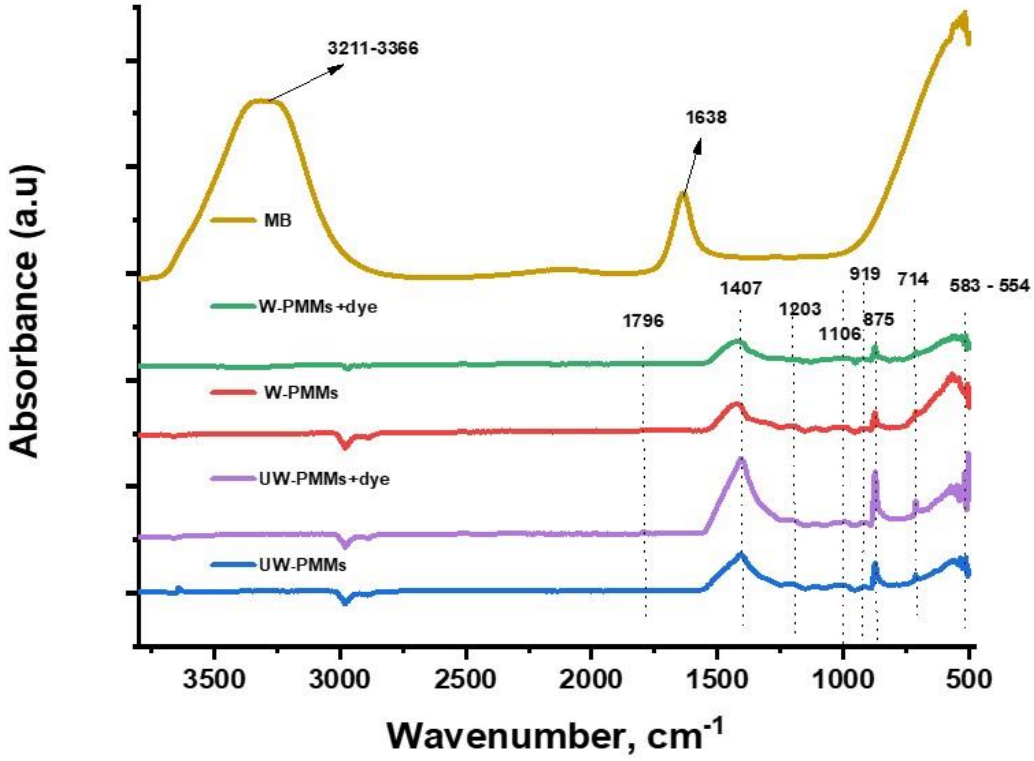



*Figure 6.31: FTIR spectra for MB, UW-PMMs and W-PMMs before and after dye adsorption.*

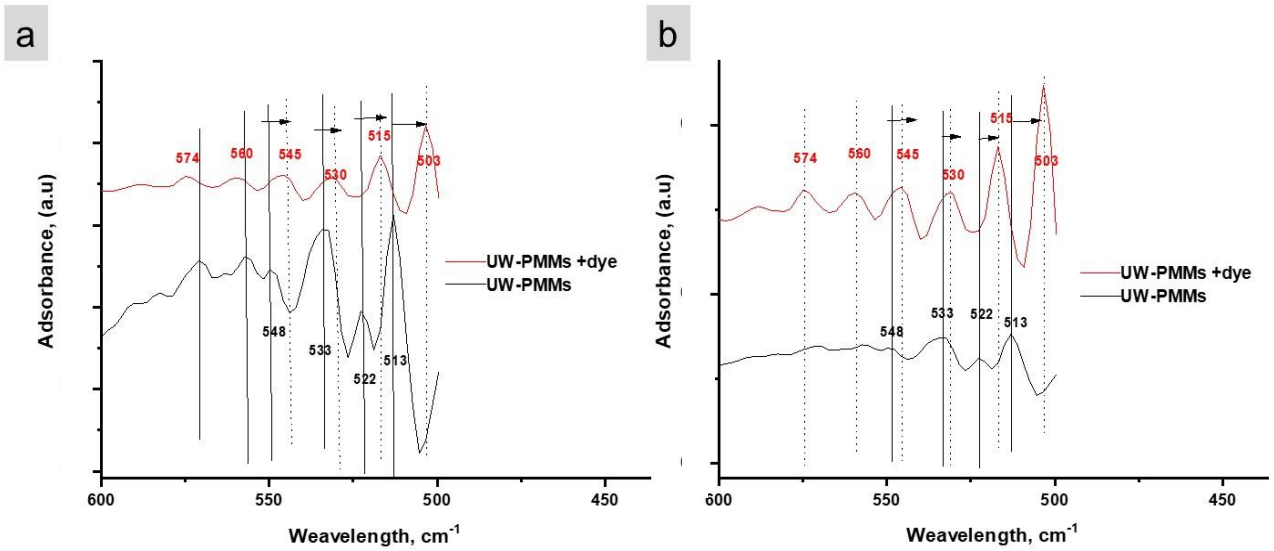



*Figure 6.32: Absorbance spectrum of a) UW-PMMs and b) W-PMMs before and after MB dye adsorption from 480-600 $cm^{-1}$. Solid and broken lines are before and after adsorption with arrow showing band shift.*

The XRD pattern of unwashed and acid washed PMMs used for the MB test shows only magnetite, $Ca_2Fe_2O_5$ and porogen ($CaCO_3$). An increase percentage of $CaCO_3$ were observed for both UW-PMMs and W-PMMs after dye adsorption.

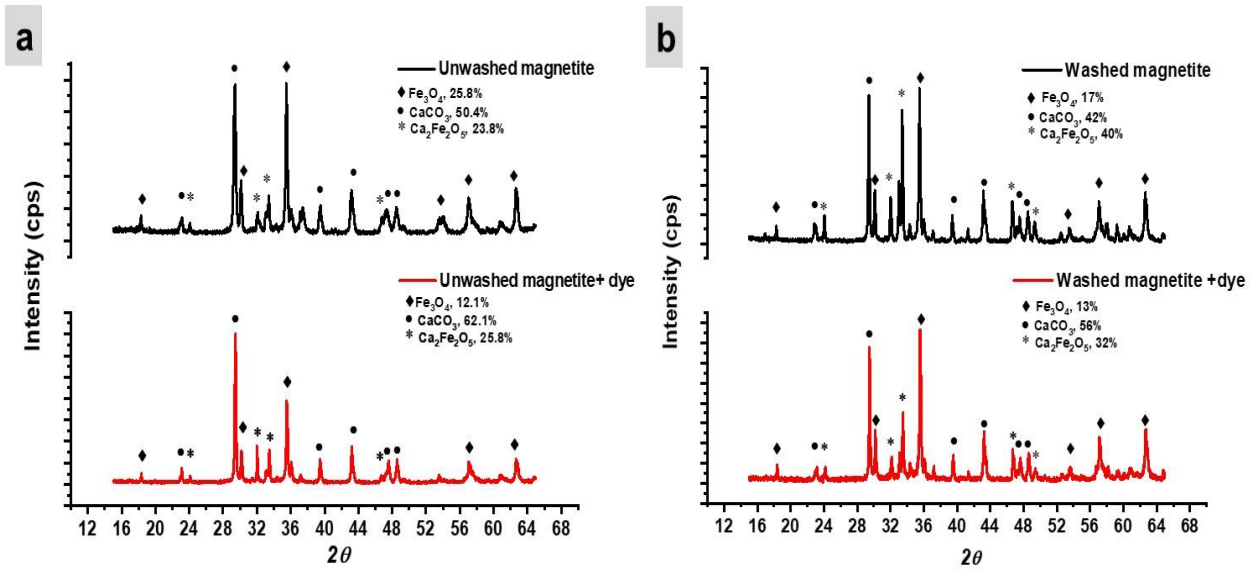



*Figure 6.33: XRD patterns for a) UW-PMMs and b) W-PMMs before and after adsorption with semi-quantitative analysis.*

## 6.3 Discussion

Magnetic materials are considered as ideal candidates for separation studies as they can be easily separated via application of a magnetic field [522-524]. Naturally occurring magnetite was

manufactured into porous microspheres via flame spheroidisation which eliminated the use of any harsh synthetic chemical routes. This chapter demonstrates the manufacturing process of producing porous magnetic microspheres (PMMs) and explores their potential for dye removal.

### 6.3.1 Processing of magnetite particles into microspheres via flame-spheroidisation

Magnetite, is a member of the cubic ferrites, also called ferrospinels, a naturally available, low cost, ecologically friendly and non-flammable material [357]. Iron atoms in magnetite occupy two different crystallographic sites, tetrahedral sites as $Fe^{2+}$ and octahedral sites as $Fe^{3+}$ ion [357]. During flame spheroidisation, oxy-acetylene flame (temperature up to ~3100°C [525]) melted the starting magnetite particles [526, 527] and the molten particles were transformed into spherical, or nearly spherical shape due to surface tension effects and being rapidly cooled when exiting the flame [527]. Variation of surface magnetic solid microspheres (MSM) topologies (see Figure 6.2) were related to the different flow paths of particles moving through the flame, as the starting magnetite particles had broad particle size distribution (below ≤45 µm) would resulting in change of particle residence time in the flame trajectory, thus a variation of particle heating and solidification processes would occur. Similar morphologies were also reported by Larr *et al*. for plasma-assisted spheroidisation of iron powders [526]. They reported that different flow paths within the flame trajectory including heating and solidification influenced the generation of pitted, grooved or smooth surface morphologies.

Initial efforts to make PMMs using our 'conventional method' failed to generate pores on the microspheres (see Figure 6.3). The unsuccessful formation was attributed to insufficient interaction between magnetite and porogen and the higher melt temperature (1620°C) of magnetite particles [528]. Thus, an alternate 'granular method' was developed for preparing PMMs.

In granulation process, PVA (a polymeric binder) allowed binding ground magnetite particles with close contact of porogen and maintained agglomerated mass together. During FS, porous structures could be formed as granules rapidly melted and bonded due to surface bonding or evaporation–condensation processes aided by in-flight heat transfer [529, 530]. Meanwhile porogen decomposes in the form of gas bubbles within the molten droplets that escapes quickly at the moment of solidification.

The cross-sectional SEM images of spheroidised ground magnetite without porogen (see Figure 6.11) revealed mostly dense core due to complete densification of the microspheres without porogen. Moreover, it was also evident that varying porogen to particle ratios also influenced the morphologies obtained, generating different pore sizes. MIP studies revealed larger pores and smaller pores with diameter ranging from 25-2 µm and 2-0.433 µm. Four different types of microspheres morphologies

were identified by varying porogen ratios (see Figure 6.9). Microspheres with large pores could be generated due to;

1) smaller gas bubbles coalesced to form larger gas bubbles inside the microspheres leading to larger pore sizes, or

2) larger quantity of porogen entrapped led to higher amounts of $CO_2$ release, forming larger voids/pores within the microspheres.

In addition, microspheres with numerous tiny pores were observed with increasing porogen ratio (see Figure 6.9).

### 6.3.2 Structural analysis of PMMs

XRD analysis of PMMs identified $Ca_2Fe_2O_5$ mineral besides magnetite. Usually $Ca_2Fe_2O_5$ is considered as anion-deficient perovskite with ordered oxygen vacancies [531]. A mineral from the brownmillerite family (general formula $ABO_{2.5}$ or $A_2B_2O_5$) have gained much attention over the past few decades for applications such as solid oxide fuel cells, sensors as well as membranes for oxygen separation and photocatalysis [532, 533]. X-ray diffraction results for the milled samples during 1 min, 5 min and 15 min showed a decrease in $CaCO_3$ content before spheroidisation. This decrease in $CaCO_3$ correlated with decrease content of $Ca_2Fe_2O_5$ mineral in the PMMs. This confirms that generation of $Ca_2Fe_2O_5$ mineral was associated with stoichiometric quantities of $CaCO_3$. During spheroidisation the $CaCO_3$ and $Fe_3O_4$ undergoes thermo-chemical reaction and was transformed to a mixture of crystalline $Ca_2Fe_2O_5$ and $Fe_3O_4$. The possible conversion reaction based on literature were described as follows [534-536]:

$$CaCO_3 \xrightarrow{\Delta} CaO + CO_2 \qquad \textit{Reaction 6.1}$$

$$Fe_3O_4 \xrightarrow{\text{oxidation}} Fe_2O_3 \qquad \textit{Reaction 6.2}$$

$$2CaO + Fe_2O_3 \xrightarrow{\Delta} Ca_2Fe_2O_5 \qquad \textit{Reaction 6.3}$$

$$2Fe_3O_4 + 0.5\ O_2 + 6CaCO_3 \xrightarrow{\text{Overall onestep reaction}} Ca_2Fe_2O_5 + CO_2 \qquad \textit{Reaction 6.4}$$

It is evident from XRD analysis of MSM that magnetite partially oxidised to hematite ($Fe_2O_3$) (Figure 6.2). Although no traces of hematite were observed for PMMs from XRD diffractogram which suggested that the hematite undergoes a thermo-chemical reaction [536]. As hematite is more reactive than magnetite, thus reaction with CaO derived from decomposition of $CaCO_3$ produced $Ca_2Fe_2O_5$ [537].

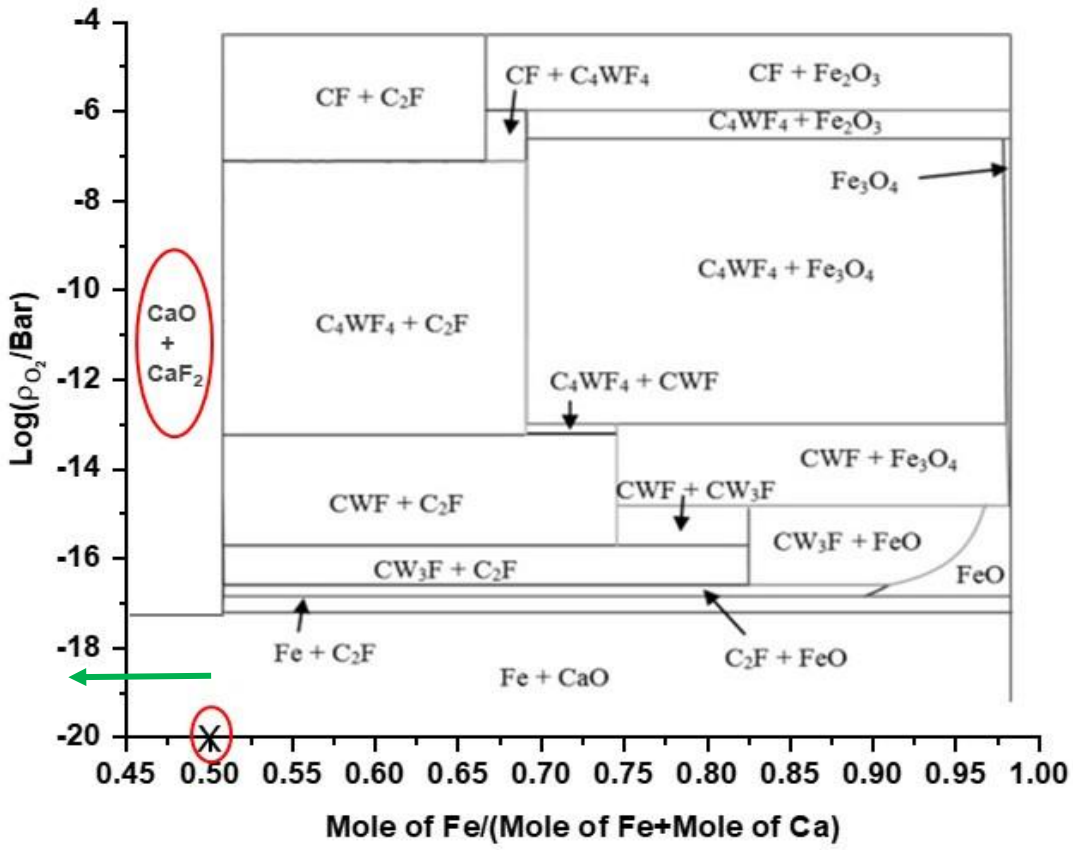



*Figure 6.34: Phase diagram of the Ca–Fe–O system at 1173 K calculated using MTDATA studied by Ismail et al. [522]. Where C = CaO, F = $Fe_2O_3$, W = FeO, CF = $CaFe_2O_4$ ($CaO.Fe_2O_3$) and $C_2F$ = $Ca_2Fe_2O_5$ ($2CaO.Fe_2O_3$). The green arrow indicating the molar ratio investigated.*

The $Ca_2Fe_2O_5$ content in UW-PMMs increased with increasing porogen ratio (from 1: 0.5 to 1:1) and then decreased (for 1: 3 porogen ratio) with increase in porogen. However, upon acid washing, the semi quantitative analysis (based on XRD) revealed that both 1:1 and 1:3 had similar quantities of $Ca_2Fe_2O_5$ content (60 % ± 4). This suggests that 1:1 porogen ratio was optimum for maximum formation of $Ca_2Fe_2O_5$. Furthermore, according to Reaction 6.3, stoichiometrically the ratio of 2:1 for Ca/Fe should be used for obtaining 1 mol of $Ca_2Fe_2O_5$. For 1:1 particles to porogen ratio the calculated molar ratio is 2.3:1 which is equivalent to 2:1. Moreover, the product combination was also in agreement of the phase diagram in the Ca-Fe-O system presented by Ismail *et al.* (see Figure 6.34) [538]. Various phases can form at equilibrium, depending on the equilibrium oxygen partial pressure (from the oxidising flame which was fixed for this study) and molar ratio of particle to porogen ratio according to Figure 6.34. In this study, the molar ratio [mole of Fe/ (mole of Fe + mole of Ca)] were

calculated at 0.33, 0.45 and 0.5 for porogen to particle ratio 1:0.5, 1:1 and 1:3 respectively which produced the $Ca_2Fe_2O_5$ phase with unreacted porogen.

Re-spheroidisation of unwashed PMMs (1:0.5 porogen ratio 15 min grinding) progressively up to 4$^{th}$ time showed that caused gradual core densification with loss of internal porosity (see Figure 6.7). The TGA studies confirmed that the remaining residual porogen decomposed during re-spheroidisation as the porogen content decreased (decrease to 1%). However, the $Ca_2Fe_2O_5$ content did not change significantly through-out the re-spheroidisation. This suggests that magnetite did not undergo oxidation to react further with the porogen to give increased $Ca_2Fe_2O_5$ content.

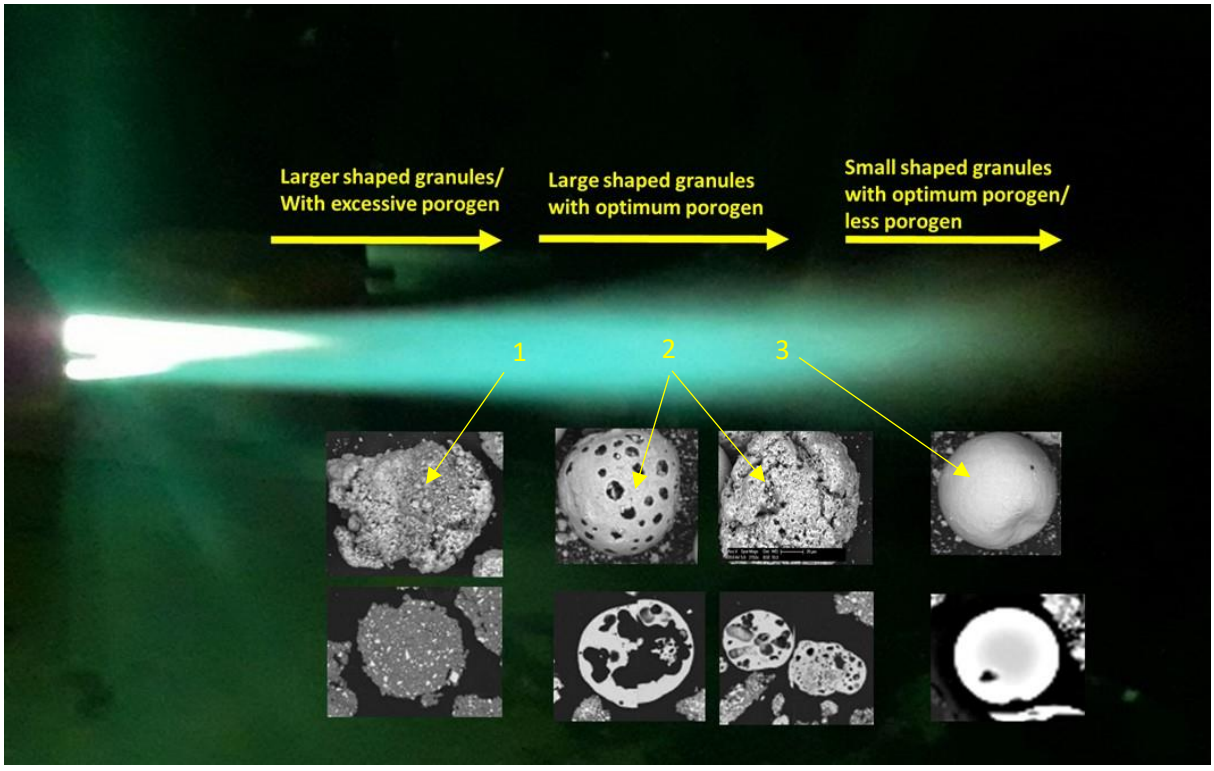



*Figure 6.35: Effect of granule size and porogen on the final morphology of microspheres. Position 1, 2 and 3 directing the exit point of microspheres.*

Residence time of granules and amount of porogen could also influence the final content and distribution of $Ca_2Fe_2O_5$ in PMMs. Considering the axial pressure exerted by the fuel gas mixture remains constant, the amount of heat-transfer from the flame to particles (agglomerates) depends on factors such as particle residence time and size of the agglomerates which are interchangeably related with each other [539, 540]. It could be suggested that depending on the residence time of the agglomerate (see Figure 6.35); a) A homogenous spherical porous and/or irregular porous structure (position 2), b) closed pore structure/dense core (position 3) can be produced.

It should be noted that the sieved agglomerates had a size of ≤200 µm. Granules of smaller size would have a longer residence time than larger granules, due to the effect of axial pressure exerted by oxy-acetylene flame. Thus, smaller granules would transform into porous structure that would again remelt due to longer residence time (see Figure 6.35 position 3). SEM images revealed 50±10 µm microspheres (for 15 min grinding with 1:0.5 porogen ratio) with smooth surface (Figure 6.5). This suggested complete densification of the microspheres due to smaller size of agglomerate that had longer residence time within the flame or could be due to inadequate amount of porogen (1:0.5). Conversely, larger granules would have an optimal residence time, to generating $Ca_2Fe_2O_5$ and then escaping the flame whilst retaining a porous structure (see Figure 6.35 position 2).

Porous irregular particles (were observed with porogen ratio 1:1 and 1:3) can be explained by presence of excessive amount of porogen that would decrease the mass of granules which were unable to maintain sufficient velocity to be sustained in the flame trajectory and thus ejected from the main flame path (see Figure 6.35, position 1). As a result, the amount of unreacted porogen found was higher for the increased porogen ratios (see Figure 6.13). A balance between thermo-chemical reaction and porogen decomposition could be achieved by optimising porogen levels with granule size. For example, MLA studies revealed that microspheres (with varying porogen ratio) typically composed of $Ca_2Fe_2O_5$ with/without entrapped magnetite particles had a size of 180 ± 10 µm.

### 6.3.3 Surface area and porosity profile of PMMs

The surface area of the PMMs was found to be greater with increasing grinding time with the same amount of porogen (ratio 1:0.5). By increasing milling time, new particles with smaller size generated interparticular gaps which fused together during spheroidisation resulting in increased number of pores showing an increase in surface area. Simultaneously, increasing porogen ratio also increased surface area (from 0.03 $m^2/g$ to 4.7 $m^2/g$ for 1:3 porogen ratio). This complemented the cross-sectional images from MLA studies, which showed increased number of pores with increasing porogen ratio. Furthermore, mercury porosimetry of PMMs with porogen ratio 1:3 also revealed greater pore volume than PMMs with 1:1 porogen ratio. This increase in pore volume was attributed to increase surface area of PMMs.

### 6.3.4 Factors influencing dye adsorption on UW-PMMs and W-PMMs

The scoping studies conducted using AR88 dye (50 mg/L solution) on PMMs (6 g/L PMMs dose) manufactured via changing process parameters such as varying flowrates (2:2-3:3), flame-type (Reducing, Neutral and Oxidising flame) and varying porogen ratio. This study showed that the oxidising-flame gave 100% dye removal within 30 min. Although structural analysis (such as XRD) was

not conducted to understand the influence of using oxidising, reducing or neutral flame with dye adsorption. After acid washing the PMMs showed a decrease in adsorption compared to the unwashed PMMs. The influence of porogen and dye adsorption was also observed for heat-treated microspheres and recycled glass microspheres (Chapter 4 and Chapter 5). W-PMMs with higher porogen ratio (1:3) showed the highest dye removal (85%) as expected. This was attributed to their higher surface area (4.7 $m^2/g$) compared to the other microspheres tested. Generally, adsorption is a surface phenomenon, and so higher surface areas exhibits greater adsorption [541].

The pH of the solution also plays a key role as it can affect the surface charge of the adsorbent [542, 543]. Varying the pH of UW-PMMs did not show any significant influence in adsorption capacity. However, the adsorption capacity of W-PMMs changed with changing pH for both dyes. Adsorption of AR88 by W-PMMs showed increased adsorption in acidic pH (2-4) while adsorption of MB increased in basic pH (8-10). It has been reported that magnetite is an amphoteric solid i.e., at a pH lower than the point of zero charge (PZC) the surface charge is positive due to the accumulation of $H^+$ ions on the surface, while negatively charged above the PZC [543-545]. AR88 is a negatively charged dye which may have electrostatically interacted with positively charged PMMs (due to protonation) in acidic pH. Simultaneously, MB is a positively charged dye that could have electrostatically interacted with negatively charged PMMs (due to de-protonation) at a basic pH. Although the PZC point / zeta potential of PMMs was not determined considering the size of the PMMs and the analysis equipment available. However, UW-PMMs were pH independent as adsorption did not change with changing pH. This indicates porogen could be affecting the final pH of the solution.

With increasing adsorbent dose, the % dye removal increased from 1g/L to 6 g/L and then reached a plateau with no significant change in % dye removal for AR88 and MB dyes. The removal efficiency of dyes improved by increasing PMMs loading due to the increased active sites within the PMMs [545, 546]. When dye removal plateaued the availability of adsorption site was greater than the adsorbate level (dye concentration) [463].

The adsorption kinetics of AR88 using UW-PMMs and W-PMMs revealed complete adsorption within 90 mins for dye concentration 50 mg/L and 100 mg/L. However, at 200 mg/L dye concentration was initially very rapid (first 10 min) followed by slower adsorption till reached a plateau (360 mins). Simultaneously, adsorption of MB (dye concentrations 5mg/L, 10 mg/L and 30 mg/L) also followed a two-step adsorption process. Similar observations were reported by Hou *et al.* while investigating adsorption progress of phosphate to the magnetite surface [466]. They reported that the adsorption process could be divided into two stages: a rapid adsorption step, followed by a relatively slow adsorption step [466]. Based on the literature studies, a rapid adsorption step where there are

sufficient adsorption sites, and the internal diffusion resistance was weak [464, 466]. This was followed by a slow adsorption step where the surface charge become more/less negative/positive, and the sites available for adsorption further decrease and internal diffusion resistance increases [464, 466]. At concentrations of 50 mg/L and 100 mg/L the AR88 was rapidly adsorbed suggesting sufficient active sites for the dye molecules in solution. For both dyes, the equilibrium adsorption capacity ($q_e$) increased with increased dye concentration. This was attributed to the driving force of the concentration gradient increased with increasing the initial dye concentration [464].

The data indicated (see Table 6.3) that the pseudo 1$^{st}$ order reaction equation was not ideal to model the adsorption data with exception of adsorption of MB with lower concentrations (5mg/L and 10 mg/L) for W-PMMs. Thus, it is speculated that the rate-limiting step of the adsorption on PMMs is mainly chemical process (fitted by pseudo 2$^{nd}$ order) which could involve electron sharing or exchange via electrostatic attraction, hydrogen bonding, covalent, ionic bond formation, between the adsorbate and the active site of an adsorbent surface [465]. It is further suggested that at lower dye concentrations of MB (5mg/L and 10 mg/L) the surface charge on PMMs was greater than dye molecules which may have resulted in agglomeration of PMMs (having a similar charge), thus active site interactions were hindered. Additionally, pseudo 2$^{nd}$ order rate constant ($k_2$) decreased with increasing initial concentrations of AR88 and MB dye. This again was related to the availability of active adsorption sites decreasing with increasing dye concentrations [464, 466]. The pseudo 2$^{nd}$ order rate constants ($k_2$) for AR88 adsorption on UW-PMMs appeared to be higher for all dye concentrations than W-PMMs referring faster adsorption using UW-PMMs. Based on literature studies, the slow adsorption on W-PMMs could be ascribed to increased accumulation of charged dyes at the external surface of W-PMMs resulting in slower diffusion to the internal pore structure of PMMs [547, 548].

In isothermal studies, the $R^2$ values of the Freundlich model are higher than Langmuir for adsorption of AR88 dye, whereas the Langmuir model showed the highest $R^2$ values for MB dye. This indicated multilayer adsorption for the AR88 dye and homogeneous adsorption for MB [467, 468]. It should be noted that the porogen had an affinity to adsorb AR88 dye (see chapter 5, Table 5.6). UW-PMMs and W-PMMs consists of approximately 50% and 5% porogen based on XRD analysis (see Figure 6.12). Furthermore, Freundlich equation includes a heterogeneity factor, 1/n; the lower the value of heterogeneity factor, the higher the heterogeneity of the adsorbent surface [468]. In this study, based on heterogeneity, it could be suggested that adsorption by PMMs was due to combined adsorption effect of $Ca_2Fe_2O_5$ and porogen. Moreover, the 1/n value for UW-PMMs was smaller than W-PMMs. This again indicates low percentage of porogen content (5%) in W-PMMs. In contrast, porogen does not have significant adsorption affinity for MB dye (see Table 6.5) indicating that homogeneous MB

adsorption was solely due to the porous $Ca_2Fe_2O_5$ mineral material. The maximum monolayer adsorption capacity ($q_m$) calculated for UW-PMMs was 80 mg/g and 14.5 mg/g for AR88 and MB dyes, respectively. However, the adsorption capacity of W-PMMs were 50 mg/g and 6 mg/g for AR88 and MB dyes, respectively. This decrease in adsorption capacity for W-PMMs could be attributed to slow adsorption kinetics due to accumulation of surface change [547, 548].

### 6.3.5 Adsorption mechanism and possible photocatalytic activity

To further explore the interaction mechanisms of PMMs with MB, XRD, FTIR and XPS analysis of UW-PMMs and W-PMMs post adsorption were conducted and compared in detail. XPS high resolution scan for C1s of UW-PMMs and W-PMMs post MB adsorption showed two new components which corresponded to either C-N, C-S or C-N-C from the MB dye. This indicated the presence of dye on the surface of PMMs. Furthermore, -OH groups appeared on the spectra revealing possible -OH group formation on the $Ca_2Fe_2O_5$ mineral due to the maintenance of basic pH during adsorption or atmospheric moisture adsorption. After MB adsorption O1s spectra for UW-PMMs and W-PMMs revealed 0.5 eV and 0.3 eV deviation for peak characteristic of $Ca_2Fe_2O_5$. This indicated possible hydrogen bond formation between oxygen in -OH group and hydrogen in MB dye. Besides, the Fe 2p region of the XPS spectrum showed a peak shift to higher binding energy after dye adsorption suggesting oxidation of Fe [549]. This suggested formation of FeO(OH) bond on the surface of $Ca_2Fe_2O_5$ [549]. Furthermore, FTIR studies revealed that the adsorption Intensities (within adsorption band 554-583 $cm^{-1}$) decreased and shifted to lower wavenumber for UW-PMMs and W-PMMs after dye adsorption. This suggested that MB dye interaction with Fe-O bonds occurs via the formation of an FeO(OH) bond. These findings are consistent with XPS study. The decrease in peak intensity could be attributed to electrostatic and hydrogen bond formation during dye adsorption. Noreen *et al.* reported adsorption of Direct Sky Blue (DSB) dye by Fe-O and observed similar peak shifts with decreased adsorption intensities referring to possible electrostatic and hydrogen bond formation [550].

The Ca2p spectra from high resolution scan showed peak shift to higher binding energy after MB dye adsorption. This could be attributed to partial transformation of Ca in $Ca_2Fe_2O_5$ into $CaCO_3$ [506]. Yang *et al.* reported on the photocatalytic activity of $Ca_2Fe_2O_5$ for the removal of methyl orange (MO) that partially converted to $CaCO_3$ during photodegradation of MO [551]. Vanags *et al.* also reported partial transformation of $Ca_2Fe_2O_5$ into $CaCO_3$ while investigating $Ca_2Fe_2O_5$ nano powders thin films for MB degradation [332]. They suggested that $Ca_2Fe_2O_5$ was unstable due to the oxygen vacancy formation which might have triggered by photoinduced electron generation during photocatalysis. Accumulation of large number of oxygen vacancies caused an imbalance between cations and anions in the lattice

which could be maintained by releasing Ca from the lattice [332]. XRD analysis post MB adsorbed PMMs showed increased levels of $CaCO_3$ which may be due to release of Ca from $Ca_2Fe_2O_5$. This investigation provided useful insight about possible photocatalytic activity of the $Ca_2Fe_2O_5$ PMMs.

In general, the dye interaction of MB with PMMs could have been a combined effect of many factors, such as surface area, phase structure, surface hydroxyl density, surface charge and photoactivity [552]. In a typical photocatalysis process, the semiconductor absorbs high energy photons (energy higher than band gap energy) which subsequently leads to formation of valence band holes ($h^+$) and conduction band electrons ($e^-$). Photogenerated electron and hole then produce reactive oxygen species (ROS) i.e. free radicals ($OH^{\cdot}$), which in turn could attack organic species (such as dyes) and mineralize to $CO_2$ and $H_2O$ [332, 553, 554]. Vavilapalli *et al.* reported that $Ca_2Fe_2O_5$ has a band gap of 2.21 eV which is suitable for sunlight-driven photocatalysis [555]. These findings suggest that a possible mechanism of PMMs with MB dye interaction could be proposed as follows:

The negatively charged PMMs surfaces show affinity to MB dye. According to the adsorption results (see Figure 6.24), the MB dyes can be rapidly adsorbed onto the PMMs surface by hydrogen bond formation via MB dye and OH of $Ca_2Fe_2O_5$ to reach dynamic adsorption/desorption equilibrium. The adsorbed dye can then partially photo-catalytically degrade into its by-products before finally degraded into simpler molecules such as $CO_2$, $NO^-_3$, $SO_4^{2-}$ and $H_2O$.

However, it should be noted that the dye removal experiments were conducted under normal conditions without the aid of sunlight or xenon lamp required to perform photocatalysis experiments [513, 556]. Therefore, to fully understand the photocatalytic performance:

i) The photocatalytic reaction under visible light using a Xe arc lamp with a cut-off filter providing the visible light ($\lambda \geq 420$ nm) should be performed [332],

ii) Photocatalytic reaction under UV light irradiation consisted of high-pressure mercury lamp could also be performed [551].

iii) Scavengers such as $AgNO_3$ as electron ($e^-$) scavenger, Ethylenediaminetetraacetic acid (EDTA) as a hole scavenger ($h^+$) and Isopropyl alcohol (IPA) as the $OH^{\cdot}$ radical trapping agent must be used to investigate the photodegrading phenomena [332].

## 6.4 Summary

In this chapter, solid magnetite microspheres (SMS) and porous magnetitic microspheres (PMMs) were successfully prepared via flame spheroidisation. XRD and MLA studies confirmed the presence of $Ca_2Fe_2O_5$ brownmillerite mineral in PMMs beside magnetite, indicating single route synthesis using the flame-spheroidisation process. This study demonstrated that magnetite particles reacted

stoichiometrically (at 1:1 ratio by wt%) with porogen to produce $Ca_2Fe_2O_5$. Structural, morphological, and surface area profiles of PMMs were tailored by varying grinding time and porogen ratio. Increased grinding time (from 1to 15 mins) and porogen ratio (1:0.5 to 1:3) revealed an increased specific surface area (from 0.03 to 4.7 $m^2/g$) of PMMs. Mercury intrusion analysis revealed PMMs with 63-65 % porosity with surface pore diameter ranged from 25-2 µm and internal pore diameter ranged from 2-0.433 µm. The capability of PMMs for the remediation of two types of dye (AR88 and MB) from water were investigated. A range of factors such as pH, adsorbent dose, dye concentration influenced the adsorption kinetics and efficacy of the PMMs. Adsorption kinetics and isotherm models (including the pseudo-first-order, Langmuir and Freundlich models) were fitted to the experimental data for mechanistic discussions. The Langmuir isotherm model of adsorption data indicated that maximum adsorption capacity ($q_m$), of UW-PMMs were generally greater than W-PMMs, which were 80 mg/g and 50 mg/g respectively for AR88 dye and 14 mg/g and 6mg/g respectively for MB dye. The adsorption of W-PMMs was pH and adsorption dose depended. Simultaneously, adsorption on UW-PMMS was pH independent and adsorption capacity attributable to porogen content, including $Ca_2Fe_2O_5$ in PMMs. Post-adsorption PMMs were investigated by XPS, FTIR and XRD in order to propose a possible mechanism of interactions of the MB dye with PMMs via electrostatic attraction, hydrogen bond formation and complex interaction with Fe-O bonds. XPS study provided useful insight about possible photocatalytic activity of the $Ca_2Fe_2O_5$ which would be a potential area of research for future work.

# Chapter 7: Conclusions and future work

## 7.1 Conclusions

The purpose of this work was to manufacture and characterise novel porous microspheres using flame-spheroidisation technique suitable for wastewater treatment applications. Existing porous materials manufactured using toxic chemical and long processing times could be avoided by simply using a solvent free flame spheroidisation process. Early research was focused on using flame spheroidised porous structures (phosphate-based glasses) for biomedical studies. No studies were conducted before exploring these porous structures for wastewater applications. In such regard, the study began by exploring phosphate glass microspheres which were later heat-treated and manufactured into increased surface area microspheres. However, considering the cost effectiveness, use of sustainable resources and reducing negative environmental impact, the most common source of material such as cheap, waste recycled glasses and naturally occurring magnetite were transformed into porous microspheres and explored for dye removal studies. The following conclusions could be made from this thesis:

Preliminary studies focused on optimising the pores of porous phosphate-based glass (PBG) microspheres to maximise dye removal efficacy. 16 different batches of microspheres were prepared from three different size ranges of glass particles (63-125 µm, 125-200 µm and 200-355 µm) and with varying ratios of porogen (1:0.5, 1:1, 1:2 and 1:3 using 45-63 µm porogen). Starting glass particle size played an important role in controlling residence time of glass particles within the flame while being spheroidised. The smaller the particle size the greater the residence time in the flame. Hence, staring particle size 63-125 µm, 125-200 µm had optimum residence time to manufacture porous microspheres with surface pores (5-45 µm) and interconnected porosities (65-70%). However, microspheres manufactured using 200-355 µm starting glass particle were seen to have distorted shape (as not all were spherical) with a solid dense core having only surface pores due to insufficient residence time within the flame.

For each starting particle size, the surface area and porosity of porous glass microspheres manufactured increased with increasing glass particle to porogen ratio. Moreover, microspheres manufactured via smaller sized glass particles showed greater surface area. For example, surface area of the microspheres measured using krypton adsorption isotherm which revealed lowest value of 0.11 $m^2$ /g and a highest value of 0.54 $m^2$ /g of which the 125-150 µm (S), 200-355 µm (L), 150-200 µm (M) and 200-355 µm (XL) achieved 0.54 $m^2$ /g, 0.35 $m^2$ /g, 0.27 $m^2$ /g and 0.11 $m^2$/g respectively with 1:3 glass particles to porogen ratio.

Adsorption capacity of porous microspheres demonstrated a direct relationship with the surface area of the microspheres. Adsorption capacity for acid red 88 (AR88) in batch studies showed increased adsorption with increasing surface area of the microspheres.

This study showed that microspheres produced using porogen sizes between 45 – 63 µm had large surface pores (55 ± 8 µm) with highly interconnected porosities. In the second stage, to explore the influence of porogen size, porous PBG microspheres were then manufactured using smaller porogen of ≤5 µm sizes. Furthermore, the produced microspheres were heat-treated at different temperatures (510-540°C) to investigate the influence of heat-treatment on surface morphology, surface area and porosity profile of the microspheres.

Surface pore of the microspheres significantly reduced to smaller pore sizes ranging between 7 (±4) to 26 (±4) µm after using ≤5 µm porogen with a surface area of 0.49 $m^2/g$ measured using nitrogen adsorption isotherm. Furthermore, heat-treatment caused pore narrowing with the pore size distribution analysis revealing a shift from macropore to mesopores (2-50 nm). The surface area of the microspheres increased due to 22-51% increase in pore volume after heat-treatment with highest surface area recorded 1.33 $m^2$ /g for P40 microsphere heat treated at 520°C.

Heat-treatment demonstrated presence of crystalline phase in porous P40 microspheres suggesting the formation of a glass-ceramic structure. It was also observed that increasing the heat-treatment temperature led to an increase in the crystallinity of the glass microspheres.

Using smaller size porogen followed by heat-treatment significantly improved the adsorption capacity of the microspheres. The monolayer adsorption capacity ($q_m$) recorded were 3 mg/g, 22 mg/g and 28 mg/g for P40, 510-P40 and 520-P40 respectively. Increased adsorption capacity was concentration dependent which increased with increasing initial AR88 dye concentration. Furthermore, kinetic data for heat-treated microspheres were fitted with Pseudo $1^{st}$ order model. Thus, referring dye adsorption occurred through mass transfer or physisorption (physical adsorption) process. Furthermore, factors such as increased surface area, open and interconnected porosities, surface charge, presence of porogen and presence of crystalline phases were accounted for batch adsorption of AR88 by heat-treated microspheres.

Column adsorption study demonstrated higher adsorption capacity (134 mg/g for 520-P40) compared to batch studies (125 mg/g). Increased adsorption had been suggested due to the unique geometry and microstructure of the microspheres produced, which provided sufficient residence time for the dye molecules to diffuse into their structure. Furthermore, Column adsorption capacity of the heat-treated and non-heat-treated microspheres increased with increasing flow rate. At higher flowrates

microspheres were more closely packed allowing more mass transfer/diffusion through inter- pore (inside microspheres).

Uptake of dye molecules occurred through a physical mechanism via diffusion, and/or a chemical mechanism via bonding at the active sites located within the pores of the microspheres. FTIR results confirmed that these bonds were electrostatic interaction, hydrogen bonding and/or Lewis's acid-base interactions.

Manufacturing porous recycled glass microspheres (PRGMs) using conventional flame spheroidisation process was challenging. Experimental studies revealed high melting temperature of RG, high viscosity at melt temperature, difference between melting point of porogen and RG and insufficient interaction between porogen and RG significantly affected the formation of PRGMs. Thus, alternate granular process was developed. The porosity and pore size distribution were influenced by the grinding time, grinding speed and porogen to glass particle ratio. Increasing grinding time increased no of pores and increasing grinding speed decreased the pore size (from 0-8 μm to 0-3.5 μm). Moreover, increasing grinding time, grinding speed and porogen to glass particle ratio increased the surface are of PRGMs (from 0.003 $m^2/g$ for RG to 7.6 $m^2/g$) with retaining a porosity of 65-69%. Increasing grinding time and porogen ratio also increased micro, meso and macro pore volume of PRGMs.

Both washed and unwashed PRGMs were explored for AR88 and methylene blue (MB) dye adsorption. The study revealed that adsorption on PRGMs were pH dependent and significantly improved with increasing PRGMs dose. The optimum PRGMs dose (Unwashed) were 10 g/L and 6 g/L and pH were 2.5 and 7 for AR88 and MB dye, respectively. AR88 dye removal in a batch process was as a result of combined effect of adsorption and coagulation. The maximum monolayer adsorption capacity calculated was 78 ± 4 mg/g for UW-PRGMs. Adsorption processes were affected by increased surface area of PRGMs, surface charge formation in acidic pH (2.5), presence of porogen. Furthermore, XPS and FTIR study confirmed that the adsorption process was due to electrostatic interaction and hydrogen bond formation.

MB adsorptions were affected by as surface area and surface charge of the PRGMs. XPS and FTIR results demonstrated possible hydrogen bonding and electrostatic interaction between dye and PRGMs. The maximum monolayer adsorption capacity calculated was 20 ± 4 mg/g for UW-PRGMs.

The column adsorption study for RG, washed and unwashed PRGMs demonstrated successful removal of AR88 dye. The adsorption capacity increased with increasing flowrate which were 381 (±3) mg/g, 305 (±3) mg/g and 42(±3) mg/g for unwashed, washed PRGMs and RG respectively. Moreover, the breakthrough curves were closely fitted to Adams-Bohart and Yoon-Nelson adsorption models ($R^2 \geq$

0.80). Both models provided an indication that increased flowrate and reduced EBCT could affect adsorption of AR88 onto PRGMs. However, there were significant discrepancy observed between calculated data and experimental data. As a result, a synergistic effect of adsorption/coagulation followed by filtration process had been considered responsible for showing discrepancy from the experimental value in column process.

Finally, magnetically separable porous magnetite microspheres (PMMs) were developed using granular method. AR88 and MB were selected as model anionic and cationic dye to investigate the adsorption property of PMMs. Flame-spheroidisation demonstrates the transformation of $Fe_3O_4$:$CaCO_3$ to a mixture of dense and highly porous $Ca_2Fe_2O_5$ magnetic microspheres. Generation of $Ca_2Fe_2O_5$ mineral was associated with stoichiometric quantities of $Fe_3O_4$ and $CaCO_3$ which is equivalent to 1:1 magnetite particle to porogen ratio.

The surface and internal morphology of the microspheres produced (dense or porous structure) were depended on the size of the granules and amount of porogen. The overall porosity and pore size distribution were influenced by the grinding time and porogen to magnetite particle ratio. Increasing grinding time and porogen ratio increased number of pores and increased the surface area. The surface area of PMMs increased (from 0.023 ± 0.003 $m^2/g$ for magnetite particles to 4.7 $m^2/g$ ± 0.003 for PMMs with 15 min grinding time, 1:3 porogen ratio) with retaining a porosity of 65-69%.

Batch adsorption by W-PMMs (washed) showed increased adsorption at acidic pH (2-4) while adsorption of MB showed at basic pH (8-10) with optimum adsorption dose 6 g/L (W-PMMs; 1:3) prepared using oxidising flame. Adsorption of AR88 and MB by UW-PRGMs were pH independent. The adsorption kinetics of AR88 and MB using UW-PMMs and W-PMMs revealed complete adsorption within 360 mins for all dye concentrations. The maximum monolayer adsorption capacity calculated for UW-PMMs and W-PMMs were 80 mg/g and 50 mg/g respectively for AR88 and 14.5 mg/g and 6 mg/g respectively for MB. It had been suggested that MB dye interaction with PMMs were due to combined effect of factors, such as surface area, phase structure, surface hydroxyl density, surface charge and photoactivity activity.

## 7.2 Suggestions for future work

This thesis demonstrated a novel route to manufacturing highly porous microspheres with suitable porosity and surface functionality to separate micropollutant (such as nano sized dyes) from wastewater. Based on the overall findings, the following suggestions have been made for future studies.

- Adsorption capacity of PRGMs and PMMs significantly influence by the pH of the solution suggesting surface charge involvement. Isoelectric point measurement was disregarded due difficulty of preparing stable suspension in aqueous media due to large sized microspheres (125-200 µm). In such regard, new alternate method could be considered for surface charge determination.
- Additional studies could involve removing micropollutants such as heavy metal, oil from wastewater to explore the multifunctionality of the microspheres produced.
- Heat-treated Phosphate glass microspheres shown improved dye removal tendency compared to non-heat-treated microspheres. Thus, heat-treating PRGMs and PMMs can be conducted to investigate and explored the impact of heat-treatment on structural and functional property.
- Only two flowrates (0.5 ml/min and 2.2 ml/min) were considered throughout column adsorption study. In depth investigation by varying flowrates and initial dye concentration is recommended to understand the overall dynamic behaviour of the adsorption column.
- For regeneration of microspheres, re-spheroidisation would also be of significant interest as as an alternate. This would allow dye desorption with few-milli seconds.
- Adsorption study can be progressed from bench scale to reliable industrial scale. The future of research in this area would likely be to establishing a catalogue of porous microspheres that can be effortlessly packed in an industrial column under continuous mode of operation.
- Sustainable manufacturing through circular economy approach is an essential requirement in order to minimize the environmental impacts, and conserve energy and natural resources. In such regards, life cycle assessment (LCA) would be considered to evaluate the environmental impact of porous microspheres and to compare with rest of existing adsorbent materials.
- Additional studies could investigate the effect of functionalisation of porous microspheres with high surface area nano materials such as MOFs, LDH's etc and investigating the adsorption property in batch and column process. Thus, in such case porous glass microspheres could potentially utilised as a substrate carrier integrating nanomaterials to improve their selectivity and treatment efficiency. Another part of the study could focus on removing multiple contaminants

by packing target (contaminant) specific microspheres, layer by layer in columns as depicted in Figure 7.1.

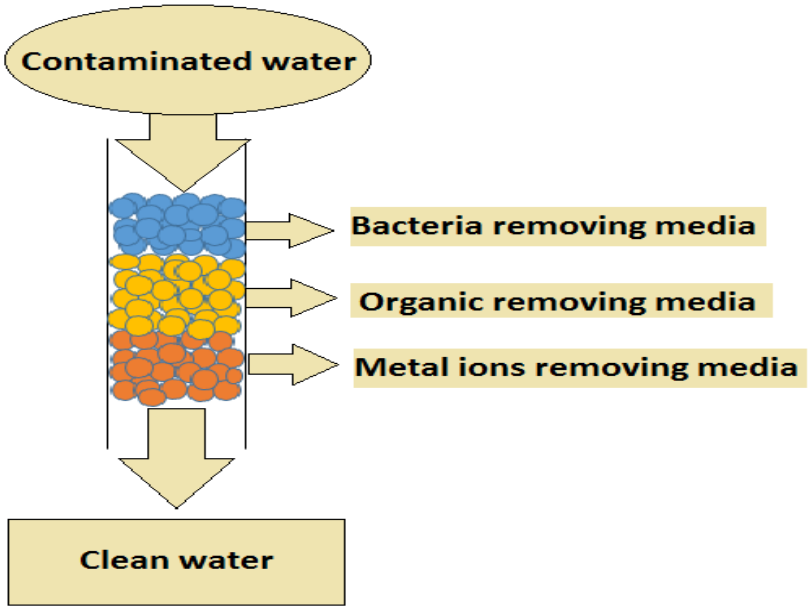



***Figure 7.1: A schematic of target specific porous glass microspheres packed in a column for purification of water contaminated by mixtures of (i) bacteria, (ii) organic pollutants and (iii) metal ions.***

- In literature, several studies demonstrated the potential of $Ca_2Fe_2O_5$ as a photocatalyst. Besides, it has a strong potential to be used for supercapacitor applications. Future study could focus manufacturing single phase $Ca_2Fe_2O_5$ and investigating its application as photocatalyst, capacitor.

# References


[1] Y.-C. Qi, J. Shen, Q.-Y. Jiang, B. Jin, J.-W. Chen, X. Zhang, J.-L. Su, Hierarchical porous hydroxyapatite microspheres: synthesis and application in water treatment, Journal of materials science 51(5) (2016) 2598-2607.

[2] X. Li, H. Liu, L. Cheng, H. Tong, Photocatalytic oxidation using a new catalyst $TiO_2$ microsphere for water and wastewater treatment, Environmental science & technology 37(17) (2003) 3989-3994.

[3] J.-R. Fu, J. Zheng, W.-J. Fang, C. Chen, C. Cheng, R.-W. Yan, S.-G. Huang, C.-C. Wang, Synthesis of porous magnetic $Fe_3O_4$/Fe@ZnO core–shell heterostructure with superior capability for water treatment, Journal of Alloys and Compounds 650 (2015) 463-469.

[4] Y. Wang, B. Zou, T. Gao, X. Wu, S. Lou, S. Zhou, Synthesis of orange-like $Fe_3O_4$/PPy composite microspheres and their excellent Cr (VI) ion removal properties, Journal of Materials Chemistry 22(18) (2012) 9034-9040.

[5] R. Connor, The United Nations world water development report 2015: water for a sustainable world, UNESCO Publishing 2015.

[6] E. Corcoran, Sick water?: the central role of wastewater management in sustainable development: a rapid response assessment, UNEP/Earthprint 2010.

[7] T. An, H. Zhao, P.K. Wong, Advances in Photocatalytic Disinfection, Springer 2017.

[8] S. Malato, P. Fernández-Ibáñez, M.I. Maldonado, J. Blanco, W. Gernjak, Decontamination and disinfection of water by solar photocatalysis: recent overview and trends, Catalysis Today 147(1) (2009) 1-59.

[9] A.J. Richardson, In hot water: zooplankton and climate change, ICES Journal of Marine Science 65(3) (2008) 279-295.

[10] S.D. Richardson, A.D. Thruston Jr, S.W. Krasner, H.S. Weinberg, R.J. Miltner, K.M. Schenck, M.G. Narotsky, A.B. McKague, J.E. Simmons, Integrated disinfection by-products mixtures research: comprehensive characterization of water concentrates prepared from chlorinated and ozonated/postchlorinated drinking water, Journal of Toxicology and Environmental Health, Part A 71(17) (2008) 1165-1186.

[11] M.N. Chong, B. Jin, C.W. Chow, C. Saint, Recent developments in photocatalytic water treatment technology: a review, Water research 44(10) (2010) 2997-3027.

[12] A. Boretti, L. Rosa, Reassessing the projections of the world water development report, NPJ Clean Water 2(1) (2019) 1-6.

[13] A. El-Ghonemy, Retracted: water desalination systems powered by renewable energy sources, Review, Elsevier, 2012.

[14] Z. Zeng, J. Liu, H.H. Savenije, A simple approach to assess water scarcity integrating water quantity and quality, Ecological indicators 34 (2013) 441-449.

[15] Y. Wada, M.F. Bierkens, Sustainability of global water use: past reconstruction and future projections, Environmental Research Letters 9(10) (2014) 104003.

[16] J. Alcamo, T. Henrichs, T. Rösch, World water in 2025: Global modeling and scenario analysis for the world commission on water for the 21st century, (2017).

[17] P. Kumar, Y. Masago, B.K. Mishra, S. Jalilov, A. Rafiei Emam, M. Kefi, K. Fukushi, Current assessment and future outlook for water resources considering climate change and a population burst: A case study of Ciliwung River, Jakarta City, Indonesia, Water 9(6) (2017) 410.

[18] J. Alcamo, P. Döll, F. Kaspar, S. Siebert, Global change and global scenarios of water use and availability: an application of WaterGAP 1.0, Center for Environmental Systems Research, University of Kassel, Kassel, Germany (1997).

[19] R. Connor, A. Renata, C. Ortigara, E. Koncagül, S. Uhlenbrook, B.M. Lamizana-Diallo, S.M. Zadeh, M. Qadir, M. Kjellén, J. Sjödin, The united nations world water development report 2017. wastewater: the untapped resource, The United Nations World Water Development Report (2017).

[20] W.F. Directive, Water Framework Directive, Journal reference OJL 327 (2000) 1-73.

[21] A. Gillespie, Waste Policy: International regulation, comparative and contextual perspectives, Edward Elgar Publishing 2015, pp 11-13.
[22] R.N. Carvalho, L. Ceriani, A. Ippolito, T. Lettieri, Development of the first watch list under the environmental quality standards directive, JRC Science Hub (2015).
[23] C. Binnie, M. Kimber, G. Smethurst, Basic water treatment, Royal society of chemistry 2002.
[24] M.C. KAMATHI, DEFLUORIDATION OF WATER BY ADSORPTION WITH TRIETHYLAMINE MODIFIED MAIZE TASSELS, Kenyatta University, 2017.
[25] I.A. Worms, Z.A.-G. Szigeti, S. Dubascoux, G. Lespes, J. Traber, L. Sigg, V.I. Slaveykova, Colloidal organic matter from wastewater treatment plant effluents: Characterization and role in metal distribution, water research 44(1) (2010) 340-350.
[26] E. Clarke, R. Anliker, Organic dyes and pigments, Anthropogenic compounds, Springer 1980, pp. 181-215.
[27] J.L. Rodriguez-Gil, R. Prosser, D. Poirier, L. Lissemore, D. Thompson, M. Hanson, K.R. Solomon, Aquatic hazard assessment of MON 0818, a commercial mixture of alkylamine ethoxylates commonly used in glyphosate-containing herbicide formulations. Part 1: Species sensitivity distribution from laboratory acute exposures, Environmental toxicology and chemistry 36(2) (2017) 501-511.
[28] M.S. Kostich, R.W. Flick, A.L. Batt, H.E. Mash, J.S. Boone, E.T. Furlong, D.W. Kolpin, S.T. Glassmeyer, Aquatic concentrations of chemical analytes compared to ecotoxicity estimates, Science of the Total Environment 579 (2017) 1649-1657.
[29] G. Mishra, M. Tripathy, A critical review of the treatments for decolourization of textile effluent, Colourage 40 (1993) 35-35.
[30] I. Toroz, V. Uyak, Seasonal variations of trihalomethanes (THMs) in water distribution networks of Istanbul City, Desalination 176(1-3) (2005) 127-141.
[31] V.A. Nzengung, C. Wang, PERCHLORATE-CONTAMINATED WATER", Perchlorate in the Environment 57 (2012) 219.
[32] Z. Xiong, D. Zhao, G. Pan, Rapid and complete destruction of perchlorate in water and ion-exchange brine using stabilized zero-valent iron nanoparticles, Water research 41(15) (2007) 3497-3505.
[33] W. Song, B. Gao, Y. Guo, X. Xu, Q. Yue, Z. Ren, Effective adsorption/desorption of perchlorate from water using corn stalk based modified magnetic biopolymer ion exchange resin, Microporous and Mesoporous Materials (2017).
[34] P.N. Smith, L. Yu, S.T. McMurry, T.A. Anderson, Perchlorate in water, soil, vegetation, and rodents collected from the Las Vegas Wash, Nevada, USA, Environmental Pollution 132(1) (2004) 121-127.
[35] K.S. Crump, J.P. Gibbs, Benchmark calculations for perchlorate from three human cohorts, Environmental health perspectives 113(8) (2005) 1001.
[36] Z. Li, F.X. Li, D. Byrd, G.M. Deyhle, D.E. Sesser, M.R. Skeels, S.H. Lamm, Neonatal thyroxine level and perchlorate in drinking water, Journal of Occupational and Environmental Medicine 42(2) (2000) 200-205.
[37] B. Gu, J.D. Coates, Perchlorate: environmental occurrence, interactions and treatment, Springer Science & Business Media2006.
[38] M. Cleuvers, Aquatic ecotoxicity of pharmaceuticals including the assessment of combination effects, Toxicology letters 142(3) (2003) 185-194.
[39] X. Wei, Y. Wang, A.J. Hernández-Maldonado, Z. Chen, Guidelines for Rational Design of High-Performance Absorbents: A Case Study of Zeolite Adsorbents for Emerging Pollutants in Water, Green Energy & Environment (2017).
[40] M. Vasquez, A. Lambrianides, M. Schneider, K. Kümmerer, D. Fatta-Kassinos, Environmental side effects of pharmaceutical cocktails: what we know and what we should know, Journal of hazardous materials 279 (2014) 169-189.
[41] Å. Wennmalm, Pharmaceuticals: environmental effects, (2011).

[42] K.A. Kidd, P.J. Blanchfield, K.H. Mills, V.P. Palace, R.E. Evans, J.M. Lazorchak, R.W. Flick, Collapse of a fish population after exposure to a synthetic estrogen, Proceedings of the National Academy of Sciences 104(21) (2007) 8897-8901.
[43] K.E. Murray, S.M. Thomas, A.A. Bodour, Prioritizing research for trace pollutants and emerging contaminants in the freshwater environment, Environmental Pollution 158(12) (2010) 3462-3471.
[44] E. Archer, B. Petrie, B. Kasprzyk-Hordern, G.M. Wolfaardt, The fate of pharmaceuticals and personal care products (PPCPs), endocrine disrupting contaminants (EDCs), metabolites and illicit drugs in a WWTW and environmental waters, Chemosphere 174 (2017) 437-446.
[45] M. Wagner, C. Kienle, E.L. Vermeirssen, J. Oehlmann, Endocrine disruption and in vitro ecotoxicology: Recent advances and approaches, In vitro Environmental Toxicology-Concepts, Application and Assessment (2017) 1-58.
[46] S.T. Glassmeyer, E.T. Furlong, D.W. Kolpin, A.L. Batt, R. Benson, J.S. Boone, O. Conerly, M.J. Donohue, D.N. King, M.S. Kostich, Nationwide reconnaissance of contaminants of emerging concern in source and treated drinking waters of the United States, Science of the Total Environment 581 (2017) 909-922.
[47] O.B. Akpor, G.O. Ohiobor, T.D. Olaolu, Heavy metal pollutants in wastewater effluents: sources, effects and remediation, Adv. Biosci. Bioeng 2(4) (2014) 37-43.
[48] B. Somashekaraiah, K. Padmaja, A. Prasad, Phytotoxicity of cadmium ions on germinating seedlings of mung bean (Phaseolus vulgaris): Involvement of lipid peroxides in chlorphyll degradation, Physiologia Plantarum 85(1) (1992) 85-89.
[49] M.A. Chia, A.T. Lombardi, G.M. Maria da Graça, C.C. Parrish, Phosphorus levels determine changes in growth and biochemical composition of Chlorella vulgaris during cadmium stress, Journal of Applied Phycology (2017) 1-9.
[50] M.A. da Conceição Gomes, R.A. Hauser-Davis, M.S. Suzuki, A.P. Vitória, Plant chromium uptake and transport, physiological effects and recent advances in molecular investigations, Ecotoxicology and Environmental Safety 140 (2017) 55-64.
[51] M. Shahid, S. Shamshad, M. Rafiq, S. Khalid, I. Bibi, N.K. Niazi, C. Dumat, M.I. Rashid, Chromium speciation, bioavailability, uptake, toxicity and detoxification in soil-plant system: A review, Chemosphere 178 (2017) 513-533.
[52] B. Lange, A. Ent, A.J.M. Baker, G. Echevarria, G. Mahy, F. Malaisse, P. Meerts, O. Pourret, N. Verbruggen, M.P. Faucon, Copper and cobalt accumulation in plants: a critical assessment of the current state of knowledge, New Phytologist 213(2) (2017) 537-551.
[53] D.A. Rizzetti, C.S. Martinez, A.G. Escobar, T.M. da Silva, J.A. Uranga-Ocio, F.M. Peçanha, D.V. Vassallo, M.M. Castro, G.A. Wiggers, Egg white-derived peptides prevent male reproductive dysfunction induced by mercury in rats, Food and Chemical Toxicology 100 (2017) 253-264.
[54] G. Genchi, M.S. Sinicropi, A. Carocci, G. Lauria, A. Catalano, Mercury Exposure and Heart Diseases, International journal of environmental research and public health 14(1) (2017) 74.
[55] Z.-Y. Hseu, Y.-J. Lai, Nickel accumulation in paddy rice on serpentine soils containing high geogenic nickel contents in Taiwan, Environmental Geochemistry and Health (2017) 1-10.
[56] S. Tong, Y.E.v. Schirnding, T. Prapamontol, Environmental lead exposure: a public health problem of global dimensions, Bulletin of the World Health Organization 78(9) (2000) 1068-1077.
[57] C. Korkmaz, Ö. Ay, C. Çolakfakioğlu, B. Cicik, C. Erdem, Heavy metal levels in muscle tissues of Solea solea, Mullus barbatus, and Sardina pilchardus marketed for consumption in Mersin, Turkey, Water, Air, & Soil Pollution 228(8) (2017) 315.
[58] L. Järup, Hazards of heavy metal contamination, British medical bulletin 68(1) (2003) 167-182.
[59] D. Woldetsadik, P. Drechsel, B. Keraita, F. Itanna, H. Gebrekidan, Heavy metal accumulation and health risk assessment in wastewater-irrigated urban vegetable farming sites of Addis Ababa, Ethiopia, International Journal of Food Contamination 4(1) (2017) 9.
[60] A. Sharma, S. Flora, NUTRITIONAL MANAGEMENT CAN ASSIST A SIGNIFICANT ROLE IN ALLEVIATION OF ARSENICOSIS, Journal of Trace Elements in Medicine and Biology (2017).

[61] T. Tyrrell, The relative influences of nitrogen and phosphorus on oceanic primary production, Nature 400(6744) (1999) 525.
[62] Z. Svirčev, D. Drobac, N. Tokodi, B. Mijović, G.A. Codd, J. Meriluoto, Toxicology of microcystins with reference to cases of human intoxications and epidemiological investigations of exposures to cyanobacteria and cyanotoxins, Archives of toxicology (2017) 1-30.
[63] L. Köker, R. Akçaalan, M. Albay, B.A. Neilan, Molecular detection of hepatotoxic cyanobacteria in inland water bodies of the Marmara Region, Turkey, Advances in Oceanography and Limnology 8(1) (2017).
[64] F.D. Mello, N. Braidy, H. Marçal, G. Guillemin, S.M. Nabavi, B.A. Neilan, Mechanisms and Effects Posed by Neurotoxic Products of Cyanobacteria/Microbial Eukaryotes/Dinoflagellates in Algae Blooms: a Review, Neurotoxicity Research (2017) 1-15.
[65] E. Sokolova, A. Kuz'mich, A. Byankina, L. Yermak, Effect of carrageenans alone and in combination with casein or lipopolysaccharide on human epithelial intestinal HT-29 cells, Journal of Biomedical Materials Research Part A (2017).
[66] W.W. Carmichael, C.L. Jones, N.A. Mahmood, W.C. Theiss, P. Krogh, Algal toxins and water-based diseases, Critical Reviews in Environmental Science and Technology 15(3) (1985) 275-313.
[67] D.A. Atwood, Radionuclides in the Environment, John Wiley & Sons 2013.
[68] J.W. Gofman, Radiation and human health, (1981).
[69] F. Zahakifar, A. Keshtkar, E. Nazemi, A. Zaheri, Optimization of operational conditions in continuous electrodeionization method for maximizing Strontium and Cesium removal from aqueous solutions using artificial neural network, Radiochimica Acta (2017).
[70] A. Baeza, A. Salas, J. Guillén, A. Muñoz-Serrano, M. Ontalba-Salamanca, M. Jiménez-Ramos, Removal naturally occurring radionuclides from drinking water using a filter specifically designed for Drinking Water Treatment Plants, Chemosphere 167 (2017) 107-113.
[71] T. Gäfvert, C. Ellmark, E. Holm, Removal of radionuclides at a waterworks, Journal of Environmental Radioactivity 63(2) (2002) 105-115.
[72] T.D. Reynold, Unit operation and process in environmental engineering, Wadsworth Inc., California (1982).
[73] J. Wiszniowski, D. Robert, J. Surmacz-Gorska, K. Miksch, J. Weber, Landfill leachate treatment methods: A review, Environmental Chemistry Letters 4(1) (2006) 51-61.
[74] M.L. Davis, Water and wastewater engineering, McGraw-Hill 2010.
[75] Metcalf, Eddy, F.L. Burton, H.D. Stensel, G. Tchobanoglous, Wastewater engineering: treatment and reuse, McGraw Hill2003.
[76] V.K. Gupta, I. Ali, T.A. Saleh, A. Nayak, S. Agarwal, Chemical treatment technologies for waste-water recycling—an overview, Rsc Advances 2(16) (2012) 6380-6388.
[77] C. Screens, Wastewater Technology Fact Sheet.
[78] N.P. Cheremisinoff, Handbook of water and wastewater treatment technologies, Butterworth-Heinemann 2001.
[79] M.T.N. Available, Eddy, Waste Water Engineering: Treatment Disposal and Reuse, McGraw Hill Offices, 1979.
[80] N.L. Nemerow, A. Dasgupta, Industrial and hazardous waste treatment, (1991).
[81] A. Latifossglu, G. Surucu, M. Evirgen, Water Pollut. IV: Model, Meas., Predict., 4th Int. Conf, 1997, pp. 733-742.
[82] S. Haydar, J.A. Aziz, Coagulation–flocculation studies of tannery wastewater using combination of alum with cationic and anionic polymers, Journal of Hazardous Materials 168(2) (2009) 1035-1040.
[83] S. Malhbtra, D. Kulkarni, S.P. Pande, Effectiveness of poly aluminum chloride (PAC) vis-a-vis alum in the removal of fluorides and heavy metals, Journal of Environmental Science & Health Part A 32(9-10) (1997) 2563-2574.
[84] K. Carlson, S. Via, B. Bellamy, M. Carlson, Secondary effects of enhanced coagulation and softening, American Water Works Association. Journal 92(6) (2000) 63.

[85] A. Arnold-Smith, R. Christie, C. Jolicoeur, Polyaluminium silicate sulphate—a new coagulant for potable and wastewater treatment, Chemical Water and Wastewater Treatment II, Springer 1992, pp. 203-219.
[86] K.E. Lee, N. Morad, T.T. Teng, B.T. Poh, Development, characterization and the application of hybrid materials in coagulation/flocculation of wastewater: A review, Chemical Engineering Journal 203 (2012) 370-386.
[87] B. Bolto, J. Gregory, Organic polyelectrolytes in water treatment, Water research 41(11) (2007) 2301-2324.
[88] E. Butler, Y.-T. Hung, R.Y.-L. Yeh, M. Suleiman Al Ahmad, Electrocoagulation in wastewater treatment, Water 3(2) (2011) 495-525.
[89] H.D. Beyene, T.D. Hailegebrial, W.B. Direrssa, Investigation of Coagulation Activity of Cactus Powder in Water Treatment, Journal of Applied Chemistry 2016 (2016).
[90] I. Sinev, O. Sinev, S. Linevich, Apparatus of flotation treatment of natural waters and wastewater, Izobreteniya 26 (1997) 369-370.
[91] I.L. Mickova, Advanced Electrochemical Technologies in Wastewater Treatment. Part II: Electro-Flocculation and Electro-Flotation, American Scientific Research Journal for Engineering, Technology, and Sciences (ASRJETS) 14(2) (2015) 273-294.
[92] N. Abdel-Raouf, A. Al-Homaidan, I. Ibraheem, Microalgae and wastewater treatment, Saudi Journal of Biological Sciences 19(3) (2012) 257-275.
[93] A. Pendashteh, A. Fakhru'l-Razi, T. Chuah, A.D. Radiah, S. Madaeni, Z. Zurina, Biological treatment of produced water in a sequencing batch reactor by a consortium of isolated halophilic microorganisms, Environmental technology 31(11) (2010) 1229-1239.
[94] A. Joss, E. Keller, A.C. Alder, A. Göbel, C.S. McArdell, T. Ternes, H. Siegrist, Removal of pharmaceuticals and fragrances in biological wastewater treatment, Water research 39(14) (2005) 3139-3152.
[95] A.M. Talarposhti, T. Donnelly, G. Anderson, Colour removal from a simulated dye wastewater using a two-phase anaerobic packed bed reactor, Water Research 35(2) (2001) 425-432.
[96] P. Csaba, J. Csaba, Water resources management and water quality protection, Debreceni Egyetem 2011.
[97] L. Huisman, W. Wood, Slow sand filtration, World Health Organization Geneva1974.
[98] M. Bahgat, A. Dewedar, A. Zayed, Sand-filters used for wastewater treatment: buildup and distribution of microorganisms, Water Research 33(8) (1999) 1949-1955.
[99] D. Fogel, J. Isaac-Renton, R. Guasparini, W. Moorehead, J. Ongerth, Removing Giardia and Cryptosporidium by slow sand filtration, Journal-American Water Works Association 85(11) (1993) 77-84.
[100] J. Haarhoff, J.L. Cleasby, Biological and physical mechanisms in slow sand filtration, Slow sand filtration, ASCE, 1991, pp. 19-68.
[101] A. Keijola, K. Himberg, A. Esala, K. Sivonen, L. Hiis-Virta, Removal of cyanobacterial toxins in water treatment processes: Laboratory and pilot-scale experiments, Environmental Toxicology 3(5) (1988) 643-656.
[102] K. Ellis, W. Wood, Slow sand filtration, Critical Reviews in Environmental Science and Technology 15(4) (1985) 315-354.
[103] J. Barrett, J. Silverstein, N. Graham, Effects of high-carbon and high-coliform feed waters on the performance of slow sand filters under tropical conditions, Ellis Horwood series in water and wastewater technology, Ellis Horwood1988, pp. 231-52.
[104] R. Ahmad, A. Amirtharajah, Detachment of particles during biofilter backwashing, American Water Works Association. Journal 90(12) (1998) 74.
[105] S. Lambert, N. Graham, A comparative evaluation of the effectiveness of potable water filtration processes, Aqua- Journal of Water Supply: Research and Technology 44(1) (1995) 38-51.
[106] L.K. Wang, M.H.S. Wang, C.S. Hwang, H. Rhow, Water filtration apparatus, Google Patents, 1991.

[107] H. Bohumir, D. Oldrich, M. Svatopluk, M. Vladimir, S. Vladimir, Method and device for separation of a suspension, Google Patents, 1968.
[108] S.N. Chaudhari, K.A. Bogawar, MODIFICATION IN RAPID SAND FILTER WITH COCONUT SHELLS AS CAPPING MEDIA.
[109] R. Bowen, Effective Industrial Membrane Processes: Benefits and Opportunities: MK Turner (Editor), Elsevier Applied Science, Oxford, UK, 1991, 417 pp, ISBN 1-851661-723-7,£ 80.00, Elsevier, 1993.
[110] X. Du, G. Liu, F. Qu, K. Li, S. Shao, G. Li, H. Liang, Removal of iron, manganese and ammonia from groundwater using a PAC-MBR system: the anti-pollution ability, microbial population and membrane fouling, Desalination 403 (2017) 97-106.
[111] D. Vries, C. Bertelkamp, F.S. Kegel, B. Hofs, J. Dusseldorp, J. Bruins, W. de Vet, B. van den Akker, Iron and manganese removal: Recent advances in modelling treatment efficiency by rapid sand filtration, Water research 109 (2017) 35-45.
[112] S. Madaeni, A. Fane, G. Grohmann, Virus removal from water and wastewater using membranes, Journal of Membrane Science 102 (1995) 65-75.
[113] L. Xu, W. Li, S. Lu, Z. Wang, Q. Zhu, Y. Ling, Treating dyeing waste water by ceramic membrane in crossflow microfiltration, Desalination 149(1) (2002) 199-203.
[114] Z. Wu, Y. Zhao, S. Chen, Ultrafiltration Technique and Its Application to Water Pollution Control, SHANGHAI ENVIRONMENTAL SCIENCES 16 (1997) 29-31.
[115] D. Patra, Reducing Energy Cost for Wastewater Treatment in the Middle East: A Physio-chemical Prospective, Water, Energy & Food Sustainability in the Middle East, Springer2017, pp. 223-244.
[116] C. Onyema, J. Ilebaye, Effects of Refinery Processes on the Quality of Various Water Samples from Kaduna Refinery and Petrochemical Company (KRPC) Limited.
[117] V. Bonnélye, L. Guey, J. Del Castillo, UF/MF as RO pre-treatment: the real benefit, Desalination 222(1-3) (2008) 59-65.
[118] A. Brehant, V. Bonnelye, M. Perez, Comparison of MF/UF pretreatment with conventional filtration prior to RO membranes for surface seawater desalination, Desalination 144(1-3) (2002) 353-360.
[119] https://liantadbir.com/en/processes/membrane-filtration/.
[120] P.S. Kumar, A. Saravanan, Sustainable Waste Water Treatment Technologies, Detox Fashion, Springer 2018, pp. 1-25.
[121] P.O.P.O.O. VODE, PERFORMANCE OF NANO-FILTRATION AND REVERSE OSMOSIS PROCESSES FOR WASTEWATER TREATMENT, Materiali in tehnologije 51(3) (2017) 541-548.
[122] A. Abdel-Karim, T.A. Gad-Allah, M.I. Badawy, A.S. Khalil, M. Ulbricht, Removal of humic acid and chloroform from drinking water by using commercial nanofiltration and reverse osmosis membranes, DESALINATION AND WATER TREATMENT 59 (2017) 48-54.
[123] J. Garcia-Ivars, L. Martella, M. Massella, C. Carbonell-Alcaina, M.-I. Alcaina-Miranda, M.-I. Iborra-Clar, Nanofiltration as tertiary treatment method for removing trace pharmaceutically active compounds in wastewater from wastewater treatment plants, Water Research (2017).
[124] A. Williams, Effective industrial membrane processes: benefits and opportunities, ed. MK Turner, Elsevier Science Publisher Ltd., Barking, Essex (1991).
[125] S.K. Nataraj, K.M. Hosamani, T.M. Aminabhavi, Distillery wastewater treatment by the membrane-based nanofiltration and reverse osmosis processes, Water Research 40(12) (2006) 2349-2356.
[126] C. Liu, J. Lee, C. Small, J. Ma, M. Elimelech, Comparison of organic fouling resistance of thin-film composite membranes modified by hydrophilic silica nanoparticles and zwitterionic polymer brushes, Journal of Membrane Science (2017).
[127] V. Vatanpour, N. Zoqi, Surface modification of commercial seawater reverse osmosis membranes by grafting of hydrophilic monomer blended with carboxylated multiwalled carbon nanotubes, Applied Surface Science 396 (2017) 1478-1489.

[128] N.C. Nguyen, S.-S. Chen, H.T. Nguyen, S.S. Ray, H.H. Ngo, W. Guo, P.-H. Lin, Innovative sponge-based moving bed–osmotic membrane bioreactor hybrid system using a new class of draw solution for municipal wastewater treatment, Water research 91 (2016) 305-313.
[129] A. Achilli, T.Y. Cath, E.A. Marchand, A.E. Childress, The forward osmosis membrane bioreactor: a low fouling alternative to MBR processes, Desalination 239(1-3) (2009) 10-21.
[130] L. Chen, Y. Gu, C. Cao, J. Zhang, J.-W. Ng, C. Tang, Performance of a submerged anaerobic membrane bioreactor with forward osmosis membrane for low-strength wastewater treatment, Water research 50 (2014) 114-123.
[131] G. Blandin, J. Comas, I. Rodriguez-Roda, Potential and Challenges of Osmotic Membrane Bioreactor (OMBR) for (Potable) Water Reuse: A Pilot Scale Study, Frontiers International Conference on Wastewater Treatment and Modelling, Springer, 2017, pp. 188-192.
[132] R.J. Bigda, Consider Fentons chemistry for wastewater treatment, Chemical Engineering Progress 91(12) (1995).
[133] E.E. Ebrahiem, M.N. Al-Maghrabi, A.R. Mobarki, Removal of organic pollutants from industrial wastewater by applying photo-Fenton oxidation technology, Arabian Journal of Chemistry 10 (2017) S1674-S1679.
[134] D. Mantzavinos, I. Poulios, A. Pintar, Advances and trends in advanced oxidation processes, Springer, 2017.
[135] M. Tichonovas, E. Krugly, D. Jankunaite, V. Racys, D. Martuzevicius, Ozone-UV-catalysis based advanced oxidation process for wastewater treatment, Environmental Science and Pollution Research (2017) 1-14.
[136] N. Daneshvar, D. Salari, A. Khataee, Photocatalytic degradation of azo dye acid red 14 in water on ZnO as an alternative catalyst to TiO 2, Journal of photochemistry and photobiology A: chemistry 162(2) (2004) 317-322.
[137] S.H.S. Chan, T. Yeong Wu, J.C. Juan, C.Y. Teh, Recent developments of metal oxide semiconductors as photocatalysts in advanced oxidation processes (AOPs) for treatment of dye waste-water, Journal of Chemical Technology and Biotechnology 86(9) (2011) 1130-1158.
[138] J. Benjumea, J. Sánchez-Oneto, J. Portela, E.M. de la Ossa, Temperature control in a supercritical water oxidation reactor: Assessing strategies for highly concentrated wastewaters, The Journal of Supercritical Fluids 119 (2017) 72-80.
[139] Y. Gong, Y. Guo, S. Wang, W. Song, D. Xu, Supercritical water oxidation of quinazoline: Reaction kinetics and modeling, Water research 110 (2017) 56-65.
[140] C. Comninellis, A. Kapalka, S. Malato, S.A. Parsons, I. Poulios, D. Mantzavinos, Advanced oxidation processes for water treatment: advances and trends for R&D, Journal of Chemical Technology and Biotechnology 83(6) (2008) 769-776.
[141] G. Del Moro, A. Mancini, G. Mascolo, C. Di Iaconi, Comparison of UV/$H_2O_2$ based AOP as an end treatment or integrated with biological degradation for treating landfill leachates, Chemical engineering journal 218 (2013) 133-137.
[142] S.A. Fast, V.G. Gude, D.D. Truax, J. Martin, B.S. Magbanua, A Critical Evaluation of Advanced Oxidation Processes for Emerging Contaminants Removal, Environmental Processes 4(1) (2017) 283-302.
[143] M.J. Gómez, C. Sirtori, M. Mezcua, A.R. Fernández-Alba, A. Agüera, Photodegradation study of three dipyrone metabolites in various water systems: Identification and toxicity of their photodegradation products, Water Research 42(10) (2008) 2698-2706.
[144] N.A. Mir, A. Khan, M. Muneer, S. Vijayalakhsmi, Photocatalytic degradation of a widely used insecticide Thiamethoxam in aqueous suspension of $TiO_2$: adsorption, kinetics, product analysis and toxicity assessment, Science of the total environment 458 (2013) 388-398.
[145] W.L. Armarego, Purification of laboratory chemicals, Butterworth-Heinemann2017.
[146] S.D. Allen, Treatment of contaminated water from gas wells, Google Patents, 2017.

[147] G. Crini, Recent developments in polysaccharide-based materials used as adsorbents in wastewater treatment, Progress in polymer science 30(1) (2005) 38-70.
[148] S. Wang, Y. Peng, Natural zeolites as effective adsorbents in water and wastewater treatment, Chemical Engineering Journal 156(1) (2010) 11-24.
[149] D.O. Cooney, Adsorption design for wastewater treatment, CRC press 1998.
[150] S.D. Faust, O.M. Aly, Adsorption processes for water treatment, Elsevier 2013.
[151] V.K. Gupta, A. Mittal, R. Jain, M. Mathur, S. Sikarwar, Adsorption of Safranin-T from wastewater using waste materials—activated carbon and activated rice husks, Journal of Colloid and Interface Science 303(1) (2006) 80-86.
[152] V.K. Gupta, S. Agarwal, T.A. Saleh, Synthesis and characterization of alumina-coated carbon nanotubes and their application for lead removal, Journal of hazardous materials 185(1) (2011) 17-23.
[153] V.K. Gupta, R. Jain, M.N. Siddiqui, T.A. Saleh, S. Agarwal, S. Malati, D. Pathak, Equilibrium and thermodynamic studies on the adsorption of the dye rhodamine-B onto mustard cake and activated carbon, Journal of Chemical & Engineering Data 55(11) (2010) 5225-5229.
[154] V.K. Gupta, A. Mittal, A. Malviya, J. Mittal, Adsorption of carmoisine A from wastewater using waste materials—bottom ash and deoiled soya, Journal of Colloid and Interface Science 335(1) (2009) 24-33.
[155] V.K. Gupta, I. Ali, V.K. Saini, Adsorption studies on the removal of Vertigo Blue 49 and Orange DNA13 from aqueous solutions using carbon slurry developed from a waste material, Journal of Colloid and Interface Science 315(1) (2007) 87-93.
[156] D. BARTHOMEUF∗, Basic zeolites: characterization and uses in adsorption and catalysis, Catalysis Reviews 38(4) (1996) 521-612.
[157] V. Gupta, S. Agarwal, T.A. Saleh, Chromium removal by combining the magnetic properties of iron oxide with adsorption properties of carbon nanotubes, Water research 45(6) (2011) 2207-2212.
[158] R.D. Ambashta, M. Sillanpää, Water purification using magnetic assistance: a review, Journal of hazardous materials 180(1) (2010) 38-49.
[159] V.K. Gupta, S. Agarwal, M. Asif, A. Fakhri, N. Sadeghi, Application of response surface methodology to optimize the adsorption performance of a magnetic graphene oxide nanocomposite adsorbent for removal of methadone from the environment, Journal of Colloid and Interface Science 497 (2017) 193-200.
[160] I. Ali, V. Gupta, Advances in water treatment by adsorption technology, Nature protocols 1(6) (2006) 2661.
[161] T. Yavini, M. Yunusa, K. Atiku, A. Musa, P. Ruth, Investigation on adsorption performance of mesoporous activated biomass prepared from Cocos nucifera husk for harzadous cyanide wastewater treatment, Journal of Fundamental and Applied Sciences 9(1) (2017) 354-377.
[162] Z. Xu, J.-g. Cai, B.-c. Pan, Mathematically modeling fixed-bed adsorption in aqueous systems, Journal of Zhejiang University SCIENCE A 14(3) (2013) 155-176.
[163] B. Crittenden, W.J. Thomas, Adsorption technology and design, Butterworth-Heinemann1998.
[164] J. Figueiredo, M. Pereira, M. Freitas, J. Orfao, Modification of the surface chemistry of activated carbons, carbon 37(9) (1999) 1379-1389.
[165] Y.C. Sharma, Optimization of parameters for adsorption of methylene blue on a low-cost activated carbon, Journal of Chemical & Engineering Data 55(1) (2009) 435-439.
[166] V.K. Gupta, S.K. Srivastava, D. Mohan, Equilibrium uptake, sorption dynamics, process optimization, and column operations for the removal and recovery of malachite green from wastewater using activated carbon and activated slag, Industrial & engineering chemistry research 36(6) (1997) 2207-2218.
[167] M. Danish, R. Hashim, M.M. Ibrahim, O. Sulaiman, Optimized preparation for large surface area activated carbon from date (Phoenix dactylifera L.) stone biomass, biomass and bioenergy 61 (2014) 167-178.

[168] J.A. Menéndez, J. Phillips, B. Xia, L.R. Radovic, On the modification and characterization of chemical surface properties of activated carbon: in the search of carbons with stable basic properties, Langmuir 12(18) (1996) 4404-4410.
[169] D. Prahas, Y. Kartika, N. Indraswati, S. Ismadji, Activated carbon from jackfruit peel waste by H 3 PO 4 chemical activation: pore structure and surface chemistry characterization, Chemical Engineering Journal 140(1) (2008) 32-42.
[170] H. Benaddi, T. Bandosz, J. Jagiello, J. Schwarz, J. Rouzaud, D. Legras, F. Béguin, Surface functionality and porosity of activated carbons obtained from chemical activation of wood, Carbon 38(5) (2000) 669-674.
[171] Z. Hu, M.P. Srinivasan, Y. Ni, Preparation of Mesoporous High-Surface-Area Activated Carbon, Advanced materials 12(1) (2000) 62-65.
[172] B.E. Reed, R. Vaughan, L. Jiang, As (III), As (V), Hg, and Pb removal by Fe-oxide impregnated activated carbon, Journal of environmental engineering 126(9) (2000) 869-873.
[173] L.V. Rajaković, The sorption of arsenic onto activated carbon impregnated with metallic silver and copper, Separation science and technology 27(11) (1992) 1423-1433.
[174] A.A. Merchant, M.A. Petrich, Pyrolysis of scrap tires and conversion of chars to activated carbon, AIChE Journal 39(8) (1993) 1370-1376.
[175] W. Hao, F. Björnerbäck, Y. Trushkina, M. Oregui Bengoechea, G. Salazar-Alvarez, T. Barth, N. Hedin, High-Performance Magnetic Activated Carbon from Solid Waste from Lignin Conversion Processes. 1. Their Use As Adsorbents for $CO_2$, ACS Sustainable Chemistry & Engineering 5(4) (2017) 3087-3095.
[176] Z. Gu, J. Fang, B. Deng, Preparation and evaluation of GAC-based iron-containing adsorbents for arsenic removal, Environmental science & technology 39(10) (2005) 3833-3843.
[177] S. Zhu, Y.-g. Liu, S.-b. Liu, G.-m. Zeng, L.-h. Jiang, X.-f. Tan, L. Zhou, W. Zeng, T.-t. Li, C.-p. Yang, Adsorption of emerging contaminant metformin using graphene oxide, Chemosphere 179 (2017) 20-28.
[178] X. Qu, P.J. Alvarez, Q. Li, Applications of nanotechnology in water and wastewater treatment, Water research 47(12) (2013) 3931-3946.
[179] D. Mohan, K.P. Singh, Single-and multi-component adsorption of cadmium and zinc using activated carbon derived from bagasse—an agricultural waste, Water research 36(9) (2002) 2304-2318.
[180] K. Cronje, K. Chetty, M. Carsky, J. Sahu, B. Meikap, Optimization of chromium (VI) sorption potential using developed activated carbon from sugarcane bagasse with chemical activation by zinc chloride, Desalination 275(1) (2011) 276-284.
[181] D. Kalderis, S. Bethanis, P. Paraskeva, E. Diamadopoulos, Production of activated carbon from bagasse and rice husk by a single-stage chemical activation method at low retention times, Bioresource technology 99(15) (2008) 6809-6816.
[182] K. Legrouri, E. Khouya, M. Ezzine, H. Hannache, R. Denoyel, R. Pallier, R. Naslain, Production of activated carbon from a new precursor molasses by activation with sulphuric acid, Journal of hazardous materials 118(1) (2005) 259-263.
[183] J. Laine, S. Yunes, Effect of the preparation method on the pore size distribution of activated carbon from coconut shell, Carbon 30(4) (1992) 601-604.
[184] C. Namasivayam, D. Kavitha, Removal of Congo Red from water by adsorption onto activated carbon prepared from coir pith, an agricultural solid waste, Dyes and pigments 54(1) (2002) 47-58.
[185] K. Kadirvelu, M. Kavipriya, C. Karthika, M. Radhika, N. Vennilamani, S. Pattabhi, Utilization of various agricultural wastes for activated carbon preparation and application for the removal of dyes and metal ions from aqueous solutions, Bioresource technology 87(1) (2003) 129-132.
[186] Ş. Parlayıcı, E. Pehlivan, Removal of metals by $Fe_3O_4$ loaded activated carbon prepared from plum stone (Prunus nigra): Kinetics and modelling study, Powder Technology 317 (2017) 23-30.
[187] F. Hayeeye, Q.J. Yu, M. Sattar, W. Chinpa, O. Sirichote, Adsorption of $Pb^{2+}$ ions from aqueous solutions by gelatin/activated carbon composite bead form, Adsorption Science & Technology (2017) 0263617417693006.

[188] V.K. Jha, M. Matsuda, M. Miyake, Sorption properties of the activated carbon-zeolite composite prepared from coal fly ash for $Ni^{2+}$, $Cu^{2+}$, $Cd^{2+}$ and $Pb^{2+}$, Journal of Hazardous Materials 160(1) (2008) 148-153.
[189] W. Khanday, F. Marrakchi, M. Asif, B. Hameed, Mesoporous zeolite–activated carbon composite from oil palm ash as an effective adsorbent for methylene blue, Journal of the Taiwan Institute of Chemical Engineers 70 (2017) 32-41.
[190] S. Dashamiri, M. Ghaedi, A. Asfaram, F. Zare, S. Wang, Multi-response optimization of ultrasound assisted competitive adsorption of dyes onto $Cu(OH)_2$-nanoparticle loaded activated carbon: Central composite design, Ultrasonics sonochemistry 34 (2017) 343-353.
[191] O. Borggaard, S. Jdrgensen, J. Moberg, B. Raben-Lange, Influence of organic matter on phosphate adsorption by aluminium and iron oxides in sandy soils, European Journal of Soil Science 41(3) (1990) 443-449.
[192] C. Lü, D. Yan, J. He, B. Zhou, L. Li, Q. Zheng, Environmental geochemistry significance of organic phosphorus: An insight from its adsorption on iron oxides, Applied Geochemistry (2017).
[193] G. Micera, C. Gessa, P. Melis, A. Premoli, R. Dallocchio, S. Deiana, Zinc (II) adsorption on aluminium hydroxide, Colloids and surfaces 17(4) (1986) 389-394.
[194] A. Bibak, Cobalt, copper, and manganese adsorption by aluminium and iron oxides and humic acid, Communications in Soil Science & Plant Analysis 25(19-20) (1994) 3229-3239.
[195] S. Hamamoto, N. Kishimoto, Characteristics of fluoride adsorption onto aluminium (III) and iron (III) hydroxide flocs, Separation Science and Technology 52(1) (2017) 42-50.
[196] E. Worch, Adsorption technology in water treatment: fundamentals, processes, and modeling, Walter de Gruyter2012.
[197] B.A. Bolto, Soluble polymers in water purification, Progress in Polymer Science 20(6) (1995) 987-1041.
[198] M.A. Shannon, P.W. Bohn, M. Elimelech, J.G. Georgiadis, B.J. Mariñas, A.M. Mayes, Science and technology for water purification in the coming decades, Nature 452(7185) (2008) 301-310.
[199] R.A. Gross, B. Kalra, Biodegradable polymers for the environment, Science 297(5582) (2002) 803-807.
[200] P. Jain, T. Pradeep, Potential of silver nanoparticle-coated polyurethane foam as an antibacterial water filter, Biotechnology and bioengineering 90(1) (2005) 59-63.
[201] M.-S. Chiou, P.-Y. Ho, H.-Y. Li, Adsorption of anionic dyes in acid solutions using chemically cross-linked chitosan beads, Dyes and pigments 60(1) (2004) 69-84.
[202] V. Singh, A.K. Sharma, R. Sanghi, Poly (acrylamide) functionalized chitosan: An efficient adsorbent for azo dyes from aqueous solutions, Journal of hazardous materials 166(1) (2009) 327-335.
[203] H. Furukawa, K.E. Cordova, M. O'Keeffe, O.M. Yaghi, The chemistry and applications of metal-organic frameworks, Science 341(6149) (2013) 1230444.
[204] Q. Xie, Y. Li, Z. Lv, H. Zhou, X. Yang, J. Chen, H. Guo, Effective Adsorption and Removal of Phosphate from Aqueous Solutions and Eutrophic Water by Fe-based MOFs of MIL-101, Scientific Reports 7 (2017).
[205] E. Haque, J.E. Lee, I.T. Jang, Y.K. Hwang, J.-S. Chang, J. Jegal, S.H. Jhung, Adsorptive removal of methyl orange from aqueous solution with metal-organic frameworks, porous chromium-benzenedicarboxylates, Journal of hazardous materials 181(1) (2010) 535-542.
[206] Z. Hasan, S.H. Jhung, Removal of hazardous organics from water using metal-organic frameworks (MOFs): plausible mechanisms for selective adsorptions, Journal of hazardous materials 283 (2015) 329-339.
[207] A. Smith, Opinion: Nanotech–the way forward for clean water?, Filtration & separation 43(8) (2006) 32-33.
[208] J. Luo, Y. Liu, H. Wei, B. Wang, K.-H. Wu, B. Zhang, D.S. Su, A green and economical vapor-assisted ozone treatment process for surface functionalization of carbon nanotubes, Green Chemistry 19(4) (2017) 1052-1062.

[209] C. Zhang, J. Sui, J. Li, Y. Tang, W. Cai, Efficient removal of heavy metal ions by thiol-functionalized superparamagnetic carbon nanotubes, Chemical engineering journal 210 (2012) 45-52.
[210] Q. Wang, D. O'Hare, Recent advances in the synthesis and application of layered double hydroxide (LDH) nanosheets, Chemical reviews 112(7) (2012) 4124-4155.
[211] V. Prevot, Y. Tokudome, 3D hierarchical and porous layered double hydroxide structures: an overview of synthesis methods and applications, Journal of Materials Science 1-22.
[212] M. Zubair, M. Daud, G. McKay, F. Shehzad, M.A. Al-Harthi, Recent progress in layered double hydroxides (LDH)-containing hybrids as adsorbents for water remediation, Applied Clay Science 143 (2017) 279-292.
[213] R. Al Nuumani, G.T. Vladisavljevic, G. Bolognesi, Microfluidic production of microspheres and microcapsules for photocatalytic water treatment and $CO_2$ capture, Green and Sustainable Chemistry Conference, 2017.
[214] A. Khanna, V. Shetty K, Solar light-driven photocatalytic degradation of Anthraquinone dye-contaminated water by engineered Ag@$TiO_2$ core–shell nanoparticles, Desalination and Water Treatment 54(3) (2015) 744-757.
[215] X. Zhang, L. Guo, H. Huang, Y. Jiang, M. Li, Y. Leng, Removal of phosphorus by the core-shell bio-ceramic/Zn-layered double hydroxides (LDHs) composites for municipal wastewater treatment in constructed rapid infiltration system, Water research 96 (2016) 280-291.
[216] Z. Liu, H. Bai, D.D. Sun, Facile fabrication of porous chitosan/$TiO_2$/$Fe_3O_4$ microspheres with multifunction for water purifications, New Journal of Chemistry 35(1) (2011) 137-140.
[217] N. Tahir, H.N. Bhatti, M. Iqbal, S. Noreen, Biopolymers composites with peanut hull waste biomass and application for Crystal Violet adsorption, International journal of biological macromolecules 94 (2017) 210-220.
[218] Q. Liu, L. Wang, A. Xiao, J. Gao, W. Ding, H. Yu, J. Huo, M. Ericson, Templated preparation of porous magnetic microspheres and their application in removal of cationic dyes from wastewater, Journal of hazardous materials 181(1) (2010) 586-592.
[219] Y. Deng, D. Qi, C. Deng, X. Zhang, D. Zhao, Superparamagnetic high-magnetization microspheres with an $Fe_3O_4$@$SiO_2$ core and perpendicularly aligned mesoporous $SiO_2$ shell for removal of microcystins, Journal of the American Chemical Society 130(1) (2008) 28-29.
[220] Z. Baolong, C. Baishun, S. Keyu, H. Shangjin, L. Xiaodong, D. Zongjie, Y. Kelian, Preparation and characterization of nanocrystal grain $TiO_2$ porous microspheres, Applied Catalysis B: Environmental 40(4) (2003) 253-258.
[221] X. Li, Z. Si, Y. Lei, X. Li, J. Tang, S. Song, H. Zhang, Hierarchically structured $Fe_3O_4$ microspheres: morphology control and their application in wastewater treatment, CrystEngComm 13(2) (2011) 642-648.
[222] H. Xiao, Z. Ai, L. Zhang, Nonaqueous sol− gel synthesized hierarchical $CeO_2$ nanocrystal microspheres as novel adsorbents for wastewater treatment, The Journal of Physical Chemistry C 113(38) (2009) 16625-16630.
[223] J.H. Pan, X. Zhang, A.J. Du, D.D. Sun, J.O. Leckie, Self-etching reconstruction of hierarchically mesoporous F-$TiO_2$ hollow microspherical photocatalyst for concurrent membrane water purifications, Journal of the American Chemical Society 130(34) (2008) 11256-11257.
[224] C. Shen, K. Pang, L. Du, G. Luo, Green synthesis and enhanced photocatalytic activity of Ce-doped $TiO_2$ nanoparticles supported on porous glass, Particuology (2017).
[225] J. Fei, Y. Cui, X. Yan, W. Qi, Y. Yang, K. Wang, Q. He, J. Li, Controlled preparation of $MnO_2$ hierarchical hollow nanostructures and their application in water treatment, Advanced Materials 20(3) (2008) 452-456.
[226] S. Zeng, K. Tang, T. Li, Z. Liang, D. Wang, Y. Wang, W. Zhou, Hematite hollow spindles and microspheres: selective synthesis, growth mechanisms, and application in lithium ion battery and water treatment, The Journal of Physical Chemistry C 111(28) (2007) 10217-10225.

[227] W. Cai, J. Yu, B. Cheng, B.-L. Su, M. Jaroniec, Synthesis of boehmite hollow core/shell and hollow microspheres via sodium tartrate-mediated phase transformation and their enhanced adsorption performance in water treatment, The Journal of Physical Chemistry C 113(33) (2009) 14739-14746.
[228] L.S. Zhong, J.S. Hu, H.P. Liang, A.M. Cao, W.G. Song, L.J. Wan, Self-Assembled 3D flowerlike iron oxide nanostructures and their application in water treatment, Advanced Materials 18(18) (2006) 2426-2431.
[229] D. Zhang, M. Wen, B. Jiang, G. Li, C.Y. Jimmy, Ionothermal synthesis of hierarchical BiOBr microspheres for water treatment, Journal of hazardous materials 211 (2012) 104-111.
[230] X. Li, S. Xiong, J. Li, J. Bai, Y. Qian, Mesoporous NiO ultrathin nanowire networks topotactically transformed from α-$Ni(OH)_2$ hierarchical microspheres and their superior electrochemical capacitance properties and excellent capability for water treatment, Journal of Materials Chemistry 22(28) (2012) 14276-14283.
[231] Y. Wang, G. Wang, H. Wang, C. Liang, W. Cai, L. Zhang, Chemical-template synthesis of micro/nanoscale magnesium silicate hollow spheres for waste-water treatment, Chemistry-A European Journal 16(11) (2010) 3497-3503.
[232] L. Shi, H. Lin, Facile fabrication and optical property of hollow $SnO_2$ spheres and their application in water treatment, Langmuir 26(24) (2010) 18718-18722.
[233] S. Liu, S.B. Mishra, Y. Zhang, L. Qi, Uptake of hexavalent chromium in electroplating wastewater by hydrothermally treated and functionalized sand and its sustainable reutilization for glass production, ACS Sustainable Chemistry & Engineering 5(2) (2017) 1509-1516.
[234] Y. Ge, X. Cui, C. Liao, Z. Li, Facile fabrication of green geopolymer/alginate hybrid spheres for efficient removal of Cu (II) in water: Batch and column studies, Chemical Engineering Journal 311 (2017) 126-134.
[235] P. McMillan, Glass-Ceramics. 2nd edn."Non-Metallic Solids", edited by JP Roberts. Vol. 1, London: Academic Press Inc.(London) Ltd, 1979.
[236] J.D. Musgraves, J. Hu, L. Calvez, Springer Handbook of Glass, Springer Nature2019.
[237] H. Nesbitt, G. Bancroft, G. Henderson, R. Ho, K. Dalby, Y. Huang, Z. Yan, Bridging, non-bridging and free ($O^{2-}$) oxygen in $Na_2O$-$SiO_2$ glasses: An X-ray Photoelectron Spectroscopic (XPS) and Nuclear Magnetic Resonance (NMR) study, Journal of Non-Crystalline Solids 357(1) (2011) 170-180.
[238] Y. Onodera, Y. Takimoto, H. Hijiya, T. Taniguchi, S. Urata, S. Inaba, S. Fujita, I. Obayashi, Y. Hiraoka, S. Kohara, Origin of the mixed alkali effect in silicate glass, NPG Asia Materials 11(1) (2019) 1-11.
[239] Y. Moustafa, K. El-Egili, Infrared spectra of sodium phosphate glasses, Journal of non-crystalline solids 240(1-3) (1998) 144-153.
[240] R.K. Brow, The structure of simple phosphate glasses, Journal of Non-Crystalline Solids 263 (2000) 1-28.
[241] E. Metwalli, M. Karabulut, D.L. Sidebottom, M. Morsi, R.K. Brow, Properties and structure of copper ultraphosphate glasses, Journal of Non-Crystalline Solids 344(3) (2004) 128-134.
[242] A. Kiani, J.V. Hanna, S.P. King, G.J. Rees, M.E. Smith, N. Roohpour, V. Salih, J.C. Knowles, Structural characterization and physical properties of $P_2O_5$–CaO–$Na_2O$–$TiO_2$ glasses by Fourier transform infrared, Raman and solid-state magic angle spinning nuclear magnetic resonance spectroscopies, Acta biomaterialia 8(1) (2012) 333-340.
[243] Y. Fu, J.K. Christie, Atomic structure and dissolution properties of yttrium-containing phosphate glasses, International Journal of Applied Glass Science 8(4) (2017) 412-417.
[244] H. Gao, T. Tan, D. Wang, Effect of composition on the release kinetics of phosphate controlled release glasses in aqueous medium, Journal of controlled release 96(1) (2004) 21-28.
[245] I. Ahmed, A. Parsons, G. Palmer, J. Knowles, G. Walker, C. Rudd, Weight loss, ion release and initial mechanical properties of a binary calcium phosphate glass fibre/PCL composite, Acta Biomaterialia 4(5) (2008) 1307-1314.
[246] A. Marino, S. Arrasmith, L. Gregg, S. Jacobs, G. Chen, Y. Duc, Durable phosphate glasses with lower transition temperatures, Journal of non-crystalline solids 289(1) (2001) 37-41.

[247] J.C. Knowles, Phosphate based glasses for biomedical applications, Journal of Materials Chemistry 13(10) (2003) 2395-2401.
[248] J. Massera, I. Ahmed, L. Petit, V. Aallos, L. Hupa, Phosphate-based glass fiber vs. bulk glass: Change in fiber optical response to probe in vitro glass reactivity, Materials Science and Engineering: C 37 (2014) 251-257.
[249] S. Balaji, S. Bose, R. Debnath, Single-walled carbon nanotube/(Pb, Zn)-phosphate glass heterostructure: an optical sensor and efficient photocurrent converter, Journal of Physics D: Applied Physics 45(32) (2012) 325106.
[250] I.W. Donald, B. Metcalfe, S.K. Fong, L.A. Gerrard, D.M. Strachan, R.D. Scheele, A glass-encapsulated calcium phosphate wasteform for the immobilization of actinide-, fluoride-, and chloride-containing radioactive wastes from the pyrochemical reprocessing of plutonium metal, Journal of nuclear materials 361(1) (2007) 78-93.
[251] K. Franks, V. Salih, J.C. Knowles, I. Olsen, The effect of MgO on the solubility behavior and cell proliferation in a quaternary soluble phosphate based glass system, Journal of Materials Science: Materials in Medicine 13(6) (2002) 549-556.
[252] V. Rajendran, A.G. Devi, M. Azooz, F. El-Batal, Physicochemical studies of phosphate based $P_2O_5$–$Na_2O$–CaO–$TiO_2$ glasses for biomedical applications, Journal of non-crystalline solids 353(1) (2007) 77-84.
[253] E.A. Abou Neel, L.A. O'Dell, M.E. Smith, J.C. Knowles, Processing, characterisation, and biocompatibility of zinc modified metaphosphate based glasses for biomedical applications, Journal of Materials Science: Materials in Medicine 19(4) (2008) 1669-1679.
[254] C. Vitale-Brovarone, G. Novajra, D. Milanese, J. Lousteau, J. Knowles, Novel phosphate glasses with different amounts of $TiO_2$ for biomedical applications: Dissolution tests and proof of concept of fibre drawing, Materials Science and Engineering: C 31(2) (2011) 434-442.
[255] M.N. Rahaman, D.E. Day, B.S. Bal, Q. Fu, S.B. Jung, L.F. Bonewald, A.P. Tomsia, Bioactive glass in tissue engineering, Acta biomaterialia 7(6) (2011) 2355-2373.
[256] C. Rey, C. Combes, C. Drouet, M.J. Glimcher, Bone mineral: update on chemical composition and structure, Osteoporosis international 20(6) (2009) 1013-1021.
[257] I. Ahmed, M. Lewis, I. Olsen, J. Knowles, Phosphate glasses for tissue engineering: Part 1. Processing and characterisation of a ternary-based $P_2O_5$–CaO–$Na_2O$ glass system, Biomaterials 25(3) (2004) 491-499.
[258] M. Hasan, I. Ahmed, A. Parsons, G. Walker, C. Scotchford, Material characterisation and cytocompatibility assessment of quinternary phosphate glasses, Journal of Materials Science: Materials in Medicine 23(10) (2012) 2531-2541.
[259] N. Sharmin, M.S. Hasan, A.J. Parsons, D. Furniss, C.A. Scotchford, I. Ahmed, C.D. Rudd, Effect of boron addition on the thermal, degradation, and cytocompatibility properties of phosphate-based glasses, BioMed research international 2013 (2013).
[260] U. Patel, L. Macri-Pellizzeri, K.M. Zakir Hossain, B.E. Scammell, D.M. Grant, C.A. Scotchford, A.C. Hannon, A.R. Kennedy, E.R. Barney, I. Ahmed, In vitro cellular testing of strontium/calcium substituted phosphate glass discs and microspheres shows potential for bone regeneration, Journal of Tissue Engineering and Regenerative Medicine 13(3) (2019) 396-405.
[261] M.T. Islam, N. Sharmin, G.A. Rance, J.J. Titman, A.J. Parsons, K.M.Z. Hossain, I. Ahmed, The effect of MgO/$TiO_2$ on structural and crystallization behavior of near invert phosphate-based glasses, Journal of Biomedical Materials Research Part B: Applied Biomaterials 108(3) (2020) 674-686.
[262] E.A. Abou Neel, D.M. Pickup, S.P. Valappil, R.J. Newport, J.C. Knowles, Bioactive functional materials: a perspective on phosphate-based glasses, Journal of Materials Chemistry 19(6) (2009) 690-701.
[263] E. Soyer, Ö. Akgiray, N.Ö. Eldem, A.M. Saatçı, Crushed recycled glass as a filter medium and comparison with silica sand, CLEAN–Soil, Air, Water 38(10) (2010) 927-935.

[264] A. Fernandez, G. Lassaletta, V. Jimenez, A. Justo, A. Gonzalez-Elipe, J.-M. Herrmann, H. Tahiri, Y. Ait-Ichou, Preparation and characterization of $TiO_2$ photocatalysts supported on various rigid supports (glass, quartz and stainless steel). Comparative studies of photocatalytic activity in water purification, Applied Catalysis B: Environmental 7(1-2) (1995) 49-63.
[265] G. Singh, M. Sharma, R. Vaish, Transparent ferroelectric glass–ceramics for wastewater treatment by piezocatalysis, Communications Materials 1(1) (2020) 100.
[266] T. Nishida, A. Morimoto, Y. Yamamoto, S. Kubuki, Waste water purification using new porous ceramics prepared by recycling waste glass and bamboo charcoal, Applied Water Science (2017) 1-6.
[267] S. Jiang, T. Luo, Q. Wang, L. Pan, Rare-earth doped gain fibers, Google Patents, 2017.
[268] R. Groth, Heat-reflecting laminated safety glass pane, Google Patents, 1974.
[269] B. Sales, L. Boatner, Lead-iron phosphate glass: a stable storage medium for high-level nuclear waste, Science 226 (1984) 45-49.
[270] T. Ando, Y. Fujita, M. Kakinaga, N. Oka, T. Nishida, Water purification using porous ceramics prepared by recycling volcanic ash and waste glass, Applied Water Science (2017) 1-7.
[271] I. Ponsot, E. Bernardo, E. Bontempi, L. Depero, R. Detsch, R.K. Chinnam, A.R. Boccaccini, Recycling of pre-stabilized municipal waste incinerator fly ash and soda-lime glass into sintered glass-ceramics, Journal of Cleaner Production 89 (2015) 224-230.
[272] J. Wu, A. Boccaccini, P. Lee, M. Kershaw, R. Rawlings, Glass ceramic foams from coal ash and waste glass: production and characterisation, Advances in Applied Ceramics 105(1) (2006) 32-39.
[273] T. Nishida, A. Morimoto, Y. Yamamoto, S. Kubuki, Waste water purification using new porous ceramics prepared by recycling waste glass and bamboo charcoal, Applied Water Science 7(8) (2017) 4281-4286.
[274] L. Sheng, Y. Zhang, F. Tang, S. Liu, Mesoporous/microporous silica materials: preparation from natural sands and highly efficient fixed-bed adsorption of methylene blue in wastewater, Microporous and Mesoporous Materials 257 (2018) 9-18.
[275] D. Enke, F. Janowski, W. Schwieger, Porous glasses in the 21st century-a short review, Microporous and mesoporous materials 60(1) (2003) 19-30.
[276] SCHOTT CoralPor® Porous Glass Product Information.
[277] K. Zheng, A.R. Boccaccini, Sol-gel processing of bioactive glass nanoparticles: A review, Advances in Colloid and Interface Science (2017).
[278] J. Maurath, J. Dittmann, N. Schultz, N. Willenbacher, Fabrication of highly porous glass filters using capillary suspension processing, Separation and Purification Technology 149 (2015) 470-478.
[279] L. O'brien Donald, Glass bubbles prepared by reheating solid glass partiles, Google Patents, 1968.
[280] V. Franklin, H.E. Alford, R.D. Croft, Method of producing hollow glass spheres, Google Patents, 1961.
[281] W. Fu, S. Liu, W. Fan, H. Yang, X. Pang, J. Xu, G. Zou, Hollow glass microspheres coated with $CoFe_2O_4$ and its microwave absorption property, Journal of Magnetism and Magnetic Materials 316(1) (2007) 54-58.
[282] Y. Hu, R. Mei, Z. An, J. Zhang, Silicon rubber/hollow glass microsphere composites: Influence of broken hollow glass microsphere on mechanical and thermal insulation property, Composites Science and Technology 79 (2013) 64-69.
[283] G. Wicks, L. Heung, R. Schumacher, Microspheres and microworlds, American Ceramic Society Bulletin 87(6) (2008) 23.
[284] L. Heung, G. Wicks, R. Schumacher, ENCAPSULATION OF PALLADIUM IN POROUS WALL HOLLOW GLASS MlCROSPl-IERES, Materials Innovations in an Emerging Hydrogen Economy: Ceramic Transactions 202 (2009) 143.
[285] S. Li, W.S. Dynan, G. Wicks, S. Serkiz, Porous-wall hollow glass microspheres as carriers for biomolecules, Google Patents, 2013.
[286] R. Mohtadi, K. Tange, T. Matsunaga, G. Wicks, K. Heung, R. Schumacher, A New Way for Storing Reactive Complex Hydrides on Board of Automobiles, Materials Innovations in an Emerging Hydrogen Economy, Ceramic Transactions, eds., GG Wicks and J. Simon 202 (2009) 91-96.

[287] J. Ge, Q. Zhang, T. Zhang, Y. Yin, Core–satellite nanocomposite catalysts protected by a porous silica shell: controllable reactivity, high stability, and magnetic recyclability, Angewandte Chemie 120(46) (2008) 9056-9060.
[288] S. Shinzato, M. Kobayashi, W.F. Mousa, M. Kamimura, M. Neo, Y. Kitamura, T. Kokubo, T. Nakamura, Bioactive polymethyl methacrylate-based bone cement: Comparison of glass beads, apatite-and wollastonite-containing glass–ceramic, and hydroxyapatite fillers on mechanical and biological properties, Journal of Biomedical Materials Research Part A 51(2) (2000) 258-272.
[289] J.J. Blaker, J.C. Knowles, R.M. Day, Novel fabrication techniques to produce microspheres by thermally induced phase separation for tissue engineering and drug delivery, Acta biomaterialia 4(2) (2008) 264-272.
[290] L.M. Kulik, B.I. Carr, M.F. Mulcahy, R.J. Lewandowski, B. Atassi, R.K. Ryu, K.T. Sato, A. Benson, A.A. Nemcek, V.L. Gates, Safety and efficacy of 90Y radiotherapy for hepatocellular carcinoma with and without portal vein thrombosis, Hepatology 47(1) (2008) 71-81.
[291] M. Todea, E. Vanea, S. Bran, P. Berce, S. Simon, XPS analysis of aluminosilicate microspheres bioactivity tested in vitro, Applied Surface Science 270 (2013) 777-783.
[292] F.F. Sene, J.R. Martinelli, E. Okuno, Synthesis and characterization of phosphate glass microspheres for radiotherapy applications, Journal of Non-Crystalline Solids 354(42) (2008) 4887-4893.
[293] S.D. Conzone, R.F. Brown, D.E. Day, G.J. Ehrhardt, In vitro and in vivo dissolution behavior of a dysprosium lithium borate glass designed for the radiation synovectomy treatment of rheumatoid arthritis, Journal of Biomedical Materials Research Part A 60(2) (2002) 260-268.
[294] H. Fu, M.N. Rahaman, D.E. Day, Effect of process variables on the microstructure of hollow hydroxyapatite microspheres prepared by a glass conversion method, Journal of the American Ceramic Society 93(10) (2010) 3116-3123.
[295] N.J. Lakhkar, J.-H. Park, N.J. Mordan, V. Salih, I.B. Wall, H.-W. Kim, S.P. King, J.V. Hanna, R.A. Martin, O. Addison, Titanium phosphate glass microspheres for bone tissue engineering, Acta biomaterialia 8(11) (2012) 4181-4190.
[296] D. Day, J. White, R. Brown, K. McMenamin, Transformation of borate glasses into biologically useful materials, Glass technology 44(2) (2003) 75-81.
[297] M. Kawashita, S. Toda, H.M. Kim, T. Kokubo, N. Masuda, Preparation of antibacterial silver-doped silica glass microspheres, Journal of Biomedical Materials Research Part A 66(2) (2003) 266-274.
[298] B. Karmakar, G. De, D. Ganguli, Dense silica microspheres from organic and inorganic acid hydrolysis of TEOS, Journal of non-crystalline solids 272(2) (2000) 119-126.
[299] G.N. Conti, A. Chiasera, L. Ghisa, S. Berneschi, M. Brenci, Y. Dumeige, S. Pelli, S. Sebastiani, P. Feron, M. Ferrari, Spectroscopic and lasing properties of $Er^{3+}$-doped glass microspheres, Journal of non-crystalline solids 352(23) (2006) 2360-2363.
[300] A. Geleil, M. Hall, J. Shelby, Hollow glass microspheres for use in radiation shielding, Journal of Non-Crystalline Solids 352(6) (2006) 620-625.
[301] J.R. Martinelli, F.F. Sene, C.N. Kamikawachi, C.d.M. Partiti, D.R. Cornejo, Synthesis and characterization of glass–ceramic microspheres for thermotherapy, Journal of Non-Crystalline Solids 356(44) (2010) 2683-2688.
[302] S.D. Conzone, D.E. Day, Preparation and properties of porous microspheres made from borate glass, Journal of Biomedical Materials Research Part A 88(2) (2009) 531-542.
[303] Y. Sun, Y. Wang, Y. Lu, T. Wang, G. Luo, Subcritical water treatment: a simple method to prepare porous glass with a core–shell structure, Journal of the American Ceramic Society 91(1) (2008) 103-109.
[304] G.J. Ehrhardt, D.E. Day, Therapeutic use of 90Y microspheres, International Journal of Radiation Applications and Instrumentation. Part B. Nuclear Medicine and Biology 14(3) (1987) 233-242.
[305] M.G. Fey, C.B. Wolf, P.E. Martin, J.H.I. Francis, Process for production of magnetite spheres with an arc heater, Google Patents, 1978.

[306] H. Jin, N. Song, N. Wang, Y. Wang, J. Zhou, J. Chen, S. Hou, Preparation of low radioactivity spherical silicon oxide powders via chemical-flame spheroidizing process, Colloids and Surfaces A: Physicochemical and Engineering Aspects 381(1) (2011) 13-16.
[307] M. Bortot, S. Prastalo, M. Prado, Production and characterization of glass microspheres for hepatic cancer treatment, Procedia Materials Science 1 (2012) 351-358.
[308] Z. Ji, H. Jin, Y. Wu, Y. Li, M. Liu, C. Xu, P. Hou, J. Dong, S. Hou, Numerical simulation of silica particle trajectory in flow field and silica particle spheroidizing in oxygen–acetylene flame spheroidization process, Powder Technology 286 (2015) 451-458.
[309] K.M.Z. Hossain, U. Patel, A.R. Kennedy, L. Macri-Pellizzeri, V. Sottile, D.M. Grant, B.E. Scammell, I. Ahmed, Porous calcium phosphate glass microspheres for orthobiologic applications, Acta biomaterialia 72 (2018) 396-406.
[310] M.T. Islam, L. Macri-Pellizzeri, K.M.Z. Hossain, V. Sottile, I. Ahmed, Effect of varying the Mg with Ca content in highly porous phosphate-based glass microspheres, Materials Science and Engineering: C (2020) 111668.
[311] E.A. Abou Neel, W. Chrzanowski, J.C. Knowles, Effect of increasing titanium dioxide content on bulk and surface properties of phosphate-based glasses, Acta biomaterialia 4(3) (2008) 523-534.
[312] R. Nisticò, F. Cesano, F. Garello, Magnetic materials and systems: Domain structure visualization and other characterization techniques for the application in the materials science and biomedicine, Inorganics 8(1) (2020) 6.
[313] Q.A. Pankhurst, J. Connolly, S.K. Jones, J. Dobson, Applications of magnetic nanoparticles in biomedicine, Journal of physics D: Applied physics 36(13) (2003) R167.
[314] A. Grillone, G. Ciofani, Magnetic nanotransducers in biomedicine, Chemistry (Weinheim an der Bergstrasse, Germany) 23(64) (2017) 16109.
[315] J.J. Abbott, E. Diller, A.J. Petruska, Magnetic methods in robotics, Annual Review of Control, Robotics, and Autonomous Systems 3 (2020) 57-90.
[316] V. Kumar, Introduction to robotics, University of Pennsylvania, Philadelphia (2014).
[317] A. Togni, Ferrocenes: homogeneous catalysis, organic synthesis, materials science, John Wiley & Sons 2008.
[318] L.M. Rossi, N.J. Costa, F.P. Silva, R. Wojcieszak, Magnetic nanomaterials in catalysis: advanced catalysts for magnetic separation and beyond, Green Chemistry 16(6) (2014) 2906-2933.
[319] M. Wiltshire, J. Pendry, I. Young, D. Larkman, D. Gilderdale, J. Hajnal, Microstructured magnetic materials for RF flux guides in magnetic resonance imaging, Science 291(5505) (2001) 849-851.
[320] J.C. Richardson, R.W. Bowtell, K. Mäder, C.D. Melia, Pharmaceutical applications of magnetic resonance imaging (MRI), Advanced drug delivery reviews 57(8) (2005) 1191-1209.
[321] R. Comstock, Review modern magnetic materials in data storage, Journal of Materials Science: Materials in Electronics 13(9) (2002) 509-523.
[322] N.A. Spaldin, Magnetic materials: fundamentals and applications, Cambridge university press 2010.
[323] H. Okumura, D. Twisselmann, R.D. McMichael, M. Huang, Y. Hsu, D. Laughlin, M. McHenry, Magnetic and structural characterization and ferromagnetic resonance study of thin film HITPERM soft magnetic materials for data storage applications, Journal of applied physics 93(10) (2003) 6528-6530.
[324] C. Heck, Magnetic materials and their applications, Elsevier 2013.
[325] T. Hashimoto, T. Kuzuhara, M. Sahashi, K. Inomata, A. Tomokiyo, H. Yayama, New application of complex magnetic materials to the magnetic refrigerant in an Ericsson magnetic refrigerator, Journal of applied physics 62(9) (1987) 3873-3878.
[326] R. Nisticò, Magnetic materials and water treatments for a sustainable future, Research on Chemical Intermediates 43(12) (2017) 6911-6949.
[327] R.D. Ambashta, M. Sillanpää, Water purification using magnetic assistance: a review, Journal of hazardous materials 180(1-3) (2010) 38-49.

[328] S.G. Arhin, N. Banadda, A.J. Komakech, I. Kabenge, J. Wanyama, Membrane fouling control in low pressure membranes: A review on pretreatment techniques for fouling abatement, Environmental Engineering Research 21(2) (2016) 109-120.
[329] H. Luo, Y. Zeng, D. He, X. Pan, Application of iron-based materials in heterogeneous advanced oxidation processes for wastewater treatment: A review, Chemical Engineering Journal (2020) 127191.
[330] G.A.P. Mateus, M.P. Paludo, T.R.T. dos Santos, M.F. Silva, L. Nishi, M.R. Fagundes-Klen, R.G. Gomes, R. Bergamasco, Obtaining drinking water using a magnetic coagulant composed of magnetite nanoparticles functionalized with Moringa oleifera seed extract, Journal of environmental chemical engineering 6(4) (2018) 4084-4092.
[331] Z. Shi, R. Zhang, J. Zhang, Role of weak magnetic field for enhanced oxidation of orange G by magnetic Fenton, (2021).
[332] M. Vanags, A. Spule, K. Gruškeviča, S. Vihodceva, A. Tamm, S. Vlassov, A. Šutka, Sol-gel auto-combustion synthesis of $Ca_2Fe_2O_5$ brownmillerite nanopowders and thin films for advanced oxidation photoelectrochemical water treatment in visible light, Journal of Environmental Chemical Engineering 7(4) (2019) 103224.
[333] F. Moradnia, S.T. Fardood, A. Ramazani, B.-k. Min, S.W. Joo, R.S. Varma, Magnetic Mg0. 5Zn0. 5$FeMnO_4$ nanoparticles: green sol-gel synthesis, characterization, and photocatalytic applications, Journal of Cleaner Production 288 (2021) 125632.
[334] D.H.K. Reddy, Y.-S. Yun, Spinel ferrite magnetic adsorbents: alternative future materials for water purification?, Coordination Chemistry Reviews 315 (2016) 90-111.
[335] A.Z.M. Badruddoza, Z.B.Z. Shawon, W.J.D. Tay, K. Hidajat, M.S. Uddin, $Fe_3O_4$/cyclodextrin polymer nanocomposites for selective heavy metals removal from industrial wastewater, Carbohydrate polymers 91(1) (2013) 322-332.
[336] Z. Jia, Q. Qin, J. Liu, H. Shi, X. Zhang, R. Hu, S. Li, R. Zhu, The synthesis of hierarchical $ZnFe_2O_4$ architecture and their application for Cr (VI) adsorption removal from aqueous solution, Superlattices and Microstructures 82 (2015) 174-187.
[337] T.R. Santos, M.F. Silva, L. Nishi, A.M. Vieira, M.R. Klein, M.B. Andrade, M.F. Vieira, R. Bergamasco, Development of a magnetic coagulant based on Moringa oleifera seed extract for water treatment, Environmental Science and Pollution Research 23(8) (2016) 7692-7700.
[338] Z. Qu, T. Su, Y. Chen, X. Lin, Y. Yu, S. Zhu, X. Xie, M. Huo, Effective enrichment of Zn from smelting wastewater via an integrated Fe coagulation and hematite precipitation method, Frontiers of Environmental Science & Engineering 13(6) (2019) 1-9.
[339] P. Marcinowski, D. Bury, M. Krupa, D. Ścieżyńska, P. Prabhu, J. Bogacki, Magnetite and hematite in advanced oxidation processes application for cosmetic wastewater treatment, Processes 8(11) (2020) 1343.
[340] H. Cai, T. Zhao, Z. Ma, J. Liu, Efficient removal of metronidazole by the photo-Fenton process with a magnetic $Fe_3O_4$@ PBC composite, Journal of Environmental Engineering 146(7) (2020) 04020056.
[341] A.M. Atta, Y.M. Moustafa, H.A. Al-Lohedan, A.O. Ezzat, A.I. Hashem, Methylene blue catalytic degradation using silver and magnetite nanoparticles functionalized with a poly (ionic liquid) based on quaternized dialkylethanolamine with 2-acrylamido-2-methylpropane sulfonate-co-vinylpyrrolidone, ACS omega 5(6) (2020) 2829-2842.
[342] M.Y. Badi, A. Azari, H. Pasalari, A. Esrafili, M. Farzadkia, Modification of activated carbon with magnetic $Fe_3O_4$ nanoparticle composite for removal of ceftriaxone from aquatic solutions, Journal of Molecular Liquids 261 (2018) 146-154.
[343] F. Unob, B. Wongsiri, N. Phaeon, M. Puanngam, J. Shiowatana, Reuse of waste silica as adsorbent for metal removal by iron oxide modification, Journal of hazardous materials 142(1-2) (2007) 455-462.
[344] Y. Xue, P. Xiang, H. Wang, Y. Jiang, Y. Long, H. Lian, W. Shi, Mechanistic insights into selective adsorption and separation of multi-component anionic dyes using magnetic zeolite imidazolate framework-67 composites, Journal of Molecular Liquids 296 (2019) 111990.

[345] G. Ghasemzadeh, M. Momenpour, F. Omidi, M.R. Hosseini, M. Ahani, A. Barzegari, Applications of nanomaterials in water treatment and environmental remediation, Frontiers of Environmental Science & Engineering 8(4) (2014) 471-482.
[346] F. Salvador, C.S. Jiménez, A new method for regenerating activated carbon by thermal desorption with liquid water under subcritical conditions, Carbon 34(4) (1996) 511-516.
[347] Cision, US Activated Carbon Market. https://www.prnewswire.com/news-releases/us-activated-carbon-market-208141301.html. (Accessed 0ctober 17, 2017.
[348] N. Savage, M.S. Diallo, Nanomaterials and water purification: opportunities and challenges, Journal of Nanoparticle research 7(4) (2005) 331-342.
[349] J. Landaburu-Aguirre, R. García-Pacheco, S. Molina, L. Rodríguez-Sáez, J. Rabadán, E. García-Calvo, Fouling prevention, preparing for re-use and membrane recycling. Towards circular economy in RO desalination, Desalination 393 (2016) 16-30.
[350] J. Fu, Z. Chen, M. Wang, S. Liu, J. Zhang, J. Zhang, R. Han, Q. Xu, Adsorption of methylene blue by a high-efficiency adsorbent (polydopamine microspheres): kinetics, isotherm, thermodynamics and mechanism analysis, Chemical Engineering Journal 259 (2015) 53-61.
[351] Z. Dong, H. Ren, C.M. Hessel, J. Wang, R. Yu, Q. Jin, M. Yang, Z. Hu, Y. Chen, Z. Tang, Quintuple-shelled SnO2 hollow microspheres with superior light scattering for high-performance dye-sensitized solar cells, Advanced Materials 26(6) (2014) 905-909.
[352] Z. Dong, X. Lai, J.E. Halpert, N. Yang, L. Yi, J. Zhai, D. Wang, Z. Tang, L. Jiang, Accurate Control of Multishelled ZnO Hollow Microspheres for Dye-Sensitized Solar Cells with High Efficiency, Advanced materials 24(8) (2012) 1046-1049.
[353] X. Fan, S. Li, Y. Wu, L. Niu, Large-scale preparation of macro-porous silica microspheres via sol–gel composite particles and a spray drying process, RSC Advances 7(88) (2017) 56081-56086.
[354] C. Zoldesi, P. Steegstra, A. Imhof, Encapsulation of emulsion droplets by organo–silica shells, Journal of colloid and interface science 308(1) (2007) 121-129.
[355] H. Jin, L. Xu, S. Hou, Preparation of spherical silica powder by oxygen–acetylene flame spheroidization process, Journal of Materials Processing Technology 210(1) (2010) 81-84.
[356] D.G. Dastidar, S. Saha, M. Chowdhury, Porous microspheres: synthesis, characterisation and applications in pharmaceutical & medical fields, International Journal of Pharmaceutics (2018).
[357] D.H. Taffa, R. Dillert, A.C. Ulpe, K.C. Bauerfeind, T. Bredow, D.W. Bahnemann, M. Wark, Photoelectrochemical and theoretical investigations of spinel type ferrites ($M_xFe_3{-}xO_4$) for water splitting: a mini-review, Journal of Photonics for Energy 7(1) (2016) 012009.
[358] S.K. Jain, A. Awasthi, N. Jain, G. Agrawal, Calcium silicate based microspheres of repaglinide for gastroretentive floating drug delivery: Preparation and in vitro characterization, Journal of controlled release 107(2) (2005) 300-309.
[359] G. Leofanti, M. Padovan, G. Tozzola, B. Venturelli, Surface area and pore texture of catalysts, Catalysis Today 41(1-3) (1998) 207-219.
[360] I. Avramov, Viscosity in disordered media, Journal of non-crystalline solids 351(40-42) (2005) 3163-3173.
[361] A. Fluegel, Glass viscosity calculation based on a global statistical modelling approach, Glass Technology-European Journal of Glass Science and Technology Part A 48(1) (2007) 13-30.
[362] W. Konicki, D. Sibera, U. Narkiewicz, Adsorption of Acid Red 88 Anionic Dye from Aqueous Solution onto ZnO/$ZnMn_2O_4$ Nanocomposite: Equilibrium, Kinetics, and Thermodynamics, Polish Journal of Environmental Studies 26(6) (2017).
[363] E.A. Mohamed, A.Q. Selim, A.M. Zayed, S. Komarneni, M. Mobarak, M.K. Seliem, Enhancing adsorption capacity of Egyptian diatomaceous earth by thermo-chemical purification: Methylene blue uptake, Journal of colloid and interface science 534 (2019) 408-419.
[364] H. Freundlich, W. Heller, The adsorption of cis-and trans-azobenzene, Journal of the American Chemical society 61(8) (1939) 2228-2230.

[365] C.S. Araújo, I.L. Almeida, H.C. Rezende, S.M. Marcionilio, J.J. Léon, T.N. de Matos, Elucidation of mechanism involved in adsorption of Pb (II) onto lobeira fruit (Solanum lycocarpum) using Langmuir, Freundlich and Temkin isotherms, Microchemical Journal 137 (2018) 348-354.
[366] S. Azizian, Kinetic models of sorption: a theoretical analysis, Journal of colloid and Interface Science 276(1) (2004) 47-52.
[367] T.H. Bui, S.P. Hong, J. Yoon, Development of nanoscale zirconium molybdate embedded anion exchange resin for selective removal of phosphate, Water research 134 (2018) 22-31.
[368] U. Maheshwari, S. Gupta, Removal of Cr (VI) from wastewater using activated neem bark in a fixed-bed column: interference of other ions and kinetic modelling studies, Desalination and Water Treatment 57(18) (2016) 8514-8525.
[369] S. Markandeya, G. Kisku, Linear and nonlinear kinetic modeling for adsorption of disperse dye in batch process, Research Journal of Environmental Toxicology 9 (2015) 320-331.
[370] A.D. Levine, G. Tchobanoglous, T. Asano, Characterization of the size distribution of contaminants in wastewater: treatment and reuse implications, Journal (Water Pollution Control Federation) (1985) 805-816.
[371] S. Madaeni, The application of membrane technology for water disinfection, Water Research 33(2) (1999) 301-308.
[372] Y. Zhang, A. Diehl, A. Lewandowski, K. Gopalakrishnan, T. Baker, Removal efficiency of micro-and nanoplastics (180 nm–125 μm) during drinking water treatment, Science of The Total Environment 720 (2020) 137383.
[373] S.J. Blott, K. Pye, Particle size distribution analysis of sand-sized particles by laser diffraction: an experimental investigation of instrument sensitivity and the effects of particle shape, Sedimentology 53(3) (2006) 671-685.
[374] P. Kippax, Measuring particle size using modern laser diffraction techniques, Chemie. De (2005) 1-2.
[375] C.M. Keck, R.H. Müller, Size analysis of submicron particles by laser diffractometry-90% of the published measurements are false, International journal of pharmaceutics 355(1) (2008) 150-163.
[376] N. Annabi, J.W. Nichol, X. Zhong, C. Ji, S. Koshy, A. Khademhosseini, F. Dehghani, Controlling the porosity and microarchitecture of hydrogels for tissue engineering, Tissue Engineering Part B: Reviews 16(4) (2010) 371-383.
[377] M. O'Neill, M.K. Haas, B.K. Peterson, R.N. Vrtis, S.J. Weigel, D. Wu, M.D. Bitner, E.J. Karwacki, Impact of pore size and morphology of porous organosilicate glasses on integrated circuit manufacturing, MRS Online Proceedings Library Archive 914 (2006).
[378] S. Dalai, S. Vijayalakshmi, P. Shrivastava, S.P. Sivam, P. Sharma, Preparation and characterization of hollow glass microspheres (HGMs) for hydrogen storage using urea as a blowing agent, Microelectronic Engineering 126 (2014) 65-70.
[379] C. Sun, D.J. Grant, Influence of crystal structure on the tableting properties of sulfamerazine polymorphs, Pharmaceutical research 18(3) (2001) 274-280.
[380] V.F. Lins, E.S. Cecconello, T. Matencio, Effect of the current density on morphology, porosity, and tribological properties of electrodeposited nickel on copper, Journal of Materials Engineering and Performance 17(5) (2008) 741-745.
[381] F. Semel, D. Lados, Porosity analysis of PM materials by helium pycnometry, Powder metallurgy 49(2) (2006) 173-182.
[382] S. Mane, Effect of porogens (type and amount) on polymer porosity: a review, Can. Chem. Trans 4(2) (2016) 210-225.
[383] I. Chang, Y. Zhao, Advances in powder metallurgy: Properties, processing and applications, Elsevier 2013.
[384] J.G. Yu, H. Guo, S.A. Davis, S. Mann, Fabrication of Hollow Inorganic Microspheres by Chemically Induced Self-Transformation, Advanced Functional Materials 16(15) (2006) 2035-2041.

[385] Y. Zhang, J. Li, W. Li, Effect of particle size on removal of sunset yellow from aqueous solution by chitosan modified diatomite in a fixed bed column, RSC Advances 5(104) (2015) 85673-85681.
[386] M. Zarezadeh-Mehrizi, A. Badiei, Highly efficient removal of basic blue 41 with nanoporous silica, Water Resources and Industry 5 (2014) 49-57.
[387] G. San Miguel, S.D. Lambert, N.J. Graham, A practical review of the performance of organic and inorganic adsorbents for the treatment of contaminated waters, Journal of Chemical Technology and Biotechnology 81(10) (2006) 1685-1696.
[388] H.K. Chae, D.Y. Siberio-Pérez, J. Kim, Y. Go, M. Eddaoudi, A.J. Matzger, M. O'keeffe, O.M. Yaghi, A route to high surface area, porosity and inclusion of large molecules in crystals, Nature 427(6974) (2004) 523-527.
[389] A.B. Dichiara, S.J. Weinstein, R.E. Rogers, On the Choice of batch or fixed bed adsorption processes for wastewater treatment, Industrial & Engineering Chemistry Research 54(34) (2015) 8579-8586.
[390] J. Broekhoff, Mesopore determination from nitrogen sorption isotherms: Fundamentals, scope, limitations, Studies in Surface Science and Catalysis, Elsevier 1979, pp. 663-684.
[391] S. Lowell, J.E. Shields, M.A. Thomas, M. Thommes, Characterization of porous solids and powders: surface area, pore size and density, Springer Science & Business Media 2012.
[392] Z.A. ALOthman, A review: fundamental aspects of silicate mesoporous materials, Materials 5(12) (2012) 2874-2902.
[393] M. Zhao, Z. Chen, X. Lv, K. Zhou, J. Zhang, X. Tian, X. Ren, X. Mei, Preparation of core–shell structured $CaCO_3$ microspheres as rapid and recyclable adsorbent for anionic dyes, Royal Society open science 4(9) (2017) 170697.
[394] T. Konishi, M. Mizumoto, M. Honda, Y. Horiguchi, K. Oribe, H. Morisue, K. Ishii, Y. Toyama, M. Matsumoto, M. Aizawa, Fabrication of novel biodegradable α-tricalcium phosphate cement set by chelating capability of inositol phosphate and its biocompatibility, Journal of nanomaterials 2013 (2013) 4.
[395] K.Y. Foo, B.H. Hameed, Insights into the modeling of adsorption isotherm systems, Chemical engineering journal 156(1) (2010) 2-10.
[396] A.W. Knight, A.B. Tigges, A.G. Ilgen, Adsorption of copper (II) on mesoporous silica: the effect of nano-scale confinement, Geochemical transactions 19(1) (2018) 1-13.
[397] O.A. Attallah, M.A. Al-Ghobashy, M. Nebsen, M.Y. Salem, Removal of cationic and anionic dyes from aqueous solution with magnetite/pectin and magnetite/silica/pectin hybrid nanocomposites: kinetic, isotherm and mechanism analysis, RSC advances 6(14) (2016) 11461-11480.
[398] N. Ayawei, A.N. Ebelegi, D. Wankasi, Modelling and interpretation of adsorption isotherms, Journal of chemistry 2017 (2017).
[399] A. Dada, A. Olalekan, A. Olatunya, O. Dada, Langmuir, Freundlich, Temkin and Dubinin–Radushkevich isotherms studies of equilibrium sorption of $Zn^{2+}$ unto phosphoric acid modified rice husk, IOSR Journal of Applied Chemistry 3(1) (2012) 38-45.
[400] D. Balarak, F.K. Mostafapour, H. Azarpira, A. Joghataei, Langmuir, Freundlich, Temkin and Dubinin–radushkevich isotherms studies of equilibrium sorption of ampicilin unto montmorillonite nanoparticles, Journal of Pharmaceutical Research International (2017) 1-9.
[401] E.A. Abou Neel, W. Chrzanowski, D.M. Pickup, L.A. O'Dell, N.J. Mordan, R.J. Newport, M.E. Smith, J.C. Knowles, Structure and properties of strontium-doped phosphate-based glasses, Journal of the Royal Society Interface 6(34) (2009) 435-446.
[402] D.S. Brauer, N. Karpukhina, R.V. Law, R.G. Hill, Effect of $TiO_2$ addition on structure, solubility and crystallisation of phosphate invert glasses for biomedical applications, Journal of non-crystalline solids 356(44-49) (2010) 2626-2633.
[403] L. Baia, D. Muresan, M. Baia, J. Popp, S. Simon, Structural properties of silver nanoclusters–phosphate glass composites, Vibrational spectroscopy 43(2) (2007) 313-318.
[404] S. Tunali Akar, T. Alp, D. Yilmazer, Enhanced adsorption of Acid Red 88 by an excellent adsorbent prepared from alunite, Journal of Chemical Technology & Biotechnology 88(2) (2013) 293-304.

[405] N. Yusof, K. Foo, B. Hameed, M.H. Hussin, H. Lee, S. Sabar, One-step synthesis of chitosan-polyethyleneimine with calcium chloride as effective adsorbent for Acid Red 88 removal, International Journal of Biological Macromolecules (2019).
[406] T.A. Saleh, The influence of treatment temperature on the acidity of MWCNT oxidized by HNO3 or a mixture of $HNO_3/H_2SO_4$, Applied surface science 257(17) (2011) 7746-7751.
[407] T.A. Saleh, Simultaneous adsorptive desulfurization of diesel fuel over bimetallic nanoparticles loaded on activated carbon, Journal of Cleaner Production 172 (2018) 2123-2132.
[408] H.M. Rootare, R.G. Craig, Characterization of the compaction and sintering of hydroxyapatite powders by mercury porosimetry, (1974).
[409] G. Müller, M. Nerding, N. Ott, H. Strunk, R. Brendel, Sintering of porous silicon, physica status solidi (a) 197(1) (2003) 83-87.
[410] S.D. Conzone, D.E. Day, Preparation and properties of porous microspheres made from borate glass, Journal of Biomedical Materials Research Part A: An Official Journal of The Society for Biomaterials, The Japanese Society for Biomaterials, and The Australian Society for Biomaterials and the Korean Society for Biomaterials 88(2) (2009) 531-542.
[411] D. Uhlmann, A kinetic treatment of glass formation, Journal of Non-Crystalline Solids 7(4) (1972) 337-348.
[412] I. Donald, Preparation, properties and chemistry of glass-and glass-ceramic-to-metal seals and coatings, Journal of materials science 28(11) (1993) 2841-2886.
[413] C. Combes, R. Bareille, C. Rey, Calcium carbonate–calcium phosphate mixed cement compositions for bone reconstruction, Journal of Biomedical Materials Research Part A: An Official Journal of The Society for Biomaterials, The Japanese Society for Biomaterials, and The Australian Society for Biomaterials and the Korean Society for Biomaterials 79(2) (2006) 318-328.
[414] M. Kruk, M. Jaroniec, K.P. Gadkaree, Determination of the specific surface area and the pore size of microporous carbons from adsorption potential distributions, Langmuir 15(4) (1999) 1442-1448.
[415] H. Saito, M. Higuchi, K. Katayama, Y. Azuma, Fabrication of sintered compacts of spherical mesoporous silica, Journal of materials science letters 22(20) (2003) 1419-1422.
[416] F. Silencieux, M. Bouchoucha, O. Mercier, S.p. Turgeon, P. Chevallier, F. Kleitz, M.-A. Fortin, Mesoporous Silica Nanoparticles under Sintering Conditions: A Quantitative Study, Langmuir 31(47) (2015) 13011-13021.
[417] K.Y. Chong, C.H. Chia, S. Zakaria, M.S. Sajab, Vaterite calcium carbonate for the adsorption of Congo red from aqueous solutions, Journal of Environmental Chemical Engineering 2(4) (2014) 2156-2161.
[418] W.-T. Tsai, K.-J. Hsien, H.-C. Hsu, C.-M. Lin, K.-Y. Lin, C.-H. Chiu, Utilization of ground eggshell waste as an adsorbent for the removal of dyes from aqueous solution, Bioresource technology 99(6) (2008) 1623-1629.
[419] A.I. Adeogun, R.B. Babu, One-step synthesized calcium phosphate-based material for the removal of alizarin S dye from aqueous solutions: isothermal, kinetics, and thermodynamics studies, Applied Nanoscience (2015) 1-13.
[420] Y.-S. Ho, G. McKay, Pseudo-second order model for sorption processes, Process biochemistry 34(5) (1999) 451-465.
[421] D. Schweich, M. Sardin, Adsorption, partition, ion exchange and chemical reaction in batch reactors or in columns—A review, Journal of Hydrology 50 (1981) 1-33.
[422] M. Jahangiri-Rad, A. Jamshidi, M. Rafiee, R. Nabizadeh, Adsorption performance of packed bed column for nitrate removal using PAN-oxime-nano $Fe_2O_3$, Journal of Environmental Health Science and Engineering 12(1) (2014) 90.
[423] A. Otaru, A.R. Kennedy, The permeability of virtual macroporous structures generated by sphere packing models: Comparison with analytical models, Scripta Materialia 124 (2016) 30-33.
[424] H. Gao, R. Cao, X. Xu, J. Xue, S. Zhang, T. Hayat, N.S. Alharbi, J. Li, Surface area-and structure-dependent effects of LDH for highly efficient dye removal, ACS Sustainable Chemistry & Engineering 7(1) (2018) 905-915.

[425] K. Dutta, A. Pramanik, Synthesis of a novel cone-shaped CaAl-layered double hydroxide (LDH): its potential use as a reversible oil sorbent, Chemical Communications 49(57) (2013) 6427-6429.
[426] D. Kang, X. Yu, M. Ge, Morphology-dependent properties and adsorption performance of $CeO_2$ for fluoride removal, Chemical Engineering Journal 330 (2017) 36-43.
[427] C.-X. Gui, Q.-Q. Wang, S.-M. Hao, J. Qu, P.-P. Huang, C.-Y. Cao, W.-G. Song, Z.-Z. Yu, Sandwichlike magnesium silicate/reduced graphene oxide nanocomposite for enhanced $Pb^{2+}$ and methylene blue adsorption, ACS applied materials & interfaces 6(16) (2014) 14653-14659.
[428] L.-g. Yan, L.-l. Qin, H.-q. Yu, S. Li, R.-r. Shan, B. Du, Adsorption of acid dyes from aqueous solution by CTMAB modified bentonite: kinetic and isotherm modeling, Journal of Molecular Liquids 211 (2015) 1074-1081.
[429] H. Deng, J. Lu, G. Li, G. Zhang, X. Wang, Adsorption of methylene blue on adsorbent materials produced from cotton stalk, Chemical Engineering Journal 172(1) (2011) 326-334.
[430] M. Ehrampoush, G. Ghanizadeh, M. Ghaneian, Equilibrium and kinetics study of reactive red 123 dye removal from aqueous solution by adsorption on eggshell, Journal of Environmental Health Science & Engineering 8(2) (2011) 101-106.
[431] J.M. Dias, M.C. Alvim-Ferraz, M.F. Almeida, J. Rivera-Utrilla, M. Sánchez-Polo, Waste materials for activated carbon preparation and its use in aqueous-phase treatment: a review, Journal of environmental management 85(4) (2007) 833-846.
[432] H. Gliemann, C. Wöll, Epitaxially grown metal-organic frameworks, Materials today 15(3) (2012) 110-116.
[433] H. Giesche, Mercury porosimetry: a general (practical) overview, Particle & particle systems characterization 23(1) (2006) 9-19.
[434] R. Han, Y. Wang, W. Yu, W. Zou, J. Shi, H. Liu, Biosorption of methylene blue from aqueous solution by rice husk in a fixed-bed column, Journal of hazardous materials 141(3) (2007) 713-718.
[435] H. Patel, Fixed-bed column adsorption study: a comprehensive review, Applied Water Science 9(3) (2019) 45.
[436] R. Singh, B. Ruj, A. Sadhukhan, P. Gupta, A TG-FTIR investigation on the co-pyrolysis of the waste HDPE, PP, PS and PET under high heating conditions, Journal of the Energy Institute 93(3) (2020) 1020-1035.
[437] J. Baltrusaitis, C.R. Usher, V.H. Grassian, Reactions of sulfur dioxide on calcium carbonate single crystal and particle surfaces at the adsorbed water carbonate interface, Physical Chemistry Chemical Physics 9(23) (2007) 3011-3024.
[438] S.K. Das, C. Dickinson, F. Lafir, D.F. Brougham, E. Marsili, Synthesis, characterization and catalytic activity of gold nanoparticles biosynthesized with Rhizopus oryzae protein extract, Green Chemistry 14(5) (2012) 1322-1334.
[439] A. Sharma, H. Jain, A. Miller, Surface modification of a silicate glass during XPS experiments, Surface and Interface Analysis: An International Journal devoted to the development and application of techniques for the analysis of surfaces, interfaces and thin films 31(5) (2001) 369-374.
[440] F. Sordello, G. Zeb, K. Hu, P. Calza, C. Minero, T. Szkopek, M. Cerruti, Tuning $TiO_2$ nanoparticle morphology in graphene–$TiO_2$ hybrids by graphene surface modification, Nanoscale 6(12) (2014) 6710-6719.
[441] H. Jiang, S. Zhao, X. Ma, S. Liu, Q. Shen, A fast π-π stacking self-assembly of cobalt terephthalate dihydrate and the twelve-electron lithiation-delithiation of anhydrous cobalt terephthalate, Journal of Power Sources 426 (2019) 23-32.
[442] H.W. Nesbitt, G.M. Bancroft, G.S. Henderson, R. Ho, K.N. Dalby, Y. Huang, Z. Yan, Bridging, non-bridging and free ($O^{2-}$) oxygen in $Na_2O$-$SiO_2$ glasses: An X-ray Photoelectron Spectroscopic (XPS) and Nuclear Magnetic Resonance (NMR) study, Journal of Non-Crystalline Solids 357(1) (2011) 170-180.
[443] J. Serra, P. González, S. Liste, C. Serra, S. Chiussi, B. León, M. Pérez-Amor, H. Ylänen, M. Hupa, FTIR and XPS studies of bioactive silica based glasses, Journal of Non-Crystalline Solids 332(1-3) (2003) 20-27.

[444] J.P. Jensen, A. Remmen, Enabling circular economy through product stewardship, Procedia Manufacturing 8 (2017) 377-384.
[445] M. Lieder, A. Rashid, Towards circular economy implementation: a comprehensive review in context of manufacturing industry, Journal of cleaner production 115 (2016) 36-51.
[446] O.J. Fisher, N.J. Watson, J.E. Escrig, R.L. Gomes, Intelligent Resource Use to Deliver Waste Valorisation and Process Resilience in Manufacturing Environments, Johnson Matthey Technology Review 64(1) (2020).
[447] B. Addis, Building with reclaimed components and materials: a design handbook for reuse and recycling, Routledge 2012.
[448] M. Garetti, M. Taisch, Sustainable manufacturing: trends and research challenges, Production planning & control 23(2-3) (2012) 83-104.
[449] Facts and Figures about Materials, Waste and Recycling, Environmental Protection Agency United States
[450] K. Miezah, K. Obiri-Danso, Z. Kádár, B. Fei-Baffoe, M.Y. Mensah, Municipal solid waste characterization and quantification as a measure towards effective waste management in Ghana, Waste Management 46 (2015) 15-27.
[451] H. Maekawa, T. Maekawa, K. Kawamura, T. Yokokawa, 29Si MAS NMR investigation of the $Na_2O$-$Al_2O_3$-$SiO_2$ glasses, Journal of Physical Chemistry 95(18) (1991) 6822-6827.
[452] J. Cheng, Z. Xiao, K. Yang, H. Wu, Viscosity, fragility and structure of $Na_2O$–CaO–$Al_2O_3$–$SiO_2$ glasses of increasing Al/Si ratio, Ceramics International 39(4) (2013) 4055-4062.
[453] L. Barbieri, A.M. Ferrari, I. Lancellotti, C. Leonelli, J.M. Rincón, M. Romero, Crystallization of ($Na_2O$–MgO)–CaO–$Al_2O_3$–$SiO_2$ glassy systems formulated from waste products, Journal of the American Ceramic Society 83(10) (2000) 2515-2520.
[454] R.K. Brow, C. Arens, X. Yu, D. Day, XPS study of iron phosphate glasses, (1994).
[455] A. Parsons, N. Sharmin, S.I. Shaharuddin, M. Marshall, Viscosity profiles of phosphate glasses through combined quasi-static and bob-in-cup methods, Journal of Non-Crystalline Solids 408 (2015) 76-86.
[456] D. Zimnyakov, R. Zdrajevsky, N. Minaev, E. Epifanov, V. Popov, O. Ushakova, Extreme Foaming Modes for SCF-Plasticized Polylactides: Quasi-Adiabatic and Quasi-Isothermal Foam Expansion, Polymers 12(5) (2020) 1055.
[457] J. König, R.R. Petersen, Y. Yue, Influence of the glass–calcium carbonate mixture's characteristics on the foaming process and the properties of the foam glass, Journal of the European Ceramic Society 34(6) (2014) 1591-1598.
[458] P.S. Kumar, T. Prot, L. Korving, K.J. Keesman, I. Dugulan, M.C. van Loosdrecht, G.-J. Witkamp, Effect of pore size distribution on iron oxide coated granular activated carbons for phosphate adsorption–Importance of mesopores, Chemical Engineering Journal 326 (2017) 231-239.
[459] O.T. Iorhemen, R.A. Hamza, J.H. Tay, Membrane bioreactor (MBR) technology for wastewater treatment and reclamation: membrane fouling, Membranes 6(2) (2016) 33.
[460] D. Beruto, L. Barco, A.W. Searcy, G. SPINOLO, Characterization of the porous CaO particles formed by decomposition of $CaCO_3$ and $Ca(OH)_2$ in vacuum, Journal of the American Ceramic Society 63(7-8) (1980) 439-443.
[461] J.C. Vaghetti, E.C. Lima, B. Royer, J.L. Brasil, B.M. da Cunha, N.M. Simon, N.F. Cardoso, C.P.Z. Noreña, Application of Brazilian-pine fruit coat as a biosorbent to removal of Cr (VI) from aqueous solution—Kinetics and equilibrium study, Biochemical Engineering Journal 42(1) (2008) 67-76.
[462] K. Boughzalaa, F. Koolib, N. Meksic, A. Bechrifad, K. Bouzouitae, Waste products from the phosphate industry as efficient removal of Acid Red 88 dye from aqueous solution: their regeneration uses and batch design adsorber, DESALINATION AND WATER TREATMENT 202 (2020) 410-419.
[463] D. Zhao, G. Sheng, J. Hu, C. Chen, X. Wang, The adsorption of Pb (II) on $Mg_2Al$ layered double hydroxide, Chemical Engineering Journal 171(1) (2011) 167-174.

[464] J. Pang, F. Fu, Z. Ding, J. Lu, N. Li, B. Tang, Adsorption behaviors of methylene blue from aqueous solution on mesoporous birnessite, Journal of the Taiwan Institute of Chemical Engineers 77 (2017) 168-176.
[465] J. Rouquerol, F. Rouquerol, P. Llewellyn, G. Maurin, K.S. Sing, Adsorption by powders and porous solids: principles, methodology and applications, Academic press 2013.
[466] L. Hou, Q. Liang, F. Wang, Mechanisms that control the adsorption–desorption behavior of phosphate on magnetite nanoparticles: the role of particle size and surface chemistry characteristics, RSC Advances 10(4) (2020) 2378-2388.
[467] H. Yan, H. Li, H. Yang, A. Li, R. Cheng, Removal of various cationic dyes from aqueous solutions using a kind of fully biodegradable magnetic composite microsphere, Chemical Engineering Journal 223 (2013) 402-411.
[468] W. Wang, K. Cai, X. Wu, X. Shao, X. Yang, A novel poly (m-phenylenediamine)/reduced graphene oxide/nickel ferrite magnetic adsorbent with excellent removal ability of dyes and Cr (VI), Journal of Alloys and Compounds 722 (2017) 532-543.
[469] T. Padmesh, K. Vijayaraghavan, G. Sekaran, M. Velan, Batch and column studies on biosorption of acid dyes on fresh water macro alga Azolla filiculoides, Journal of Hazardous Materials 125(1-3) (2005) 121-129.
[470] D. Balarak, Y. Mahdavi, Experimental and Kinetic Studies on Acid Red 88 Dye (AR88) Adsorption by Azolla Filiculoides, Biochem & Physiol 5(1) (2016) 1-5.
[471] S. Chen, Q. Yue, B. Gao, Q. Li, X. Xu, K. Fu, Adsorption of hexavalent chromium from aqueous solution by modified corn stalk: a fixed-bed column study, Bioresource technology 113 (2012) 114-120.
[472] A. Abdolali, H.H. Ngo, W. Guo, J.L. Zhou, J. Zhang, S. Liang, S.W. Chang, D.D. Nguyen, Y. Liu, Application of a breakthrough biosorbent for removing heavy metals from synthetic and real wastewaters in a lab-scale continuous fixed-bed column, Bioresource technology 229 (2017) 78-87.
[473] G. Nazari, H. Abolghasemi, M. Esmaieli, E.S. Pouya, Aqueous phase adsorption of cephalexin by walnut shell-based activated carbon: A fixed-bed column study, Applied Surface Science 375 (2016) 144-153.
[474] G. Bohart, E. Adams, Some aspects of the behavior of charcoal with respect to chlorine, Journal of the American Chemical Society 42(3) (1920) 523-544.
[475] H.C. Thomas, Heterogeneous ion exchange in a flowing system, Journal of the American Chemical Society 66(10) (1944) 1664-1666.
[476] X. Sun, T. Imai, M. Sekine, T. Higuchi, K. Yamamoto, A. Kanno, S. Nakazono, Adsorption of phosphate using calcined Mg3–Fe layered double hydroxides in a fixed-bed column study, Journal of Industrial and Engineering Chemistry 20(5) (2014) 3623-3630.
[477] G. Bohart, E. Adams, Behavior of charcoal towards chlorine, J. Chem. Soc 42(7) (1920).
[478] M. Ahmed, B. Hameed, Removal of emerging pharmaceutical contaminants by adsorption in a fixed-bed column: a review, Ecotoxicology and Environmental Safety 149 (2018) 257-266.
[479] S. Benjedim, L.A. Romero-Cano, A.F. Pérez-Cadenas, M.I. Bautista-Toledo, F. Carrasco-Marín, Removal of emerging pollutants present in water using an E-coli biofilm supported onto activated carbons prepared from argan wastes: Adsorption studies in batch and fixed bed, Science of The Total Environment 720 (2020) 137491.
[480] T.C. Egbosiuba, A.S. Abdulkareem, A.S. Kovo, E.A. Afolabi, J.O. Tijani, M.T. Bankole, S. Bo, W.D. Roos, Adsorption of Cr (VI), Ni (II), Fe (II) and Cd (II) ions by KIAgNPs decorated MWCNTs in a batch and fixed bed process, Scientific Reports 11(1) (2021) 1-20.
[481] H. Esfandian, A. Samadi-Maybodi, B. Khoshandam, M. Parvini, Experimental and CFD modeling of diazinon pesticide removal using fixed bed column with Cu-modified zeolite nanoparticle, Journal of the Taiwan Institute of Chemical Engineers 75 (2017) 164-173.

[482] Y. Zhang, F. Jin, Z. Shen, F. Wang, R. Lynch, A. Al-Tabbaa, Adsorption of methyl tert-butyl ether (MTBE) onto ZSM-5 zeolite: Fixed-bed column tests, breakthrough curve modelling and regeneration, Chemosphere 220 (2019) 422-431.
[483] A. Gupta, A. Garg, Adsorption and oxidation of ciprofloxacin in a fixed bed column using activated sludge derived activated carbon, Journal of environmental management 250 (2019) 109474.
[484] L. Tan, A. Shariff, K. Lau, M. Bustam, Factors affecting $CO_2$ absorption efficiency in packed column: A review, Journal of Industrial and Engineering Chemistry 18(6) (2012) 1874-1883.
[485] Z. Yang, T.-A. Asoh, H. Uyama, Removal of cationic or anionic dyes from water using ion exchange cellulose monoliths as adsorbents, Bulletin of the Chemical Society of Japan 92(9) (2019) 1453-1461.
[486] M. Jahangiri-Rad, A. Jamshidi, M. Rafiee, R. Nabizadeh, Adsorption performance of packed bed column for nitrate removal using PAN-oxime-nano $Fe_2O_3$, Journal of Environmental Health Science and Engineering 12(1) (2014) 1-5.
[487] N. Miralles, C. Valderrama, I. Casas, M.a. Martínez, A. Florido, Cadmium and lead removal from aqueous solution by grape stalk wastes: modeling of a fixed-bed column, Journal of Chemical & Engineering Data 55(9) (2010) 3548-3554.
[488] F. Kafshgari, A.R. Keshtkar, M.A. Mousavian, Study of Mo (VI) removal from aqueous solution: application of different mathematical models to continuous biosorption data, Iranian journal of environmental health science & engineering 10(1) (2013) 1-11.
[489] A. Aroonwilas, A. Veawab, Characterization and comparison of the $CO_2$ absorption performance into single and blended alkanolamines in a packed column, Industrial & engineering chemistry research 43(9) (2004) 2228-2237.
[490] H. Yu, S. Morgan, A. Allport, A. Cottrell, T. Do, J. McGregor, L. Wardhaugh, P. Feron, Results from trialling aqueous $NH_3$ based post-combustion capture in a pilot plant at Munmorah power station: Absorption, Chemical Engineering Research and Design 89(8) (2011) 1204-1215.
[491] M. Askari, E. Salehi, M. Ebrahimi, A. Barati, Application of breakthrough curve analysis and response surface methodology for optimization of a hybrid separation system consisting of fixed-bed column adsorption and dead-end depth filtration, Chemical Engineering and Processing-Process Intensification 143 (2019) 107594.
[492] S. Singh, V.C. Srivastava, I.D. Mall, Fixed-bed study for adsorptive removal of furfural by activated carbon, Colloids and Surfaces A: Physicochemical and Engineering Aspects 332(1) (2009) 50-56.
[493] Y.-H. Lee, J.-W. Lee, S.-Y. Yang, H. Lee, Y.-H. Koh, H.-E. Kim, Dual-scale porous biphasic calcium phosphate gyroid scaffolds using ceramic suspensions containing polymer microsphere porogen for digital light processing, Ceramics International (2020).
[494] S. Netpradit, P. Thiravetyan, S. Towprayoon, Evaluation of metal hydroxide sludge for reactive dye adsorption in a fixed-bed column system, Water research 38(1) (2004) 71-78.
[495] C. Qi, L. Zhao, Y. Lin, D. Wu, Graphene oxide/chitosan sponge as a novel filtering material for the removal of dye from water, Journal of colloid and interface science 517 (2018) 18-27.
[496] S. Dimitrova, Use of granular slag columns for lead removal, Water Research 36(16) (2002) 4001-4008.
[497] S. Zhang, T. Shao, H.S. Kose, T. Karanfil, Adsorption kinetics of aromatic compounds on carbon nanotubes and activated carbons, Environmental Toxicology and Chemistry 31(1) (2012) 79-85.
[498] M.H. Marzbali, M. Esmaieli, Fixed bed adsorption of tetracycline on a mesoporous activated carbon: Experimental study and neuro-fuzzy modeling, Journal of applied research and technology 15(5) (2017) 454-463.
[499] D. Li, Y. Wu, L. Feng, L. Zhang, Surface properties of SAC and its adsorption mechanisms for phenol and nitrobenzene, Bioresource technology 113 (2012) 121-126.
[500] Z. Yi, Q. Tang, T. Jiang, Y. Cheng, Adsorption performance of hydrophobic/hydrophilic silica aerogel for low concentration organic pollutant in aqueous solution, Nanotechnology Reviews 8(1) (2019) 266-274.

[501] W. Xie, D. Liang, L. Li, S. Qu, W. Tao, Surface chemical properties and pore structure of the activated coke and their effects on the denitrification activity of selective catalytic reduction, International Journal of Coal Science & Technology 6(4) (2019) 595-602.
[502] M. Suzuki, S. Maruyama, N. Umesaki, T. Tanaka, Hydroxyl-Group Identification Using O K-Edge XAFS in Porous Glass Fabricated by Hydrothermal Reaction and Low-Temperature Foaming, Molecules 24(19) (2019) 3488.
[503] Y. Liu, L. Xu, J. Liu, X. Liu, C. Chen, G. Li, Y. Meng, Graphene oxides cross-linked with hyperbranched polyethylenimines: preparation, characterization and their potential as recyclable and highly efficient adsorption materials for lead (II) ions, Chemical Engineering Journal 285 (2016) 698-708.
[504] H. Hongping, Y. Zhong, X. Liang, T. Wei, Z. Jianxi, C.Y. Wang, Natural Magnetite: an efficient catalyst for the degradation of organic contaminant, Scientific reports 5(1) (2015) 1-10.
[505] Y. Grosu, A. Faik, I. Ortega-Fernández, B. D'Aguanno, Natural Magnetite for thermal energy storage: Excellent thermophysical properties, reversible latent heat transition and controlled thermal conductivity, Solar Energy Materials and Solar Cells 161 (2017) 170-176.
[506] Z. Sun, X. Wu, C.K. Russell, M.D. Dyar, E.C. Sklute, S. Toan, M. Fan, L. Duan, W. Xiang, Synergistic enhancement of chemical looping-based CO 2 splitting with biomass cascade utilization using cyclic stabilized $Ca_2Fe_2O_5$ aerogel, Journal of materials chemistry A 7(3) (2019) 1216-1226.
[507] J. Fu, Q. Xin, X. Wu, Z. Chen, Y. Yan, S. Liu, M. Wang, Q. Xu, Selective adsorption and separation of organic dyes from aqueous solution on polydopamine microspheres, Journal of colloid and interface science 461 (2016) 292-304.
[508] F. Qiao, J. Wang, S. Ai, L. Li, As a new peroxidase mimetics: The synthesis of selenium doped graphitic carbon nitride nanosheets and applications on colorimetric detection of $H_2O_2$ and xanthine, Sensors and Actuators B: Chemical 216 (2015) 418-427.
[509] M. Šetka, R. Calavia, L. Vojkůvka, E. Llobet, J. Drbohlavová, S. Vallejos, Raman and XPS studies of ammonia sensitive polypyrrole nanorods and nanoparticles, Scientific reports 9(1) (2019) 1-10.
[510] A. Bhattacharyya, M.P. Schmidt, E. Stavitski, C.E. Martínez, Iron speciation in peats: chemical and spectroscopic evidence for the co-occurrence of ferric and ferrous iron in organic complexes and mineral precipitates, Organic Geochemistry 115 (2018) 124-137.
[511] K.S. Siow, L. Britcher, S. Kumar, H.J. Griesser, XPS study of sulfur and phosphorus compounds with different oxidation states, Sains Malaysiana 47(8) (2018) 1913-1922.
[512] S. Dhankhar, G. Bhalerao, S. Ganesamoorthy, K. Baskar, S. Singh, Growth and comparison of single crystals and polycrystalline brownmillerite $Ca_2Fe_2O_5$, Journal of Crystal Growth 468 (2017) 311-315.
[513] R. Rao, S. Singh, nitrogen incorporated photoactive Brownmillerite $Ca_2Fe_2O_5$ for energy and environmental Applications.
[514] D. Maity, S. Kale, R. Kaul-Ghanekar, J.-M. Xue, J. Ding, Studies of magnetite nanoparticles synthesized by thermal decomposition of iron (III) acetylacetonate in tri (ethylene glycol), Journal of Magnetism and magnetic Materials 321(19) (2009) 3093-3098.
[515] C. Bloed, J. Vuong, A. Enriquez, S. Raghavan, I. Tran, S. Derakhshan, H. Tavassol, Oxygen Vacancy and Chemical Ordering Control Oxygen Evolution Activity of $Sr_{2-x}Ca_xFe_2O_{6-\delta}$ Perovskites, ACS Applied Energy Materials 2(9) (2019) 6140-6145.
[516] A.P.d.S. Pereira, M.H.P.d. Silva, É.P. Lima Júnior, A.d.S. Paula, F.J. Tommasini, Processing and characterization of PET composites reinforced with geopolymer concrete waste, Materials Research 20 (2017) 411-420.
[517] F. Ahangaran, A. Hassanzadeh, S. Nouri, Surface modification of $Fe_3O_4$@$SiO_2$ microsphere by silane coupling agent, International Nano Letters 3(1) (2013) 23.
[518] P. Benjwal, M. Kumar, P. Chamoli, K.K. Kar, Enhanced photocatalytic degradation of methylene blue and adsorption of arsenic (iii) by reduced graphene oxide (rGO)–metal oxide ($TiO_2$/$Fe_3O_4$) based nanocomposites, Rsc Advances 5(89) (2015) 73249-73260.

[519] S. Rana, J. Philip, B. Raj, Micelle based synthesis of cobalt ferrite nanoparticles and its characterization using Fourier Transform Infrared Transmission Spectrometry and Thermogravimetry, Materials Chemistry and Physics 124(1) (2010) 264-269.
[520] L. Khanna, N.K. Verma, PEG/$CaFe_2O_4$ nanocomposite: Structural, morphological, magnetic and thermal analyses, Physica B: Condensed Matter 427 (2013) 68-75.
[521] Y. Xia, Q. Yao, W. Zhang, Y. Zhang, M. Zhao, Comparative adsorption of methylene blue by magnetic baker's yeast and EDTAD-modified magnetic baker's yeast: equilibrium and kinetic study, Arabian Journal of Chemistry 12(8) (2019) 2448-2456.
[522] G. Giakisikli, A.N. Anthemidis, Magnetic materials as sorbents for metal/metalloid preconcentration and/or separation. A review, Analytica chimica acta 789 (2013) 1-16.
[523] J. Oberteuffer, Magnetic separation: A review of principles, devices, and applications, IEEE Transactions on Magnetics 10(2) (1974) 223-238.
[524] D.H.K. Reddy, S.-M. Lee, Application of magnetic chitosan composites for the removal of toxic metal and dyes from aqueous solutions, Advances in colloid and interface science 201 (2013) 68-93.
[525] G. Shanmugam, Basic Mechanical Engineering, Tata McGraw-Hill 2000.
[526] J.H. Van Laar, I. Van der Walt, H. Bissett, J. Barry, P.L. Crouse, Spheroidisation of iron powder in a microwave plasma reactor, Journal of the Southern African Institute of Mining and Metallurgy 116(10) (2016) 941-946.
[527] Y.-W. Sheng, Z.-M. Guo, J.-J. Hao, D.-H. Yang, Effect of Spheroidization of Ti–6Al–4 V Powder on Characteristics and Rheological Behaviors of Gelcasting Slurry, Procedia Engineering 36 (2012) 299-306.
[528] L. Battezzati, A. Greer, The viscosity of liquid metals and alloys, Acta Metallurgica 37(7) (1989) 1791-1802.
[529] T. Ohji, M. Fukushima, Macro-porous ceramics: processing and properties, International Materials Reviews 57(2) (2012) 115-131.
[530] J. Shepherd, R. Friederichs, S. Best, Synthetic hydroxyapatite for tissue engineering applications, Hydroxyapatite (HAp) for Biomedical Applications, Elsevier 2015, pp. 235-267.
[531] B. Amorim, M. Morales, F. Bohn, A. Carriço, S. de Medeiros, A. Dantas, Synthesis of stoichiometric $Ca_2Fe_2O_5$ nanoparticles by high-energy ball milling and thermal annealing, Physica B: Condensed Matter 488 (2016) 43-48.
[532] J. Young, J.M. Rondinelli, Crystal structure and electronic properties of bulk and thin film brownmillerite oxides, Physical Review B 92(17) (2015) 174111.
[533] S. Dhankhar, K. Gupta, G. Bhalerao, N. Shukla, M. Chandran, B. Francis, B. Tiwari, K. Baskar, S. Singh, Anomalous room temperature magnetoresistance in brownmillerite $Ca_2Fe_2O_5$, RSC Advances 5(112) (2015) 92549-92553.
[534] Z. Su, Y. Zhang, Y. Chen, G. Li, T. Jiang, Reaction between CaO and $Fe_3O_4$ under CO–$CO_2$ Atmosphere at 800° C–1100° C, ISIJ International 57(1) (2017) 62-67.
[535] A. Hassankhani, From egg shell wastes (ESWs) into advanced materials: A rapid and simple synthesis of CaO/$Ca_2Fe_2O_5$ as a novel nanocomposite-derived ESW biomaterial, Journal of Advanced Materials and Processing 6(3) (2018) 26-33.
[536] M.S. Chan, W. Liu, M. Ismail, Y. Yang, S.A. Scott, J.S. Dennis, Improving hydrogen yields, and hydrogen: steam ratio in the chemical looping production of hydrogen using $Ca_2Fe_2O_5$, Chemical Engineering Journal 296 (2016) 406-411.
[537] A. Hassankhani, E. Mosaddegh, From egg shell wastes (ESWs) into advanced materials: A rapid and simple synthesis of CaO/$Ca_2Fe_2O_5$ as a novel nanocomposite-derived ESW biomaterial, Journal of Advanced Materials and Processing 6(3) (2018) 26-33.
[538] M. Ismail, W. Liu, M.T. Dunstan, S.A. Scott, Development and performance of iron based oxygen carriers containing calcium ferrites for chemical looping combustion and production of hydrogen, International journal of hydrogen energy 41(7) (2016) 4073-4084.

[539] M. Li, P.D. Christofides, Computational study of particle in-flight behavior in the HVOF thermal spray process, Chemical Engineering Science 61(19) (2006) 6540-6552.
[540] H. Xiong, L.-L. Zheng, S. Sampath, J. Fincke, Melting/Oxidation Behavior of In-Flight Particles in Plasma Spray Processes, ASME International Mechanical Engineering Congress and Exposition, 2002, pp. 317-326.
[541] R. Cossu, H.-J. Ehrig, A. Muntoni, Physical-chemical leachate treatment, (2019).
[542] H. Yan, H. Yang, A. Li, R. Cheng, pH-tunable surface charge of chitosan/graphene oxide composite adsorbent for efficient removal of multiple pollutants from water, Chemical Engineering Journal 284 (2016) 1397-1405.
[543] E. Illés, E. Tombácz, The role of variable surface charge and surface complexation in the adsorption of humic acid on magnetite, Colloids and Surfaces A: Physicochemical and Engineering Aspects 230(1-3) (2003) 99-109.
[544] W. Rongcheng, Q. Jiuhui, Removal of azo dye from water by magnetite adsorption–Fenton oxidation, Water environment research 76(7) (2004) 2637-2642.
[545] S. Giri, N. Das, G. Pradhan, Synthesis and characterization of magnetite nanoparticles using waste iron ore tailings for adsorptive removal of dyes from aqueous solution, Colloids and Surfaces A: Physicochemical and Engineering Aspects 389(1-3) (2011) 43-49.
[546] C.-C. Lin, Y.-S. Lin, J.-M. Ho, Adsorption of Reactive Red 2 from aqueous solutions using $Fe_3O_4$ nanoparticles prepared by co-precipitation in a rotating packed bed, Journal of Alloys and Compounds 666 (2016) 153-158.
[547] X. Wang, W. Li, R. Harrington, F. Liu, J.B. Parise, X. Feng, D.L. Sparks, Effect of ferrihydrite crystallite size on phosphate adsorption reactivity, Environmental science & technology 47(18) (2013) 10322-10331.
[548] I. Willett, C. Chartres, T. Nguyen, Migration of phosphate into aggregated particles of ferrihydrite, Journal of Soil Science 39(2) (1988) 275-282.
[549] L. O'Neill, C. Johnston, P.S. Grant, Enhancing the supercapacitor behaviour of novel $Fe_3O_4$/FeOOH nanowire hybrid electrodes in aqueous electrolytes, Journal of Power Sources 274 (2015) 907-915.
[550] S. Noreen, U. Khalid, S.M. Ibrahim, T. Javed, A. Ghani, S. Naz, M. Iqbal, ZnO, MgO and FeO adsorption efficiencies for direct sky Blue dye: equilibrium, kinetics and thermodynamics studies, Journal of Materials Research and Technology (2020).
[551] Y. Yang, Z. Cao, Y. Jiang, L. Liu, Y. Sun, Photoinduced structural transformation of $SrFeO_3$ and $Ca_2Fe_2O_5$ during photodegradation of methyl orange, Materials Science and Engineering: B 132(3) (2006) 311-314.
[552] S.G. Kumar, K.K. Rao, Zinc oxide based photocatalysis: tailoring surface-bulk structure and related interfacial charge carrier dynamics for better environmental applications, Rsc Advances 5(5) (2015) 3306-3351.
[553] B.C. Hodges, E.L. Cates, J.-H. Kim, Challenges and prospects of advanced oxidation water treatment processes using catalytic nanomaterials, Nature nanotechnology 13(8) (2018) 642-650.
[554] M. Pelaez, N.T. Nolan, S.C. Pillai, M.K. Seery, P. Falaras, A.G. Kontos, P.S. Dunlop, J.W. Hamilton, J.A. Byrne, K. O'shea, A review on the visible light active titanium dioxide photocatalysts for environmental applications, Applied Catalysis B: Environmental 125 (2012) 331-349.
[555] D.S. Vavilapalli, S. Banik, R.G. Peri, B. Muthuraaman, M. Miryala, M. Murakami, K. Alicja, K. Asokan, R. Rao, S. Singh, Nitrogen Incorporated Photoactive Brownmillerite $Ca_2Fe_2O_5$ for Energy and Environmental Applications, Scientific reports 10(1) (2020) 1-13.
[556] J. Guo, S. Yuan, W. Jiang, H. Yue, Z. Cui, B. Liang, Adsorption and photocatalytic degradation behaviors of rhodamine dyes on surface-fluorinated $TiO_2$ under visible irradiation, RSC advances 6(5) (2016) 4090-4100.